N° d'ordre:

Ecole Doctorale Mathématiques, Sciences de l'Information et de l'Ingénieur

UNISTRA – INSA – ENGEES

THESE

Présentée pour obtenir le grade de

Docteur de l'Université de Strasbourg
Discipline : Electronique, Electrotechnique, Automatique
Spécialité Photonique

Par

Andri ABDURROCHMAN

Photonic jet for spatial resolution improvement in direct pulse near-IR laser micro-etching

Soutenue publiquement le 15 septembre 2015

Membres du jury :

Rapporteurs externe :
- Philippe DELAPORTE, DR CNRS, Université d'Aix-Marseille
- Bruno SAUVIAC, Professeur, Université Jean Monnet

Examinateurs :
- Patrick MEYRUEIS, Professeur, Université de Strasbourg
- Bernard TUMBELAKA, Professeur, Université Padjadjaran, Indonésie

Directeurs de thèse :
- Joël FONTAINE, Professeur, INSA de Strasbourg
- Sylvain LECLER, MCF HDR, Université de Strasbourg

TABLE OF CONTENTS

TABLE OF FIGURES

INTRODUCTION

This thesis is the result of a three years investigation of the “photonic jet” (PJ) phenomenon and its potential use for direct laser etching. The work has been done in the context of collaboration between IPP (Photonics Instrumentation and Process) team of ICube laboratory of University of Strasbourg and Irépa Laser. The PhD scholarship has been funded by the Directorate General of Higher Education of Indonesian government from 2011 to 2015. The main objective of this thesis was to propose a new way to improve the spatial resolution of direct laser micro-processing for industrial applications.

Regardless of many advanced developments of laser systems technology, the proposed direct laser micro-processing methods employ existing nanosecond pulsed of near-infrared laser systems which are usually practiced in micro-marking, especially metallic marker. However, this thesis shows that by applying the PJ coming out of a glass microsphere, this type of laser is capable of reducing its spatial laser etching size on a silicon wafer down to more than 40 times smaller than a direct laser without PJ [1]. The laser that was used is a Trumpf VectorMark® Nd:YAG laser with 28 ns pulsed duration and a wavelength λ = 1064 nm. Moreover, with this laser and PJ, it is possible to etch a material with a high transmission in the IR, which would not be possible directly. We have used a slightly different laser, a 160 ns YLIA fiber laser with a wavelength of 1060 nm. It has been used to produce a PJ out of optical fibers with a spheroid tip with a core diameter of 100 and 200 µm. A direct laser etching on silicon wafer with a size of 1 µm has been produced.

These improvements can be explained by the fact that the PJ corresponds to a beam concentration on a small size that may go beyond the diffraction limit and extend along several wavelengths [2-4].

The possibility for the beam size to go beyond the diffraction limit has already known in some applications, such as scanning near-field optical microscopy [5-7], which are regarded as near-field optic phenomena. The difference between

PJ and near-field optic is that the PJ does not depend of evanescent waves.

1. Context of the research

Since its invention in 1960 the laser has been used for many applications which may be grouped into three according to the power requirement i.e.: optical uses, power uses (as in material processing) and ultrahigh power use for atomic fusion for example. In material processing, the laser must be reasonably powerful to be employed for cutting, welding, drilling or marking any kind of materials. The most popular systems for material processing are CO_2, Nd:YAG and fiber lasers [8]. Even so, each laser is unique and possesses some limitations. In theory the laser beam spot size is limited by the diffraction. PJ offers a way to overcome the diffraction limit.

There are many reported attempts to apply spatial optical concentration in the near-field for marking/engraving/etching various materials surface. Nevertheless, most of them make use of ultrafast laser systems (such as femto-/picosecond lasers) [9-14] or shorter wavelength lasers (visible to UV or near-UV) [9, 10, 13-18] or special environments [17], which are not cost-effective as required in industrial processes. UV lasers like excimers have the advantage that most materials absorb the energy but are expensive and delicate to use. Another drawback is that the components have limited lifetime.

In this thesis we have considered specifically nanosecond pulsed near-infrared lasers. Namely, these lasers are commonly used in industrial processes because their price is low and well-packaged sources are available. For this reason we have used such lasers to generate the PJ in our attempt to improve the spatial resolution of direct laser micro-processing. The possibilities of applying PJ for this improvement have been assessed by both simulations and experiments. First PJ etching has been achieved using glass microspheres, however, then, we have shown that PJ etching can be applied easily for direct laser micro-processing using an optical fiber with a spheroid tip. Even though the spatial resolution can still be improved, the possibility to reduce the spatial feature of PJ etching by spheroid tipped optical fiber using nanosecond pulse near-infrared laser down to a size of 1 µm has been experimentally demonstrated.

2. Thesis content

In order to understand how the PJ can improve the spatial resolution of direct laser micro-processing, this thesis is structured into four chapters.

In the first chapter, we mainly discuss the fundamental background in laser application for micro-processing. Accordingly, it will consider any possible interactions whenever laser beam affects materials. Any interaction which may occur basically depends on two groups of parameters that are the material and the laser parameters. The main material parameters considered in the interaction are optical absorption, melting threshold and laser-induced damage threshold. Whereas the typical laser parameters are wavelength, pulse durations, repetition rate and laser fluence. Since the experiments consider the

ns-pulsed near-infrared laser, the chapter continues with a discussion of Nd:YAG and yttribium-doped fiber (YLIA) lasers. This chapter will be finalized by previewing nanosecond infrared laser in the application of micro-processing.

In chapter two, the PJ concept will be defined, and its calculation methods will be described i.e. mainly the Mie theory and the finite element method. The term PJ, originally photonic nanojet, was coined in 2004 [2, 3] to describe the concentrated beam generated at the vicinity of a dielectric cylinder or sphere when it is illuminated by a light having a wavelength smaller than the size of the dielectric object. This phenomenon was expected to increase the resolution of optical microscopy. In this chapter, the PJ theoretical backgrounds are followed by some reported experimental works for micro-patterning. In addition to micro-etching, PJs have many other potential applications which will be reviewed: PJ microscopy, PJ for small propagation losses waveguide, PJ laser-surgery, fluorescence enhancement, PJ for nanoparticle detection and optical tweezers, also for increasing optical data storage.

The third chapter demonstrates the utility of the PJ for direct laser micro-etching and discusses the PJ interaction with matter. The chapter begins with the electromagnetic simulations of PJ coming out of microspheres in free-space. These simulations consider a beam source with a wavelength of 1 µm and microspheres with different diameter sizes. The PJ parameters obtained from these simulations are then compared to experiments considering:

- two types of laser source, i.e. 28 ns Nd:YAG laser with a wavelength of 1064 nm and 160 ns YLIA fiber laser with a wavelength of 1060 nm;
- two types of microsphere, i.e.: glass and barium-titanate microspheres, with different diameters;
- two types of etched materials, i.e.: silicon wafers and glass plates.

The ability of the PJ to improve direct laser etching using microspheres is demonstrated; on silicon wafer the etching lateral size is ~40 times smaller than without microsphere. Moreover, the PJ coming out of microspheres is also capable to leave an etching mark on glass plate, despite its low-absorbance to near-infrared light. Any different etching results that may occur are discussed depending on sphere sizes, laser properties and etched materials. The chapter concludes with the synthesis and the limitations of PJ etching using dielectric microspheres.

To get over the limitation of laser etching using microspheres, the fourth chapter deals with PJ etching using optical fiber. The structure of this chapter is almost similar to the previous one, but here the micro-spheres are replaced by elliptical tipped optical fibers. The main idea of changing microspheres with elliptical tipped optical fiber is to acquire more flexibility to move the PJ processing area and to control the distance between the tip and the material. The use of an optical fiber tip adds freedom degrees in the process and makes possible more applications of PJs for direct laser micro-processing. Before the discussion of PJ etching by spheroid tipped optical fiber attempts, the chapter begins by electromagnetic simulation of PJ coming out of elliptical tipped wave guide in free space. The possibility to achieve a PJ coming out of optical

waveguide is demonstrated. The theoretical background that must be taken into account to construct the geometrical shape of the elliptical-tipped optical fiber is discussed: basics of the used optical fiber and the definition of the optical fiber tip curvature and length. For the simulations discussed in this chapter, a source with a wavelength of 1 µm, four sizes of optical fiber core (10, 50, 100 and 200 µm) and two types of curvature (circular and elongated) are considered. The PJ parameters obtained from these simulations are used to design the spheroid-tipped optical fiber used for the experimental demonstrations. For practical considerations, the experimental works to achieve PJ etching using spheroid optical fiber have been carried out with a 160 ns fiber laser (YLIA) with a wavelength of 1060 nm. Experiments have been achieved on two types of material (i.e. silicon wafer and glass plates). As in simulation, three types of optical fiber have been considered for laser injection and photonic achievement:

- a single-mode silica fiber with a core diameter of 10 µm that is typically used for optical communication (SMF28),
- a multi-mode silica fiber with a core diameter of 50 µm (numerical aperture is 0.17),
- a multi-mode silica fiber with a core diameter of 100 µm (numerical aperture is 0.22),
- a TEQS$_{TM}$ coated multi-mode fiber with a core diameter of 200 µm with double optical cladding that is typically used for high power laser propagation (numerical aperture is 0.22).

It appears from our work, that by using an optical fiber, the PJ etching size is not as small as initially predicted by simulations, but has the potential to create patterns of the order of 1 µm.

References

[1] Abdurrochman, S. Lecler, F. Mermet, B. Y. Tumbelaka, B. Serio, and J. Fontaine, "PJ breakthrough for direct laser microetching using nanosecond near-infrared laser," *Applied Optics,* vol. 53, pp. 7202-7207, 2014.

[2] Z. G. Chen, A. Taflove, and V. Backman, "Photonic nanojet enhancement of backscattering of light by nanoparticles: a potential novel visible-light ultramicroscopy technique," *Optics Express,* vol. 12, pp. 1214-1220, Apr 2004.

[3] Z. G. Chen, A. Taflove, V. Backman, and Ieee, "Photonic nanojets," *Ieee Antennas and Propagation Society Symposium, Vols 1-4 2004, Digest,* pp. 1923-1926, 2004 2004.

[4] S. Lecler, Y. Takakura, and P. Meyrueis, "Properties of a three-dimensional PJ," *Optics Letters,* vol. 30, pp. 2641-2643, Oct 2005.

[5] D. W. Pohl, W. Denk, and M. Lanz, "Optical stethoscopy: Image recording with resolution l/20," *Applied Physics Letters,* vol. 44, pp. 651-653, 1984.

[6] R. C. Reddick, R. J. Warmack, and T. L. Ferrell, "New form of scanning optical microscopy," *Physical Review B,* vol. 39, pp. 767-770, 1989.

[7] E. Betzig and J. K. Trautman, "Near-Field Optics: Microscopy, Spectroscopy, and Surface Modification Beyond the Diffraction Limit," *Science,* vol. 257, pp. 189-195, 1992.

[8] W. M. Steen and J. Mazumder, *Laser Material Processing*, 4th ed. London: Springer-Verlag, 2010.

[9] H. J. Münzer, M. Mosbacher, M. Bertsch, J. Zimmermann, P. Leiderer, and J. Boneberg, "Local field enhancement effects for nanostructuring of surfaces," *Journal of Microscopy,* vol. 202, pp. 129-135, 2001.

[10] Y. F. Lu, L. Zhang, W. D. Song, Y. W. Zheng, and B. S. Luk'yanchuk, "Laser writing of a subwavelength structure on silicon (100) surfaces with particle-enhanced optical irradiation,"*Journal of Experimental and Theoretical Physics Letters,* vol. 72, pp. 457-459, 2000.

[11] N. Fukuda, K. Kunishio, and S. Nakayama, ""Dry-Etching System" with Q-switched DPSS Laser for Flat Panel Displays," *Journal of Laser Micro Nanoengineering,* vol. 2, pp. 241-246, Oct 2007.

[12] D. Grojo, L. Charmasson, A. Pereira, M. Sentis, and P. Delaporte, "Monitoring Photonic Nanojets from Microsphere Arrays by Femtosecond Laser Ablation of Thin Films," *Journal of Nanoscience and Nanotechnology,* vol. 11, pp. 9129-9135, Oct 2011.

[13] A. Plech, V. Kotaidis, M. Lorenc, and J. Boneberg, "Femtosecond laser near-field ablation from gold nanoparticles," *Nature Physics,* vol. 2, pp. 44-47, Jan 2006.

[14] A. Plech, P. Leiderer, and J. Boneberg, "Femtosecond laser near field ablation," *Laser & Photonics Reviews,* vol. 3, pp. 435-451, Sep 2009.

[15] S. M. Huang, M. H. Hong, B. S. Luk'yanchuk, Y. W. Zheng, W. D. Song, Y. F. Lu*, et al.*, "Pulsed laser-assisted surface structuring with optical near-field enhanced effects," *Journal of Applied Physics,* vol. 92, pp. 2495-2500, Sep 2002.

[16] W. Guo, Z. B. Wang, L. Li, D. J. Whitehead, B. S. Luk'yanchuk, and Z. Liu, "Near-field laser parallel nanofabrication of arbitrary-shaped patterns," *Applied Physics Letters,* vol. 90, p.3, Jun 2007.

[17] E. McLeod and C. B. Arnold, "Subwavelength direct-write nanopatterning using optically trapped microspheres," *Nature Nanotechnology,* vol. 3, pp. 413-417, Jul 2008.

[18] W. Wu, A. Katsnelson, O. G. Memis, and H. Mohseni, "A deep sub-wavelength process for the formation of highly uniform arrays of nanoholes and nanopillars," *Nanotechnology,* vol.18, Dec 2007.

I. DIRECT LASER MICRO-ETCHING

1. Introduction

Miniaturization is an important feature in modern trend. It requires sub-micron material processing resolution at low cost and fast realization in almost all manufacturing industries. In a view of this trend in miniaturization, micro-fabrication, i.e. micro-deposition and micro-machining or micro-etching, becomes a significant activity. This chapter will elaborate state of the art concerning micro-fabrication (i.e. micro-etching) using direct pulsed laser. It is because in micro-fabrication it contributes a truly enabling solution, reduces thermo-mechanical damages compared to continuous-wave laser, also facilitates the integration of heterogeneous components into functional systems. And laser is adjusted-flexible since laser can be set its power/fluence and repetition rate, also its wavelength and pulse width [1], for any material that is going to be processed. These processes are employed lasers to realize surface relief by pulsed ablation of material. And it is possible when laser-material interaction properties are well-known. So, the first section of this chapter will talk about the basis on laser-material interaction we need. The materials considered in our researches are silicon wafers and microscope glass-slides. The lasers are nanosecond pulsed near-infrared Nd:YAG and 160 fiber.

A. Microfabrication: Laser vs. other techniques

In the early 1960s, contact lithography – an early photo-lithography technique – was employed in developing integrated circuits. Then the dimension of integrated circuits has been shrinking at a rate of 30% smaller every three years, corresponding to Moore's law [2]. This progress is possible by adopting many methods to enhance the yield and throughput of photo-lithography patterning. And lasers technology is one of these methods, so-called laser direct writing which mainly for masking process.

The term laser direct writing is often used to call a material addition process by laser onto another or deposition, such as laser chemical vapor deposition (LCVD) or laser-induced forward transfer (LIFT) or laser-induced printing [1, 3]. All these deposition processes are not comprised in this chapter, which deals with ablative direct writing when material is removed (etched) in a sequential mode. So, we call this process direct laser micro-etching. This process has the same objective like chemical etching processes that proceeds photo-lithography: removing some part of material from surfaces. Chemical agents called etchants are classified as isotropic or anisotropic, and also as wet etching or dry etching. Wet etching is a process in which reaction products are released into a solution phase on the surface. Whilst dry etching is a process in which surface is volatilized by chemical reaction [4]. And direct laser etching is ideally an isotropic dry etching process.

Nowadays the chemical-free and low-cost manufacturing has a great deal interest in industry. This leads to new invention for surface micro-fabrication: ion beams, electron beams and near-field optics [5-8] are chemical-free process with high resolution but too expensive and have to proceed in vacuum. In opposite, laser dry etching (LDE) is very useful for selective removal of thin film, has less post-processes, low operational-cost and low pollution excess [9]; also

it can be proceeded in ambient air [10]. The method allows precisely control the position in the material and the energy rate applied [11]. Other common advantages of laser surfacing compared to alternative process are mentioned in [12]:

- Chemical cleanliness;
- Controlled thermal penetration and therefore distortion;
- Controlled thermal profile and therefore shape and location of the heat affected zone (HAZ);
- Less after-machining, if any, is required;
- Remote noncontact processing is usually possible;
- Relatively easy to automate.

Therefore, for industrial context, these reasons justify our choice to consider LDE method in this thesis.

B. Existing power laser

Laser is an acronym from “light amplification by stimulated emission radiation”. The concept of laser was first published by Arthur Schawlow and Charles Towns in 1958 and the first working ruby laser was invented by Theodore Harold “Ted” Maiman in 1960. Laser is entirely due to the stimulated emission phenomenon, which has been predicted by Einstein since 1916 using mathematical argument and was confirmed in 1928 by observing negative absorption in Ladenburg’s spectroscopic work. The outline history of the invention of laser has been summarized by William M. Steen [12] from the book of “Laser Pioneers” by Jeff Hetch.

For material processing the laser must be reasonably powerful, which reduces the number of eligible lasers to only a few. Washio summarized some laser devices for micro-fabrication applications capable of operating in wavelength region from ultraviolet (UV) class to infrared (IR) class [13]. These lasers, including their features, are listed in Table 1.1.

Table 1.1. Some power-laser devices for micro-fabrication applications

Active medium/species (center wavelength)	**Physical states**	**Excitation methods**	**Features**
ArF (193 nm) **KrF (248 nm)** **XeCl (308 nm)**	Gas (excimer)	Electric discharge	High energy, ns pulses, low-repetition rate (less than several kHz)
Nonlinear crystals (visible or UV)	Solid state	Pumping by high-power IR lasers	Harmonic generation with nonlinear optic
Ti: Al_2O_3 (800 nm) **Nd:YAG (1064 nm)** **Nd:YVO_4 (1064 nm)** **Yb:YAG (1030 nm)** **Yb:glass fiber (~1060 nm)**	Solid State	Optical pumping	Capable of ultrafast emission Wide variety of operation modes Wide variety of operation modes Wide variety of operation modes Efficient and high beam quality
CO_2 (10.6 or 9.4 μm)	Gas (molecular)	Electric discharge	Efficient and high power in mid IR

Table 1.1 shows some lasers devices for micro-fabrication application. It shows three types of which corresponding to the wavelength class UV, visible/near-IR and far-IR. Understanding the lasers features may also be useful in studying laser-material interaction. The name excimer comes from “excited

dimer". Laser emission in rare gas halogen excimer was reported for the first time in 1975 for XeBr (281.8 nm) and XeF (354 nm). The pulse duration of typical discharge pumped excimer lasers used for material processing are in the range of 5 ns to100 ns and repetition rate up to 6 kHz with an average power up to 90 W have become now available. Although excimer lasers have some attractive features, its complexity, high cost and limited repetition rate are drawback for some practical applications [13].

Most solid-state lasers emit the spectral radiation in a region of 400 nm to 3 μm. Their host materials may be grouped into crystalline solids and glasses. Ti:Al_2O_3 lasers have a broad emission tunable band between 670 and 1070 nm and they are most widely used in the scientific research but tend to be expensive for industrial use. Whilst, neodymium-doped lasers (Nd:YAG and Nd:YVO_4 lasers) and ytterbium-doped lasers (Yb:YAG and YB:glass fiber) are high importance lasers because of their excellent lasing properties in term of energy efficiency, maximum output power and pulse operation capability. Therefore, these rare-earth solid-state lasers are more practical than Ti:Al_2O_3 lasers. For these reasons, two nanosecond pulsed lasers that usually used in industrial laser application have been considered in this thesis: Nd:YAG laser and Ytterbium fiber-laser. Therefore we will contemplate the main physical parameters which link these laser and material up.

At the other hand, CO_2 lasers, with operating wavelength at 10.6 μm, are also well suited for micro-processing for alumina ceramics scribing and marking on plastic packages. Introducing radio-frequency exciting method add CO_2 lasers capability with large peak power enhancement up to 38 times the continuous wave (CW) power level; and pulse width reduction as short as 10 μs. And by controlling waveguide loss in the laser resonator the wavelength of CO_2 laser shift to 9.4 μm. This wavelength operating mode is substantial because there are many materials, e.g. polyimide, which exhibit higher absorption at 9.4 μm than 10.6 μm wavelength and can be processed with better quality and faster speed.

2. Laser-material interaction

Laser-material interaction depends on both the laser and the material condition [11]. For the basis in discussing laser-material interactions, first we will discuss the fundamental of laser energy absorption by material, and mainly we consider silicon wafer and glass.

A. Fundamentals of laser energy absorption by material

In first view, the fundamental equations in light propagation and material responses are the Maxwell equations. The light is described as electromagnetic fields (E, H), whereas the material response is described by the dielectric permittivity ε and the magnetic permeabilityμ. For macroscopically uniform materials, which ε and μ are constants independent of position, the following relations are:

$$\nabla \times \vec{E} = -\frac{\partial \vec{B}}{\partial t} \quad (1.1)$$

$$\nabla \times \frac{\vec{B}}{\mu} = \vec{J_0} + \varepsilon \frac{\partial \vec{E}}{\partial t} \quad (1.2)$$

$$\nabla . \vec{D} = \rho \quad (1.3)$$

$$\nabla . \vec{B} = 0 \quad (1.4)$$

with, $\vec{D} = \varepsilon_o(1+\chi)\vec{E} = \varepsilon_r\varepsilon_o\vec{E} = \varepsilon\vec{E}$, $\vec{B} = \mu\vec{H} = \mu_r\mu_o\vec{H}$ and $\vec{J} = \sigma\vec{E}$.

For our case, dielectric permittivity of silicon wafer is 3.45 x 10^{-11} F/m [14].

a) Boundary condition

In free-space/vacuum, the Maxwell's equations have a simple traveling plane solution with the fields ($\vec{E}$ and $\vec{H}$) orthogonal to each other and to the propagation direction.

When the laser arrives on the surface of material, at this sharp and distinct interface between two mediums, medium 1 (ε_1 and μ_1) and medium 2 (the material: ε_2 and μ_2), the wavefront of laser has to satisfy the boundary conditions [15]. If the local normal at the interface pointing into medium 1 is:

$$\vec{n}_{21}.(\vec{B}_2 - \vec{B}_1) = 0 \quad \text{or} \quad (1.5)$$

$$\vec{n}_{21}.(\vec{D}_2 - \vec{D}_1) = \sigma_S \quad (1.6)$$

with $\vec{D}$ is equal to σ_S in magnitude.

These boundary conditions (1.5) and (1.6) may be expressed as

$$B_{2n} = B_{1n}, \quad (1.7)$$

$$D_{2n} - D_{1n} = \sigma_S\,, \quad (1.8)$$

with $B_{2n} = \vec{n}_{21}.\vec{B}_2$, $B_{1n} = \vec{n}_{21}.\vec{B}_1$, $D_{2n} = \vec{n}_{21}.\vec{D}_2$ and $D_{1n} = \vec{n}_{21}.\vec{D}_1$ which mean that the normal components of $\vec{B}$ are always continuous and the normal components of $\vec{D}$ is equal to the surface charge density σ_S.

Now the contour integral of $\vec{E}$ becoming:

$$\vec{n} \times (\vec{E}_2 - \vec{E}_1) = 0\,. \quad (1.9)$$

When the same procedure is also applied to equation (1.2), resulting:

$$\vec{n} \times (\vec{H}_2 - \vec{H}_1) = \vec{K}\,. \quad (1.10)$$

for $\vec{K}$ is the surface current density. These boundary conditions (1.9) and (1.10) may be expressed as:

$$E_{2t} = E_{1t} \quad (1.11a)$$

$$H_{2t} - H_{1t} = K_t, \quad (1.11b)$$

Thus, the tangential component of $\vec{E}$ is always continuous at the boundary

interface and the difference between the tangential components of $\vec{H}$ is equal to the line current density. Consequently, the normal components of $\vec{D}$ and $\vec{B}$, and the tangential components of $\vec{E}$ and $\vec{H}$ are continuous across interface separating medium.

Because of these boundary conditions, a part of the incident light will be reflected. The reflectance is given by the Fresnel's law:

$$R = \frac{(n_0 - n_1)^2}{(n_0 + n_1)^2} . \tag{1.12}$$

In this thesis, the incident angle is perpendicular to the surface. Hence equation (1.12) is adequate to calculate the reflectance of the laser beam incidence on our concerned materials. Therefore the reflectance of silicon wafer ($n_1 = 3.4$ [16]) and glass ($n_1 = 1.5$) are 30% and 4%, respectively.

b) Energy balance

At this interface the laser-material interactions are occurred when the laser energy is absorbed into the material. The laser carries energy in the form of electromagnetic radiation. The total rate of work per unit volume is $\vec{J} \cdot \vec{E}$. The energy balance can be expressed as:

$$\frac{\partial U}{\partial t} + \nabla \cdot \vec{\boldsymbol{S}} = -\vec{J} \cdot \vec{E} , \tag{1.13}$$

where U represent the energy density of the electromagnetic field that has units of [J/m^3]:

$$U = \frac{1}{2}\left(\vec{E} \cdot \vec{D} + \vec{B} \cdot \vec{H}\right) . \tag{1.14}$$

And $\vec{\boldsymbol{S}}$ is Poynting vector that has units of [W/m^2]:

$$\vec{\boldsymbol{S}} = \vec{E} \times \vec{H} . \tag{1.15}$$

Hence, the quantity $\nabla \cdot \vec{\boldsymbol{S}}$ indicates the net electromagnetic power flowing out of a unit volume.

The laser energy absorption into material is determined by the material's optical properties, that is the complex refractive index $n^c = n - \mathrm{i}k$, which depends on laser wavelength λ and the material temperature T. The absorption depth is $d_{abs} = {}^{1}/_{\gamma} = {}^{\lambda}/_{(4\pi k)}$. In our case, at λ = 1064 nm, the absorption depth for silicon wafer is 900 μm [17]. Thus the volumetric energy intensity absorbed by the material at a depth z from the surface is,

$$Q_{\mathrm{ab}}(x, y, z, t) = (1 - R) I(x, y, t) \gamma e^{-\gamma |z|}, \tag{1.16}$$

where *R* is the material surface reflectivity in equation (1.12). Generally, for a temperature-dependent absorption coefficient the energy absorbed is

$$Q_{\mathrm{ab}}(x, y, z, t) = \big(1 - R(T_s)\big) I(x, y, t) \gamma\big(T(z)\big) \exp\left[-\int_0^z \gamma\big(T(z')\big) \mathrm{d}z'\right] \tag{1.17}$$

for T_s is the surface temperature. The sudden thermal gradient into the

material causes nonlinear effects that will shift the absorbed-energy profile. For the rough surfaces (RMS roughness > λ/2) the absorption is complicated because of the light scattering. The light propagation in the nonhomogeneous material is also subject to volumetric scattering. Surface oxides may also affect the material absorptivity. Finally for ultra-small particles and thin material less than 1/λ, the concept of the complex refractive index is inadequate for describing laser energy absorption. In this case the excitation of plasmons and electrons scattering can be dominant [1]. In this thesis, the materials are considered as the bulk material with low roughness and no volumetric scattering.

c) Thermal effect

For nanosecond of longer laser pulses, the electrons and the lattice are at thermal equilibrium, characterized by a common temperature T. The transient temperature field can then be calculated by solving the heat-conduction equation

$$\rho C_p(T)\frac{\partial T}{\partial t} = \nabla \cdot (K(T)\nabla T) + Q_{\text{ab}}(x,y,z,t) \tag{1.18}$$

where ρ, C_p, K and T represent density, specific heat for constant pressure, thermal conductivity and temperature, respectively. But for a first estimate, constant thermal properties may be assumed in order to derive approximate analytical solutions. For a laser impact on the material surface, $z = 0$, a bulk substrate of thickness d and initial temperature T_0, the initial condition for the heat-transfer problem is $T(t = 0) = T_0$, and the boundary condition are

$$K\frac{\partial T}{\partial xz}|_{z=0} = h_{conv,u}(T(x,y,0,t) - T_\infty) + \varepsilon_{em,u}\sigma_{SB}(T(x,y,0,t)^4 - T_\infty^4) \tag{1.19}$$

$$K\frac{\partial T}{\partial xz}|_{z=d} = h_{conv,L}(T(x,y,d,t) - T_\infty) + \varepsilon_{em,L}\sigma_{SB}(T(x,y,d,t)^4 - T_\infty^4) \tag{1.20}$$

Here, $h_{conv,u}$ and $h_{conv,L}$are the coefficients for linear convective heat transfer from the top and bottom surface of the material, $\varepsilon_{em,u}$ and $\varepsilon_{em,L}$ are the corresponding emissivity, σ_{SB} is the Stefan-Boltzmann constant and T_∞ is the ambient temperature.

The thermal-diffusion penetration depth into the material is given by $d_{th} = \sqrt{\alpha.t_{pulse}}$, where α is the thermal diffusivity, $\alpha = K/(\rho C_p)$, and $t_{pulse}$is the pulse duration. For d is the thick of material, if $d_{th} \ll d$ and $d_{abs} \ll d$ then the material can be considered semi-infinite. If $d_{abs}/d_{th} \ll 1$ then the absorption of laser radiation is essentially a skin surface phenomenon, which is a valid approximation for metals irradiated by laser pulses of duration longer than nanoseconds. Barring plasma effects, the efficiency of energy coupling with the materials is in this case to a considerable degree determined by the surface reflectivity. For metals, the surface reflectivity is high in the IR range, typically over 0.90 for > 5 μm, but it may be lower in the near-IR and visible ranges[18, 19]. Upon melting, the absorptivity is enhanced in a step-wise manner [20]. If the absorption coefficient is weak and $d_{abs}/d_{th} \gg 1$, radiation penetrates deeper into the material, giving rise to shallower thermal gradients and a more

uniform temperature field.

Concerning our research, if the thermal diffusivity of silicon is 1.02 cm²/s [16], the ratio d_{abs}/d_{th} of silicon is much higher than one, which will lead to shallower thermal gradients and uniform temperature field.

Analytical expressions for increasing temperature induced by Gaussian intensity of laser (on the basis of 1/e intensity, $w = w_{1/e}$, for w is the Gaussian beam waist) on semi-infinite materials, finite slabs and thin films are given in [21] and [22]. When the laser is Gaussian cross section is considered, the heat flow is perpendicular to the surface direction if the laser radius is larger than the thermal depth, $w \gg \sqrt{\alpha . t_{pulse}}$. In contrary condition, $w \ll \sqrt{\alpha . t_{pulse}}$, the heat source may be considered as a point source. In our research, the beam waists of laser source are 32.2 µm for Nd:YAG laser and 45.8 µm for YLIA laser; which higher than d_{th}, so our laser source cannot be considered as a point source.

More complex expressions of laser energy absorption into material can be derived using Green-function methods [23]. For fast estimation and because the ratio d_{abs}/d_{th} of our silicon is much higher than one, the estimate peak surface temperature at the end of one laser pulse [1]:

$$T_{\mathrm{su,pk}} = \frac{(1-R)E_{\mathrm{pulse}}}{\rho C_p d_{abs} \pi w^2} \ . \tag{1.21}$$

We can see from (1.21) that this temperature is in direct proportional to the laser pulse energy. And $E_{\mathrm{pulse}}/\pi w^2$ is also known as the laser fluence. In our case the laser fluence of Nd:YAG laser and YLIA laser at focal point are 16.9J/cm² and 14.3 J/cm², respectively. If we submit the silicon wafer properties: ρ = 2330 kg/m^3, C_p = 710 J/(kg.K) and equation (1.12) for *R*, hence the estimate peak surface temperature on silicon wafer for these two lasers, respectively, are 846 K and 719 K (eq. 1.21). These peak temperatures are below the melting temperature of silicon wafer, T_m = 1683 K [16], therefore it will need subsequent pulses. This estimated surface temperature is also known as the temperature rise of the surface by defining the time for inception of melting t_m, using the expression [1] :

$$T_{su}(t_m) = T_m \ . \tag{1.22}$$

So that for high repetition rate, the initial pulse shall rise-up the surface temperature, next preceding pulses shall rise it up again until it reaches the melting temperature. Therefore, next section will discuss laser fluence in correlation to material properties such as threshold melting and fluence of material.

B. Laser fluence versus melting threshold of material

Among material properties, it is important to understand laser-material interaction, we have already listed: optical reflectance & transmittance, thermal conductivity, but there are also the melting point and the laser-induced damage threshold (LIDT). The material surface response to an incidence laser depends on the material and the laser conditions [11]. We will first consider ratio between laser fluence and material's melting threshold.

If the center of the laser beam reaches the melting point T_m of the material, the a damage threshold of material can be approximated [16] by:

$$E_D = C_p(T_m - T_a)/\gamma \quad , \tag{1.23}$$

where C_p and γ are the specific heat and absorption coefficient of material, and T_a is the ambient temperature.

A variety of temperature dependent processes within the material are activated despite the laser fluence is lower than the threshold melting of material. The heating processes enhance diffusion doping or reorganization of the crystal structure [24], sinter porous materials [25] and also increase reaction kinetics beyond room temperature rates [11]. Another activated family processes are rapid transformations to high temperature. These processes can lead to rapid self-quenching of the material. Also, they can induce thermal stresses and thermo-elastic excitation of acoustic waves [26] which can contribute to the material hardening, warping or cracking.

When the laser fluence became higher than the threshold melting of material, the surface can be melted which will lead to formation of transient pools of molten material. The molten material will support much higher atomic mobility and solubility resulting in rapid material homogenization. It also supports high self-quenching rates with solidification velocities up to several m/s [12, 27]. Fast re-solidification may result in defects, supersaturated solutes [28] and form metastable material phases. On contrary, slower re-solidification rates can allow recrystallization of larger grains than the origin. But it must be note, in all these cases it only molten the material, no etching is realized.

The enthalpy functions are used to account for phase change. H_s is enthalpy value of solid material and H_l is enthalpy value of pure liquid; both are at melting temperature.

The heat-conduction equation (1.18) is written

$$\frac{\partial H}{\partial t} = \nabla \cdot (K(T)\nabla T) + Q_{\text{ab}}(x, y, z, t). \tag{1.24}$$

This scheme can be readily implemented numerically used explicit or implicit schemes in multi-dimensional domains [29].

The melt depth induced by laser is depended on the threshold fluence necessary to melt the surface. This threshold can be calculated like we have been done before for silicon wafer and the laser sources we considered in our researches base on equation (1.23). This threshold fluence also has been estimated in [1] as:

$$F_{th,m} = \frac{1}{2(1-R)}\sqrt{\frac{\pi}{\alpha}}K(T_m - T_0)\sqrt{t_{pulse}}\,, \tag{1.25}$$

where T_0 is the surface temperature before a laser pulse irradiation with pulse length t_{pulse}. It shows that faster pulsed lasers will decrease the threshold fluence of material for which $d_{abs} << d_{th}$.

Moreover, the maximum melt depth, $d_{l,max}$, also has been estimated in [21]

according to the threshold fluence (1.25):

(a) for laser fluence, F, near $F_{th,m}$

$$d_{l,max} \approx \sqrt{\frac{\alpha t_{pulse}}{\pi}} \frac{F - F_{th,m}}{F_{th,m}} \; ; \tag{1.26}$$

(b) for $F > F_{th,m}$

$$d_{l,max} \approx \sqrt{\alpha t_{pulse}} \left[\ln \left(\frac{F - F_{th,m}}{F_{th,m}} \right) \right]^{\frac{1}{2}} \approx \sqrt{\alpha t_{pulse}} \left(\frac{F - F_{th,m}}{F_{th,m}} \right)^{\frac{1}{2}} ; \tag{1.27}$$

(c) for $F \gg F_{th,m}$ but below the vaporization fluence

$$d_{l,max} \approx \frac{(1 - R)F - q_{los}}{\rho C_p (T_m - T_0) + L_{sl}}, \tag{1.28}$$

where q_{los} is the total heat loss.

Ablation starts at a fluence level close to melting threshold where a small amount of high velocity ions exit the surface; this is referred as gentle ablation [30].

When the surface temperatures is far above the melting temperature, hydrodynamic motion can reshape and redistribute material which will develop in melt pools and causing convective flows [27]. This convective and thermo-capillary force can cause significant deformations that are frozen during solidification. It will emerge a variety of shapes (Figure 1.1) such as rimmed indentations, sombrero shaped craters, and even nanometer scale tips [31, 32].

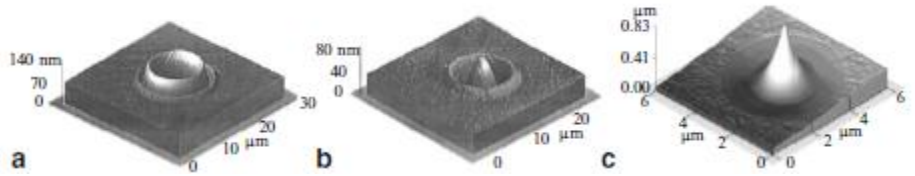

Figure 1.1. AFM images of the surface deformation recorded on Ni-P hard-disk substrate at (a) high energy, (b) intermediate energy [31] and (c) 0.8 μm nano-tip formed on Si – silicon on insulator [32]

C. Laser fluence versus ablation threshold fluence of material

Ablation is occurred when some part of material is removed by direct absorption of laser energy without molten the material. The material is experienced direct evaporation where the laser beam is converted to liberate atomic material from the bulk surface [1]. Laser ablation is usually discussed in the context of pulsed lasers [11], especially ultra-fast lasers such picosecond (ps) and femtosecond (fs) lasers. In this case, the laser fluence must be higher than the necessity fluence in equation (1.25), which can be regarded as the threshold fluence of material. Moreover, the ablation process is dependent to some parameters [11, 33], such:

- The absorption mechanism.
- Particular material properties: microstructure, morphology, the presence of defects.
- Laser parameters: wavelength, fluence and pulse duration.

For low laser fluence the ablation will be accompanied with others processes like evaporation and sublimation. As for higher fluence, it will cause heterogeneous nucleation of vapor which leads to normal/explosive boiling carrying off solid and liquid material fragments [11].

For a surface absorber, $1/\gamma \ll \sqrt{\alpha t_{pulse}}$ (this is not a part of our studies), simple energy-balance consideration give the following estimate for the material-removal depth,

$$d_{abl} = \frac{(1-R)(F-F_{sh}) - q_{los}}{\rho C_p\left(T_{bp} - T_0\right) + L_{sl} + L_{lv}}, \tag{1.29}$$

where F_{sh} represents the fluence loss due to plasma shielding. This estimation is more appropriate for short pulses, since conduction losses become more significant for longer pulses. For laser intensity $I < 10^8$ W/cm^2, energy absorption by evaporated particles is insignificant, so they may be considered transparent [1].

When excitation time is less than the thermalization time in material, the process of non-thermal of photochemical ablation is occurred. The thermalization time is the time needs for material to reach thermal balance. For example, if we use an ultrafast pulses laser there will be direct ionization and the deformation in the material which lead to thermal phase transformation, direct bond breaking and explosive disintegration (Coulomb explosion) [35].

The material removal is a continuous process. However, as the temperature of liquid surface increases, the ablation rate also rises steeply. For nanosecond pulsed laser, the duration of melting is in the order of a few tens of nanoseconds. Hydrodynamics motion due to the melt instability caused by the acceleration of molten phase following the volumetric expansion upon melting may thus develop over hundreds of pulses [36, 37].

The material removal is accompanied by a highly direct plume ejection, also contained solid and liquid clusters. At high intensities, a cluster may become ionized, producing plasma. For laser pulses longer than picosecond, interaction between the laser beams with the plume may be significant. The plume can absorb and scatter radiation, changing the actual laser intensities received by the surface. In nanosecond ablation, shielding plume can reduce the energy absorption. Figure 1.2 shows the schematic illustration of ablation processes under long pulsed and ultrafast pulsed laser. When the laser beam is engineered so it develops higher light concentration, such as the photonic jet, a smaller etching on material also can be obtained [5, 38-42]. It is because the smaller beam yielded by photonic jet reduces the contact-area between the beam and material.

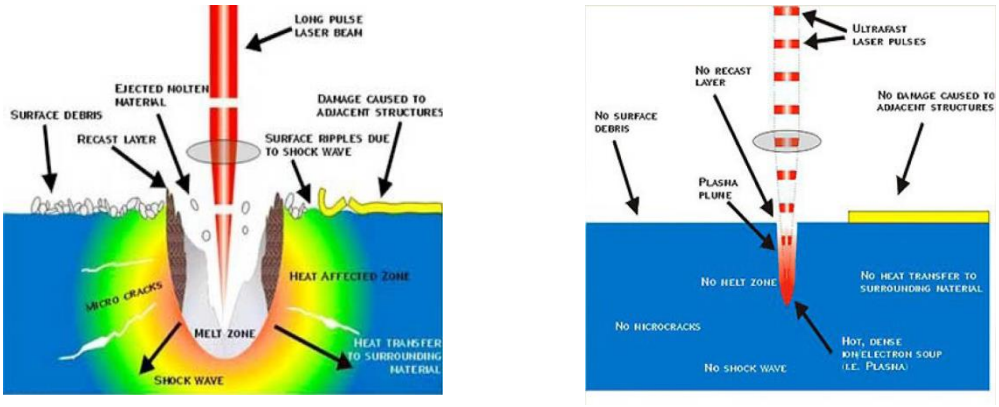

a. b.

Figure 1.2. Schematic illustration of the ablation process under (a) long pulse and (b) ultrafast laser beam (the figures are taken from www.aoficorp.com)

Generally, as the pulse length is shortened, the laser energy is more rapidly deposited into the material leading to more rapid material ejection. The ablated volume of material becomes more precisely defined by the laser's spatial profile and optical penetration depth, and the remaining material has less residual energy, which reduces the heat affected zone (HAZ) [43]. These effects are most apparent in the ablation of metals [44].

In ultrafast laser, laser-material interaction is separated in time from material response and ejection. Femtosecond pulses laser can cause optical breakdown, which reduces the optical absorption depth and strong absorption. Also, the laser-material interaction is separated in time from material response and ejection. Whilst in ns ablation, the ejected ablation plumes that shield the surface can reduce the laser energy absorbed by the material. This process may occur in our experiments which have been done using ns pulsed laser.

Material responses to the incidence laser often involve a combination between ablation, surface melting and thermally effects. This combination may lead to cumulative changes surface texture, morphology and chemistry of the material that we will try to identify in our experiments.

3. Infrared lasers

Since we used infrared lasers in our experiments, i.e. Nd:YAG and YLIA lasers, we will review these two lasers in this section.

A. Neodymium-doped Yttrium Aluminum Garnet Lasers (Nd:YAG)

YAG is the best commercially available crystalline laser host for Nd^{3+}, providing low threshold and high gain. YAG also has been doped with Tm^{3+}, Er^{3+}, Ho^{3+}, and Yb^{3+}[46, 47].This neodymium-doped yttrium aluminum garnet (Nd:YAG) rod possesses unique properties that advantageous for laser operation. YAG has good optical quality (colorless), mechanically hard and excellent thermal stability and properties (high thermal conductivity). Moreover, its cubic structure gives narrow fluorescence line-width that leads to high gain and low threshold for laser operation [48]. Ever since the first successful lasing of Nd:YAG reported by Geusic et al. [45], a rapid strides had been made just

within five years in improving either the material quality and pumping techniques. So that instead a fractional watt, several hundred watts can be obtained from a single laser Nd:YAG rod [49], even by a pump power as small as 1 mW [50].

A Nd:YAG laser can be depicted like Figure 1.5. The Nd:YAG rod and flashlamp are placed at different focus of a reflective elliptical cavity as a resonator. The preferred pumping for Nd:YAG is 0.809 μm. If krypton flashlamp is used for pumping, the operating efficiency is around 2%. It is because the krypton emits a broadband light, so only a small part is able to excite the Nd^{3+} ions in the crystal. This means that more energy must be pumped into the crystal rod which will cause a serious cooling problem. It is the reason why the YAG laser operation is limited to around 4 W/mm before the thermal effects distort the beam or even crack the rod.

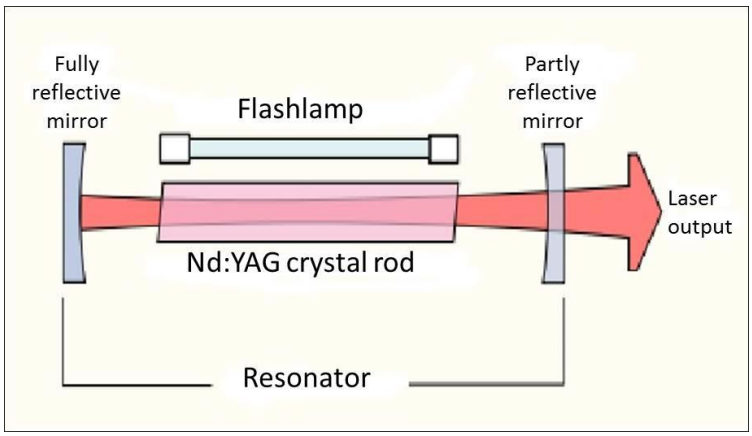

Figure 1.3.The simplified construction of Nd:YAG laser

Changing the flash lamp with diode laser is a good option for pumping the crystal. Laser pumping has many advantages, e.g.:

- Directly pump the crystal at its optical fluence.
- The pump emission is potentially overlaps with the absorption band of the gain medium.
- The inversion profile created by the pump beam is able to match the fundamental laser resonator mode volume in the gain medium.

However, there are also disadvantages concerning diode lasers for optical pump sources. The following are summarized from [51], e.g.:

- The unit cost per watt of a diode for the wavelength of 808 nm AlGaAs laser diode (a low-duty-cycle pulsed diode) is about 20,000 times more expensive than of a flash lamp. So for other wavelengths are even more expensive.
- A diode will permanently damage because of its sensitivity to electrical transients and electrostatic discharge.
- The diode emits the light in a bandwidth spectrum, around its peak wavelength, of 1 nm for high power single diode and 2 – 4 nm for linear diode arrays.
- Effective pumping by diode laser is challenging due to highly divergent of its output, it is also multi-aperture for diode arrays.

The laser excitation of VectorMark® Nd:YAG laser, the laser source system we used in our experiments, takes place via laser diode-pumped. The cooling system is also integrated into the compact laser unit.

In Figure 1.3, the laser coming out of resonator is a continuous wave. For many laser applications such as material processing, pulsed lasers are more useful because the laser energy in pulsed wave is compressed into concentrated package. This concentrated energy is more powerful than the natural-strength energy from a continuous-wave laser. One of the methods used to make a continuous wave laser into a pulsed wave laser is Q-switching. This method is almost exclusively used in optical pumped solid state lasers. It is because the spontaneous lifetime of dye lasers and most of gas lasers, is too short for significant energy storage, so these lasers simply cannot be Q-switched [52].

A Q-switch (“Q” stands for the quality of the resonator) is mounted at the output mirror of resonator. The work concept of Q-switch is relative simple; the energy is kept in the population inversion until it reaches the hold level and then it is released very fast in a pulse. There is a possibility this energy draining out of the population inversion. In order to prevent the laser for lasing at least one of these two must be eliminated either the population inversion or the feedback. Obviously, if energy is stored in the population inversion, it doesn't make sense to eliminate it. So, eliminating feedback is chose for preventing lasing and thus storing all extra energy in the population inversion by blocking one of the mirrors. In fact, the resonator with blocked mirror is not high quality resonator. But when this blocked is suddenly moved the quality is switched from low to high. Therefore, a Q-switch laser is a laser whose resonator can be switched from low quality to high quality and back again repeatedly.

There are two types of Q-switch, active and passive, which differentiate by the control source. The active Q-switch is an externally controlled variable attenuator, such as mechanical Q-switch – like mechanical shutter, chopper wheel, or spinning mirror/prism placed inside the cavity – or some kind of modulator – like an acousto-optic switch or an electro-optic shutter, such as Pockels cell or Kerr cell. The pulse repetition rate can therefore be externally controlled. Mechanical Q-switches are simple but they have poor reliability for long-term operational and synchronization difficulties with any external events

[52].

The passive Q-switch – also called saturable-absorber or dye Q-switches [52] – is a switch that works based on the incident light intensity on a material whose transmission increases when the intensity of light exceeds some threshold. The material may be an ion-doped crystal, a bleachable dye or a passive semiconductor device. Because of their simplicity also inexpensive, dye Q-switches are often used – ion-doped crystal like Cr:YAG is used for Q-switching of Nd:YAG lasers. But they have several draw-backs including pulse jitter, dye degradation and synchronization difficulties – like in mechanical Q-switches. Meanwhile, VectorMark® Nd:YAG laser we used in our experiments is used Q-switch-driver with expander and shutter. This Q-switch-driver delivers pulse repetition rate commonly via acousto-optic system.

The pulse repetition rate in Q-switched solid-state lasers is typically in hertz to few megahertz and always much lower than frequency of the cavity round-trip. Using Q-switched diode-pumped microchip lasers a picosecond pulse durations can be obtained [53, 54]; as short as 115 ps for active Q-switching using electro-optic light modulators [55] and 37 ps for passive Q-switching using SEmicondutor Saturable Absorber Mirrors (SESAMs) [56, 57].

B. Ytterbium-doped fiber laser

Glass is one of the popular host materials in laser generation. It has some advantageous properties compare to crystalline [48] as shown next (Table 1.2).

Table 1.2 Properties of host material of laser: glasses vs. crystalline

Glasses	**Crystalline**
- The tremendous size capability for high-energy applications. - Easily fabricated and can be prepared in an excellent optical quality so beam angles near the diffraction limit can be achieved. - Laser ions in glass show a larger fluorescent line-width, so that glasses laser's threshold is higher than crystalline. - Have a much lower thermal than most crystalline that leads to a large thermally induced birefringence and optical distortion in when operated at high average powers. - Glass doped with Er3+ radiates of 1.55 μm that is safe for the human eye. - It is necessary to dope Nd3+ and Yb3+ in glass doped Er3+ to obtain satisfactory efficiency [61].	- Optical quality is poorer than glass. - Higher thermal conductivity than glass. - Narrower fluorescence line-width than glass. - Greater hardness, mostly. - Doping homogeneity is poorer than glass. - Absorption lines are generally narrower.

Since the fibers are based from material of glass, the discussion on a fiber laser also related to the glass laser that is the laser using the glasses as the host material. After first reported in 1962 by Etzel et.al [58], ytterbium-doped glass laser behaviors were detailed by Snitzer' in 1966 [59]. The ytterbium laser possesses some interesting aspects, e.g.:

- There is a broad spectral range observed in fluorescence [59]. It has been confirmed that a significant tuning range can be achieved [60], in this case from 1.015 – 1.140 μm.
- A commercially available AlGaAs diode lasers at the wavelength of 840 nm can pump the ytterbium system since a long absorption length can be

tolerated in the form of a fiber so a weak absorption exploited [60].

The simplified construction of an Yb-doped fiber laser is presented in Figure 1.4. The resonator consists in two Bragg grating as the ends of the fiber. The pump light can be coupled by free-space optics such as lenses and mirrors or can be delivered in one or more multimode fibers that are fused onto the active fiber. Approximately 80 percent of the pump light can be converted to the signal light for Yb-doped fiber.

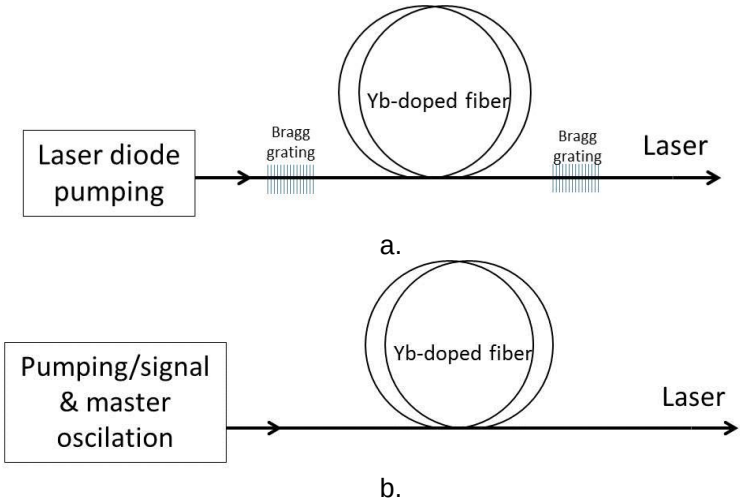

Figure 1.4. Yb-doped fiber laser is configured (a) using two Bragg grating as a resonator, or (b) configured as master oscillator power amplifier which is amplified the input signal

Figure 1.5 shows the set-up. The laser diode pumping light is coupled into the active fiber by a lens. This active fiber is doped with rare-earth element, e.g.Yb^{3+}. The primary advantage of the double-clad design is the large pump area and high numerical aperture, enabling pumping with relatively low-cost multimode diode stacks [62].

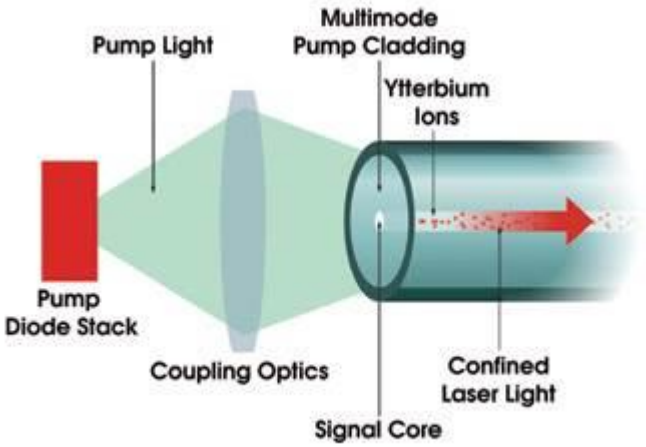

Figure 1.5. The Yb3+-doped fiber laser injection (taken from [63])

C. Nanosecond IR laser application for micro-etching

Nanosecond laser pulses have some limitations for material patterning. Thermal effects play an important role, tend to increase the size of the etching and can affect the material properties. It is particularly the case for materials like

metals, semiconductors and thin films of high-temperature superconductors. The reason is that they have high thermal conductivity so that equation (1.25) can only be fulfilled easily using picosecond- or femtosecond- pulsed lasers. The same case also arises for materials for which bandgap energy exceeds the photon energy of the UV laser, so that $l_\alpha \gg \alpha^{-1}$and equation (1.25) cannot be fulfilled. However, well-defined patterning of other wide-bandgap materials, e.g., glasses such as a-SiO_2, has been demonstrated with picosecond and femtosecond laser pulses. With these ultra-short pulsed laser the linear optical properties of materials become less relevant [64].These elaborations above are quite obvious so that using nanosecond pulsed IR laser is generally out of the options in material processing, e.g. micro-etching.

In addition, the laser beam is delivered from laser generator to the target material using optical system. However, there is an ultimate limit in optical resolution that is often referred to as the diffraction limit. This limitation restricts the ability of laser head to focus the beam size less than approximately half the wavelength of laser beam used for micro-etching. That is the major reason why shorter wavelength-lasers are mostly used for micro etching.

In the next chapter, a new method is proposed to improve the resolution of micro-etching with the use of nanosecond pulsed IR lasers. This method is based on the use of photonic jet.

References

[1] C. P. Grigoropoulos, *Transport in laser microfabrication fundamentals and applications*. New York: Cambridge University Press, 2009.

[2] R. F. Pease and S. Y. Chou, "Lithography and other patterning techniques for future electronics," *Proceedings of the IEEE*, vol. 96, pp. 248-270, Feb 2008.

[3] K. Sugioka, M. Meunier, A. Piqué, and J. Ihlemann, "Micromachining and Patterning," in *Laser Precision Microfabrication*. vol. 135, ed: Springer Berlin Heidelberg, 2010, pp. 239-257.

[4] K. W. Kolasinski, "Growth and Etching of Semiconductors," in *Dynamics*. vol. Volume 3, E. Hasselbrink and B. I. Lundqvist, Eds., ed: North-Holland, 2008, pp. 787-870.

[5] Y. F. Lu, L. Zhang, W. D. Song, Y. W. Zheng, and B. S. Luk'yanchuk, "Laser writing of a subwavelength structure on silicon (100) surfaces with particle-enhanced optical irradiation," *Journal of Experimental and Theoretical Physics Letters*, vol. 72, pp. 457-459, 2000.

[6] S. J. Rehse, A. D. Glueck, S. A. Lee, A. B. Goulakov, C. S. Menoni, D. C. Ralph, *et al.*, "Nanolithography with metastable neon atoms: Enhanced rate of contamination resist formation for nanostructure fabrication," *Applied Physics Letters*, vol. 71, pp. 1427-1429, Sep 1997.

[7] A. S. Bell, B. Brezger, U. Drodofsky, S. Nowak, T. Pfau, J. Stuhler, *et al.*, "Nano-lithography with atoms," *Surface Science*, vol. 433, pp. 40-47, Aug 1999.

[8] J. Jersch and K. Dickmann, "Nanostructure fabrication using laser field enhancement in the near field of a scanning tunneling microscope tip," *Applied Physics Letters*, vol. 68, pp. 868-870, Feb 1996.

[9] N. Fukuda, K. Kunishio, and S. Nakayama, ""Dry-Etching System" with Q-switched DPSS Laser for Flat Panel Displays," *Journal of Laser Micro Nanoengineering*, vol. 2, pp. 241-246, Oct 2007.

[10] D. J. Hwang, C. P. Grigoropoulos, and T. Y. Choi, "Efficiency of silicon micromachining by femtosecond laser pulses in ambient air," *Journal of Applied Physics*, vol. 99, Apr 2006.

[11] M. Brown and C. Arnold, "Fundamentals of Laser-Material Interaction and Application to Multiscale Surface Modification," in *Laser Precision Microfabrication*, K. Sugioka, M. Meunier, and A. Piqué, Eds., ed Berlin Heidelberg: Springer-Verlag, 2010, pp. 91-120.

[12] W. M. Steen and J. Mazumder, *Laser Material Processing*, 4th ed. London: Springer-Verlag, 2010.

[13] K. Washio, "Laser Devices and Optical Systems for Laser Precision Microfabrication," in *Laser Precision Microfabrication*. vol. 135, K. Sugioka, M. Meunier, and A. Piqué, Eds., ed: Springer Berlin Heidelberg, 2010, pp. 63-89.

[14] A. Rehman, "Microstrip Design in a Silicon Technology using Closed Form Analytical Expressions," 2007.

[15] M. Born and E. Wolf, *Principles of optics: electromagnetic theory of propagation, interference and diffraction of light*, 7th ed.: Cambridge University Press, 1999.

[16] R. M. Wood, *Laser-induced Damage of Optical Materials*. Bristol and Philadelphia: Institute of Physics Publishing, 2003.

[17] M. A. Green and M. J. Keevers, "Optical properties of intrinsic silicon at 300 K," vol. 3, pp. 189-192, 1995.

[18] E. D. Palik, *Handbook of Optical Constants of Solids* vol. I: Elsevier Science, 1985.

[19] E. D. Palik, *Handbook of Optical Constants of Solids* vol. II: Academic Press, 1991.

[20] J. C. Miller, "Optical properties of liquid metals at high temperatures," *Philosophical Magazine*, vol. 20, pp. 1115-1132, 2014/09/10 1969.

[21] D. Bäuerle, *Laser Processing and Chemistry*: Springer Berlin Heidelberg, 1996.

[22] A. M. Prokhorov, *Laser heating of metals*. New York: Adam Hilger, 1990.

[23] M. N. Özisik, *Heat Conduction*, 2nd ed. New York: John Wiley, 1993.

[24] A. J. Hick, "Rapid surface heat treatments - a review of laser and electron beam hardening," *Heat Treatment of Metals*, vol. 10, 1983.

[25] D. L. Bourell, H. L. Marcus, J. W. Barlow, and J. J. Beaman, "Selective laser sintering of metals and ceramics," *International Journal of Powder Metal*, vol. 28, 1992.

[26] X. Wang and X. Xu, "Thermoelastic wave induced by pulsed laser heating," *Applied Physics A: Materials Science & Processing*, vol. 73, pp. 107-114, 2001.

[27] J. C. Ion, *Laser Processing of Engineering Materials: Principles, Procedure and Industrial Applications*. Oxford: Elsevier Butterworth-Heinemann, 2005.

[28] M. J. Aziz, J. Y. Tsao, M. O. Thompson, P. S. Peercy, and C. W. White, "Solute Trapping: Comparison of Theory with Experiment," *Physical Review Letters*, vol. 56, pp. 2489-2492, 1986.

[29] C. P. Grigoropoulos, A. A. Rostami, X. Xu, S. L. Taylor, and H. K. Park, "Localized Transient Surface Reflectivity Measurements and Comparison to Heat Transfer Modeling in Thin Film Laser Annealing," *Int. Journal of Heat Mass Transfer*, vol. 36, pp. 1219-1229, 1993.

[30] D. P. Korfiatis, K. A. T. Thoma, and J. C. Vardaxoglou, "Numerical modeling of ultrashort-pulse laser ablation of silicon," vol. 255, pp. 7605-7609, 2009.

[31] S. C. Chen, D. G. Cahill, and C. P. Grigoropoulos, "Melting and Surface Deformation in Pulsed Laser Surface Micro-modification of NiP Disks," *Journal of Heat Transfer*, vol. 122, 2000.

[32] J. Eizenkop, I. Avrutsky, D. G. Georgiev, and V. Chaudchary, "Single-pulse excimer laser nanostructuring of silicon: A heat transfer problem and surface morphology," *Journal of Applied Physics*, vol. 103, 2008.

[33] D. B. Chrisey and G. K. Hubler, *Pulsed Laser Deposition of Thin Films*: Wiley, 1994.

[34] N. M. Bulgakova and A. V. Bulgakov, "Pulsed laser ablation of solids: transition from normal vaporization to phase explosion," *Applied Physics A: Material Science & Processing*, vol. 73,

pp. 199-208, 2001.

[35] R. Stoian, D. Ashkenasi, A. Rosenfeld, and E. E. B. Campbell, "Coulomb explosion in ultrashort pulsed laser ablation of Al2O3," *Physical Review B,* vol. 62, pp. 13167-13173, 2000.

[36] R. Kelly and J. E. Rothenberg, "Laser sputtering: Part III. The mechanism of the sputtering of metals low energy densities," vol. 7–8, Part 2, pp. 755-763, 1985.

[37] T. D. Bennett, C. P. Grigoropoulos, and D. J. Krajnovich, "Near-threshold laser sputtering of gold," *Journal of Applied Physics,* vol. 77, pp. 849-864, 1995.

[38] A. Abdurrochman, S. Lecler, J. Fontaine, F. Mermet, P. Meyrueis, B. Y. Tumbelaka, *et al.*, "Photonic jet to improve the lateral resolution of laser etching," in *Photonic Europe 2014:Laser Sources and Applications II*, Brussels, Belgium, 2014, pp. 913523-913523-11.

[39] A. Abdurrochman, S. Lecler, F. Mermet, B. Y. Tumbelaka, B. Serio, and J. Fontaine, "Photonic jet breakthrough for direct laser microetching using nanosecond near-infrared laser," *Applied Optics,* vol. 53, pp. 7202-7207, 2014.

[40] M. Mosbacher, H. J. Munzer, J. Zimmermann, J. Solis, J. Boneberg, and P. Leiderer, "Optical field enhancement effects in laser-assisted particle removal," *Applied Physics a-Materials Science & Processing,* vol. 72, pp. 41-44, Jan 2001.

[41] H. J. Münzer, M. Mosbacher, M. Bertsch, J. Zimmermann, P. Leiderer, and J. Boneberg, "Local field enhancement effects for nanostructuring of surfaces," *Journal of Microscopy,* vol. 202, pp. 129-135, 2001.

[42] Y. Lu, S. Theppakuttai, and S. C. Chen, "Marangoni effect in nanosphere-enhanced laser nanopatterning of silicon," *Applied Physics Letters,* vol. 82, pp. 4143-4145, Jun 2003.

[43] X. Liu, D. Du, and G. Mourou, "Laser ablation and micromachining with ultrashort laser pulses," *Quantum Electronics, IEEE Journal of,* vol. 33, pp. 1706-1716, 1997.

[44] B. N. Chichkov, C. Momma, S. Nolte, F. von Alvensleben, and A. Tünnermann, "Femtosecond, picosecond and nanosecond laser ablation of solids," *Applied Physics A,* vol. 63, pp. 109-115, 1996.

[45] J. E. Geusic, H. M. Marcos, and L. G. Van Uitert, "Laser Oscilations in Nd-doped Yttrium Aluminum, Yttrium Gallium and Gadolinium Garnets," *Applied Physics Letters,* vol. 4, pp. 182-184, 1964.

[46] L. F. Johnson, J. E. Geusic, and L. G. Van Uitert, "Coherent Oscilations from Tm^{3+}, Ho^{3+}, Yb^{3+} and Er^{3+} Ions in Yttrium Aluminum Garnet," *Applied Physics Letters,* vol. 7, pp. 127-129, 1965.

[47] D. Devor and B. H. Soffer, "2.1-μm Laser of 20-W Output Power and 4-Percent Efficiency from Ho^{3+} in sensitized YAG," *Quantum Electronics, IEEE Journal of,* vol. 8, pp. 231-234, 1972.

[48] W. Koechner, *Solid-state laser engineering*, 5th ed. New York: Springer-Verlag Berlin Heidelberg, 1999.

[49] W. Koechner, "Multihundred Watt Nd:YAG Continuous Laser," *Review of Scientific Instruments,* vol. 41, pp. 1699-1706, 1970.

[50] C. A. Burrus and J. Stone, "Single−crystal fiber optical devices: A Nd:YAG fiber laser," *Applied Physics Letters,* vol. 26, pp. 318-320, 1975.

[51] R. Scheps, *Introduction to Laser Diode-pumped Solid State Lasers*. Washington: SPIE-The International Society for Optical Engineering, 2002.

[52] C. B. Hitz, J. J. Ewing, and J. Hecht, *Introduction to Laser Technology*, 3 ed. New York: IEEE Press, 2001.

[53] J. J. Zayhowski and A. Mooradian, "Single-frequency microchip Nd lasers," *Optics Letters,* vol. 14, pp. 24-26, 1989.

[54] J. J. Zayhowski and J. Harrison, "Miniature Solid-state Lasers," in *Handbook of Photonics*, M.

C. Gupta, Ed., ed New York: CRC Press, 1997, pp. 326-392.

[55] J. J. Zayhowski and C. Dill III, "Coupled cavity electro-optically Q-switched Nd:YVO_4 microchip lasers," *Optics Letters,* vol. 20, pp. 405-407, 1995.

[56] G. J. Spühler, R. Paschotta, R. Fluck, B. Braun, M. Moser, G. Zhang, *et al.*, "Experimentally confirmed design guidelines for passively Q-switched microchip lasers using semiconductor saturable absorbers," *Journal of the Optical Society of America B,* vol. 16, pp. 376-388, 1999.

[57] G. J. Spühler, R. Paschotta, R. Fluck, B. Braun, M. Moser, G. Zhang, *et al.*, "Experimentally confirmed design guidelines for passively Q-switched microchip lasers using semiconductor saturable absorbers: errata," *Journal of the Optical Society of America B,* vol. 18, p. 886, 2001.

[58] H. W. Etzel, H. W. Gandy, and R. J. Ginther, "Stimulated Emission of Infrared Radiation from Ytterbium Activated Silicate Glass," *Applied Optics,* vol. 1, pp. 534-536, 1962.

[59] E. Snitzer, "Glass lasers," *Proceedings of the IEEE,* vol. 54, pp. 1249-1261, 1966.

[60] D. C. Hanna, R. M. Percival, I. R. Perry, R. G. Smart, P. J. Suni, J. E. Townsend, *et al.*, "Continuous-wave oscillation of a monomode ytterbium-doped fiber laser," *Electronics Letters,* vol. 24, pp. 1111-1113, Aug 1988.

[61] E. Snitzer, R. Woodcock, and J. Segre, "Phosphate glass Er^{3+} laser," *Quantum Electronics, IEEE Journal of,* vol. 4, pp. 360-360, 1968.

[62] E. Snitzer, H. Po, F. Hakimi, R. Tumminelli, and B. C. McCollum, "Double clad, offset core Nd fiber laser," in *Optical Fiber Sensors*. vol. 2, ed Washington, D.C.: Optical Society of America, 1988.

[63] K. P. Hansen and J. Broeng. (2006, 1 October). *High-power photonic crystal fiber lasers: Holey fiber overcomes limitations of conventional fiber for applications in lasers and amplifiers*.

[64] D. Bäuerle, *Laser Processing and Chemistry*: Springer Berlin Heidelberg, 2011.

II. PHOTONIC JET: THEORY, EXPERIMENTAL OBSERVATIONS AND APPLICATIONS

1. Introduction

This chapter will discuss the state of the art of photonic jet which allows concentrating field enhancement beyond the diffraction limit. Since this thesis concern on photonic jet application for surface structuring, this chapter is commenced with the first reported publications in laser structuring using microspheres [1-6] and the early assumptions of this field enhancement, continued by theory and computation methods, and closed by other potential applications of photonic jet. Photonic jet takes place very near to the surface of the particle in concern; therefore some parts of near-field optics also are reviewed briefly because when the particle surface is circularly curved the near-field phenomenon shows different features as later called photonic nanojet [7] or photonic jet.

In this chapter we present the state of the art of the phenomenon known as photonic nanojet which allows a significant field enhancement in a volume smaller than the diffraction limit. The expression “photonic nanojet” was first coined by Z. Chen and A. Taflove and V. Backman in 2004 [7]; we use the abbreviation PJ in the following. This unusual field enhancement is observed when a plane wave is used to illuminate micron scale dielectric cylinders or spheres. Although the spatial confinement obtained in this situation reaches subwavelength size, the field is a propagating one and not evanescent. The distance involved depends on the size of the crossed cylinder or sphere and index contrast. The observed concentration area falls inside the microsphere in some cases, outside in other cases, for appropriate parameters. Since we are interested in applying PJ for surface patterning, we first consider publications where microspheres have been used to produce the effect, with this application in view [1-6]. We summarize the early description of the field enhancement and give a short description of the theory and computation methods used by different authors. Near-field optics is a subject to be discussed since we consider dimensions close to the wavelength of light. We describe finally the applications that have been proposed in the literature.

2. Field enhancement and diffraction limit

The first paper to mention a novel lithography technique by applying sphere-enhanced laser field, was published by Lu et al. in 2000 [1]. The authors realized subwavelength structures on Si(100) substrate (silicon wafer cut along the (100) plane) by applying 200 pulses of 23 ns ultraviolet laser with a fluence of 340 mJ/cm² to the surface where dried-suspension of 0.5 µm silica spheres were deposited. Normally these laser settings are not appropriate to damage the Silicon surface. It was then assumed that the microspheres enhanced the incident intensity near the contact area. Hence, the wavelength size microspheres do not contribute as micro-lens in far-field but relate to the optical resonance in near-field, because the distance between spheres and substrate surface is smaller than the wavelength of incident beam. The surface views before and after laser illuminations is shown on Figure 2.6.

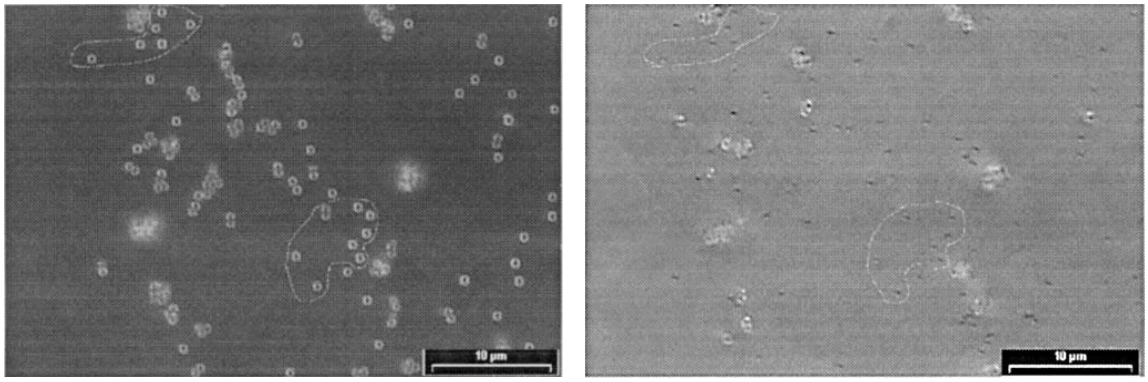

a. b.

Figure 2.6. Patterns on a Si(100) substrate obtained by irradiating microspheres deposited on the surface. The source is a UV laser ((λ = 248 nm; τ = 23 ns). The silicon surface is observed by an optical microscope (a) before and (b) after laser illuminations. The curved line show the microspheres location and corresponding spots observed after illumination (illustrations taken from [1]).

The same type of field enhancement was also suspected to be at the origin of the creation of holes on silicon in an experiments of dry laser cleaning [2]. Mosbacher et al. observed holes of micrometric size, corresponding to the spherical nano-particles of polystyrene to be removed from the surface by the laser pulsed irradiation (Figure 2.7). This discovery led the authors to propose surface nano-structuring by utilizing microsphere field enhancement. Just after the publication of Mosbacher et al., Munzer et al. [3] reported similar observations and proposed a method to nanostructure surfaces with intense laser pulses illuminating wavelength size polystyrene spheres deposited on the surface. Influence of illumination angle was discussed. The possibility of parallel structuring of large surface with a single laser shot appears was expressed for the first time.

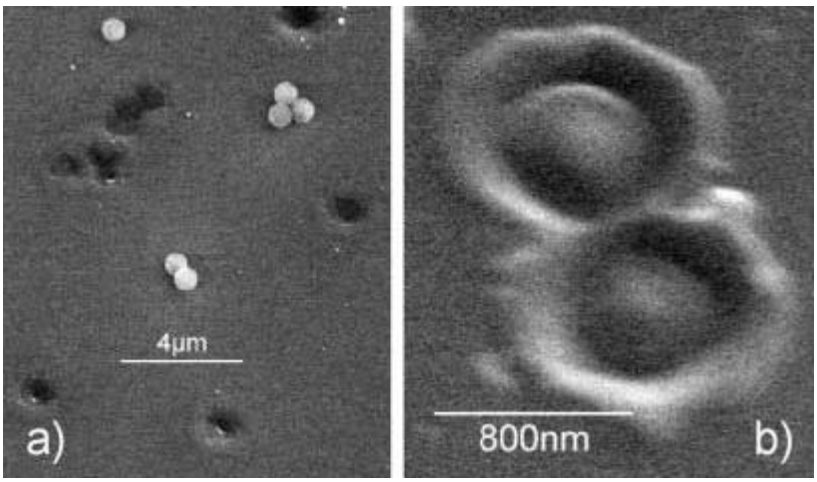

Figure 2.7. Holes observed on silicon surface during laser removal of small polystyrene spherical particles. Laser 6.5 ns pulses at λ = 800 nm have been used. (a) Higher and (b) lower laser fluence (Figures is taken from [2])

The field enhancement observed in a PJ cannot be predicted from the approximation of geometrical optics. In the three articles mentioned above the Mie theory [8] was used to describe the field distribution and estimation of the enhancement observed in shadow side of the illuminated particles. Taking the

computation in free space is a reasonable approach for transparent surface materials with a low refractive index [9]; hence it only provides a first estimation [2]. If the presence of an Si surface is taken into account in calculation, the intensity enhancement might even be higher than in free space [9]. The field enhancement was assumed to be the near-field optical resonance effect induced by microsphere on the surface [1]. This assumption corresponds to the resonance of the electric wave in the metal colloids (Au, Pt, Ag, Cu, Ni, Co) which brings color variation [10]. This phenomenon was later interpreted in terms of surface plasmon resonances [11].

In another experiment of laser marking using a UV laser, Lu et al. [1], [2]] measured their etching marks obtained under silica spheres and found 100 nm for an estimated FWHM intensity distribution of 80 nm. These sizes are smaller than a half of incident wavelength (λ = 248 nm). This observation ($D_{etch} \leq \lambda/2$) was also reported in [2, 3, 5, 6] ; this was a clear demonstration of the possibility light concentration beyond the diffraction limit encountered in optical microscopy and the use of it for surface nano-patterning.

3. From near-field optics to photonic jet

To describe the theoretical aspects of the effect we consider in our work, the photonic nanojet, it is reasonable to start with that part of optics called near-field optics (NFO). NFO is essentially the study of non-propagating fields and their interaction with materials. NFO concerns optical interactions where non-radiative interactions are the key of interest in sub-wavelength scale [12] whereas, the PJ contains strong radiative mode components [13]. Non-radiative interactions are found in many different fields of study; it is not straightforward to incorporate them consistently into NFO theory. NFO is not limited to near-field microscopies with light beam as the source, but also concerns any application involving evanescent electromagnetic waves. Developments in NFO were essential for the advance of the more general field of nano-optics, single molecule spectroscopy and nano-plasmonic [12].

Evanescent waves are important in near-field optics since the field decay also occurs within a range of the order of the wavelength [14]. The role of evanescent electromagnetic wave was not reckoned in optics until the emergence of scanning near-field optical microscopy (SNOM). Nowadays a broad variety of SNOM has been elaborated and is continuously improved.

The situations where PJ are observed are limited to mesoscopic systems, characterized by object sizes of the order of the incident wavelength λ or smaller. At this scale evanescent fields play an important role and NFO is the right theory to use for describing their properties. Usual approximations used either in macroscopic systems or microscopic systems are not appropriate to study mesoscopic; therefore the full set of Maxwell equations should be considered to approach a correct solution. Early papers by Mie [8] and Debye [15] about the scattering of electro-magnetic waves by a sphere have given some insight on the solution of the vector wave equation in the near-field range not only for the microscopic but also for mesoscopic. But these works have

received limited attention in the NFO theory developed later [14]. The development is based on the Green function theory applied to the wave equation where a source term is introduced. It is also known as the field susceptibility or Green dyadic technique. Scattering theory has been used in quantum mechanical problems and in electrodynamics involving external sources of currents where the solution in the source region is not required. And some variants of electromagnetic scattering theory where applied successfully for near-field optical modelling. The Green function may be expanded in Fourier series but since NFO phenomena occur on a sub-wavelength scale, most variants make use of a discretization in the direct space.

The most important feature of all variants of scattering theory is the correct description of the self-consistent coupling between all particles. It raises the numerical implementation to the level of an accurate predictive procedure. In order to illustrate this versatility, Girard et.al [14] review the results of numerical applications to the study of optical tip–sample interactions arising in different contexts: optical near-field distributions, near-field spectroscopy and radiation pressure effects; by applying the discretization procedure on perturbation volumes, near-field distributions are obtained [16-21]. Another way to obtain an exact numerical method is to transform volume integrals into surface integrals; this approach is useful in the case of near-field scattered by a rough surface with a local probe [22, 23].

The traditional way, by transforming volume integrals into surface integrals, also can be used to describe the interaction of the near-field scattered by a rough surface in an interaction with a local probe. This method has been applied and established an exact numerical method [22, 23].

We consider now situation where a scattered field can be concentrated into a volume with a size below the diffraction limit. As mentioned previously, SNOM technique gives the possibility to do that and extend the range of optical measurements. However, SNOM usefulness is limited because of the low light-collection efficiency, slow image-acquisition rate and incapability to sense the objects below the surface [24].

PJ is an alternative phenomenon, which occurs in the near-field of dielectric particles; however it is not just a NFO effect, there is an important contribution of a propagative wave.

PJ refers to the phenomenon of the localized nano-scale beam generated at the shadow-side surfaces of micro-scale dielectric cylinders [7] or spheres [24-27], illuminated by a plane wave. Depending on the polarization of the incident wave, the photonic jet may not have a cylindrical symmetry [25]. The key properties of photonic jet have been summarized by Heifetz et.al [26], e.g.:

(1) PJ is a non-evanescent propagating beam that can maintain its sub-wavelength beam-width along a path that can extend more than ~2λ [24].

(2) Its minimum full-width at half-maximum (FWHM) beam can be smaller than the classical diffraction limit even as small as ~λ/3 for microspheres [1, 5, 6, 28].

(3) PJ is a non-resonant phenomenon that can appear in a wide range of the

dielectric micro-cylinder or sphere sizes (from ~2λ to more than 40λ) [25] as long as the refractive index contrast relative to the medium is less than about 2:1.

(4) Photonic jet has a high intensity that can significantly exceed that of the illuminating wave; factors of 20 to more than 200 have been reported [3, 28, 29].

The existence of a photonic nanojet emerging out of micro-cylinder was first stated by Chen et.al [7] on the base of the calculation of the resulting electric fields obtained through high-resolution FDTD computational solution of Maxwell's equations.

For microspheres, the solution was given by Lecler [25] and Li [27] by implementing an exact eigen-function series solution of Maxwell's equations in spherical coordinates (i.e. Mie theory). Using this method, a plane-wave illuminating the dielectric microsphere can be shown to generate a fully 3D photonic jet having properties that are similar to its 2D counterpart reported by Chen et.al. However, the PJ generated by microsphere has higher intensity than that of micro-cylinder. In both situations (cylinder and microsphere) it is observed that light is scattered in far field and concentrated in the near field.

Two methods can be deployed for light scattering analysis by dielectric particles, i.e. analytic and numerical method. Itagi and Challener [30] stated that analytical solutions are better at providing more insight than numerical modeling. Therefore, an analytical method such as Mie theory can be used as a numerical evaluation of their analytical solution since it has several algorithms which allow avoiding numerical errors when the cylinder size becomes much larger than the wavelength. Mie theory is the method most often applied in analysis of light scattering [2, 3, 5, 25, 30-34]. In the case of non-spherical particles, it is possible to generalize the method to use it as standard for finite difference time-domain algorithm (FDTD) [31]. A finite elements method (FEM) has to be used in more general situation (non-spherical particles for instance) [35-38].

A. Mie theory

This section deals with a description of light scattering by dielectric spherical particles based on Gustave Mie's theory published in a paper in 1908 [8]. It is the theory that we used to simulate and analyze photonic jet at the shadow side of spherical particles in our work. Mie worked on electromagnetic waves, theoretically as well as experimentally; he was also an expert on colloids. At that time colloids were something new and unusual, and their properties were surprising. For example, gold colloids show surprisingly color changing: usually brilliant red for particles size of 10–80 nm, when the size exceeds 100 nm the color changes to blue, indigo and eventually to blue-green for size of 180 nm. Surprisingly, no color effects could be seen for larger sizes. The gold particles themselves, when the particle size increases, have colors starting from green then becoming yellow and red. At first, some scientists speculated that the various modifications size of gold which could give the distinct colors corresponds to the case of the different modifications of phosphorus (white, red,

scarlet and black phosphorus have distinctly different colors). But this assumption could never been proven [39].

Applying Rayleigh scattering [40] only gives blue scattered light. Applying a theory for inhomogeneous media (theory of Lorenz [41]) Maxwell–Garnett [42] could explain only the red color of gold colloids. Ehrenhaft [10], who had investigated experimentally the color of many metal colloids (Au, Pt, Ag, Cu, Ni, Co), concluded that this color variation could be due to resonances of the electric wave in the particles and he determined the range of particles size to be between 30 and 50 nm. Finally, no comprehensive comparison of experimental results with theoretical findings had been done before 1908 when Mie and his student published their reports [8, 43]. In his paper, Mie gives a first outline using Maxwell's electromagnetic theory to describe light scattering by small spherical particles. He explains the color variation of gold colloids versus spheres size, which was later interpreted in terms of surface plasmon polariton resonances. Mie was not the first who formulated the electromagnetic scattering problem, but electromagnetic scattering by a homogeneous and isotropic sphere is commonly referred as Mie theory [44]. In 1909, Peter Debye [15] considered the related problem of radiation pressure on a spherical particle utilizing two scalar potential functions like Mie. Therefore, plane wave scattering by a homogeneous isotropic sphere is also referred as Lorenz-Mie theory [45], or Lorenz-Mie-Debye theory [46]. The basic principle of electromagnetic fields using Mie theory is presented in Appendix 1. Most of the published articles on electromagnetic simulation only considered electric field because electric dipoles have the main contribution in the interaction of radiation with matter [33].

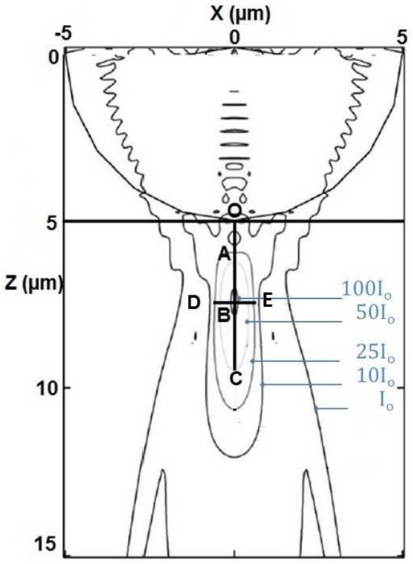

Figure 2.8. The photonic jet parameters: $d_{AXIAL} = \overline{OA}$ is the distance from the spheres surface to the nearest point of I_{MAX}/e^2 intensity, B is the central lobe of photonic jets where E_{max} or I_{max} is located, $f_c = \overline{OB}$ is the distance of central lobe from the sphere's surface, horizontal line across B is Γ_{FWHM} the full-width at half-maximum of the photonic jet and $\lambda_{FWHM} = \overline{AC}$ is the length of photonic jets (from [25])

An example of a clear representation of the geometry of the photonic jet issued from calculation based on Mie theory has been given by McCloskey *et*

al. [47]. As the result, adapted from Lecler et.al [25], is shown in Figure 2.8.

It appears that the main features of a PJ are:

1. I_{MAX}: the maximum intensity in the optical axis (I_{MAX} in Figure 2.8 is at B where $I_{MAX} = 100I_0$).
2. Γ_{FWHM}: the full width of half maximum (FWHM) of the central diffraction lob, which also defined as a double of the photonic jet beam's waist or (the line $\overline{DE}$ in Figure 2.8 is FWHM with D and E are at the rim of $I_{MAX}/2$).
3. θ: the divergence angle of the main lobe, defined as the angle subtended by the line joining points on the FWHM of the jet (the angle $\angle$DOB in Figure 2.8 with D is at the rim of $I_{MAX}/2$).
4. f_c: the distance of I_{MAX} from the surface of the sphere where the beam is focused or concentrated the most in the optical axis (the length of line $\overline{OB}$ in Figure 2.8).
5. $d_{AXIAL} = I_{MAX}/e^2$: the distance from the spheres surface to the nearest point of I_{MAX}/e^2 intensity (the length of line $\overline{OA}$ in Figure 2.8 with A is at the rim of I_{MAX}/e^2).
6. $C = \frac{I_{MAX}-I_1}{I_{MAX}+I_1}$: the contrast of the central lobe intensity I_{MAX} to the two symmetric adjacent lobe intensities I_1.
7. ℓ_{FWHM}: the length of the beam lobe with intensities of $I_{MAX}/2$ (the length of line $\overline{AC}$ in Figure 2.8 with A and C are at the rim of $I_{MAX}/2$).

These above geometrical parameters of a PJ are closely related to the interaction condition like:

- the refractive index contra M between the sphere and the surrounding medium ($M = n_s/n_0$),
- the diameter D_s of the sphere,
- the wavelength λ_0 of the incident light in free space.

Relations between those parameters have been reported in the abundant literature on the subject. Lecler et.al [25] reported that the sub-wavelength waist of the photonic jet ($\Gamma_{FWHM}/2$) is a consequence of the proximity of the microsphere's shadow-side surface and its focus point in the exterior region (microsphere considered as a lens with a large NA). Chen et.al [24] mentioned that in the optimum case observed for f_c = 0 or when the photonic jet is concentrated on the surface, the waist $\Gamma_{FWHM}/2$ is determined by the incident wavelength in the surrounding medium [7]. It should be pinpointed that there are no analytical formulae to find the numerical values of all these parameters [47].

The spot position of photonic jet (f_c) and its spot size (Γ_{FWHM}) also depend on the wave-front shape of the incident wave [48]; the divergence of a spherical wave-front can push or pull f_c position from the surface of the sphere, while the ratio of the center lobe size of a Bessel-Gauss beam to the sphere size can change Γ_{FWHM}. The size of Γ_{FWHM} is larger than the center lobe of the beam if

the ratio is smaller than one. But if the ratio is larger than one, the Γ_{FWHM} is similar to that obtained with a plane incident wave.

Itagi and Challener [30] used a combination of geometrical optics, Mie theory, and angular spectrum analysis to describe the PJ. Their method yields a compact expression that connects the physical and optical geometry properties of the PJ and allows a straightforward electric field analysis. Overall, they show that the photonic jet is the result of a unique combination of features:

- a peak in the angular spectrum,
- a finite content of propagating spatial frequencies,
- a small but finite content of evanescent spatial frequencies, and
- a peculiar distribution of the phase.

The phase distribution is observed since they used angular spectrum analysis to relate the spatial characteristics of the field to its spatial frequency content. Hence the total field is presented in Fourier transform form:

$$F(s,x) = \frac{1}{2\pi}\int_{y=-\infty}^{+\infty} h(x,y)\exp(-isy)\,ds \tag{2.7}$$

Finally they conclude that PJ that appears in the shadow side of a spherical particle results from a specific combination of the particle shape and size, and the refractive index ratio particle/environment. This conclusion is similar to that formulated by McCloskey et.al. [50].

B. Finite elements method

The finite element method (FEM) is a well-established numerical method used in simulation of complex engineering problems. It is a powerful tool to obtain approximate solutions of differential equations describing various physical processes. The strength of the method relies on the fact that by adding computation power, e.g. larger computer capacity, it is always possible to improve the solution [49]. FDTD approach has been for the first time applied to NFO situations by Kann et al [50, 51]. The advantage is that it can solve directly the time-dependent Maxwell equations by imposing time averaging over a period of time. Harmonically oscillating fields are considered. However the procedure is time-consuming and requires a supercomputer or huge memory capacity even in the case of relatively simple problems.

FEM was firstly used in 1960 [52], but the concept has been considered much earlier since it relies on intuition and physical argument. Ancient mathematicians approximated a circle by perimeter of a polygon. Each side of the polygon can be called a finite element. If the number of polygon sides is increased, the approximate values converge to the true value. Thus, in order to acquire the differential equations out of a surface of minimum area bounded by a specific closed curve, for example a circle surface boundary, in 1851 Schellback discretized the surface into several triangles then used a finite difference to express the total discretized area [53]. Then, another effective method for the approximate solution in solid deformation developed in 1909.

This method introduced by Ritz [53], includes an approximation of energy functional with a restriction: it should satisfy to the boundary condition of the problem [54]. The Ritz method was later modified by introducing the special linear functions defined over triangular regions by Courant in 1943 [55]. Thus, Ritz method together with Courant modification is similar to the first FEM proposed by Clough in 1960 [52]. From then, rapid expansion of FEM occurred due to the availability of computers.

In FEM a differential equation is solved by replacing it with a set of algebraic equations. These algebraic equations are the approximation equations resulting from the domain discretization of a differential equation by involving their boundary conditions. There are five boundary conditions which are usually used [56] :

1. Dirichlet boundary condition, setting a fixed value for the solution on the boundary. This condition allows approaching the calculation domain, e.g. by setting a fixed voltage potential.
2. Neumann boundary condition, setting a value of the derivative in the normal direction on the boundary. This is a typical boundary condition to employ field symmetries or to apply a fixed flux.
3. Robin boundary condition (mixed boundary condition), are a special type of Neumann boundary condition, in which the constant is replaced by a linear function of the local solution, containing parameters on the boundary. This is a typical boundary condition in thermal problems where convection is to be considered.
4. Periodic boundary conditions, linking the solution on geometrically different boundaries. These boundary conditions are used to impose symmetries, equivalent to an infinite spatial periodicity. When only two boundaries are involved, this boundary condition type is often referred to as binary boundary condition. This is a typical boundary condition to employ field and geometrical symmetries simultaneously.
5. Floating boundary, indicating that the solution on this boundary is equal to a single value that is yet to be determined. This condition is similar to a floating Dirichlet condition inside the considered domain.

Therefore, discretization – as the primary step in standard FEM procedures – followed by other steps, is a critical issue in the success of FEM application. The standard FEM procedures are given by S. S. Quek and G. R. Liu [57] :

1. Domain discretization,
2. Displacement interpolation,
3. Formation of finite element in local coordinate system,
4. Coordinate transformation,
5. Assembly of finite element equations,
6. Imposition of displacement constraints,
7. Solving the finite element equations.

We have applied FEM approach in the second part or our work, dealing with the design of special tip at the end of an optical fiber to generate a PJ. It will be the subject of chapter 4 of the thesis. Moreover, basic of FEM approach for describing the interaction of electric field with matter is given in Appendix 2.

4. Experimental validation of photonic jet

Originally when it was coined, the photonic jet was observed through FDTD calculation [7, 24], but its existence has been reported in several publications [1-6]. Experimental demonstration of its existence can be done through direct or indirect observation. Direct observation is done by direct capturing of photonic jet using such apparatus like a microscope in the visible range [34, 58-61] or an antenna for the radio/microwave frequency range [62-64].

An indirect proof of the occurrence of PJ can be found as a pattern formed on a substrate surface. Such a pattern occurs when the surface covered with some microspheres are irradiated with the laser at intensity level below material standard ablation level. This can be explained only by the field enhancement due to the presence of microspheres. In fact, indirect observation of field enhancement in a situation of particle/nano-sphere optical irradiation had been reported before the term of photonic jet was coined; the authors called the phenomenon resulting the marking as particle/nano-sphere enhanced optical irradiation or resonance [1-6].

There are many reports validating the correspondences between the computational/simulation works of photonic jet in the near-field optic and experiment works. These experiment validation works include photonic jet capturing/measurement and micro-etching applications.

A. Photonic jet capturing and measurement

Photonic jet existences have been observed and captured for measurement in visual range frequency [34, 59-61] and microwave frequency [64]. Figure 2.9 shows images of PJs. Charge-coupled devices (CCD) camera was used for capturing the PJ in visual range frequency, and for microwave frequency, an antenna-probe was used. These observations correspond to PJ generated by a single dielectric sphere [34, 59], by dielectric spherical cavities [60, 61] and by a dielectric cylinder [64].

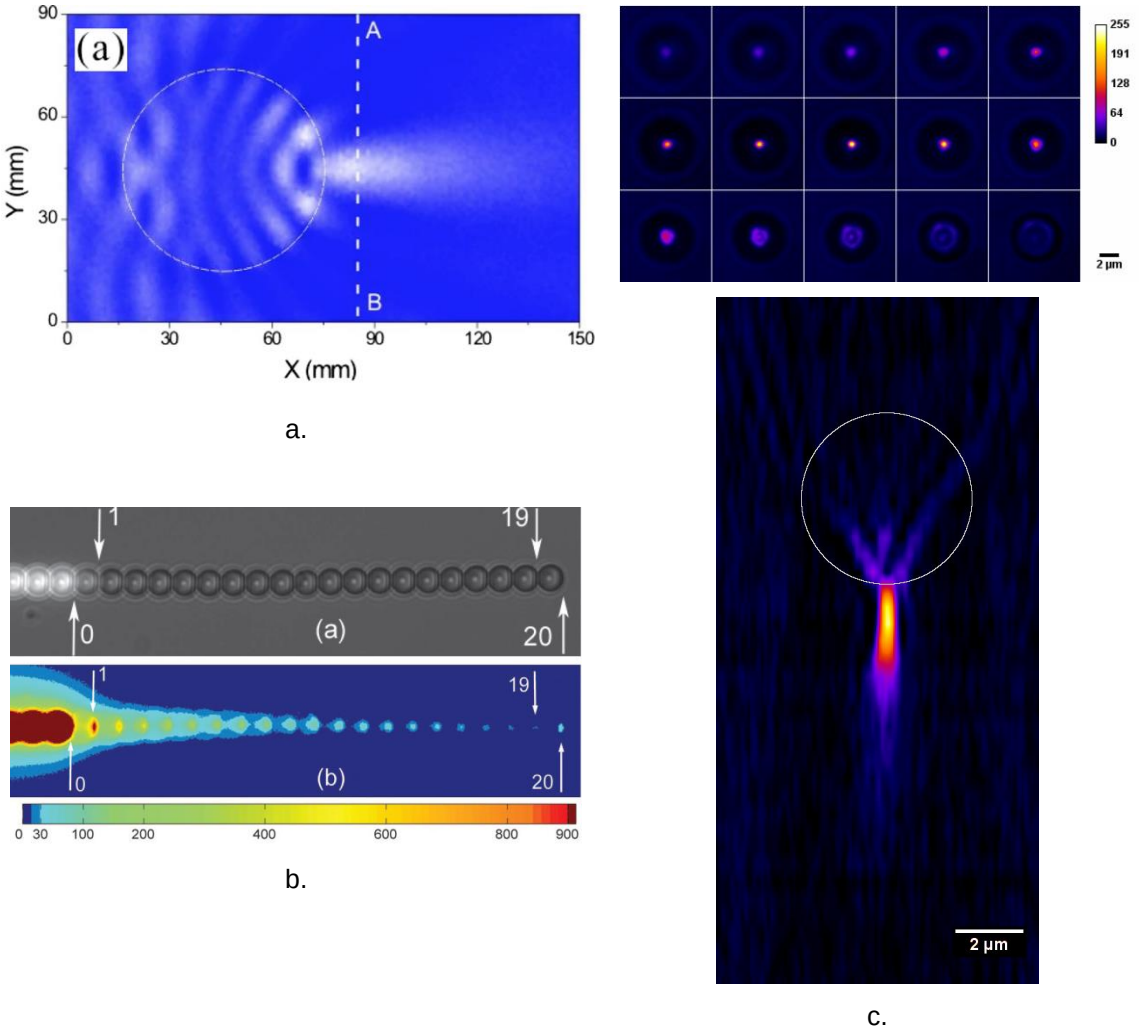

Figure 2.9. Capture of PJ appearance:
(a) Spatial distribution of the field intensity at 12 GHz using a Teflon cylinder with a diameter of 60 mm [64]; (b) Nanojet induced mode (NIM) visualization in a chain of 2.9 µm spheres in white-light illumination and without background illumination [60]; (c) A stack of raw images from a 5 µm sphere captured with a steps of 500 nm towards the sphere which and the PJ reconstruction on optical axis build from the stack of raw images [34]

B. Photonic jet marks on sample materials

The first papers reporting PJ photonic jet application for micro-etching or nano- lithography mentioned if the etching was the results of near-field optics. The first report of a mask-less nano-patterning technique was made started by Lu et al. in 2000 [1]. The authors used a laser to illuminate Si(100) having some silica microspheres of 0.5 µm diameter, that has been dipped in 5% hydrofluoric acid randomly on the surface. Their laser illumination experimental scheme is illustrated shown in Figure 2.10a. They reported that a single pulse duration of 23 ns with 340 mJ/cm^2 of a KrF excimer laser (λ = 248 nm) did not leave any marking on Si(100). With the number of pulses increased up to 200 pulses, they found many hillock markings related to the spheres positions were observed on the surface. The hillock size was of the order of 100 nm, which agreed with the 80 nm computed FWHM obtained by solving the

electromagnetic boundary problem of one particle on the surface. This small difference between experiment and calculation was explained due to material response or the effect of scattering-induced focusing beam coming out of exiting microsphere.

Therefore, in order to eliminate the scattering effect that might cause the difference, a subsequent experiment [5] was conducted by irradiating silica spheres of 640 nm diameter on the substrate from the opposite direction; in this case the substrate was a thin borosilicate plate of 500 µm, with low absorption in the visible range. This new laser illumination scheme is draw in Figure 2.10b. These spheres were diluted with de-ionized water then applied on the substrate and by self-organizing process forming a hexagonally closed-packed monolayer. Then they were led dry and stick to the surface. Theppakuttai and Chen [5] employed this illumination scheme because they found in their simulations based on Mie theory that the field enhancement is not due to the scattering-induced focusing effect. The effect is eliminated by passing the incidence beam through the substrate before it hits the spheres.

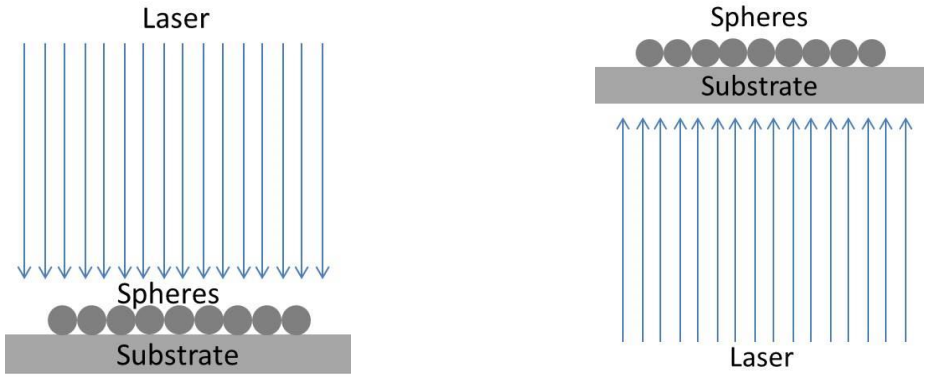

Figure 2.10. Two possible laser illumination schemes, (a) normal and (b) opposite normal direction to the spheres

Wu et al. observed that marking size due to PJ may be controlled by the exposure time or laser pulse frequency [28]. Munzer et al. [3] showed that the heat diffusion also must be taken into account. Nevertheless, none of experimental reports of that time used the simulation with heat diffusion, or realistic material response to explain the experimental results. This is probably the reason why slight discrepancies between experiments and electromagnetic simulations existed: the feature size ratio of experiment, that is mark size divided by the incident wavelength, was 0.6 while the simulation feature size, that is the computed FWHM divided by the incident wavelength, was 0.5 [28]. Nevertheless, the result was satisfactory enough to consider that this field enhancement could be used for nano-patterning application.

Despite this slight difference, the etching size range can be estimated from the electromagnetic simulation of the sphere, even achieved in free space [3]. Therefore the parameters of photonic jet from the computational works which have been mentioned in the previous section are substantial for photonic jet micro-etching application.

Another similar experiment scheme as done by Lu et al. [1] has also was reported by Huang et al. [6]. The authors first diluted some silica microspheres (with 0.95 and 0.47 µm diameters) and polystyrene spheres (0.14 µm diameter) with deionized water forming a colloidal suspension. Then they applied the solution on a 35 nm aluminum film over a silicon wafer; this was done to order the microspheres were more orderly. The particles, however, they were not well closely packed. A periodic pattern on of holes was obtained. Actually, hexagonally closed-packed colloidal monolayers can be directly prepared on to the surface by a spin-coating or a self-assembling process.

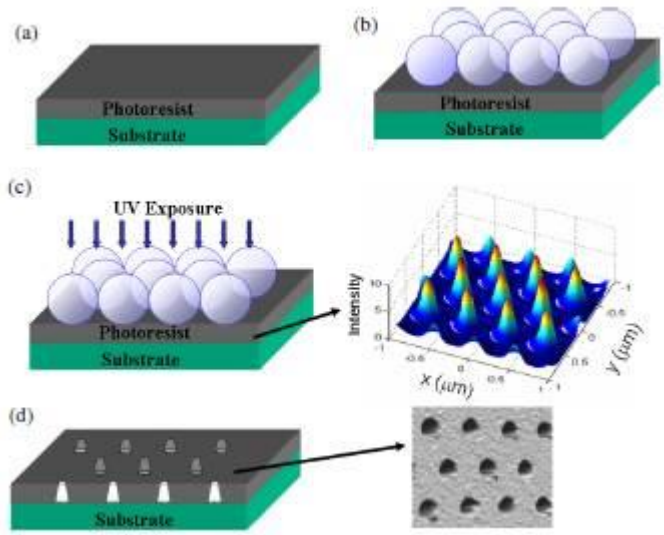

Figure 2.11. The schematic illustration of Wu et al. [28] experiment; (a) Photoresist film is spin-deposited on a substrate. (b) A monolayer of silica or polystyrene microspheres formed on the photoresist by self-assembling planar array. (c) Ultra violet beams (UV) illuminated the photoresist covered microspheres and the UV intensity in photoresist calculated by 3-D FDTD on the right. (d) Sub-wavelength holes pattern obtained after microspheres removal and the AFM image acquired on the right.

The technique to assembly microspheres on substrate is discussed more detail in [65]. In 2007, Wu et al. [28] used self-assembled planar array of microspheres as optical lenses to generate deep sub-wavelength regular patterns over large areas on a photoresist. The microspheres were silica or polystyrene (a diameter of 0.97 µm) illuminated during 0.8 second by a broadband UV source centered at 400 nm. The photoresist surface was not exposed by the beam except at the high-intensity PJ location under the microspheres. This yielded a regular 0.97 µm period array of 250 nm diameter holes (Figure 2.11). If the surface was changed to negative resist, nano-pillars were obtained. The features of hole or pillar size were determined by varying the exposure time, while the array period could be accurately and independently controlled by using different microsphere sizes.

In contrast to experiments mentioned above in which the laser beam arrived at a normal incidence at the surface, Guo et al [66] reported an experiment where the beam was applied at different angles (Figure 2.12).

The test was done for the case of 1 µm silica microspheres prepared by self-assembly on the substrate. It was found that at an incidence angle of α = 30°

the marks diameter is much smaller than those obtain at normal incidence (α = 0°) and is beyond the diffracted limit of $\sim \lambda/2$. Furthermore, they also varied the incidence angle with scanning resolution of 5° ($\alpha \leq 45°$) but avoiding the normal incident beam to prevent microsphere removal; it yielded an array pattern of lines with an average line length and width of 1400 and 360 nm, respectively (Figure 2.13a). They also made the experiment using a scanned beam with different azimuthal angle; the result was the array pattern of c-shaped nanostructures shown on Figure 2.13b.

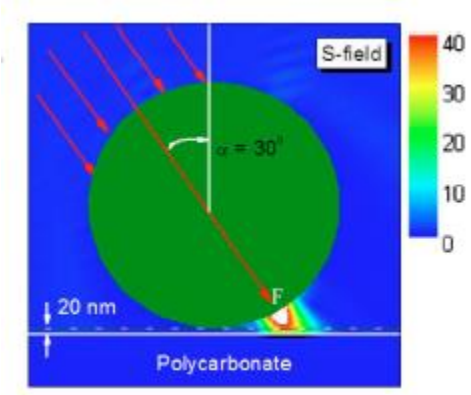

Figure 2.12. The field enhancement of a 1 µm silica sphere on the sample surface illuminated by a 248 nm laser at angle α = 30° (the figure taken from Guo et al. [66])

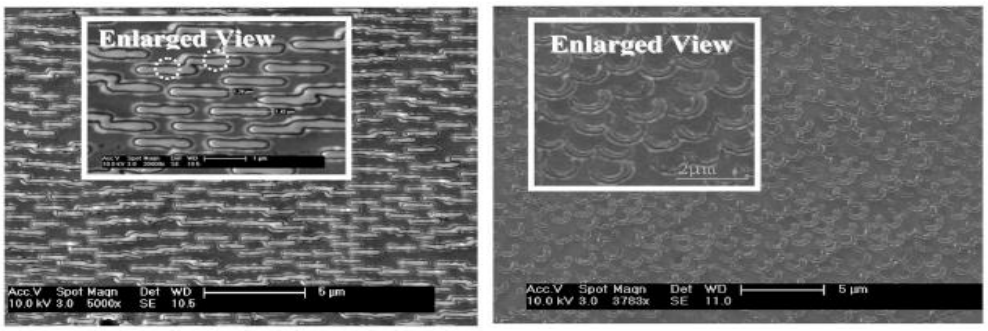

a. b.

Figure 2.13. SEM image of (a) lines pattern and (b) c-shaped nanostructures (the figure taken from Guo et al. [66])

Another reported direct writing of nano-patterns was published by McLeod and Arnold [67] in Nature Nanotechnology. They demonstrated more complex nano patterning on a polyimide substrate using optically trapped microspheres. A continuous-wave laser with a wavelength of 532 nm generated a Bessel beam which trapped a polystyrene or silica microsphere in the aqueous medium. Meanwhile, a Gaussian laser pulse (wavelength of 355 nm) simultaneously illuminated this microsphere to generate the photonic jet which directly modified the substrate that was translated in certain manner to obtain the desire patterns. Their schematic experimental setup and calculation are presented in Figure 2.14. This technique succeeded in producing arbitrary patterns and individual etching with minimum size of ~ 100 nm with a positioning accuracy of better than 40 nm and a submicron distance between the microsphere and the substrate maintained without active feedback control.

The experimental validation of PJ in the literature is summarized in Table 2.3.

Table 2.3. Experimental validation of photonic jet in micro-etching

Year	Name	Experiments detail/remarks
2000	Y.F. Lu et al.	**Laser source**: KrF excimer laser (τ=23 ns, Fluence=340 mJ/cm²). **Sphere**: Silica (D_s=0.5 µm). **Substrate**: Si[100]. **Remarks**: A single laser-pulse left no marking. 200 laser-pulses created 100 nm hillocks marking which agreed with the 80 nm computed FWHM by solving the electromagnetic boundary problem of one particle on the surface. [1]
2001	M. Mosbacher et al.	**Laser source**: Ti:sapphire laser (λ= 800 and 400 nm; τ = 150fs, 30ps and 2.5ns). **Sphere**: Polystyrene and Silica (D_s= 320 – 1700 nm), and irregular alumina particles. **Substrate**: Silicon wafer. **Remarks**: Experiments were intended for particles removal. Dry laser cleaning (DLC) for sub-ns pulses seem to be governed by the local ablation of the substrate rather by surface acceleration. [2]
2001	H.J. Münzer et al.	**Laser source**: Ti:sapphire laser (τ=100 fs, Fluence=90, 25 and 10 mJ/cm²) and Nd:YAG laser (τ=8 ns). **Sphere**: Polystyrene (D_s=320, 800 and 1700 nm). **Substrate**: Silicon wafer, Si[100] and BK7 glass plate. **Remarks**: The spheres are "glued" by polymer on to the substrate avoiding ejected during laser illumination. Simulation in free space with taking the heat diffusion into account is able to estimate the shape of the etching holes. [3]
2003	Y. Lu et al.	**Laser source**: Nd:YAG laser (τ=10 ns, Fluence=3 J/cm²). **Sphere**: Silica (D_s=640 nm). **Substrate**: Si(100) with oxide layer of 2 – 3 nm. **Remarks**: A Marangoni effect in nano-sphere enhanced laser. [4]
2003	S.Theppakuttai et al.	**Laser source**: Nd:YAG laser (τ=10 ns, Fluence=3 J/cm²). **Sphere**: Silica (D_s=640 nm). **Substrate**: Borosilica (500 µm). **Remarks**: Laser illumination conducted at a reverse normal angle in order to eliminate the scattering-induced focusing effect. [5]
2002	S.M. Huang et al.	**Laser source**: KrF excimer laser (τ=23 ns, Fluence=300 and 750 mJ/cm²). **Sphere**: Silica (D_s=0.95 and 0.47 µm) and Polystyrene (D_s=140 nm). **Substrate**: Aluminum film (35 nm) on silicon wafer. **Remarks**: The spheres are "glued" by deionized water on to the substrate. Smaller spheres yield smaller etching holes while higher fluence yields larger etching holes. [6]
2007	W. Wu et al.	**Laser source**: Broad-band UV laser (λ_{center}=400 nm, τ=0.8 s, Intensity=11.4 nW/cm²). **Sphere**: Silica (D_s=0.5, 1, 2 and 5 µm) and polystyrene (D_s=0.97 µm). **Substrate**: GaAs. **Remarks**: The marking size was controlled by the exposure time or laser pulse periods. [30]
2007	W. Guo et al.	**Laser source**: KrF excimer laser (τ=15 ns). **Sphere**: Silica (D_s=1.0 µm). **Substrate**: $Sb_{70}Te_{30}$ film (20 nm) on polycarbonate. **Remarks**: The incidence angle is not perpendicular. An array scanned beam illuminations create different array pattern. [68]
2008	E. Mcleod et al.	**Laser source**: Gaussian laser of near-UV (λ=355 nm, τ=15 ns) for etching and Bessel beam of near-IR (λ=532 nm) for trapping microsphere. **Sphere**: Silica (D_s=0.52 µm) and polystyrene (D_s=0.49, 0.76 µm). **Substrate**: Polymide thin film, polycarbonate and polyester. **Remarks**: A sphere is trapped by Bessel beam to make it floating in aqueous medium while the Gaussian laser illuminated on it generating photonic jet for etching on the substrate. [37]

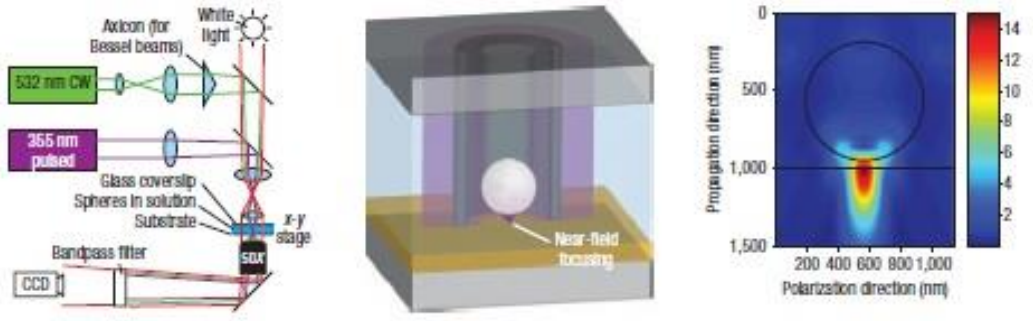

a. b. c.

Figure 2.14. Figures from McLeod and Arnold [67]: (a) schematic of experimental setup, (b) a microsphere is trapped by a Bessel beam and floated in aqueous medium writing on the substrate, (c) FDTD model of the intensity at the vicinity of a 0.76 µm polystyrene sphere (n=1.62) in water medium (n=1.34).

5. Other potential applications of photonic jet

Micro-etching is one of the potential applications of PJ. Many other possible used have been reported in the literature.

A. Photonic jet microscopy

The first ever mention potential application of photonic jet was visible-light ultra-microscopy technique [7]. Chen et al. showed that photonic jet may have the ability to detect a nano scale particles with the size below the diffraction limit using visible light, such as protein, virus or even a single molecule. This application is possible due to the enhancement of backscattering from metallic particles located inside the photonic jets' lobe. In order to support this proposal many studies and experiments have been conducted and reported [27, 58, 62, 64, 68, 69].

The use the microsphere and photonic jet for microscopy also gives idea to add microsphere between objective lens and the object to improve the resolution of traditional optical microscopes [36, 70-74]. One of the proposed designs is presented on Figure 2.15.

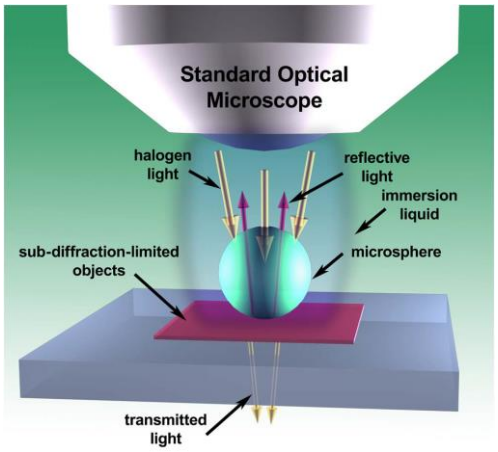

Figure 2.15. A design schematic applying photonic jet for microscopy is proposed by Lee et al. [74] called microsphere optical nanoscopy (MONS).

B. Small propagation losses waveguide

It is known that some non-classical optical phenomena can create waveguide in dielectric microstructures, such as tight binding high-quality cavities which behave as coupled resonator optical waveguide [75]. It can be due to resonance effect known as whispering gallery modes (WGMs) or photonic jet chain. Kapitonov and Astrotov [60] constructed experimentally an optical waveguide based on a chain of several tens of connected polystyrene microspheres. Occurrence of PJ in this chain of spheres, resulted in periodic modes, called nanojet-induced modes (NIMs) in (Figure 2.16). Optical waveguide using microsphere chains by NIMs may be advantageous to optical wave-guiding by inter-sphere coupling of WGMs. Indeed, at long distances from the source, the measured propagation losses for NIMs were as low as 0.08 dB per microsphere [76].

C. Photonic jet laser surgery

The small propagation losses of NIMs in integrated chains of microspheres gave Astratov et al. the idea to put only a few of these microspheres inside a micro-capillary tube [77]. A beam of 630 nm wavelengths was injected into the open tube by a single mode fiber, while the other end of the tube was filed by a short chain of 125 μm diameters of barium titanate glass microspheres. The beam was focused at the vicinity of the last microsphere, located at the tip of tube, with a beam waist measuring about 5 μm. One of the potential applications could be ultra-precise laser surgery [78, 79]. By analyzing parameters' influence, it had been demonstrated that a chain of three of five microspheres (Figure 2.16) with refractive index around 1.65 – 1.75 will improve by a factor of 2, the spatial resolution compared to a single microsphere for a cost of intensity attenuation around 0.2 - 0.4.

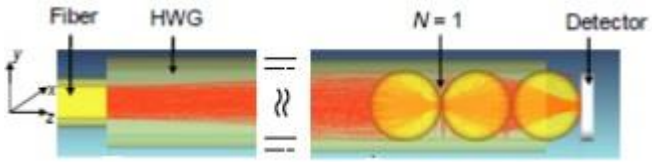

Figure 2.16. Darashes et al.'s [79] design of three microsphere chain for ultraprecise laser tissue surgery

D. Fluorescence enhancement

Lecler et al. [80] reported an enhancement of two-photon excited fluorescence from a dye molecule solution by adding drops of a suspension of silica microspheres (diameter of 0.59 ± 0.1 μm and refractive index of 1.5). The authors showed that this nonlinear enhancement is due to the PJ generated by the microspheres. In the following year, another group of researchers published observation of single-molecule PJ fluorescence enhancement using a latex microsphere (diameter from 1 to 5 μm) adhered on a microscope slide and positioned at the focal point of an objective lens illuminated by He-Ne laser beam at 633 nm [70, 71]. Moreover, they proposed disposable microscope objective lenses [71] and optical-fiber-microsphere probe [81] to elevate the functionality of the system they have developed. In general, despite any existing chemical method PJ are offering non-chemical approach for nonlinear optical effects-enhancement [80] and surface Raman scattering microscopy [70, 71].

E. Nanoparticle detector for location, sizing, counting and velocity measurement

Essentially, PJ microscopy technique can be used to detect any nanoparticles entering the photonic jets lobe [7]. Li et al [27] reported the detection of a gold-sphere with a diameter as small as 2 nm ; the particle was sized by exploiting the super-enhanced backscattering perturbation of the photonic jet generated by a dielectric microsphere. In another experiment, the detected gold particle was located at approximately $\lambda/4$ behind the dielectric microsphere [82]. The backscattering perturbation signal used to locate the gold nanoparticle is one order of magnitude below the backscattering of the isolated microsphere, even though the nanoparticle has a diameter 100 times smaller

than the microsphere. These all indicate that it is possible to detect, size, and locate nanoparticles using visible light. This is a potential application for bio-molecular detection where it is necessary to prevent a potential damage to biological sample with high incident power.

An application of flow cytometry, for counting such nanoparticles [83, 84] and controlling the flow speed and flow directions has been proposed. The idea is to generate a couple of identical PJ along the flowing channel and acquire the backscattered light parameters. A solution would be to combine two microspheres [85]. However, for practical application, it would be better to use a waveguide, where injection and detection are conducted in the same canal.

F. Optical tweezers using photonic jets

First reported optical tweezers was made in 1970 [86]. It is a tightly focused beam of light capable of holding microscopic particles in a stable position along the three dimensions [87]. The radiation pressure of this focused beam is able to trap and manipulate micro-particles array on substrates surface in order, for example, to form colloidal mask for nanolithography [88]. The investigation of photonic jets for optical tweezers was started by Cui et al. [89] in 2-D; it made use of a PJ generated by a plane wave illuminated dielectric micro-cylinder. It was found that sub-wavelength metal nanoparticles can be efficiently trapped within the lobe of the PJ. In addition, the attractive force can be changed to a repulsive one by varying the polarization of the incident plane wave; the result is related to the nanoparticle's polarizability and excitation of localized surface plasmons. More recent investigations have been reported in 3-D by Yannopapas [90]; their PJ was produced by a right-circularly plane wave illuminating polymer microsphere. This author also proposed multiple atom trapping using light scattered off an array of polymer microspheres (Figure 2.17). Furthermore, by properly tuning the geometric characteristics of each microsphere, different atoms can be trapped.

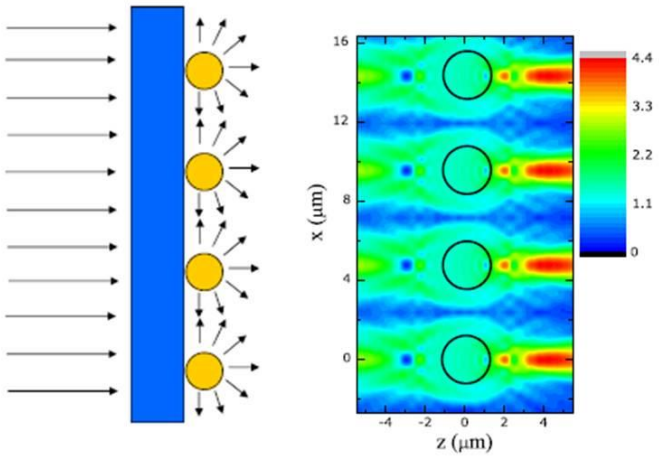

a. b.

Figure 2.17. A multiple atom traps using scattered of an array of polymer microspheres designed by Yannopapas [90], (a) schematic design and (b) its total electric field distribution in aqueous medium.

G. Photonic jet for optical data storage

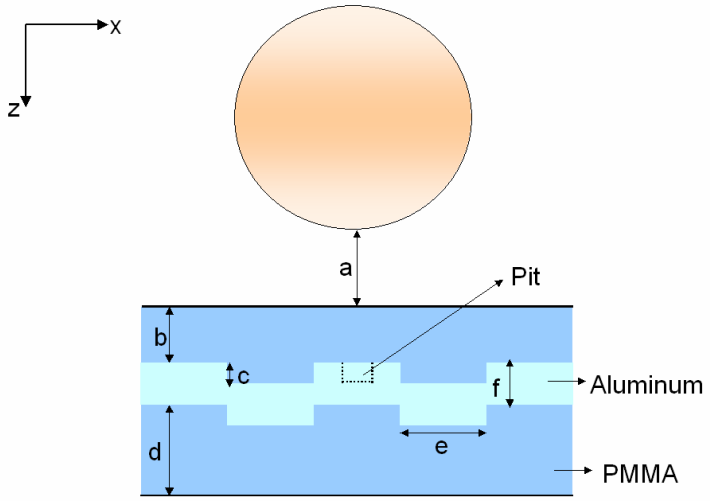

Figure 2.18. The proposed optical data-storage geometry using a 2 μm diameter microsphere with refractive index of 1.59 and the measurements of a = 160 nm, b = 480 nm, c =40 nm, d = 360 nm, e =160 nm and f = 200 nm [91].

The photonic jet potential application for optical data storage has been investigated through computer simulation and experimentally by Kong et al. [63, 91]. Here the PJ is used to read encoded data as nanoscale pits in a metal substrate of a disk. Based on scaled-up disk model substrate and FDTD computation, the pits have a lateral area of 0.025 square wavelengths, which is much smaller than current BluRay™ features. The data reader process is based on the backscattering perturbation phenomenon for nanoparticles located inside the photonic jet lobe; the nanoscale pits on the disk substrate are acting as nanoparticles that generate the backscattering. The contrast ratio was approximately 28 dB greater than that obtained with a traditional optical system. These results could lead to the development of faster optifcal-disk data storage technology with larger capacity. They also proposed the geometry of the optical data-storage using photonic jet (Figure 2.18).

References

[1] Y. F. Lu, L. Zhang, W. D. Song, Y. W. Zheng, and B. S. Luk'yanchuk, "Laser writing of a subwavelength structure on silicon (100) surfaces with particle-enhanced optical irradiation," *Journal of Experimental and Theoretical Physics Letters,* vol. 72, pp. 457-459, 2000.

[2] M. Mosbacher, H. J. Munzer, J. Zimmermann, J. Solis, J. Boneberg, and P. Leiderer, "Optical field enhancement effects in laser-assisted particle removal," *Applied Physics a-Materials Science & Processing,* vol. 72, pp. 41-44, Jan 2001.

[3] H. J. Münzer, M. Mosbacher, M. Bertsch, J. Zimmermann, P. Leiderer, and J. Boneberg, "Local field enhancement effects for nanostructuring of surfaces," *Journal of Microscopy,* vol. 202, pp. 129-135, 2001.

[4] Y. Lu, S. Theppakuttai, and S. C. Chen, "Marangoni effect in nanosphere-enhanced laser nanopatterning of silicon," *Applied Physics Letters,* vol. 82, pp. 4143-4145, Jun 2003.

[5] S. Theppakuttai and S. Chen, "Nanoscale surface modification of glass using a 1064 nm pulsed laser," *Applied Physics Letters,* vol. 83, pp. 758-760, Jul 2003.

[6] S. M. Huang, M. H. Hong, B. S. Luk'yanchuk, Y. W. Zheng, W. D. Song, Y. F. Lu, *et al.*, "Pulsed laser-assisted surface structuring with optical near-field enhanced effects," *Journal of Applied Physics*, vol. 92, pp. 2495-2500, Sep 2002.

[7] Z. G. Chen, A. Taflove, and V. Backman, "Photonic nanojet enhancement of backscattering of light by nanoparticles: a potential novel visible-light ultramicroscopy technique," *Optics Express*, vol. 12, pp. 1214-1220, Apr 2004.

[8] G. Mie, "Beiträge zur optik trüber medien speziell kolloidaler goldlösungen (contributions to the optics of turbid media, particularly of colloidal metal solutions)," *Annalen der Physik*, vol. 25, pp. 377-445, 1908.

[9] B. S. Luk'yanchuk, Y. W. Zheng, and Y. Lu, "Laser cleaning of solid surface: optical resonance and near-field effects," 2000, pp. 576-587.

[10] F. Ehrenhaft, "Das optische verhalten der metallkoloide und deren teilchengröße (the optical properties of metal colloids and their size)," *Sitzungsberichte der mathematisch-naturwissenschaftlichen Klasse der Kaiserlichen Akademie der Wissenschaften ("Wiener Sitzungsberichte"),* vol. 112, pp. 181–209, 1903.

[11] T. Wriedt, "Mie Theory: A Review," in *The Mie Theory*. vol. 169, W. Hergert and T. Wriedt, Eds., ed Berlin Heidelberg: Springer-Verlag, 2012, pp. 53-71.

[12] L. Novotny, "The history of near-field optics," in *Progress in Optics*. vol. 50, E. Wolf, Ed., ed: Elsevier, 2007, pp. 137-184.

[13] Z. Chen, A. Taflove, and V. Backman, "Highly efficient optical coupling and transport phenomena in chains of dielectric microspheres," *Optics Letters*, vol. 31, pp. 389-391, 2006.

[14] C. Girard and A. Dereux, "Near-field optics theories," *Reports on Progress in Physics*, vol. 59, pp. 657-699, May 1996.

[15] P. Debye, "Der lichtdruck auf kugeln von beliebigem material (light pressure on spheres of arbitrary material)," *Annalen der Physik*, vol. 30, pp. 57-136, 1909.

[16] J.-J. Greffet, A. Sentenac, and R. Carminati, "Surface profile reconstruction using near-field data," vol. 116, pp. 20-24, 1995.

[17] C. Girard, X. Bouju, and A. Dereux, "Optical Near Field Detection and Local Spectroscopy of a Surface: A Self-Consistent Theoretical Study," in *Near Field Optics*. vol. 242, D. Pohl and D. Courjon, Eds., ed: Springer Netherlands, 1993, pp. 199-208.

[18] R. Carminati and J.-J. Greffet, "Influence of dielectric contrast and topography on the near field scattered by an inhomogeneous surface," *Journal of the Optical Society of America A*, vol. 12, pp. 2716-2725, 1995.

[19] R. Carminati and J.-J. Greffet, "Two-dimensional numerical simulation of the photon scanning tunneling microscope. Concept of transfer function," vol. 116, pp. 316-321, 1995.

[20] O. J. F. Martin, C. Girard, and A. Dereux, "Generalized Field Propagator for Electromagnetic Scattering and Light Confinement," *Physical Review Letters*, vol. 74, pp. 526-529, 1995.

[21] O. J. F. Martin, C. Girard, and A. Dereux, "Light confinement by subwavelength objects in near-field optics," *Helv. Phys. Acta*, vol. 10, pp. 12–13, 1995.

[22] M. Nieto-Vesperinas and A. Madrazo, "A Theoretical Study of Near Field Interactions with Local Probes," in *Photons and Local Probes*. vol. 300, O. Marti and R. Möller, Eds., ed: Springer Netherlands, 1995, pp. 35-45.

[23] R. Carminati, A. Madrazo, and M. Nieto-Vesperinas, "Electromagnetic wave scattering from a cylinder in front of a conducting surface-relief grating," *Optics Communications*, vol. 111, pp. 26-33, 9/15/ 1994.

[24] Z. G. Chen, A. Taflove, V. Backman, and Ieee, "Photonic nanojets," *Ieee Antennas and Propagation Society Symposium, Vols 1-4 2004, Digest*, pp. 1923-1926, 2004 2004.

[25] S. Lecler, Y. Takakura, and P. Meyrueis, "Properties of a three-dimensional photonic jet," *Optics*

Letters, vol. 30, pp. 2641-2643, Oct 2005.

[26] A. Heifetz, S. C. Kong, A. V. Sahakian, A. Taflove, and V. Backman, "Photonic Nanojets," *Journal of Computational and Theoretical Nanoscience*, vol. 6, pp. 1979-1992, Sep 2009.

[27] X. Li, Z. Chen, A. Taflove, and V. Backman, "Optical analysis of nanoparticles via enhanced backscattering facilitated by 3-D photonic nanojets," *Optics Express*, vol. 13, pp. 526-533, 2005.

[28] W. Wu, A. Katsnelson, O. G. Memis, and H. Mohseni, "A deep sub-wavelength process for the formation of highly uniform arrays of nanoholes and nanopillars," *Nanotechnology*, vol. 18, p. 485302, Dec 2007.

[29] N. Fukuda, K. Kunishio, and S. Nakayama, ""Dry-Etching System" with Q-switched DPSS Laser for Flat Panel Displays," *Journal of Laser Micro Nanoengineering*, vol. 2, pp. 241-246, Oct 2007.

[30] A. V. Itagi and W. A. Challener, "Optics of photonic nanojets," *Journal of the Optical Society of America a-Optics Image Science and Vision*, vol. 22, pp. 2847-2858, Dec 2005.

[31] D. Grojo, L. Charmasson, A. Pereira, M. Sentis, and P. Delaporte, "Monitoring Photonic Nanojets from Microsphere Arrays by Femtosecond Laser Ablation of Thin Films," *Journal of Nanoscience and Nanotechnology*, vol. 11, pp. 9129-9135, Oct 2011.

[32] D. Grojo, N. Sandeau, L. Boarino, C. Constantinescu, N. De Leo, M. Laus, *et al.*, "Bessel-like photonic nanojets from core-shell sub-wavelength spheres," *Optics Letters*, vol. 39, pp. 3989-3992, 2014.

[33] C. H. Li, G. W. Kattawar, P. W. Zhai, and P. Yang, "Electric and magnetic energy density distributions inside and outside dielectric particles illuminated by a plane electromagnetic wave," *Optics Express*, vol. 13, pp. 4554-4559, Jun 13 2005.

[34] P. Ferrand, J. Wenger, A. Devilez, M. Pianta, B. Stout, N. Bonod, *et al.*, "Direct imaging of photonic nanojets," *Optics Express*, vol. 16, pp. 6930-6940, May 2008.

[35] D. McCloskey, Y. P. Rakovich, J. F. Donegan, and Ieee, "Controlling the Properties of Photonic Jets," in *12th International Conference on Transparent Optical Networks (ICTON)*, Munich, GERMANY, 2010.

[36] J. J. Wang, D. McCloskey, and J. F. Donegan, "Optimization of parameters of photonic nanojet generated by dielectric microsphere for laser nanojet SNOM," in *Seventh International Symposium on Precision Engineering Measurements and Instrumentation*, Yunnan, China, 2011, pp. 83213Z-83213Z-6.

[37] H. Yang, H. C. Tekin, A. Sayah, and M. A. M. Gijs, "Self-assembled melamine microlens arrays for immunofluorescence enhancement," in *17th International Conference on Miniaturized Systems for Chemistry and Life Sciences (MicroTAS 2013)*, Freiburg, Germany, 2013, pp. 1291 - 1293.

[38] P. K. Upputuri, Z. Wu, L. Gong, C. K. Ong, and H. Wang, "Super-resolution coherent anti-Stokes Raman scattering microscopy with photonic nanojets," *Optics Express*, vol. 22, pp. 12890-12899, 2014.

[39] H. Horvath, "Gustav Mie and the scattering and absorption of light by particles: Historic developments and basics," *Light Scattering: Mie and More Commemorating 100 years of Mie's 1908 publication*, vol. 110, pp. 787-799, 2009.

[40] L. Rayleigh and J. W. Strutt, "On the transmission of light through the atmosphere containing small particles in suspension and on the origin of the blue sky," *Phil. Mag.*, vol. 47, pp. 375-384, 1909.

[41] L. Lorenz, "Über die refraktionsconstante (on the constant of refraction)," *Wiedmanns Ann. Phys. Chem.*, vol. 11, pp. 70–103, 1880.

[42] J. C. Maxwell-Garnett, "Colours in metallic glasses and in metallic films," *Phil. Trans. R. Soc.*, vol. 203, pp. 385–420, 1904.

[43] W. Streubing, "Über die optische Eigenschaften von kolloidalen Gold Lösungen (on the optical

properties of gold colloids)," *Ann. Phys.*, vol. 26, pp. 329–371, 1908.

[44] T. Wriedt, "Mie Theory: A Review," in *The Mie Theory*. vol. Springer Series in Optical Sciences, W. Hergert and T. Wriedt, Eds., ed Berlin Heidelberg: Springer-Verlag, 2012, pp. 53-71.

[45] W. T. Grandy, *Scattering of Waves from Large Spheres*. Cambridge: Cambridge Univ. Press,, 2000.

[46] E. Davis and G. Schweiger, *The Airborne Microparticle*: Springer, Berlin, Heidelberg, 2002.

[47] D. McCloskey, Y. P. Rakovich, and J. Donegan, "Controlling the properties of Photonic Jets," in *Transparent Optical Networks (ICTON), 2010 12th International Conference on*, 2010, pp. 1-3.

[48] M. S. Kim, T. Scharf, S. Muhlig, C. Rockstuhl, and H. P. Herzig, "Engineering photonic nanojets," *Optics Express*, vol. 19, pp. 10206-10220, May 2011.

[49] S. S. Rao, "Chapter 1 - Overview of Finite Element Method," ed Boston: Butterworth-Heinemann, 2011, pp. 3-50.

[50] J. L. Kann, T. D. Milster, F. F. Froehlich, R. W. Ziolkowski, and J. B. Judkins, "Near-field optical detection of asperities in dielectric surface," *Journal of the Optical Society of America A*, vol. 12, pp. 501-512, 1995.

[51] J. L. Kann, T. D. Milster, F. F. Froehlich, R. W. Ziolkowski, and J. B. Judkins, "Linear behavior of a near-field optical scanning system," *Journal of the Optical Society of America A*, vol. 12, pp. 1677-1682, 1995.

[52] R. W. Clough, "The finite element method in plane stress analysis," in *Second ASCE conference on electronic computation*, Pitssburgh, PA, 1960, pp. 345-378.

[53] F. Williamson, "An historical note on the finite element method," *International Journal for Numerical Methods in Engineering*, vol. 15, pp. 930-934, 1980.

[54] W. Ritz, "Über eine Neue Metode zur Lösung gewisser Variationsprobleme der Matematischen Physik," *J. Reine Angew. Math.*, vol. 135, pp. 1-61, 1909.

[55] R. Courant, "Variational methods for the solution of problems of equilibrium and vibrations," *Bulletin of the American Mathematical Society*, vol. 49, pp. 1-23, 1943.

[56] C. Johnson, *Numerical Solution of Partial Differential Equations by the Finite Element Method*: Cambridge University Press, 1987.

[57] S. S. Quek and G. R. Liu, *Finite Element Method: A Practical Course*: Elsevier Science, 2003.

[58] S. Yang, A. Taflove, and V. Backman, "Experimental confirmation at visible light wavelengths of the backscattering enhancement phenomenon of the photonic nanojet," *Optics Express*, vol. 19, pp. 7084-7093, 2011.

[59] M. S. Kim, T. Scharf, S. Muhlig, C. Rockstuhl, and H. P. Herzig, "Photonic Nanojet engineering: Focal point shaping with scattering phenomena of dielectric microspheres," in *Conference on Integrated Optics - Devices, Materials, and Technologies XV*, San Francisco, CA, 2011.

[60] A. M. Kapitonov and V. N. Astratov, "Observation of nanojet-induced modes with small propagation losses in chains of coupled spherical cavities," *Optics Letters*, vol. 32, pp. 409-411, 2007.

[61] M. Gerlach and Y. P. Rakovich, "Nanojets and directional emission in symmetric photonic molecules," *Optics Express*, vol. 15, pp. 17343-17350, 2007.

[62] A. Heifetz, K. Huang, A. V. Sahakian, X. Li, A. Taflove, and V. Backman, "Experimental confirmation of backscattering enhancement induced by a photonic jet," *Applied Physics Letters*, vol. 89, Nov 2006.

[63] S. C. Kong, A. V. Sahakian, A. Heifetz, A. Taflove, and V. Backman, "Robust detection of deeply subwavelength pits in simulated optical data-storage disks using photonic jets," *Applied Physics Letters*, vol. 92, May 2008.

[64] L. Zhao and C. K. Ong, "Direct observation of photonic jets and corresponding backscattering

enhancement at microwave frequencies," *Journal of Applied Physics*, vol. 105, Jun 2009.

[65] A. N. Shipway, E. Katz, and I. Willner, "Nanoparticle arrays on surfaces for electronic, optical, and sensor applications," *Chem Phys Chem*, vol. 1, pp. 18-52, 2000.

[66] W. Guo, Z. B. Wang, L. Li, D. J. Whitehead, B. S. Luk'yanchuk, and Z. Liu, "Near-field laser parallel nanofabrication of arbitrary-shaped patterns," *Applied Physics Letters*, vol. 90, p. 3, Jun 2007.

[67] E. McLeod and C. B. Arnold, "Subwavelength direct-write nanopatterning using optically trapped microspheres," *Nature Nanotechnology*, vol. 3, pp. 413-417, Jul 2008.

[68] Z. Chen, X. Li, A. Taflove, and V. Backman, "Backscattering enhancement of light by nanoparticles positioned in localized optical intensity peaks," *Applied Optics*, vol. 45, pp. 633-638, 2006.

[69] Z. Chen, A. Taflove, X. Li, and V. Backman, "Superenhanced backscattering of light by nanoparticles," *Optics Letters*, vol. 31, pp. 196-198, 2006.

[70] D. Gérard, J. Wenger, A. Devilez, D. Gachet, B. Stout, N. Bonod, *et al.*, "Strong electromagnetic confinement near dielectric microspheres to enhance single-molecule fluorescence," *Optics Express*, vol. 16, pp. 15297-15303, 2008.

[71] J. Wenger, D. Gérard, H. Aouani, and H. Rigneault, "Disposable microscope objective lenses for fluorescence correlation spectroscopy using latex microspheres," *Analytical Chemitry*, vol. 80, pp. 6800-6804, 2008.

[72] Z. Wang, W. Guo, L. Li, B. Luk'yanchuk, A. Khan, Z. Liu, *et al.*, "Optical virtual imaging at 50 nm lateral resolution with a white-light nanoscope," *Nature Communications*, vol. 2, pp. 1211-1218, 2011.

[73] Z. Wang and L. Li. (2011) White-light microscopy could exceed 50 nm resolution. *Laser Focus World*. 61-63. Available: www.laserfocusworld.com

[74] S. Lee, L. Li, Z. Wang, W. Guo, Y. Yan, and T. Wang, "Immersed transparent microsphere magnifying sub-diffraction-limited objects," *Applied Optics*, vol. 52, pp. 7265-7270, 2013.

[75] A. Yariv, Y. Xu, R. K. Lee, and A. Scherer, "Coupled-resonator optical waveguide: a proposal and analysis," *Optics Letters*, vol. 24, pp. 711-713, 1999.

[76] S. Yang and V. N. Astratov, "Photonic nanojet-induced modes in chains of size-disordered microspheres with an attenuation of only 0.08 dB per sphere," *Applied Physics Letters*, vol. 92, 2008.

[77] V. N. Astratov, A. Darafsheh, M. D. Kerr, K. W. Allen, and N. M. Fried, "Focusing microprobes based on integrated chains of microspheres," *PIERS Online*, vol. 6, pp. 793-797, 2010.

[78] V. N. Astratov, A. Darafsheh, M. D. Kerr, K. W. Allen, N. M. Fried, A. N. Antoszyk, *et al.* (2010) Photonic nanojets for laser surgery. *SPIE-Newsroom*.

[79] A. Darafsheh, A. Fardad, N. M. Fried, A. N. Antoszyk, H. S. Ying, and V. N. Astratov, "Contact focusing multimodal microprobes for ultraprecise laser tissue surgery," *Optics Express*, vol. 19, pp. 3440-3448, 2011.

[80] S. Lecler, S. Haacke, N. Lecong, O. Cregut, J. L. Rehspringer, and C. Hirlimann, "Photonic jet driven non-linear optics: example of two-photon fluorescence enhancement by dielectric microspheres," *Optics Express*, vol. 15, pp. 4935-4942, Apr 2007.

[81] H. Aouani, F. Deiss, J. Wenger, P. Ferrand, N. Sojic, and H. Rigneault, "Optical-fiber-microsphere for remote fluorescence correlation spectroscopy," *Optics Express*, vol. 17, pp. 19085-19092, 2009.

[82] A. Heifetz, J. J. Simpson, S.-C. Kong, A. Taflove, and V. Backman, "Subdiffraction optical resolution of a gold nanosphere located within the nanojet of a Mie-resonant dielectric microsphere," *Optics Express*, vol. 15, pp. 17334-17342, 2007.

[83] R. M. Zucker, E. J. Massaro, K. M. Sanders, L. L. Degn, and W. K. Boyes, "Detection of TiO_2

nanoparticles in cells by flow cytometry," *Cytometry A*, vol. 77, pp. 677-685, 2010.

[84] E. V. B. van Gaal, G. Spierenburg, W. E. Hennink, D. J. A. Crommelin, and E. Mastrobattista, "Flow cytometry for rapid size determination and sorting of nucleic acid containing nanoparticles in biological fluids," *Pharmaceutical Nanotechnology: Unmet Needs in Drug Delivery*, vol. 141, pp. 328-338, 2010.

[85] L. E. McNeil, A. R. Hanuska, and R. H. French, "Orientation dependence in near-field scattering from TiO_2 particles," *Applied Optics*, vol. 40, pp. 3726-3736, 2001.

[86] A. Ashkin, "Acceleration and Trapping of Particles by Radiation Pressure," *Physical Review Letters*, vol. 24, pp. 156-159, 1970.

[87] A. Ashkin, J. M. Dziedzic, J. E. Bjorkholm, and S. Chu, "Observation of a single-beam gradient force optical trap for dielectric particles," *Optics Letters*, vol. 11, pp. 288-290, 1986.

[88] D. L. J. Vossen, D. Fific, J. Penninkhof, T. van Dillen, A. Polman, and A. van Blaaderen, "Combined optical tweezers/ion beam technique to tune colloidal masks for nanolithography," *Nano Letters*, vol. 5, pp. 1175-1179, Jun 2005.

[89] X. Cui, D. Erni, and C. Hafner, "Optical forces on metallic nanoparticles induced by a photonic nanojet," *Optics Express*, vol. 16, pp. 13560-13568, 2008.

[90] V. Yannopapas, "Photonic nanojets as three-dimensional optical atom traps: A theoretical study," *Optics Communications*, vol. 285, pp. 2952-2955, Jun 1 2012.

[91] S. C. Kong, A. Sahakian, A. Taflove, and V. Backman, "Photonic nanojet-enabled optical data storage," *Optics Express*, vol. 16, pp. 13713-13719, Sep 2008.

III. PJS ETCHING USING MICROSPHERES

1. Introduction

There are many applications for PJ, as mentioned in chapter two. In this chapter we consider mask-less laser nano-patterning using spherical micro-spheres, also called nano-sphere lithography (NSL) [1]. The process takes place in the near-field of spherical particles. As discussed before, the microspheres can be considered as micro-lenses, but, since the concentrated beam is beyond the diffraction limits, it is not a classical optical phenomenon, and is called Photonic Jet [2, 3]. Many methods have already been implemented to improve the lateral resolution of laser etching using the PJs. Generally dielectric microspheres deposited on the sample surface are illuminated by a laser beam, at normal incidence. Micro or nano-patterning of holes or pillars are performed on the sample [4-10]. An angular scanning with the laser beam can be used to make more complex nano patterns [11]. Dual beams can also be considered [12] i.e. a Bessel beam (λ = 532 nm) for trapping the microsphere in an aqueous medium and a Gaussian beam (λ = 355 nm) applied on the microsphere to etch the sample (50 nm from the microsphere) and to create a pattern.

The method considered in this chapter do not differ significantly from the first method mentioned above; it consist in using a near-infrared nano-pulsed laser beam commonly used in industrial processes and adapted micro-spheres. The goal we have pursued was not just to repeat the results already obtained by other authors; we essentially made our simulations and experiments in order to define the kind of PJ that would be relevant for highly resolved laser etching process. Thermal effects and ablation thresholds are evaluated. The collected data will be used to optimize the new method that will be described in the following chapter.

This chapter begins with the electromagnetic simulation of PJs coming out dielectric microspheres in free-space. The incidence wave is a unitary plane wave, linear polarized, at a wavelength λ_o = 1 µm. Then the experimental setup and results achieved with microspheres are described and discussed.

For easy comparison, the same dielectric microspheres have been considered for simulations and the experimental works. Experiments have been carried out on two different samples i.e. a silicon wafer and a glass plate; silicon is easy to etch with a nanosecond near-infrared laser, glass has low absorption at the considered wavelength. Two lasers have been used: a Nd:YAG laser and fiber type Ytterbium, both mode-locked.

2. Electromagnetic simulations of PJs

The electromagnetic simulations of PJ generated by a dielectric microsphere can be realized using the Lorenz-Mie theory [12-19]. This theory expresses the total electromagnetic field inside and outside a dielectric sphere as function of the incident field. The field outside the sphere is considered as the sum of the incident field and of the scattered field. All fields can be expanded in spherical vector functions as:

$$E(\mathbf{r}) = \sum_{l=0}^{L} a_l \psi_{\mathrm{TE,l}}(\mathbf{r}) + \sum_{l=0}^{L} b_l \psi_{\mathrm{TM,l}}(\mathbf{r}) \qquad (3.1)$$

where $\psi(r)$ are the electromagnetic eigenmodes for a sphere [17]. The expansion order L is at least $\pi D_s/\lambda_o$, for a sphere diameter of D_s and an incident wavelength of λ_o. Using this analytical 3D vectorial solution, the calculations are faster than other methods like FEM or FDTD. Our simulations have been achieved with LightScatPro software developed in our team; it is based on the Mie theory. Most of the published articles on electromagnetic simulation only considered electric field because the electric dipole transitions are dominant in the interaction of radiation with matter. In one article (Li et al. [18]), magnetic and electric field are considered in the simulations; similar results are obtained. In our simulations described next, we considered only electric field.

We have used the following parameters. The incident beam is described as a unitary plane wave in the near-infrared (λ_o = 1 µm), with a linear polarization. The microspheres can be in glass (n_g = 1.5) or barium-titanate $BaTiO_3$ (n_b = 1.9) in free space. We have been limited in our choice or microspheres sizes by the commercial offers. Thus we have tested glass microspheres with diameter D_s of 4λ, 6λ, 24λ and 35λ, and barium-titanate ($BaTiO_3$) microspheres of 42λ, 69λ and 87λ. In simulation, the center of the sphere is placed in the center of the 3D coordinates (Figure 3.19).

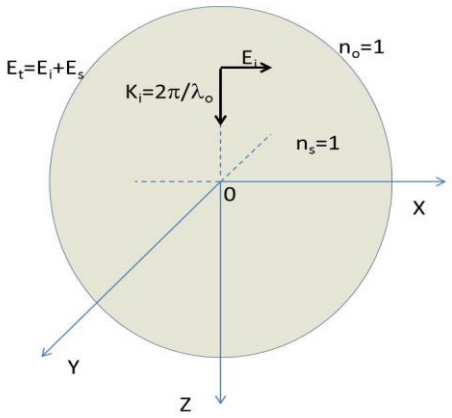

Figure 3.19. A sphere in free space is illuminated by a plane wave (E_x,H_y,k_z). The incident wave propagates in the +z direction

The PJ parameters are deducted from the simulations, as has been illustrated in Figure 2.8: the maximum beam intensity or the maximum electric field ($I_{\max} = |E_{\max}|^2$), the distance between the sphere surface and the position of this maximum on the axis (f_c), the full-width of half maximum (I_{FWHM}) and its length (ℓ_{FWHM}), also considered as the full-length at half maximum but along th axis.

The total electric field (E) simulated in the OXY plane in the shadow side of glass spheres are shown in Figure 3.20. The deduced PJ parameters for glass micro-spheres are presented in Table 3.4. We see that larger spheres generate higher electric field (E_{max}) than smaller ones and smaller spheres pull the PJ closer to the sphere surface. It can also be noticed that for largest micro-spheres, i.e. D_s of 35λ and 24λ in Figure 3.20a and Figure 3.20b, some high beam-concentration nodes can be inside the sphere.

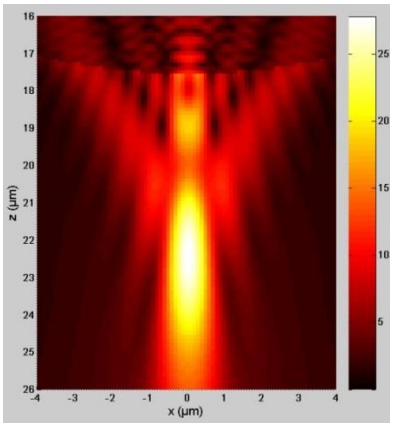

a.Diameter D_s of 35λ

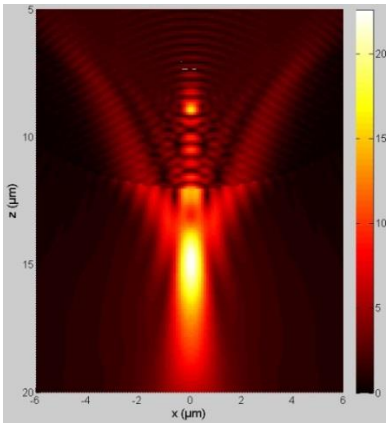

b.Diameter D_s of 24λ

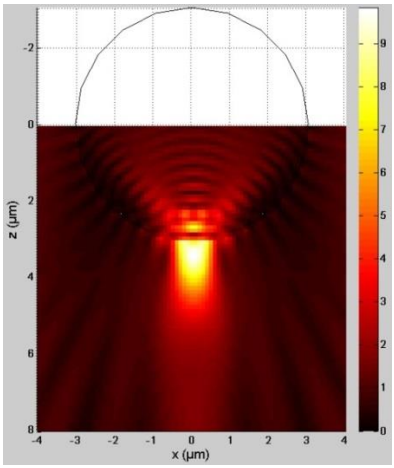

c.Diameter D_s of 6λ

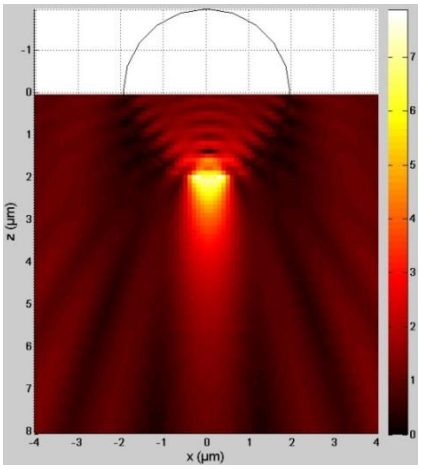

d.Diameter D_s of 4λ

Figure 3.20. The total electric field distribution in XZ plane for a glass microsphere (n_s = 1.5) with a diameter D_s of (a) 35λ, (b) 24λ, (c) 6λ and (d) 4λ

D_s (µm)	f_c (µm)	E_{max}	I_{max}	Γ_{FWHM} (µm)	ℓ_{FWHM} (µm)	F_{PJ} (J/cm²)
35	5	27.8	776	0.8	3.9	551
24	3	22.6	529	0.7	4.3	371
6	0.4	9.8	100	0.6	3.5	71
4	0.15	6.9	47	0.7	3.5	43

Table 3.4.The PJs parameters deducted from simulation in Figure 3.21

F_{PJ} is the maximum fluence of the photonic jet. From Table 3.4, as the microsphere diameter D_s increases, we can see that f_c, E_{max}, I_{max} and F_{PJ} also increase. With the increase of D_s, the increase of f_c means that the photonic jet will be no more on the sample surface. Therefore the fluence F_{PJ} is not necessary the good one to take into account to evaluate if ablation can occur or not.

If now we consider spheres with a higher refractive index as barium-titanate spheres (n_{BaTiO3} = 1.9), simulations are shown in Figure 3.21 and the deduced photonic parameters are in Table 3.5. The electric field coming out of barium-

titanate microspheres is also focused in a PJ. Since they have larger diameter the intensity concentrations are higher than those generated by glass microspheres. However, the field is not concentrated further outside the spheres, as in Table 3.4, but inside. This yields the minus sign of f_c in Table 3.5. So a sphere diameter increase makes the PJ further, but it can be compensated by a refractive index increase which makes the PJ closer to sphere center. Nevertheless a situation, with the high concentrated beam inside the microspheres, is not such a situation to have interest for an etching. Barium-titanate has probably a too high refractive index.

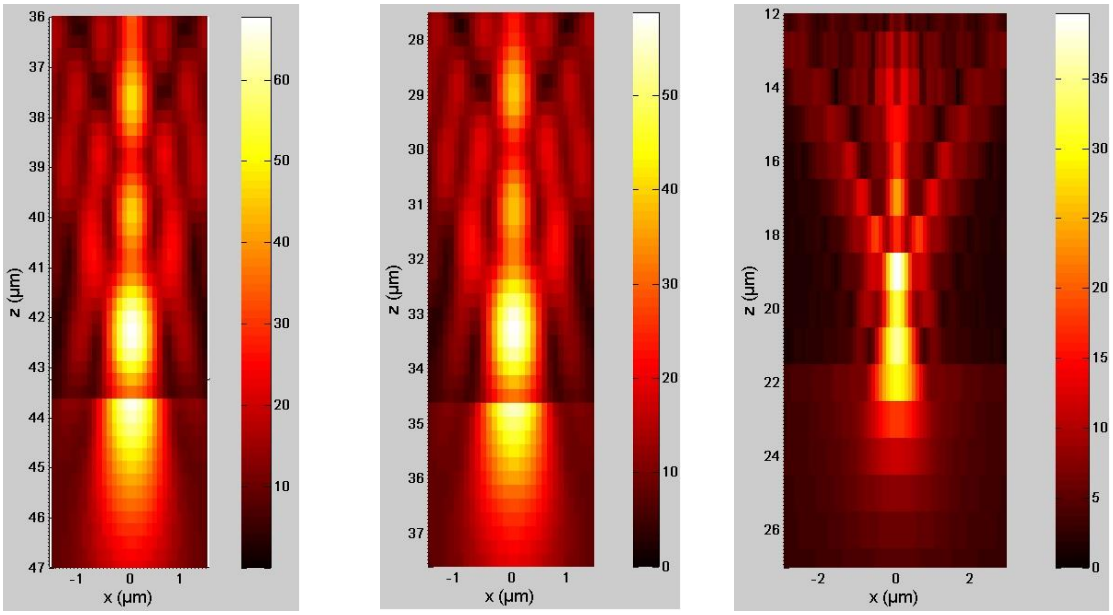

a. Diameter D_s of 87λ b. Diameter D_s of 69λ c. Diameter D_s of 42λ

Figure 3.21. The total electric field distribution in XZ plane for a barium-titanate microspheres (n_{BaTiO3} = 1.9) with a diameter D_s of (a) 87λ, (b) 69λ and (c) 42λ

D_s (µm)	f_c (µm)	E_{max}	I_{max}	α
87	- 0.5	67	4489	4489
69	- 1.0	60	3600	3600
42	- 2.0	40	1600	1600

Table 3.5. The PJ parameters from simulation in Figure 3.24

From these electromagnetic simulations, it seems that PJs coming out of our glass microspheres could be applicable for material micro-processing since the focused beams (PJ) appears outside the spheres. In the case of barium-titanate spheres, the interest seems limited, even though some secondary maxima at the boundary of the spheres emerge out. We have made experiments for the two situations as described next.

3. Experimental setup

The experimental setup considered in this chapter is quite classical [5-10]: the microspheres are sown on the substrate randomly; the laser beam illuminates the substrates surface at normal incidence, at some distance from the beam waist. Figure 3.22 shows a schematic view of the experimental setup to test PJ etching using microspheres. The sample is at a defocused position, at

a distance z from the waist. This distance is chosen large enough to allow the illumination of many spheres at the same time. Knowing the distance z it is possible to evaluate the beam size w_z at this location from the divergence law of a Gaussian beam [20]:

$$w_z{}^2 = \left(\frac{z^2}{z_R{}^2} + 1\right) w_0{}^2 \tag{3.2}$$

where z_R is the Rayleigh distance given by:

$$z_R = {}^{\pi w_o{}^2}/_{\lambda} \tag{3.3}$$

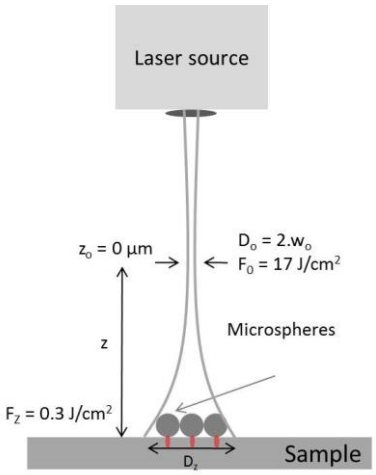

Figure 3.22.The laser illumination scheme

A. Laser sources and characterization

a.

b.

Figure 3.23. The near-infrared laser sources: (a) Trumpf VectorMark® Nd:YAG laser, (b) .YLIA M20 Quantel fiber laser

Pulsed lasers emits ns pulses in the near-IR are commonly used in industry.

We used the following two sources:

1. Trumpf VectorMark® Nd:YAG laser, with 28 ns pulses and wavelength λ=1064 nm (Figure 3.23a).
2. YLIA M20 Quantel Ytterbium fiber laser, with 160 ns pulses and wavelength λ=1064 nm (Figure 3.23b).

Table 3.6 lists the main features of the two lasers.

Table 3.6. The main features of Trump VectorMark® Nd:YAG laser and YLIA M20 Quantel fiber laser (from datasheet)

	Nd:YAG laser	**YLIA laser**
Wavelength (λ)	1064 nm	1060 nm
Pulse duration	28 ns	160 ns
Maximum average power (P_{av})	5.5 watt	20 watt
Laser power control	0 – 100 %	20 – 255 relative unit
Repetition rate (f_{rate})	4 – 60 kHz	20 – 100 kHz
Maximum energy per pulse	1 mJ at 5 kHz	1 mJ
Galvanometer scanning speed	1 – 10000 mm/s	1 – 10000 mm/s
Coverage area	120 x 120 mm	120 x 120 mm
Measured beam diameter (D_o)	64.4 µm	91.7 µm

The etching marks on the samples are observed and measured using an Olympus® Vanox-T microscope (Figure 3.24a) and a Zygo® optical profilometer (Figure 3.24b).

a. b.

Figure 3.24.Observation and measuring instruments:
(a) Olympus® Vanox-T microscope and (b) Zygo® profilometer

We have first characterized the laser beam profile with the beam analyzer NanoScan™. Figure 3.25 shows the measurement set-up for the YLIA laser. Here, a 50% reflector is placed between the laser-head and the NanoScan™ sensor to reduce the laser fluence on the sensor avoiding damage or power-saturation. The sensor is placed at the focus point of the laser beam. A similar method has been applied to characterize the Trumpf VectorMark™ Nd:YAG laser.

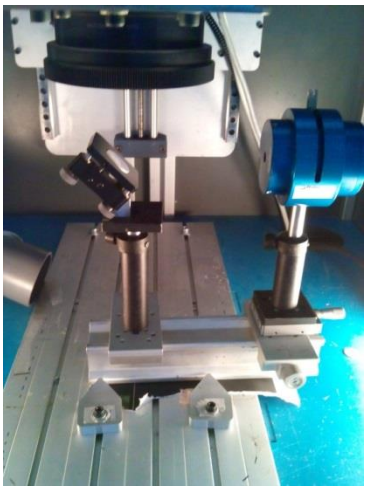

Figure 3.25. Setup to measure the beam profile of the YLIA M20 Quantel fiber laser system; the laser comes out from the galvanometer head is filtered and reflected into the NanoScan™ sensor.

The Nd:YAG laser beam profile captured by NanoScan™ is shown in Figure 3.26. The profile is close to a Gaussian beam with an intensity distribution given by:

$$I = I_0 e^{-2r^2/w_o{}^2}, \tag{3.4}$$

for w_o the beam waist.

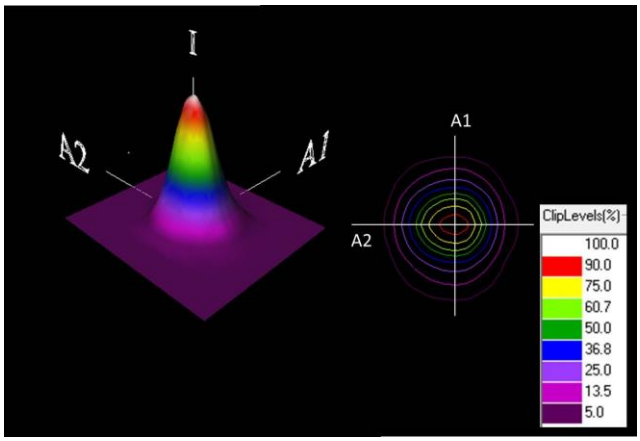

Figure 3.26. Nd:YAG laser beam profile in 3D and 2D

The NanoScan™ laser profile retrieves the four-sigma widths $D_{4\sigma}$ [21] (3.5) of the focus spot: 62.5 µm in A1 direction and 66.4 µm in A2 direction. So the beam has a small ellipticity around 0.96.

$$D_{4\sigma} = 4\sigma, \tag{3.5}$$

with σ the standard deviation of beam intensity profile, linked with the beam waist w_0 by formula (3.6) [22].

$$W \equiv 2\sigma. \tag{3.6}$$

Inserting the mean four-sigma width[1] of Nd:YAG laser retrieved from NanoScan™, that is $D_{4\sigma}$ = 64.4 µm, into equation (3.5) and (3.6) will yield the

[1] *The four-sigma width, also called variance diameter [23], is defined as a standard beam width in ISO standard 11146 [24, 25]. However, in real situation the second moment is not practical, so another method – knife-edge method – is used because it is the most practical method which can be readily related to the second-moment method [26].*

beam radius of Nd:YAG laser at focus point w_0= 32.2 µm.

The YLIA laser beam profile captured by NanoScan™ is presented in Figure 3.27. Its four-sigma widths in both axes are 85.6 µm and 97.8 µm (ellipticity of 0.888), so the mean four-sigma width $D_{4\sigma}$ is 91.7 µm, and therefore the waist of the YLIA laser is w_0= 45.8 µm.

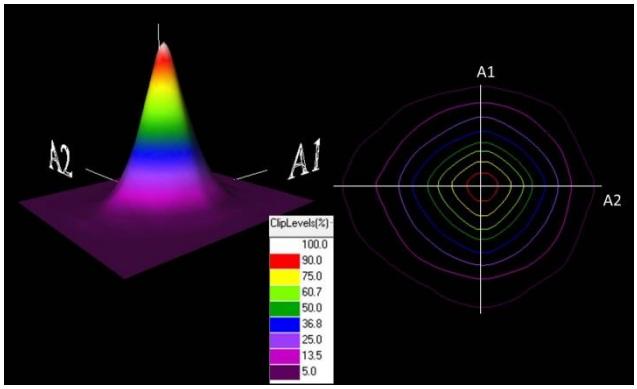

Figure 3.27. YLIA laser beam profile in 3D and 2D

After the determination of the waist of laser beams, the beam width w_z at the surface sample can be calculated using equation (3.2) and (3.3). The distance z from the beam waist to the sample for our Nd:YAG laser is 22 mm, whereas for the YLIA laser, it is respectively 11.5 mm and 108 mm (see corresponding fluence in Table 3.7). The first distance allows illuminating all the 300 µm square-cell as with the Nd:YAG laser. The second distance has been chosen to illuminate a larger area to check a possible correlation between the etching size and the localization of the spheres with respect to the Gaussian beam center. Such a correlation has not been observed. Once the threshold condition has been reached, power density doesn't seem to influence the etching size significantly.

Table 3.7. Beam waist, laser affected zone and beam fluence at focal point and defocused range of Nd :YAG and YLIA laser

Laser	$D_{4\sigma}$ (µm)	f_{rate} (kHz)	Beam waist (µm)		Laser affected zone (cm²)		Beam fluence (J/cm²)	
			w_0	w_z	A_0	A_z	F_0	F_z
Nd:YAG	64.4	10	32	229 µm at z = 22 mm	3.3×10^{-5}	1.7×10^{-3}	16.9	0.33
Nd:YAG	64.4	20	32	229 µm at z = 22 mm	3.3×10^{-5}	1.7×10^{-3}	16.9	0.17
YLIA	91.7	20	46	798 µm at z = 108 mm	6.6×10^{-5}	2.0×10^{-2}	14.3	0.05
YLIA	91.7	20	46	354 µm at z = 11.5 mm	6.6×10^{-5}	2.9×10^{-4}	14.3	3.25

The peak power of laser beam can be calculated using [20]:

$$P_{max} = \frac{2\,P_{av}}{T.f_{rate}\sqrt{\pi}}\,, \tag{3.7}$$

with T the pulse duration. So the laser power density at z is

$$P_{dens} = \frac{P_{max}}{A_z}\,. \tag{3.8}$$

with $A_z = \pi w_z{}^2$.The average power P_{av} can be obtained from the datasheet given in Table 3.6 or from the direct measurement using a calorimeter.

To obtain the laser fluence on the sample, we have performed a characterization of the beam to take into account the real operational frequency rate. The details are given in Appendix.

B. Samples and microspheres

The samples considered in this research are silicon wafer and glass plates. The first one is easy to etch with a nanosecond near-infrared laser, whereas the second one has a low absorption for the considered wavelength. The two materials can be found with surface having low roughness (experimental criterion) and are involved in a lot of applications that requires micro-structuration. In coherence with the simulation, two sphere-materials have been considered: glass and barium-titanate spheres. Table 3.8 lists the microspheres specifications used in the experiments (refractive index, diameter and size dispersion). They have been ordered from Cospheric and Bangs Laboratories Inc.

Table 3.8. Microspheres specification origin from Cospheric (1) and Bangs Laboratories Inc. (2)

Microsphere material	Refractive Index (n_s)	Range Diameter (µm)	Mean Diameter (µm)	Origin
Glass	1.5	3.5 – 4.4	4	1
		5.5 – 6.7	6	1
		22 – 27	24	2
		32 – 38	35	2
Barium titanate	1.9	38 – 45	42	2
		63 – 75	69	2
		75 – 90	87	2

C. Micro-localization and repeatability

Square cells (Figure 3.28) are created to ease the localization of the microspheres on the sample. The illumination set-up is adjusted to allow the beam to cover the square cell.

The cell is a square of size of ~300 x 300 µm like. Not too large to be easily observed under microscope in one way and not to small in order that several spheres could be put inside the cell and illuminated in one time. The cells have been created on silicon wafer at the focal point of the beam square. The samples are placed on the laser table at a fixed position assured by the mechanical system (Figure 3.29). This system allows a repositioning of a few microns after sample removal for microscope observations.

Figure 3.30 shows four square cells on silicon wafer. Each cell has notations indicating illumination information. Here for example five points indicate that five laser pulses have illuminated the cell, one point indicates one laser pulse, etc. Two points inside the cell and six points around the cell boundary are also etched as markers to facilitate easy positioning under profilometer. They can also be used as size reference illustrating the direct laser etching size at the focal point of the laser beam without using any microsphere. The diameter of

this direct laser etching, limited by the optical head diffraction, is in the range of 40 – 60 µm.

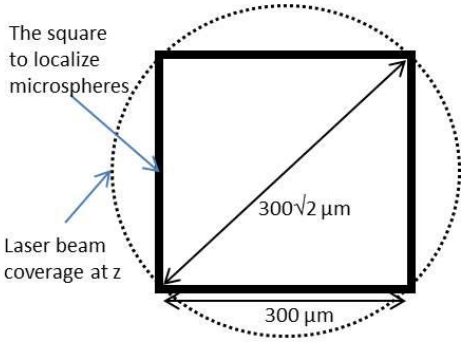

a. Geometry of the illumination area

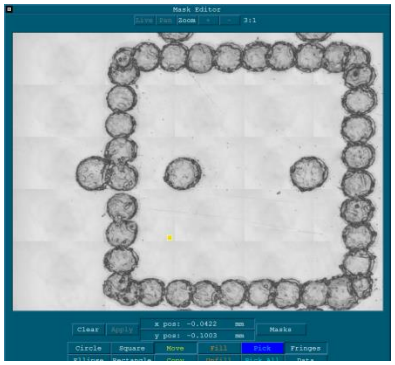

b. The cell is etched on the surface and captured using the Zygo® profilemeter

Figure 3.28. Square cell used to localize the spheres on the substrate surface

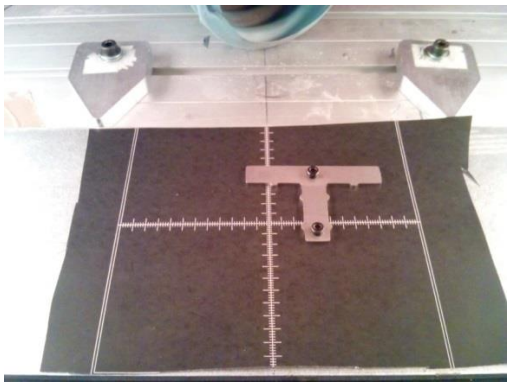

a.

b.

Figure 3. 29. Mechanical system used to place the sample at the center point of the laser table in repeateable way on (a) the Nd:YAG laser and (b) the YLIA laser

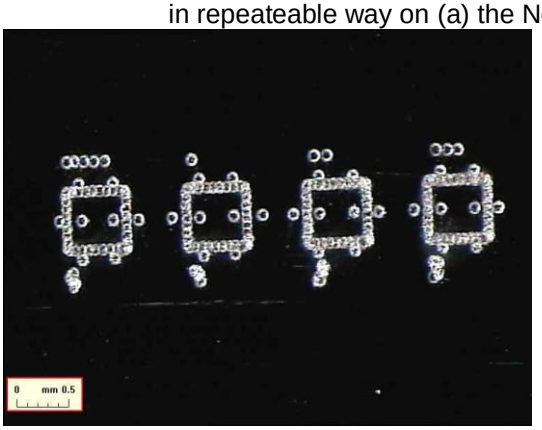

Figure 3.30. Four square-cells on silicon wafer to ease localization

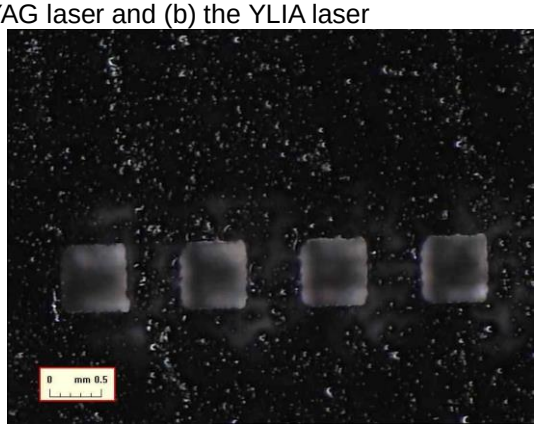

Figure 3.31. Four square-cells on ink-covered glass plate to ease localization. The additional marks above the cells need higher magnification to be visible.

The process is more difficult on glass. Glass is transparent to near-infrared; a direct etching of the square cell is not possible. Therefore, a different method is used. First, the surface is covered by ink. Then, the focused laser scrubs the ink out of the surface to create the cells as depicted in Figure 3.31. To make sure that the laser beam is in the correct position on the surface, the cell is created

just before the PJ etching experiment, using the same laser.

D. Laser setting scheme for PJ etching experiments

The laser parameters used in our experiments on PJ etching are shown on the table below. The choice has been made to have comparable values of laser fluences on the substrate.

Table 3.9. Laser setting scheme in experiments of PJ etching using microspheres

	Trumpf VectorMark® Nd:YAG	**YLIA Ytterbium**
Frequency rate (f_{rate})	10, 20 kHz	20 kHz
Number of pulse (pulses)	1, 2, 3, 5	2, 3, 4, 5
Defocussed position (z)	14.2, 21.6 mm	108.2 mm
Laser power control variation ($P_{applied}$)	10, 20, 30, 40, 50, 60, 70, 80, 100 %	160, 180, 200, 220 (relative unit)

E. Experimental protocol

Figure 3.32 below shows the substrate surface at different states of illumination. The following protocol has been used.

1. Once the localization cells is created on sample surface, as explained in section C above, the sample is cleaned using isopropanol to remove any debris that may exist due to the cell etching (Figure 3.32a). Then a first microscopic view of each cell is captured to detect possible defects.
2. The microspheres are sown down on the cells. A needle can be used for this purpose: put in contact of the sphere (dry powder) and then hit on the sample to make the microspheres fall down. Then, the cell with microspheres on the sample surface is captured (Figure 3.32b). Hence the initial position of all microspheres is known.
3. The sample with microspheres inside the cells is carefully placed on laser table at the same position when the cells were created. As we have verified, during the sample motion the spheres are naturally stick onto the sample. After that, the laser is defocused to illuminate the whole cell. Then, each cell is illuminate with particular laser setting. Afterwards, the cells are captured again to characterize the sample and sphere state after laser illumination (Figure 3.32c).
4. By poking the sample onto a table almost all microspheres are removed. If necessary, isopropanol can also be applied to clean the sample. Then the cells are captured again to observe the sample without spheres and after PJ etching (Figure 3.32.d).
5. Measurements of the PJ etching features are made using a Zygo® profilometer. **We make measurement only on PJ etching correlated with a sphere at the same position before and after illumination**.

The illustration in Figure 3.32 also shows that the position of one the spheres is related to the position a mark on the substrate. This mark, identified as a PJ etching, has been measured using the Zygo® profilometer. An example of profile is shown in Figure 3.33.

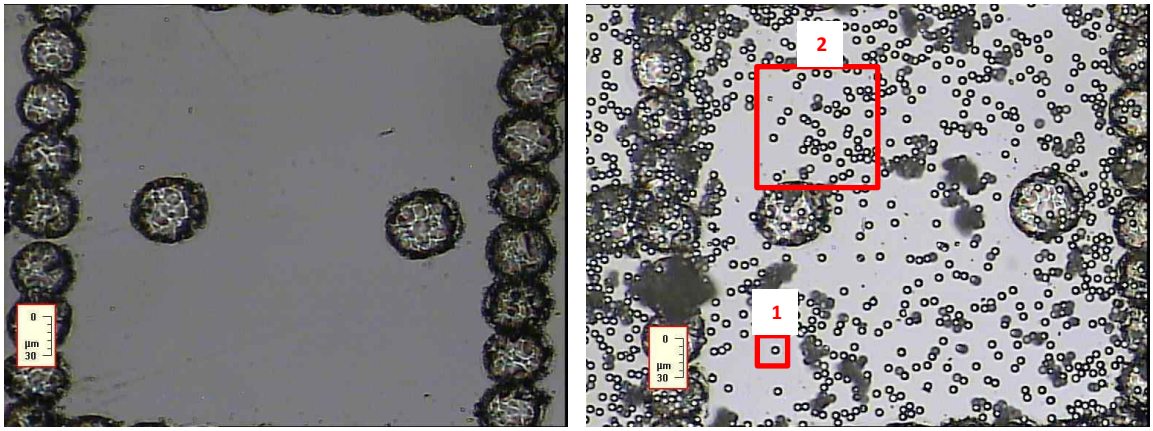

a. b.

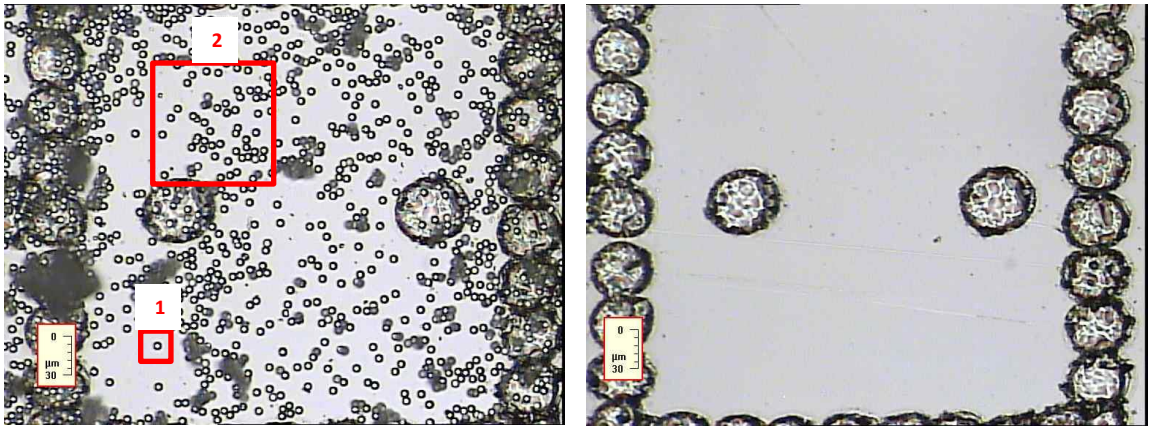

c d.

Figure 3.32. Microscopic view of a cell at different stages of the experiment: (a) a clean cell without microsphere, (b) a cell with microspheres (Ds = 6 µm) inside before laser illumination, (c) a cell with microspheres inside after 5 pulses of laser illumination and (d) a clean cell after all microspheres are removed. The number (1) indicates a microsphere that remained at its place after laser illuminations and the number (2) indicates a zone where it appears that some microspheres move during laser illuminations.

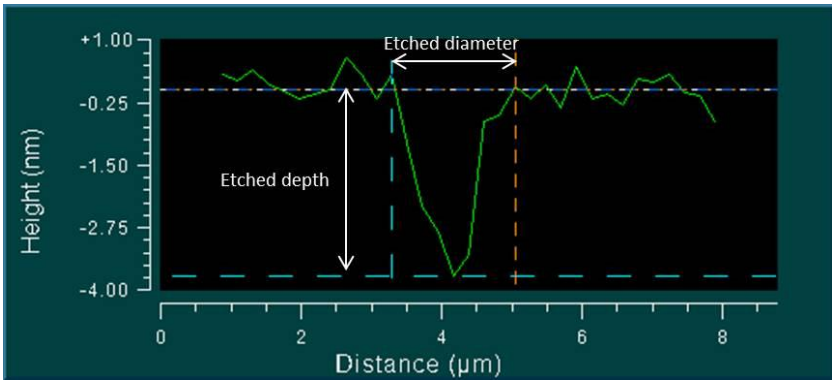

Figure 3.33. An etching mark profile with its parameters

4. PJ etching on silicon wafer using glass microspheres

In this section we demonstrate that PJ can be used to reduce the etching size on silicon wafer using glass microspheres. We describe the experimental tests that gave us some insights in the interaction between the PJ-matter (here silicon) interaction. We discuss also the influence of the laser beam features like

pulse duration, power and number of pulses on the feature size of PJ etching

A. PJ etching on silicon wafer using 28ns Nd:YAG laser

Each type of glass microspheres described in Table 3.8 has been tested. The sample is a silicon wafer. First, the source is the 28ns Nd:YAG laser, the frequency is at f_{rate} = 10 kHz. The laser illuminates the sample at the defocused position z = 21.6 mm. The laser is at its maximal power (5.5 W). The fluence on the spheres is 0.7 J/cm². There is no etching mark inside the cells illuminated by a single laser pulse. And at least two pulses are needed to etch silicon wafer. Probably the first pulse creates some surface defects making decrease the ablation threshold allowing the second pulse to etch. Table 3.10 gives the mean value of PJ etching parameters measured as function of the sphere diameters and pulse numbers. The smallest etching mean diameter measured is D_{etch} = 1.14 ± 0.16 µm, yielded by microspheres having diameter D_s = 4 µm with the maximum PJ fluence F_{PJ} = 43 J/cm² on the sample (Table 3.4) and 2 laser pulses illumination, close to the size obtained using the 6 µm spheres. Some specific etchings can be smaller, the smallest etching has a diameter of 0.60 ± 0.14 µm (microsphere D_s = 6 µm, 3 laser pulses and with a maximum PJ fluence F_{PJ} = 71 J/cm²). Figure 3.34 shows this smallest PJ etching profile.

Table 3.10. Mean value of PJ etching parameters on silicon wafer using Nd:YAG laser (5.5 W) at frequency rate f_{rate} = 10 kHz (F_z= 0.7 J/cm²) as function of sphere size and pulse number

Number of pulse	Microsphere size D_s (µm)	Etched diameter (µm)		Etched depth (nm)	
		D_{etch}	ΔD_{etch}	d_{etch}	Δd_{etch}
1	4,6, 24, 35	-	-	-	-
2	4	1.1	0.16	4.6	3.7
	6	1.7	0.41	28	22
	24	3.4	1.27	760	545
	35	5.1	1.89	895	253
3	4	1.4	0.27	15	16
	6	1.3	0.36	63	0
	24	2.8	1.24	614	432
	35	5.4	1.16	1392	400
5	4	1.4	0.20	13	7
	6	1.4	0.14	17	14
	24	4.4	0.90	930	414
	35	6.6	1.19	933	199

These observations clearly demonstrate the PJs ability reducing the lateral size of direct laser etching on silicon. The etching diameter is reduced from ~50 µm (points inside the localization square cells) to 1.14 µm using PJ (4 µm sphere, 2 pulses), that is 44 time smaller.

Figure 3.35 depicts the etching diameters as function of microspheres size and pulse number. Clearly bigger microspheres induce larger etching diameter. When these etched diameters (D_{etch}) are compared to the full-widths at half maximum (Γ_{FWHM}) of PJs simulations coming out of glass microspheres, it is obvious that D_{etch} is larger than Γ_{FWHM}; between 20% and 100% for smaller spheres to more than 600% in the case of 35 µm microspheres. Larger is the sphere, larger is the PJ fluence (Table 3.4), and larger is the power density, larger is the etching diameter.

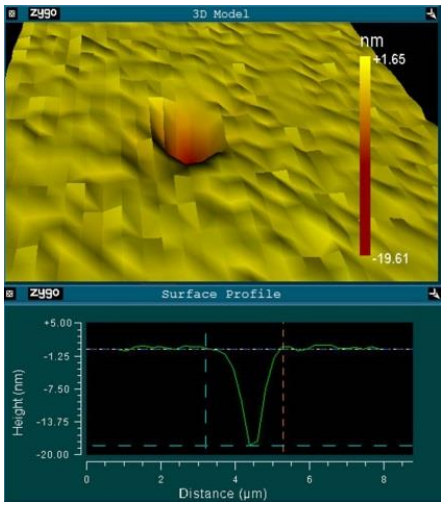

Figure 3.34. The smallest PJ etching on silicon wafer using a glass microsphere Ds = 6 µm ($(F_z$= 0.7 J/cm²))

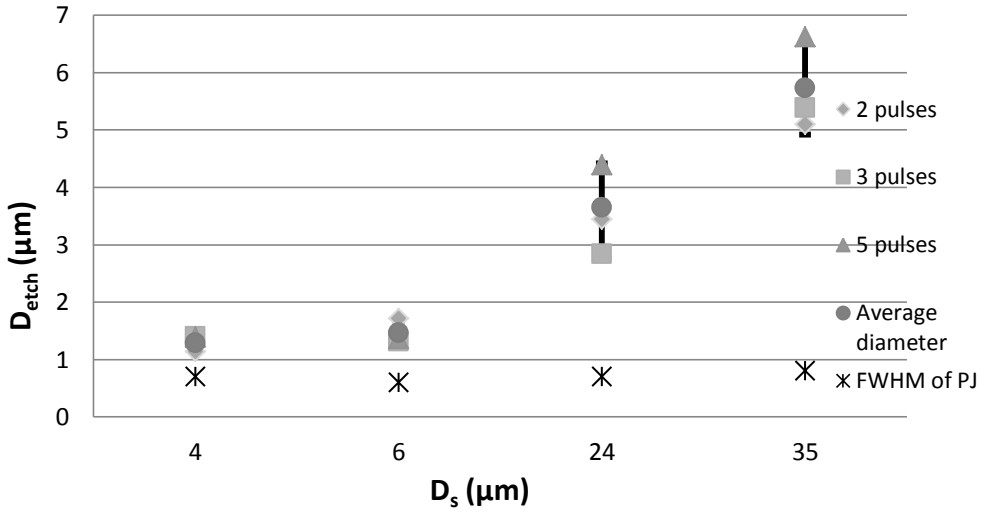

Figure 3.35. Etching diameter (D_{etch}), with measurement standard deviation, on silicon wafer and the FWHM of PJ from simulations as a function of microsphere size (D_s)

Figure 3.36 depicts the etching depth as function of microspheres size. It shows that bigger microspheres induce deeper etching depths.

Another observation is, that the difference of diameter (Figure 3.35) or depth (Figure 3.36) measured when we increase the number of pulses, is not significant because it is smaller than the standard deviation of the measurements. Therefore, there is no obvious correlation between the etching diameter or depth and the pulse number. Also, adding more pulses do not significantly enlarge the etching (5, 10, 15 pulses have also been tested). It may because after the first etching the sphere is dirty by the etched material and thus no more PJ is generated by the next pulses.

The depth is not related to the PJ position (f_c) (simulation Figure 3.20 and Table 3.4). In simulations microspheres are in free space, so the PJs is located at few micrometers from microspheres and do not interact with any material. In the experiments, microspheres are directly in contact with the silicon wafer.

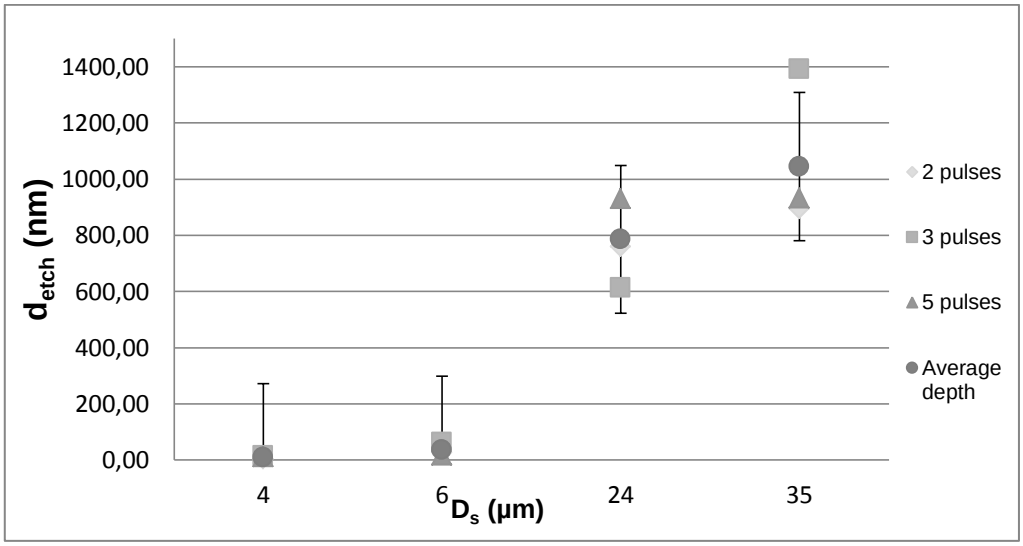

Figure 3.36. Etching depth (d_{etch}) on silicon wafer as a function of microsphere size (D_s)

Some PJ etching marks do not have smooth profiles, but sharp spikes/ columns and hillocks around the mark (Figure 3.37). These shapes emerge for nanosecond pulse lasers and strongly depend on the number of pulses and the fluency of the laser applied at the same spot in oxidizing/halogen atmosphere (ambient air). In this case the high laser fluence seems to be the main variable responsible for these shapes. These sharp spikes and hillock shapes are obtained only for larger spheres (D_s = 24 µm and 35 µm). The simulations results in Table 3.4 has revealed that these two microspheres can enhance the incident laser intensities to over than 500 times and generate the maximum PJ fluence, respectively, 371 and 551 J/cm² for D_s = 24 µm and 35 µm. Meanwhile two others (D_s = 4 µm and 6 µm) concentrate the intensity less than 100 times to reach PJ fluence of 43 and 71 J/cm², respectively. This higher enhancement yields to higher fluence that gives rise of the column and hillock shape.

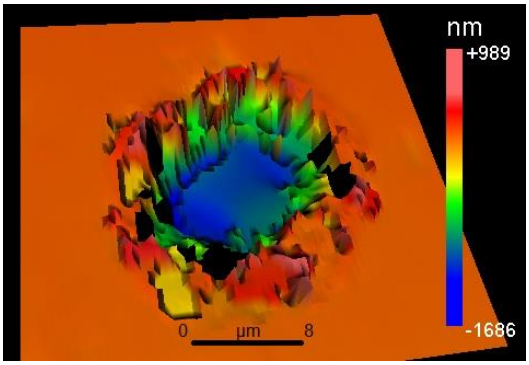

Figure 3.37. Sharp spikes/column and hillocks around a crater yielded by the larger glass microspheres (D_s of 24 µm and 35 µm)

B. Comparison with the 160 ns YLIA laser

Similar experiments have been done at f_{rate} = 20 kHz, to allow the comparison at the same repetition rate of the 28 ns Nd:YAG laser and the 160 ns YLIA laser. For this comparison the incident peak power has been considered. The lasers setting for the test is summarized in Table 3.11. Only glass micro-spheres of diameters D_s of 4 µm and 6 µm have been considered, since the smaller etching was achieved with these ones.

Table 3.11. Lasers setting scheme in compatibility comparison experiments

	Nd:YAG	**YLIA**
Frequency rate (f_{rate})	20 kHz	20 kHz
Number of pulse (pulses)	2, 3	2, 3, 4, 5
Defocussed position (z)	21.6 mm	108.2 mm
Fluence on the spheres F_z	0.16 J/cm² (100%)	0.05 J/cm² (100%)
Laser power control variation (P_{peak})	10, 20, 30, 40, 50, 60, 70, 80 %	160, 180, 200, 220 (relative unit)

The PJ etching parameters measured for the Nd:YAG laser, are presented in Table 3.12. It shows that at least a peak power of 4.43 kW (40% of maximum peak power) is needed to obtain a PJ etching using glass microsphere D_s = 4 µm. Afterward, beyond 4.43 kW the D_{etch} seems to be not affected much by the variation of the number of pulses neither by the incident power. The diameter D_{etch} of PJ etching stay in the range of 1.45 to 1.70 µm and the mean depth is of 31.8 ± 12.8 nm. Similar results are obtained with the 6 µm spheres.

Table 3.13 shows the features size of PJ etching obtained using glass microspheres of 4 µm and 6 µm sizes with YLIA laser at 20 kHz. Similarly to the case of the Nd:YAG laser, the etch thickness is only slightly affected by the variation of the number of pulses or peak power applied.

We conclude from these observations that for a given sphere the PJ etching sizes on silicon wafer have a low dependence on pulse duration, pulse number and incident power. For these reasons the tests are not enough to determine if the main threshold parameter is the fluence rather than the peak power density.

Table 3.12. PJ etching parameters on silicon wafer using 20 kHz Nd:YAG laser at z = 22 mm

$P_{applied}$		Pulses	Microsphere size D_s = 4 µm				Microsphere size D_s = 6 µm			
			Etched diameter (µm)		Etched depth (nm)		Etched diameter (µm)		Etched depth (nm)	
%	kWatt		D_{etch}	ΔD_{etch}	d_{etch}	Δd_{etch}	D_{etch}	ΔD_{etch}	d_{etch}	Δd_{etch}
10%	1.11	2	-	-	-	-	1.55	0.08	25.82	9.80
		3	-	-	-	-	1.62	0.16	25.00	14.17
20%	2.22	2	-	-	-	-	1.53	0.09	106.77	143.56
		3	-	-	-	-	1.60	0.17	25.16	14.23
30%	3.32	2	-	-	-	-	1.48	0.10	16.17	5.34
		3	-	-	-	-	1.40	0.09	18.49	5.29
40%	4.43	2	1.67	0.14	21.63	21.63	1.50	0.14	10.18	4.19
		3	1.67	0.21	19.30	2.83	1.43	0.11	31.04	10.59
50%	5.54	2	1.56	0.06	35.63	35.63	1.59	0.11	82.75	87.58
		3	1.60	0.09	23.52	10.13	1.42	0.07	20.68	11.00
60%	6.65	2	1.58	0.12	27.99	27.99	1.53	0.11	23.78	8.97
		3	1.46	0.13	26.34	16.97	1.48	0.17	26.07	11.44
70%	7.76	2	1.55	0.17	63.39	63.39	1.58	0.12	27.29	14.70
		3	1.55	0.18	23.44	9.04	1.42	0.12	25.39	16.61
80%	8.87	2	1.44	0.19	31.11	31.11	1.69	0.10	44.46	24.23
		3	1.72	0.19	46.01	25.57	1.55	0.13	92.98	149.09

Table 3.13. PJ etching parameters on silicon wafer using 20 kHz YLIA laser at z = 108 mm

P_{peak}		Pulses	Microsphere size 4 µm				Microsphere size 6 µm			
			Etched diameter (µm)		Etched depth (nm)		Etched diameter (µm)		Etched depth (nm)	
	kWatt		D_{etch}	ΔD_{etch}	d_{etch}	Δd_{etch}	D_{etch}	ΔD_{etch}	d_{etch}	Δd_{etch}
	3.9	2	1.47	0.14	31.72	22.07	1.57	0.05	36.11	8.78
		3	1.33	0.31	13.72	10.44	1.67	0.21	10.18	7.08
		4	1.37	0.05	5.43	2.83	1.23	0.12	4.80	1.23
		5	1.53	0.12	7.65	3.45	1.57	0.21	4.20	1.26
	4.5	2	1.42	0.08	20.28	7.96	1.58	0.12	27.99	11.33
		3	1.50	0.08	6.37	2.92	1.77	0.12	7.22	4.15
		4	1.53	0.09	7.90	7.67	1.57	0.25	10.75	3.20
		5	1.50	0.08	17.56	6.78	1.63	0.19	7.63	1.93
	5.11	2	1.54	0.09	27.74	15.06	1.55	0.17	63.39	62.29
		3	1.40	0.08	10.97	9.39	1.37	0.17	13.51	11.38
		4	1.33	0.05	16.83	8.01	1.53	0.12	6.88	1.47
		5	1.57	0.12	11.98	6.49	1.47	0.09	17.33	5.94
	5.8	2	1.46	0.11	15.14	5.20	1.60	0.14	17.54	12.49
		3	1.40	0.08	9.01	1.39	1.33	0.05	16.36	7.84
		4	1.37	0.05	19.61	9.31	1.50	1.50	22.70	21.45
		5	1.67	0.17	10.37	0.77	1.47	0.12	7.52	2.73

5. PJ etching on glass using glass microspheres

Glass has a low absorption in the near infrared region, a standard nanosecond pulsed laser cannot be used to produce etching. Generally, at this wavelength, picosecond or femtosecond laser are required. We have made tests on this material with the ns IR laser and PJ produced by microspheres. We have used the same experimental protocol than for silicon substrate.

A. PJ etching on glass plates using the Nd:YAG laser

In this experiment, the laser beam has the following characteristics: frequency rate f_{rate} = 10 kHz, laser power P_{av} = 5.5 W, pulse width 28 ns, defocus position z = 22 mm and fluence on the sphere F_z = 0.7 J/cm².

Similarly to observations made for silicon, there is no PJ etching after a single pulse. We are probably just under the ablation threshold, the first pulse make some surface defects making decrease the threshold and allowing the second pulse to etch. Independently of the pulse number, no etching has been observed using 4 µm and 6 µm glass microspheres. Etchings are only observed using 24 µm and 35 µm spheres. These are reasonable, since the maximum PJ fluence F_{PJ} generate by smaller glass microspheres (4 and 6 µm) are respectively 43 and 71 J/cm², below the LIDT of glass that is ~ 100 J/cm². Whilst, F_{PJ} generate by larger microspheres (24 and 35 µm) are respectively 371 and 551 J/cm², above of LIDT of glass. However, the PJ etching profiles are completely different to the ones on silicon. They have a ring shape with a crater in the center, as illustrated in Figure 3.38. The centered crater diameter is

around 2 µm and the ring diameter measures between 4 and 6 µm. Discussion on how this etching profile can be created, by taking into account the power density in the shadow-side of the microspheres, will be presented in section 6 of this chapter.

Table 3.14 summarizes the mean value of PJ etching parameters on glass obtained using glass microspheres with the size of 24 µm and 35 µm. These mean values were calculated without taking into account the number of pulses applied since this number doesn't seem to influence the result significantly.

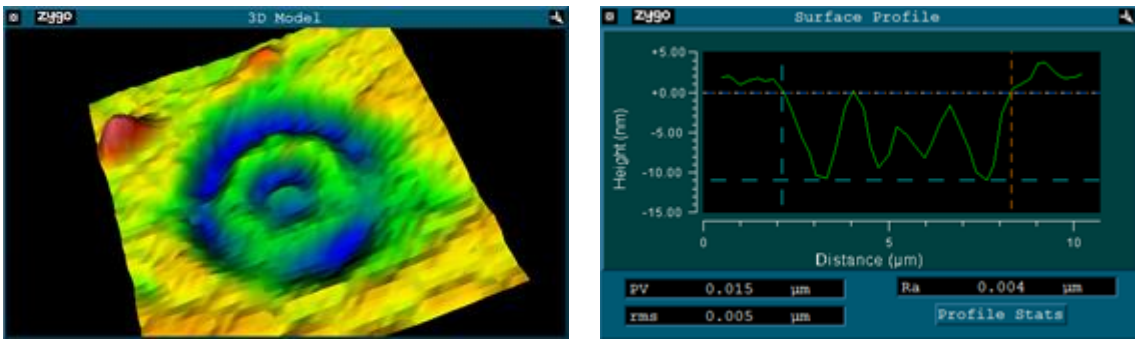

Figure 3. 38. Typical ring shape with a crater in the center of PJ etching profile on glass plates using 24 µm and 35 µm glass microspheres (F_z = 0.7 J/cm²)

Table 3.14. Mean values of PJ etching features on glass plates obtained using Nd:YAG laser at 10 kHz (F_z = 0.7 J/cm²)

Microsphere diameter (µm)	Ring diameter (µm)		Ring depth (nm)		Center etched diameter (µm)		Centre etched depth (nm)	
	D_{ring}	ΔD_{ring}	r_{etch}	Δr_{etch}	D_{center}	ΔD_{center}	d_{center}	Δd_{center}
35	6	0.4	10.5	2	2.4	0.3	8.9	3.5
24	4.6	0.5	12.2	11	1.6	1.1	10.9	7.3

B. PJ etching on glass plates using YLIA laser

In previous experiments, with the 28 ns Nd:YAG Laser, the 4 µm and 6 µm glass microspheres did not yield any PJ etching on glass plates. That is why this experiment with the 160 ns YLIA laser has been done directly with the 24 µm spheres.

In doing these tests we were pursuing two goals: first, determine if the etching threshold of glass can be expressed in terms of fluence or maximum power density; second, see if some induced thermal effects can be observed. The setting was chosen to reach the same peak power density on the sphere that the one obtained with the Nd:YAG laser. For this the distance from beam waist to surface was adjusted to z = 11.5 mm, the average power was P_{av} = 17 W. Etching has been observed with sizes similar to that of silicon. The same experiment has been done with the 35 µm glass microspheres, the results were similar. Now by setting the YLIA laser at the same fluence as the Nd:YAG laser, no etching has been obtained.

In conclusion, as expected, the etching threshold on glass is related to peak power density. The pulse duration increase from one laser to the other must be compensated by an increase of the incident power or by a larger focusing.

6. Discussion on PJ using glass microspheres: experiments to simulations

It is experimentally observed that the PJ etching size differs from the PJ full-width at half maximum obtained by the simulation in free space (without materials). This result is not surprising since the material response depends on several threshold effects that can be expressed in terms of fluence or peak power density. These physical values can be evaluated. The specific conditions of interaction like the direct contact between microspheres and sample can also influence the result of interaction.

A. Laser induced damage threshold: case of silicon

From the laser fluence illuminating the microsphere and from the PJ parameters obtained from electromagnetic simulations (Table 3.4), we can evaluate the fluence and the peak power density under each glass microsphere.

As first approximation the energy of one pulse E_s in the PJ is related to the fluence upon the sphere F_z (or integrated by the sphere) by

$$E_s = F_z \, \pi \left({D_s}/{2} \right)^2 . \tag{3.11}$$

and the fluence in PJ at the backside of microsphere is

$$F_p = \frac{E_s}{\pi \left({\Gamma_{FWHM}}/{2} \right)^2} . \tag{3.12}$$

Hence, the energy of one pulse collected by one microsphere E_s and the fluence in PJ F_p are presented in Table 3.15 for the maximum laser power applied ($P_{av,Nd:YAG}$ = 5.5 W and $P_{av,YLIA}$ = 16.4 W)

Table 3.15. The maximum energy collected by a microsphere and the maximum PJ fluence for each glass microsphere regarding the laser source at concerned f_{rate} and z. In gray: the fluence is smaller than LIDT of silicon

		Microsphere diameter D_s (µm)	**35**	**24**	**6**	**4**
1.	Nd:YAG laser at f_{rate} = 10 kHz and z = 14 mm	E_s,max (µJ)	7.2	3.4	0.2	0.09
		F_p,max (J/cm²)	760	433	42	13
2.	Nd:YAG laser at f_{rate} = 10 kHz and z = 22 mm	E_s (µJ)	3.2	1.5	0.09	0.04
		F_p,max (J/cm²)	337	192	19	6
3.	Nd:YAG laser at f_{rate} = 20 kHz and z = 22 mm	E_s,max (µJ)	1.6	0.8	0.05	0.02
		F_p,max (J/cm²)	169	96	9.4	3
4.	YLIA laser at f_{rate} = 20 kHz and z = 108 mm	E_s,max (µJ)	0.5	0.2	0.01	0.006
		F_p,max (J/cm²)	48	27	2.7	0.8

Thus the evaluated fluence can be first compared with the laser-induced damage-threshold (LIDT) of silicon for nanoseconds pulse Nd:YAG laser which is around 2 – 5 J/cm2 [27-29]. In only one case (highlighted in gray in Table 3.15), with the smallest spheres and the higher repetition rate, etchings of a few

nanometers depth have been achieved despite the fluence is estimated to be smaller than the usual LIDT.

The previous evaluation of the fluence in the PJ had been made on the basis of geometrical considerations. With this assumption, a microsphere achieves a fluence gain that is the ratio between the PJ spot surface and the sphere surface:

$$\text{Fluence gain} = \frac{F_p}{F_z} = \frac{E_s \Big/ \pi\left(\Gamma_{FWHM}/2\right)^2}{E_s \Big/ \pi\left(D_s/2\right)^2}$$

$$\frac{F_p}{F_z} = \left(\frac{D_s}{\Gamma_{FWHM}}\right)^2. \qquad (3.13)$$

It is important to emphasize that equation (3.13) is valid if whole incident beam on microsphere D_s is focused only on the area with a diameter of Γ_{FWHM}. A more realistic gain is intensity concentration factor α_p which is obtained from PJ simulations in Figure 3.21 where the beam is focused as $I_{max.p}$.

The comparison of this approximate fluence gain to the simulated intensity concentration factor is given in Table 3.16. The geometric approximation over-evaluates the fluence gain for the larger spheres and under-evaluate it for the smaller ones. This can also explain why etchings have been observed in all the cases.

Table 3.16. Approximate fluence gain and simulated intensity concentration ratio for each glass microsphere

Microsphere diameter D_s (µm)	**35**	**24**	**6**	**4**
Fluence gain (F_p/F_z)	1012	576	56	18
$\alpha_p = I_{max.p}/I_0$	773	511	96	48

B. Correspondence between etchings and electric field maps

This comparison mainly concerns the etching on glass in order to explain their shape: a ring with a crater in the center. The direct contact between glass microspheres and the glass plate is supposed to be the main reason. So that is reasonable to study the beam distribution not only around the PJ position but on the sample surface. Therefore, the electromagnetic simulations have been re-conducted to determine the electric field map on the sample surface.

In the previous simulations, the electric fields distribution was given in the OXZ plane (the incident plane) for a linearly polarized incident plane wave. Here the simulations have been conducted in the plane parallel to the OXY plane and tangent to the sphere, to yield the electric field distribution on the sample surface. Moreover to take into account the axis symmetry of the observed etchings, the simulations have been conducted for an incidence laser that is circularly polarized plane wave. The simulations are depicted in Figure 3.39. These distribution maps are made only in a half plane in order to save computer processing time taking into account the symmetry.

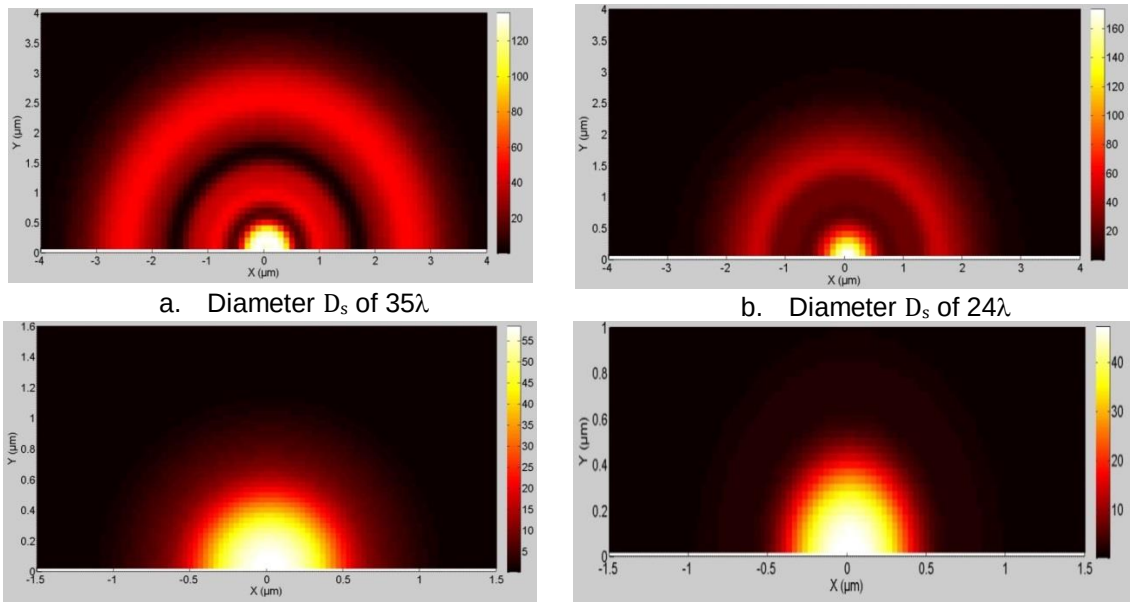

a. Diameter D_s of 35λ

b. Diameter D_s of 24λ

c. Diameter D_s of 6λ

d. Diameter D_s of 4λ

Figure 3. 39. Intensity ($I = |E|^2$) in the plane parallel to the OXY plane and tangent to the sphere for glass microspheres having diameter D_s of (a) 35λ, (b) 24λ, (c) 6λ and (d) 4λ

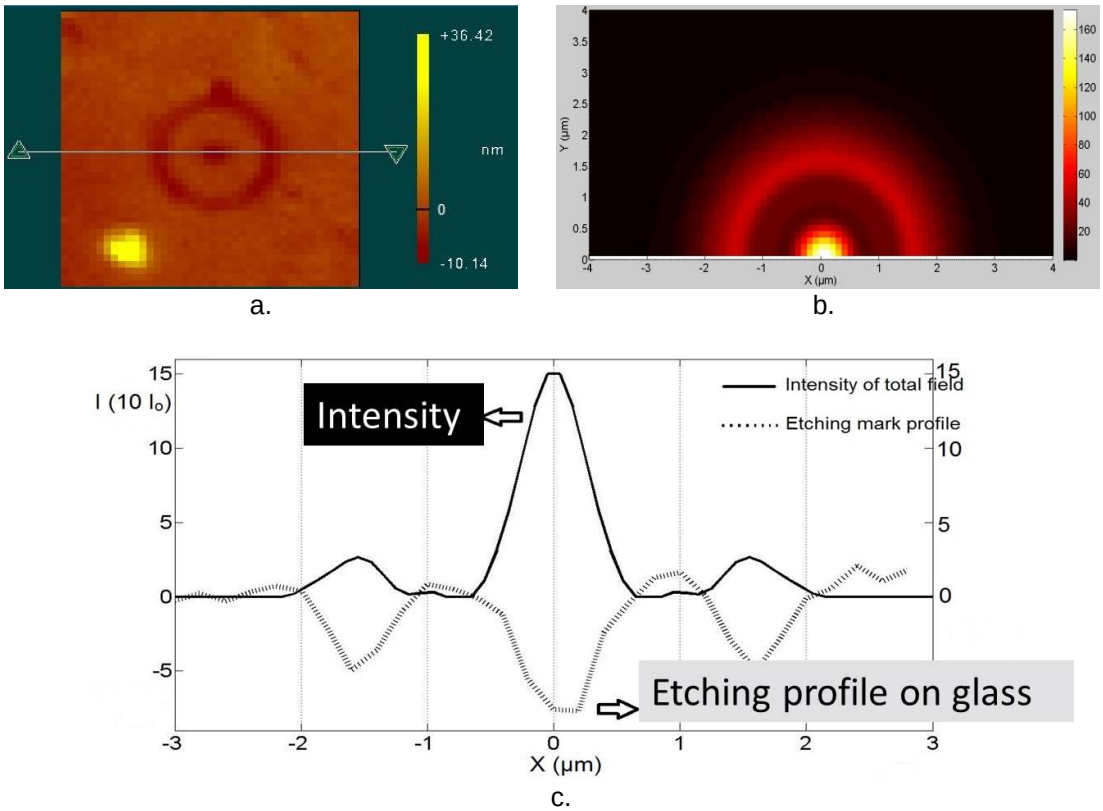

a.

b.

c.

Figure 3.40 The correlation between total intensity distribution map and PJ etching profile on glass in the case of glass microspheres D_s of 24 μm; (a) A PJ etching taken by Zygo®. (b) The intensity distribution map on the surface. (c) The correspondence between PJ etching profile and intensity profile.

From Figure 3.39 we can extract the beam parameters, i.e. the maximum

total field intensity I_{max}, the beam diameter or Γ_{FWHM} and the maximum beam fluence F_{sur} in the center. These parameters for each microspheres size are presented in Table 3.17. The maximum beam fluence F_{sur} is the fluence interacts with the material surface in our experiments (silicon wafers or glass plates).

Table 3.17. Beam parameters for each microsphere diameter

D_s (µm)	4	6	24	35
I_{max} (I_0)	47	58	173	136
α	47	58	173	136
Γ_{FWHM} (µm)	0.7	0.9	0.7	0.8
F_{sur} (J/cm²)	33	41	123	97

The intensity maps simulated for the two larger glass microspheres D_s of 35 µm and 24 µm are closely related to the PJ etching shape on glass. Figure 3.40 displays the intensity distribution on the surface and the resulting etched profile. The correlation is clear.

7. PJ etching using $BaTiO_3$ microspheres on silicon wafer and glass plate

The electromagnetic simulations of PJ coming out of barium-titanate microspheres in Section 2 show that in the case barium-titanate microsphere, the maximum intensity region is located inside microsphere. Therefore, it is not obvious that the intensity outside the microsphere remains high enough to etch silicon wafer or glass plate; an experimental validation was made to answer the question. The conditions were similar to that previously described for etching silicon wafer. The source is Nd:YAG laser with frequency rate at f_{rate} = 10 kHz, defocused range z = 22 mm and average laser power of 5.5 W (F_z = 0.7 J/cm²). We observed that some of the microspheres do not stay in position during laser irradiation, as it was observed for large size glass microspheres. As expected, in relation with the internal location of the radiation, some of the microspheres are damaged during the process (Figure 3.41).

When a glass is used as a substrate, the PJ etchings have profiles of the $BaTiO_3$ microspheres are similar to the ones obtained with glass microspheres. They also have a circular ring shape (Figure 3.42) in accordance to simulated intensity on the sample surface. Our experiments demonstrate that the ablation threshold is reached and material is ablated. However the etching mark takes a complex form that has little interest from a practical point of view.

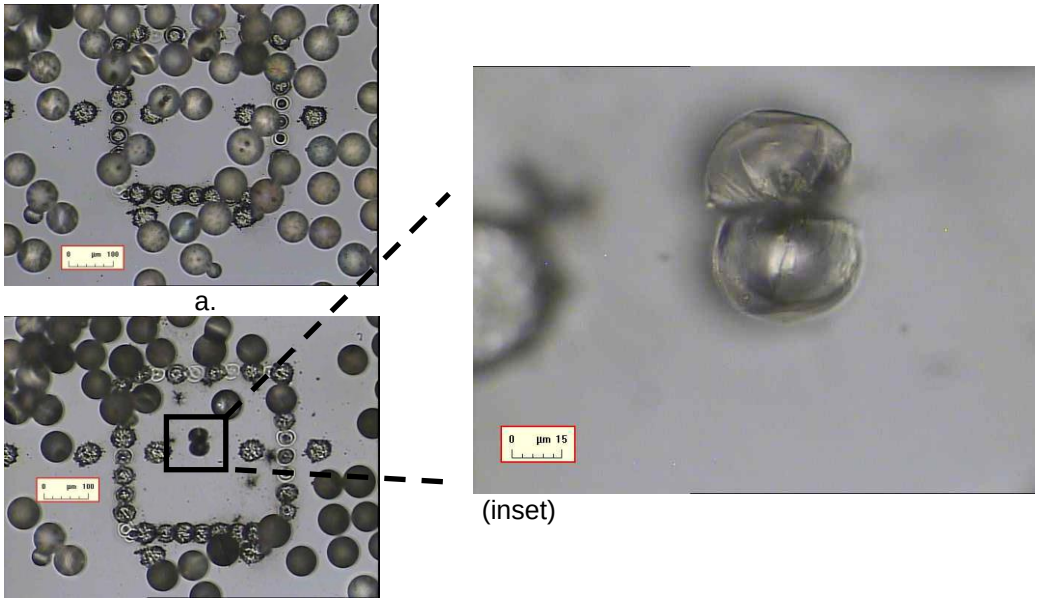

Figure 3.41. Barium-titanate microspheres (D_s = 69 µm) on silicon wafer (a) before and (b) after laser illuminations with (inset) a broken microsphere inside the cell (F_z = 0.7 J/cm²).

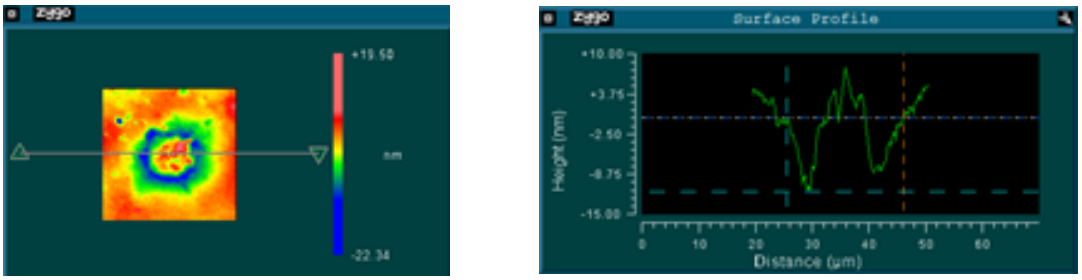

Figure 3.42. A PJ etching profile obtained on glass plate using a barium-titanate microsphere D_s= 87 µm (F_z = 0.7 J/cm²)

8. Synthesis and limitations

In this chapter the PJs potentials for etching have been demonstrated and investigated. Simulations have been performed to show that the laser beam is concentrated into a sub-wavelength spot. Then a series of experiments has been conducted to test whether these potentials were realistic. Two types of materials have been used: silicon wafer and glass. These experiments have been conducted considering different microspheres sizes and materials and two near-infrared lasers, a Nd:YAG laser and a YLIA fiber laser. As a result, it was clearly established that PJs has etching potentials. The study has allowed us also to formulate the following remarks that have to be taken account in PJs etching applications:

1. The microsphere properties (size and material) are very important. The PJ size and intensity concentration factor depend on this choice. The right selection is also important to avoid the beams internal concentration that may break the microsphere during the first laser illumination.
2. The selection of size or refractive index of microsphere depends on the

material to be etched and the desired etching shape. The increase of the size of microspheres can be a way to increase intensity concentration factor to reach the LIDT of the substrate. Refractive index has also an influence on intensity concentration factor and is critical in specifying the PJs highest concentration location. The PJs etching size on material depends critically on both parameters.

3. The etching size and shape obtained on silicon wafer or glass plate are well correlated with the PJ intensity distribution on the sample surface.
4. In case where the PJ waist is located at some distance from the microsphere surface, it is necessary to find a way to control this distance. In the absence of such control, the etch marks take form of unwanted rings.
5. A realistic use of PJ for etching requires the possible use of several laser pulses. The contact between the spheres and the substrate surface is a problem, because after the first pulse the sphere is polluted by the material debris which avoid next etching.

The first series of simulations and experiments described in this chapter has helped us to study a new configuration for PJ generation, where the microsphere is combined with the exit of an optical fiber. Some of the drawbacks mentioned above will be released by the new set-up described in the next chapter.

References

[1] K. W. Kolasinski and E. H. a. B. I. Lundqvist, "Chapter 16 Growth and Etching of Semiconductors," in *Dynamics*. vol. Volume 3, ed: North-Holland, 2008, pp. 787-870.

[2] Z. G. Chen, A. Taflove, and V. Backman, "Photonic nanojet enhancement of backscattering of light by nanoparticles: a potential novel visible-light ultramicroscopy technique," *Optics Express,* vol. 12, pp. 1214-1220, Apr 2004.

[3] A. Heifetz, S. C. Kong, A. V. Sahakian, A. Taflove, and V. Backman, "Photonic Nanojets," *Journal of Computational and Theoretical Nanoscience,* vol. 6, pp. 1979-1992, Sep 2009.

[4] Y. Liu, B. Wang, and Z. Ding, "Influence of incident light polarization on photonic nanojet," *Chinese Optics Letters,* vol. 9, pp. 072901-072901, 2011.

[5] W. Guo, Z. B. Wang, L. Li, D. J. Whitehead, B. S. Luk'yanchuk, and Z. Liu, "Near-field laser parallel nanofabrication of arbitrary-shaped patterns," *Applied Physics Letters,* vol. 90, p. 3, Jun 2007.

[6] Y. F. Lu, L. Zhang, W. D. Song, Y. W. Zheng, and B. S. Luk'yanchuk, "Laser writing of a subwavelength structure on silicon (100) surfaces with particle-enhanced optical irradiation," *Journal of Experimental and Theoretical Physics Letters,* vol. 72, pp. 457-459, 2000.

[7] E. McLeod and C. B. Arnold, "Subwavelength direct-write nanopatterning using optically trapped microspheres," *Nature Nanotechnology,* vol. 3, pp. 413-417, Jul 2008.

[8] D. McCloskey, Y. P. Rakovich, J. F. Donegan, and Ieee, "Controlling the Properties of Photonic Jets," in *12th International Conference on Transparent Optical Networks (ICTON)*, Munich, GERMANY, 2010.

[9] Y.-l. Ku, C.-f. Kuang, X. Hao, H.-f. Li, and X. Liu, "Parameter optimization for photonic nanojet of dielectric microsphere," *Optoelectronics Letters,* vol. 9, pp. 153-156, 2013.

[10] M. S. Kim, T. Scharf, S. Muhlig, C. Rockstuhl, and H. P. Herzig, "Engineering photonic nanojets," *Optics Express,* vol. 19, pp. 10206-10220, May 2011.

[11] D. J. Hwang, C. P. Grigoropoulos, and T. Y. Choi, "Efficiency of silicon micromachining by femtosecond laser pulses in ambient air," *Journal of Applied Physics,* vol. 99, Apr 2006.

[12] H. J. Münzer, M. Mosbacher, M. Bertsch, J. Zimmermann, P. Leiderer, and J. Boneberg, "Local field enhancement effects for nanostructuring of surfaces," *Journal of Microscopy,* vol. 202, pp. 129-135, 2001.

[13] M. Mosbacher, H. J. Munzer, J. Zimmermann, J. Solis, J. Boneberg, and P. Leiderer, "Optical field enhancement effects in laser-assisted particle removal," *Applied Physics a-Materials Science & Processing,* vol. 72, pp. 41-44, Jan 2001.

[14] S. Theppakuttai and S. Chen, "Nanoscale surface modification of glass using a 1064 nm pulsed laser," *Applied Physics Letters,* vol. 83, pp. 758-760, Jul 2003.

[15] P. Ferrand, J. Wenger, A. Devilez, M. Pianta, B. Stout, N. Bonod, *et al.*, "Direct imaging of photonic nanojets," *Optics Express,* vol. 16, pp. 6930-6940, May 2008.

[16] D. Grojo, L. Charmasson, A. Pereira, M. Sentis, and P. Delaporte, "Monitoring Photonic Nanojets from Microsphere Arrays by Femtosecond Laser Ablation of Thin Films," *Journal of Nanoscience and Nanotechnology,* vol. 11, pp. 9129-9135, Oct 2011.

[17] S. Lecler, Y. Takakura, and P. Meyrueis, "Properties of a three-dimensional photonic jet," *Optics Letters,* vol. 30, pp. 2641-2643, Oct 2005.

[18] C. H. Li, G. W. Kattawar, P. W. Zhai, and P. Yang, "Electric and magnetic energy density distributions inside and outside dielectric particles illuminated by a plane electromagnetic wave," *Optics Express,* vol. 13, pp. 4554-4559, Jun 13 2005.

[19] A. V. Itagi and W. A. Challener, "Optics of photonic nanojets," *Journal of the Optical Society of America a-Optics Image Science and Vision,* vol. 22, pp. 2847-2858, Dec 2005.

[20] C. B. Hitz, J. J. Ewing, and J. Hecht, *Introduction to Laser Technology*, 3 ed. New York: IEEE Press, 2001.

[21] Y. Wang and K. Hirofumi, "Influences of CCD nonlinear response on measurement of propagation factor M 2 of a laser beam," *Journal of Optics,* vol. 13, p. 015708, 2011.

[22] A. E. Siegman, "Defining, measuring, and optimizing laser beam quality," 1993, pp. 2-12.

[23] B. Eppich. (2008) Optical design of beam delivery and beam forming systems: ISO-defined beam parameters enable quick and easy layout of optical system in real-time. *Optik & Photonik*.

[24] I. S. 11146, "Lasers and laser-related equipment – Test methods for laser beam widths, divergence angles and beam propagation ratios," ed, 2005.

[25] C. Roundy. ((14 January 2015) 2006) Beam profilers provide crucial laser statistics. *Product Guide*. Available: http://optics.org/article/25153

[26] C. B. Roundy, "Maximizing laser performance using laser beam diagnostics," in *9th Meeting on Optical Engineering*, Tel-Aviv, Israel, 1995, pp. 528-539.

[27] X. Wang, Z. H. Shen, J. Lu, and X. W. Ni, "Laser-induced damage threshold of silicon in millisecond, nanosecond, and picosecond regimes," *Journal of Applied Physics,* vol. 108, p. 033103, Aug 2010.

[28] V. K. Arora and A. L. Dawar, "Laser-induced damage studies in silicon and silicon-based photodetectors," *Applied Optics,* vol. 35, pp. 7061-7065, 1996.

[29] J. R. Meyer, F. J. Bartoli, and M. R. Kruer, "Optical heating in semiconductors," *Physical Review B,* vol. 21, pp. 1559-1568, 1980.

[30] S. M. Company. (2013, 14 June 2013). *Optical transmission curve*. Available: http://www.sinclairmfg.com/datasheets/optical3.html

[31] Wikipedia. (27 January 2015). *Microscope slides*. Available:

http://en.wikipedia.org/wiki/Microscope_slide

[32] K. Yoshida, H. Yoshida, T. Kamimura, and N. Kuzuu, "Laser-Induced Bulk Damage of Various Types of Silica Glasses with Fundamental and Higher Harmonics of Nd:YAG Laser," *Japanese Journal of Applied Physics,* vol. 37, p. 1882, 1998.

[33] N. Kuzuu, K. Yoshida, H. Yoshida, T. Kamimura, and N. Kamisugi, "Laser-induced bulk damage in various types of vitreous silica at 1064, 532, 355, and 266 nm: evidence of different damage mechanisms between 266-nm and longer wavelengths," *Applied Optics,* vol. 38, pp. 2510-2515, 1999.

[34] N. Kuzuu, K. Yoshida, K. Ochi, Y. Tsuboi, T. Kamimura, H. Yoshida, *et al.*, "Laser-Induced Bulk Damage of Various Types of Silica Glasses at 532 and 355 nm," *Japanese Journal of Applied Physics,* vol. 43, p. 2547, 2004.

[35] D. S. Hobbs and B. D. MacLeod, "High laser damage threshold surface relief micro-structures for anti-reflection applications," 2007, pp. 67200L-67200L-10.

[36] D. S. Hobbs, "Laser damage threshold measurements of anti-reflection microstructures operating in the near UV and mid-infrared," 2010, pp. 78421Z-78421Z-13.

[37] J. Bonse, J. Solis, L. Urech, T. Lippert, and A. Wokaun, "Femtosecond and nanosecond laser damage thresholds of doped and undoped triazenepolymer thin films," *Photon-Assisted Synthesis and Processing of Functional Materials E-MRS-H Symposium,* vol. 253, pp. 7787-7791, 2007.

IV. PJ ETCHING BY OPTICAL FIBER

The experimental works with microspheres described in Chapter 3 have allowed a better understanding of PJ interaction with matter. We have shown that PJ has an interest for direct laser etching of material. However, it has been outlined that a controlled space between sample and microsphere is necessary for practical purpose. There are several advantages having this space, e.g.: always placing the maximum intensity of PJ on the surface of the sample and avoiding the material debris which can stick to the microsphere surface and stop the etching process. To have access to this space, we have considered the use an optical fiber instead of microsphere to create the PJ. There are several advantages in doing so. An optical fiber can easily be positioned with a precise way at an expected distance from the material. The fiber can also easily be translated above the material to etch complex design. Therefore we can apply more pulses and we can use the optical fiber several times without destroying the optical fiber.

And so, this chapter will discuss the waveguide driven PJ in near IR region for PJ etching applications. After a brief review of waveguide driven PJ studies, we describe the Comsol® multi-physics two dimensional simulations of the tip that is required; next we present the practical designing of our spheroid tipped optical fiber. Finally our etching experimental setup and results are exposed.

1. Waveguide driven PJ

The first study putting in relation waveguide and PJ phenomena considered chains of dielectric microspheres [1] act like a waveguide. And the first reported experiment applying these chains of microspheres was done by Kapitonov and Astratov [2]. They coined that nanojet-induced modes (NIMs) was the phenomena responsible for the light propagation in these chains. The chains were formed by depositing microspheres on a glass substrate using self-assembly technique by micro-flows of a water suspension of spheres. Here, each microsphere produces PJ with elongated shape and subwavelength lateral size. In calculation, this chain of microspheres demonstrated small propagation losses with an attenuation of only 0.08 dB per sphere [3]. Therefore the experiment continued by inserting the chain in a capillary tube so that the surface of the end sphere was in contact with the considered sample: a tissue-like medium [4]. It was to be in conditions similar to ultra-precise laser surgery [5]. The laser source used in this experiment was in the visual wavelength range. Calculations using ZEMAX EE ray tracing then have been reported by Darafsheh et al. [6] in 2011 for a 2.94 µm wavelengths laser beam source – normally generated by a Er:YAG laser – propagating inside a 150 µm diameter of multimodal hollow waveguide with a sphere or chain of spheres at the other side to generate the PJ.

In a different way, Allen et al. used a single 53 µm barium titanate glass (n = 1.87) at the outlet of a photonic crystal optical fiber in the experiment reported in [7]. This sphere was fixed directly into the air core of hollow-core microstructure optical fiber (HC-MOF) or hollow-core photonic crystal fibers (HC-PCF) [8]. Due to the tight match between the diameter of sphere and the size of the air core, i.e. 53 µm, the sphere was slightly extended from the edge of the fiber. The PJ

measurement showed a peak with full-width at half-maximum around 4λ which was not in a good agreement with the 2D numerical modeling finite element method (FEM). Namely the FEM simulations performed by COMSOL® for a 50 µm dielectric cylinder (n = 1.87) illuminated by a 2.94 µm wavelength plane wave, show a compact beam with diffraction-limited dimension in the order of λ/2. They assumed this difference occurred due to an incomplete collection of light by the objective lens used to image the focused beam, and due to the transmission losses by the lens and microsphere which consist of Fresnel reflection loses, material absorption at λ = 2.94 µm and scattering losses at the edge of optical fiber. The experimental demonstration was for fluorescence imaging and direct laser writing on a thin absorbing layer on a glass plate [8].

There is one more recent study almost similar to Darafsheh et al. and Ghenusche et al, but using etching-core optical fiber [9]. Here, a particle was planted in a micro-well on the fiber distal face corresponding to the particle shape. This micro-well can be made by wet-chemical etching. Then, by neglecting the divergence in the micro-void formed between fiber and spherical particle, the calculation using generalized Lorenz-Mie theory was conducted by varying the spheroid's ellipticity as well as the refractive index. And it turned out that the ellipticity increase tends to shift the PJ's maximum intensity close to the spheroid. This shift has also reported by Li et al. nine years earlier [10].

It can be said that we are the first research group study wave-guides driven PJ without sphere or chain of spheres [11-13]. First in a project, different to this PhD, a waveguide in the hyper-frequency domain with an elliptical or cylindrical tip was used, so there are no void between the core and the spheroidal tip. Many techniques can be used to realize this kind of tips on single or multi-mode waveguide like describing in [14-16].The tip can be designed to generate a single PJ [11], as well as dual PJs. In this work, the electromagnetic simulation has been done using a two dimensional integral method and has been experimentally validated in the microwave region [12, 13].

2. Electromagnetic simulations of PJ generated by a dielectric waveguide with a spheroid tip

As mentioned, the first reported electromagnetic simulation of PJ generated by a spherical tipped waveguide using finite element method was made by Halaq et.al. in our team in collaboration with the LT2C (now Laboratory Hubert Curien) in Saint-Etienne [11]. The source was a 30 GHz radio-frequency wave (wavelength of λ_o = 1 cm) propagates inside a $3\lambda_o$ width planar waveguide in Teflon (relative dielectric permittivity ε_r = 2) with perfectly electric conductive boundary condition (copper). This waveguide is a multimode waveguide. The tip shape was rather elliptical with the semi-major axis of $4\lambda_o$. The objective was to generate a high concentrated PJ out of the tip in the free space.

In this thesis, for PJ etching being relevant for industrial application, we consider near-infrared laser (λ ≈ 1 µm rather than 1 cm) and an optical fiber rather than Teflon waveguide with perfectly conductive boundaries. Therefore, specific simulations are needed. Ideally, the simulations may be achieved in

three dimensions. An optical fiber is axis symmetric but the vectorial nature of the incident wave breaks this symmetry. However to save time and computer resources, the simulations have been preceded only in two dimensions. The similar behavior observed for cylinder (2D) and sphere (3D) can justify this first approach. Therefore all the simulations of PJ by a spheroid tipped “optical fiber” in this section are conducted for two dimensions waveguide, so that rather than spheroid tipped optical fiber, it is elliptical tipped dielectric waveguide.

A. Basics of optical fiber for simulation

A waveguide is a system that confines propagating wave. So, an optical fiber is a cylindrical dielectric waveguide that confines propagating light. The light confining and propagation mechanism inside an optical fiber is the total internal reflection. This total internal reflection occurs when the incident light from medium one is totally reflected at the interface with medium two (Figure 4.43).

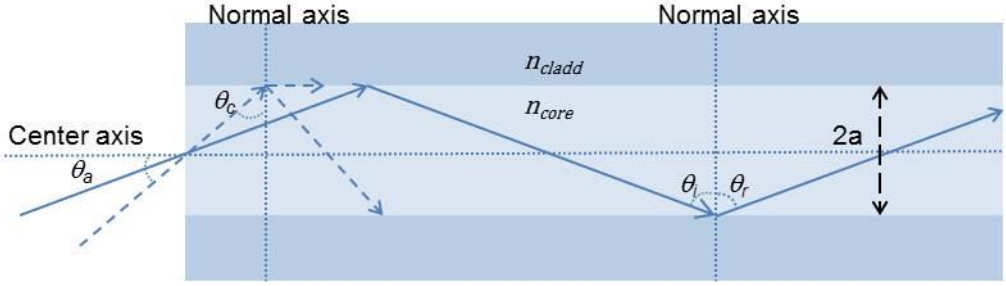

Figure 4.43. Total internal reflection inside an optical fiber with the core diameter of 2a = D

This mechanism occurs when the refractive index of medium one (n_{core}) is higher than the refractive index of medium two (n_{clad}) and when the incident angle (θ_i) exceeds the critical angle (θ_c) that is the incident angle generating the refractive light parallel to the medium interface.

The critical angle is fixed by the refractive ratio of cladding and core by:

$$\sin\theta_c = \frac{n_{clad}}{n_{core}}\,, \tag{4.1}$$

Whereas the maximum allowed angle (θ_a) of incident light inserts the optical fiber is linked to the numerical aperture of optical fiber:

$$\sin\theta_a = \mathrm{NA}\,, \tag{4.2}$$

with

$$\mathrm{NA} = \sqrt{\mathrm{n_{core}}^2 - \mathrm{n_{clad}}^2}. \tag{4.3}$$

The number of modes propagates inside the core depends on the ratio between the optical fiber core radius over the wavelength and on the numerical aperture of the fiber. A single-mode fiber (SMF) is an optical fiber which supports only a single propagation mode that is the fundamental mode. In SMF, the normalized frequency V, given formula (4.4), is less than the cut-off frequency of the second mode: V < Vc, Vc ≈ 2.405 [17].

$$\mathrm{V} = \mathrm{k_0 a\ NA} \tag{4.4}$$

for $k_0 = \frac{2\pi}{\lambda_o}$.

Different to SMF, a multi-mode fiber (MMF) supports multiple propagating modes for a given optical frequency and polarization. Contrarily to SMF, MMFs have normalized frequency beyond the cut-off frequency of the second mode. For large V, the number of modes M is

$$M \approx \frac{V^2}{2}. \tag{4.5}$$

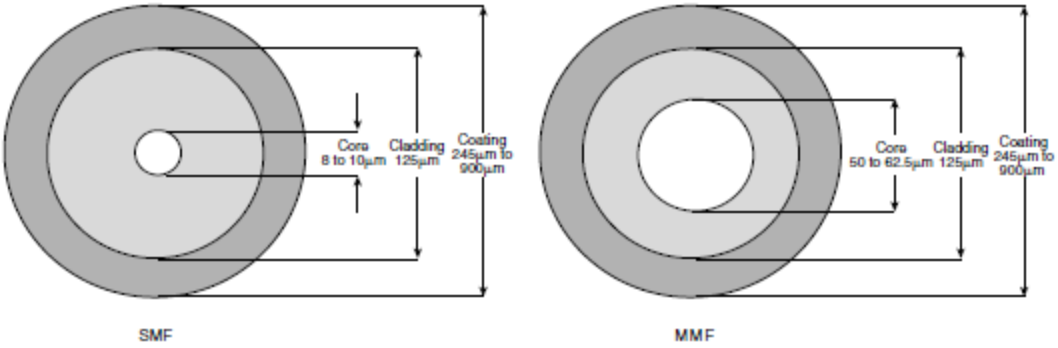

Figure 4.44. The cross-sectional comparison of optical fibers that support single-mode (SMF) and multi-modes (MMF) propagation in telecommunication, taken from [18]

The standard telecommunication SMF core diameters measure between 8 to 10 μm, whereas the standard MMF core diameter are between 50 to 62.5 μm [18] for λ_0 = 1300 nm or 1500 nm. The core size of SMF is very small compared to the cladding, but not for MMF. In Figure 4.44, two optical fibers with the same cladding size of 125 μm but different core size of 8 to 10 μm and of 50 to 62.5 μm are depicted.

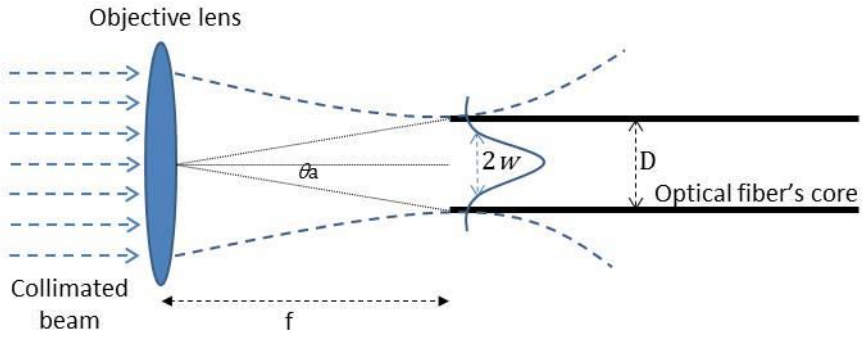

Figure 4.45. Modal field radius propagating inside an optical fiber

The beam propagating inside an SMF (Figure 4.45), in low guiding approximation ($n_{core}/n_{clad} \approx 1$), is often approximated by a Gaussian distribution [17] in the form of

$$E_x(x, y, z, \boldsymbol{\omega}) = E_0(\boldsymbol{\omega}) \exp\left[-\frac{x^2 + y^2}{w^2}\right] \exp[i\beta(\boldsymbol{\omega})z]\,. \tag{4.6}$$

where w is the waist of the Gaussian wave and β is the propagation constant.

In practical use, the beam spot difference to the core radius can be

calculated using the approximation expression [19]:

$$\frac{w}{\mathrm{a}} \approx 0.65 + 1.619\mathrm{V}^{-\frac{3}{2}} + 2.879\mathrm{V}^{-6} \ . \tag{4.7}$$

B. Mathematical description of the shape of optical fiber tip for simulation

First, the ellipticity of the considered waveguide tip can be described with the minor half-axis (a) and the major half-axis (b), as illustrated in Figure 4.46.

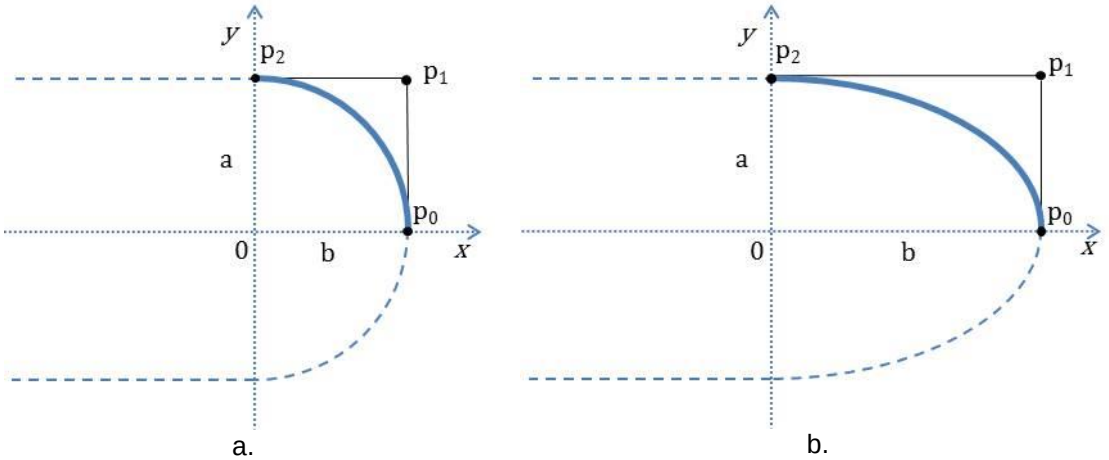

Figure 4.46. Two symmetric rational quadratic Bézier functions are able to describe the optical fiber tip; (a) circular tip and (b) elliptical tip.

An issue was to be able to describe more generalized shape that only the elliptical one. The mathematical function we have used to define the tip shapes is the rational quadratic Bézier function. The general form of rational quadratic Bézier curve [20] is:

$$\mathbf{p}(t) = \frac{(1-t)^2\boldsymbol{p}_0 + 2(1-t)tw\boldsymbol{p}_1 + t^2\boldsymbol{p}_2}{(1-t)^2 + 2(1-t)tw + t^2} \ , \tag{4.8}$$

where w is the Bézier's weight curvature, $\boldsymbol{p}_0$, $\boldsymbol{p}_1$, $\boldsymbol{p}_2$ are coordinates of three control points and t is a parameter between 0 and 1. Here $\boldsymbol{p}_0 = (\mathrm{b};0), \boldsymbol{p}_1 = (\mathrm{b};\mathrm{a}), \boldsymbol{p}_2 = (0;\mathrm{a})$. This function is able to create a curve close to a quarter of a circle or ellipse like bold line in Figure 4.46 when the Bézier weight curvature w = 0.7. And so the shape of our optical fiber tip can be described by two symmetrical rational quadratic Bézier functions. Bézier curve with w < 0.7 correspond to sharper tip, where as w = 1 to rectangular one.

C. Physics of PJ coming out of spheroid-tipped optical fiber

The simulations reported here are conducted to help us to choose the optical fiber and its elliptical tip shape. However, as explained before, the simulations are conducted in two dimensions.

The physical cases considered in the simulations are:

- The incident beam is a Gaussian beam (fundamental mode) with a wavelength of λ_0 = 1 µm and maximum electrical field of E_{max} = 1 V/m (waist is computed using equation (4.7).

- The planar waveguides are in free space (n_o = 1):
  - A waveguide inspired of an optical fiber in catalogue with cladding diameter of $125\lambda_0$ and core diameters $10\lambda_0$ (SMF28); the refractive index of n_{core} = 1.46 and n_{cladd} = 1.45 (NA = 0.17).
  - A waveguide inspired of an optical fiber in catalogue with cladding diameter of $125\lambda_0$ and core diameters $50\lambda_0$; the refractive index of n_{core} = 1.46 and n_{cladd} = 1.45 (NA = 0.17).
  - A waveguide inspired of an optical fiber in catalogue with cladding diameter of $240\lambda_0$ and a core diameter of $200\lambda_0$; the refractive index of n_{core} = 1.457 and n_{cladd} = 1.44 (NA = 0.22).
  - A waveguide inspired of an optical fiber in catalogue with cladding diameter of $240\lambda_0$ and a core diameter of $200\lambda_0$; the refractive index of n_{core} = 1.457 and n_{cladd} = 1.44 (NA = 0.22).
- The tip:
  - Two ratio between major and minor axis of the tip: b/a = 1 (circular tip), b/a = 2 (elliptical example).
  - The Bézier's curvature weight is w = 0.7.

a. 2D-simulation of PJ coming out of spheroid-tipped "SMF-28" waveguide

The SMF-28 is a standard single-mode fiber for optical communications with a diameter of 10 µm and operating in a wavelength region of 1300 or 1500 nm. The waist of fundamental optical fiber mode for λ_0 = 1 µm can be estimated using equation (4.7): w = 3.90 µm.

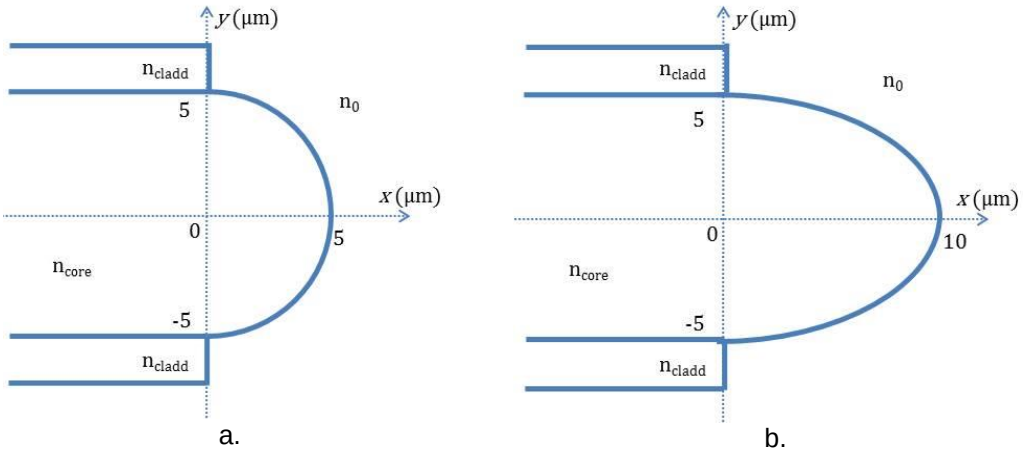

Figure 4.47. Geometrical design of SMF-28, 10 µm optical fiber core diameter in 2D: (a) circular tip and (b) elliptical tip ($b = 2a$)

In Comsol® the half waveguide geometry (taking into account the symmetry) with respectively the circular and the elliptical tips are created (Figure 4.47) with perfectly matched layer (PML) boundary conditions around the free space and scattering boundary in the cladding. The excitation of the fundamental mode is defined as a source port or input port at the entrance of waveguides. The norms of electrical fields concentrated at the vicinity of the tips are presented in Figure 4.48 for the circular tip and in Figure 4.49 for the elliptical tip.

Figure 4.48 shows some high electric field nodes inside the tip, but the

highest concentration electric fields in a PJ at ~5.6 µm from the tip surface. The field is concentrated ~4.3 times compared to the maximum of the incident beam (16 times for the intensity. It is slightly weaker than the one obtained using elliptical tip; that is ~5.4 times, in a PJ located closer (at 2.6 µm) to the tip (Figure 4.49). In both cases, $\Gamma_{FWHM} = 0.625\lambda_o$. A closer look inside the elliptical tip shows electric field peaks higher than in the PJ. Referring to this simulation, to those of barium-titanate microspheres in chapter 2 and to their corresponding experimental observations, the high concentrate-field nodes inside the tip may break the tip up. Therefore, for the SMF28 fiber, the circular tip seems better.

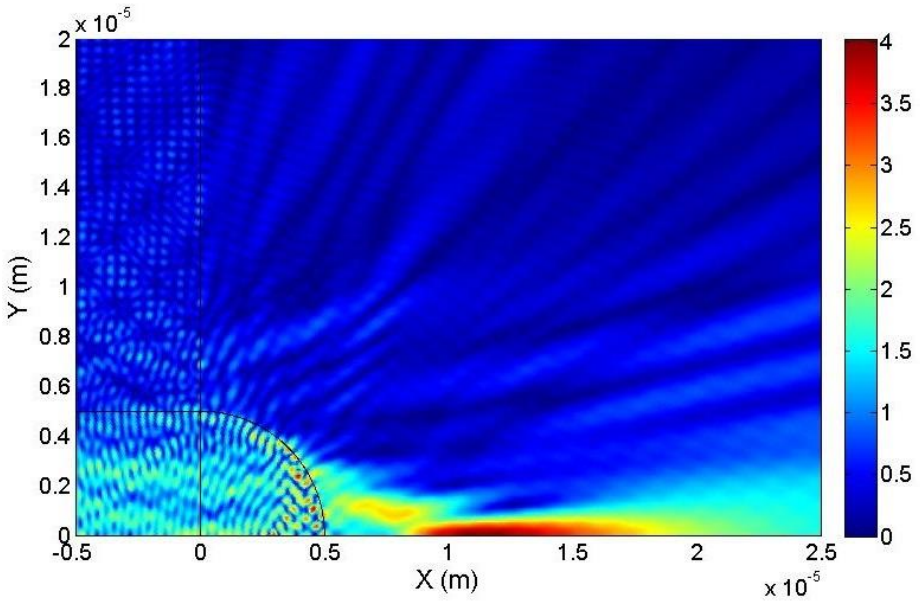

Figure 4.48. Total electric field of a half of planar waveguide (D_s = 10 µm) with a circular tip (b = a, NA = 0.17)

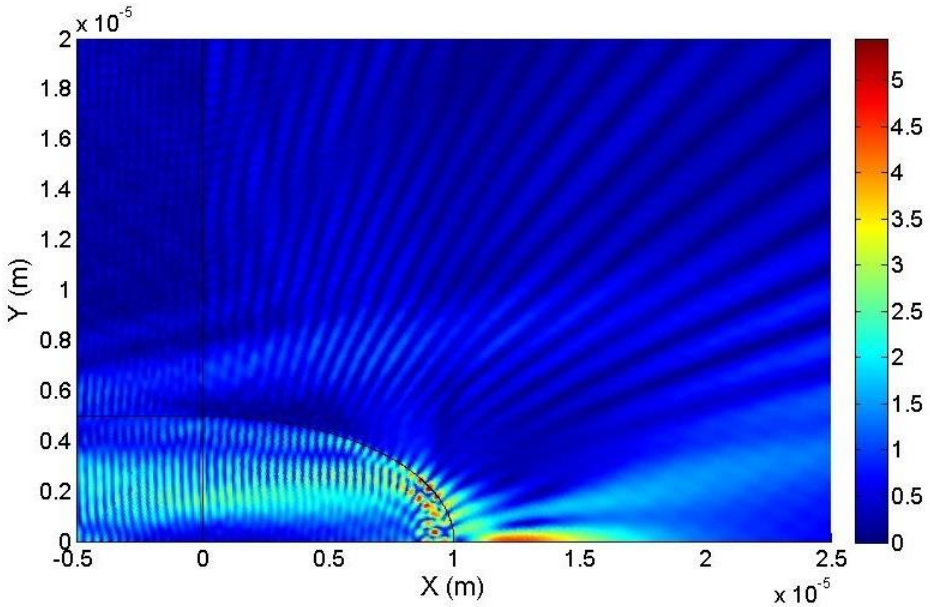

Figure 4.49. Total electric field of a half of planar waveguide (D_s = 10 µm) with a circular end (ellipticity = 0.5 or b = 2a, NA = 0.17)

Figure 4.50 is a complementary simulation of a sharper tip (a=b, w = 0.2). The PJ is also closer to the tip. High concentration nodes are observed inside the tip.

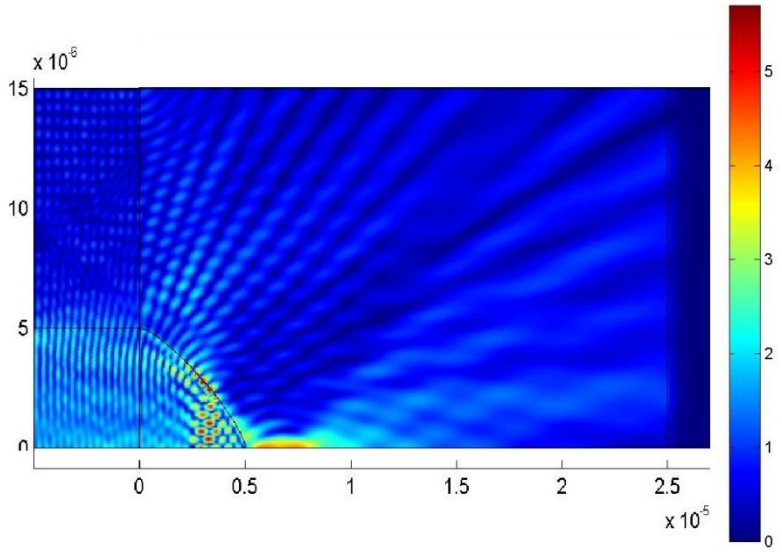

Figure 4.50. Total electric field of a half planar waveguide (D_s = 10 µm) with a sharp-curvature tip (Bézier weight = 0.2, NA = 0.17)

b. 2D-simulation of PJ coming out of spheroid-tipped of 50 µm waveguide

A silica multimode fiber (MMF) with a diameter of 50 µm is also a standard optical fiber. Using equation (4.7) with the considered parameters, the waist of fundamental optical fiber mode is w = 16.5 µm.

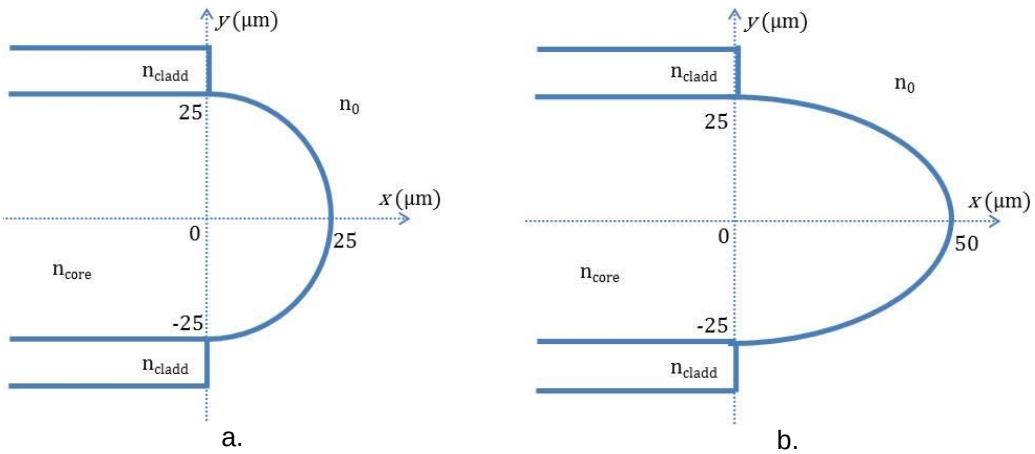

Figure 4.51. Geometrical design of MMF 50 µm optical fiber in 2-D: (a) circular tip and (b) elliptical tip.

Figure 4.51 are the geometries of the waveguides with respectively the circular and the elliptical tips in free space with the same boundary condition as for the SMF28 simulations. The simulations of the total electrical field norm revealed the concentrated light at the vicinity of the tips which are presented in Figure 4.52 for the circular tip and in Figure 4.53 for the elliptical tip.

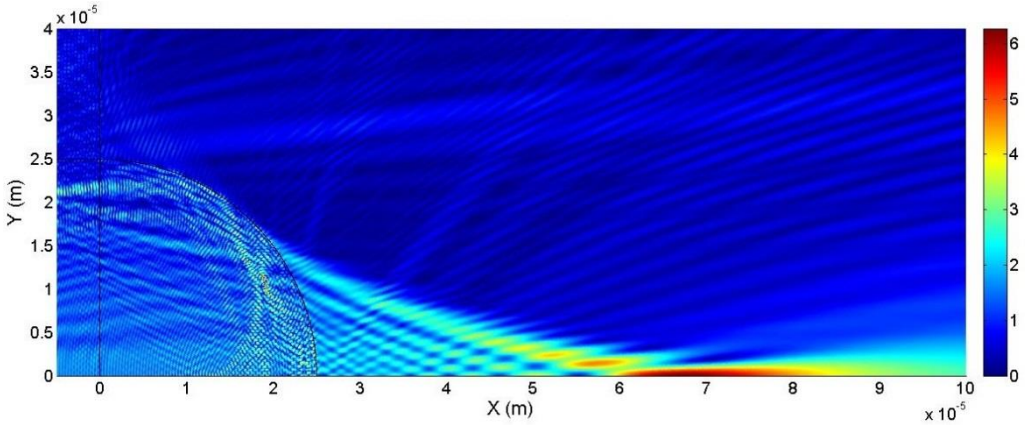

Figure 4.52. Total electric field of a half planar waveguide (D_s = 50 µm) with a circular tip (b = a, NA = 0.17)

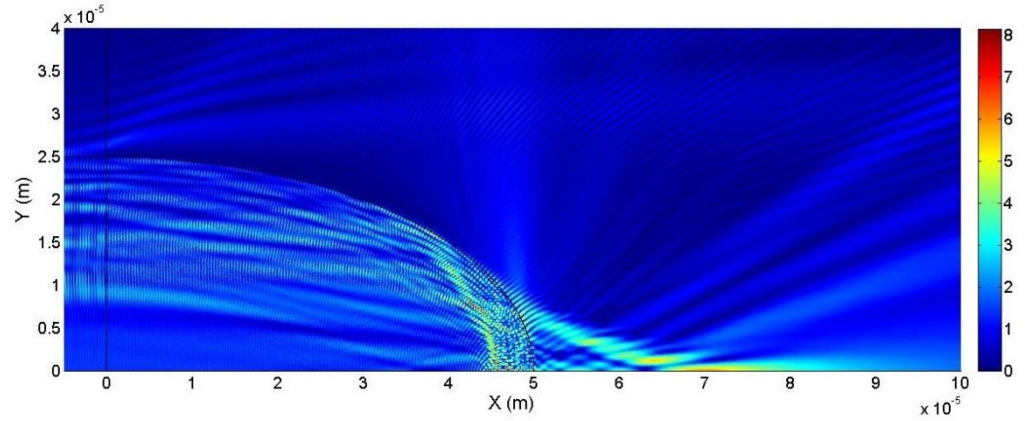

Figure 4.53. Total electric field of a half planar waveguide (D_s = 50 µm) with an elliptical tip (b = 2a, NA = 0.17)

Compared to the SMF-28 simulations, the MMF 50 µm concentrates more electrical field, respectively 6.2 times with the circular tip and 8 times with the elongated one. It is not only because the optical fiber can propagate more modes, but also because, as for spheres, the fiber can collect more light since it has larger diameter. The light is focused in a PJ at 45 µm and 20 µm respectively from the circular tip surface and from the elongated one. As for the SMF28, the PJ is closer to the elongated tip. In both case, Γ_{FWHM} = 1,25λ_0. There are also fewer high intensity nodes inside the tip.

The light enhancements by a glass sphere in chapter 2 seem to be greater than generated by a spherical tipped of 50µm MMF, even the PJ width obtained using glass microspheres is larger than of multi-mode waveguide. It is due to the incident waves in the two simulations are different; plane wave and Gaussian wave respectively in microspheres and optical fibers simulations. The second reason is that microspheres simulations were in 3D and tipped fiber simulations are in 2D. If the intensity concentration factor is α in 2D, α^2 can be expected in 3D. Larger waveguides can still be considered. And so, next simulations consider a waveguide with a 200 µm core. This diameter is the smallest available for high power multimode optical fiber with double cladding that we have found.

c. 2D-simulation of PJ coming out of spheroid-tipped of TEQS™ coated 200 µm multi-mode fiber

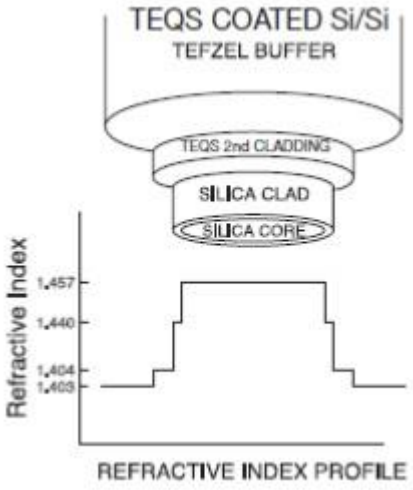

Figure 4.54. Step refractive indexes of a TEQS™ coated multimode fiber

A MMF with a diameter of 200 µm is not a standard optical fiber for optical communications. This 200 µm multimode fiber with TEQS™ coated (Thorlabs) has steps refractive indexes presented in Figure 4.54 and a numerical aperture of 0.22. The silica cladding is made from low-index fluorine-doped silica which provides superior near-infrared transmission. Whereas the TEQS™ secondary cladding provides a dual-waveguide designing, resulting in improved bend performance also allowing high-power handling capability. It can stand up to 0.2 kW for a continuous wave or 1.0 MW for a 10 ns Nd:YAG laser with a wavelength of 1064 nm and spot size of 80% of the core diameter.

The half-geometry was designed in Comsol® only with a single-cladding 2D planar-waveguides with circular and elliptical tips as shown in Figure 4.55.

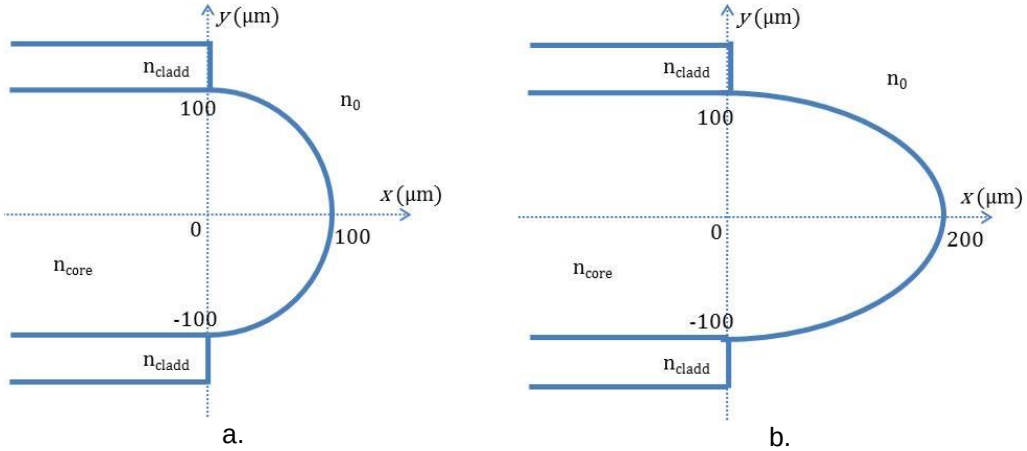

Figure 4.55. Geometrical design of MMF 200 µm core optical fiber in 2D: (a) circular tip and (b) elliptical tip.

Using equation (4.7), the waist of fundamental optical fiber mode is $w = 65.1$ µm. The electric fields norm simulations reveal the concentrated light at the vicinity of the tips in Figure 4.56 for the circular tip and in Figure 4.57 for the elliptical tip. The electric field concentration yielded by circular tip is ~10 times

(in 2D) in a PJ at 194 µm outside the tip and with $\Gamma_{FWHM} = 2.2\lambda_0$, whereas the concentration obtained using the elliptical tip is slightly over 23 times at 94 µm from the tip, with $\Gamma_{FWHM} = 1.2\lambda_0$. Some high electric field peaks are also presence inside the waveguide. The concentrated beam is closer to the elongated tip.

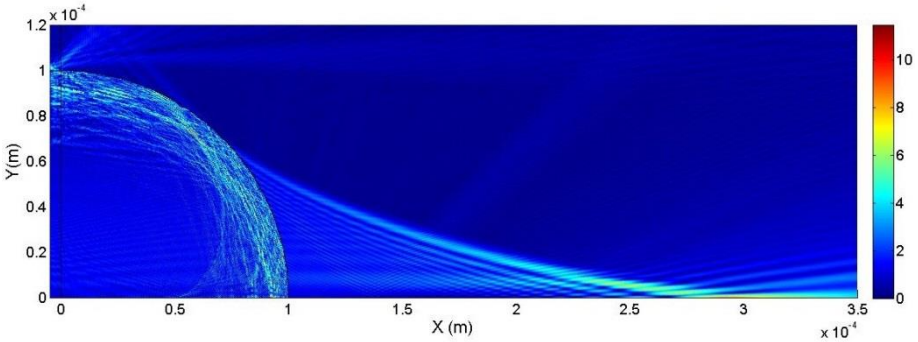

Figure 4.56. Total electric field of a half planar waveguide (D_s = 200 µm) with a circular tip (b = a, NA = 0.22)

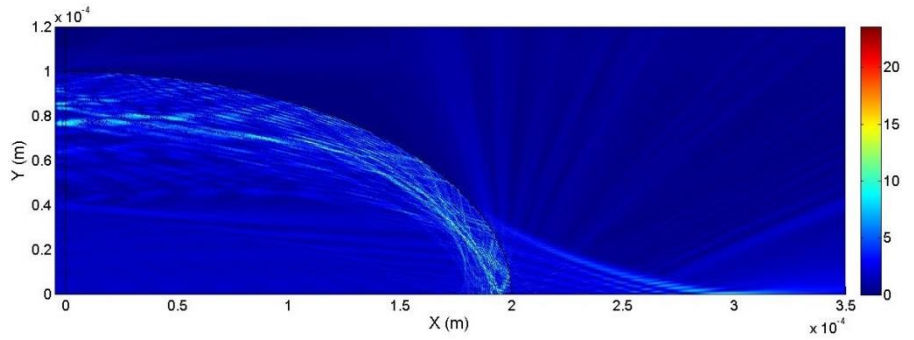

Figure 4.57. Total electric field of a half planar waveguide (D_s = 200 µm) with an elliptical tip (b = 2a, NA = 0.22)

d. 2D-simulation of PJ coming out of spheroid-tipped 100 µm multi-mode fiber

The last considered fiber is a 100 µm core silica optical fiber (140 µm cladding) with a numerical aperture of 0.22 and a spheroid tip (a=b). The simulation is given in Figure 4.58. This part has been done with the contribution of Julien Zelgowski. The PJ is located at 89 µm of the tip. The electric field concentrated 5 times (in 2D), that is 25 times in intensity (~25^2=625 in 3D) with a ΓFWHM = 1.8λo (1.2λo if the Bézier's weight is w = 0.45)

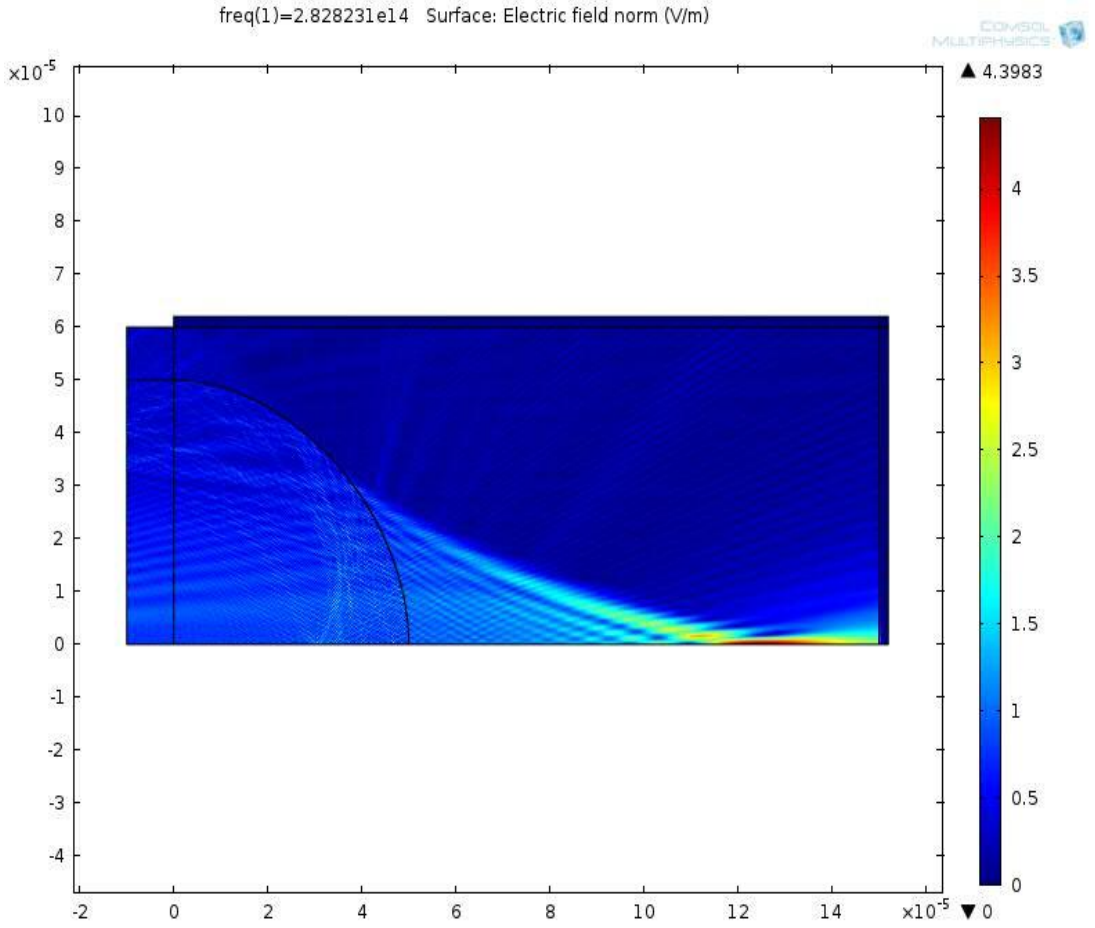

Figure 4.58. Total electric field of a half planar waveguide (D_s = 100 µm) with a spheroid tip (b = a, NA = 0.22)

D. Justification of the chosen tip shape

PJ parameters from the simulations of the considered spheroid tipped waveguides are summarized in Table 4.18. We must now decide which optical fiber and tip shape must be chosen for the experimental work.

Accordingly to Table 4.18, it seems that larger core diameters yield PJ with higher concentration factors, further positions and larger FWHM than small ones. Concerning the tip shape, the elongated shape (b=2a) yields PJs closer with higher concentrations than circular ones, and smaller FWHM. Finally, we have decided to prepare a spheroid tips made out of TEQS™ coated multi-mode fiber with a diameter of 200 µm and a second one with classical silica cladding and a 100 µm core. This optical fiber is more adapted to transmit high-power near-infrared light than a SMF-28 or a MMF-50 µm.

Namely, as it will be confirmed in section 4.3.B, because its larger core diameter, it is easier to inject the laser beam into the optical fiber and the double-cladding reduces the risk of destruction of the optical fiber due to bad injection. Moreover, the risk to the etched material to affect the tip integrity decreases by increasing the PJ position from it. This last point also justifies the circular shape tip rather than the elongated. It assures a further PJ position (194

µm for the 200 µm core optical fiber).

Another reason justifies our choice of a circular tip shape/curvature. The circular shape is assumed to be easier to achieve.

Table 4.18. PJ parameters coming out of spheroid tipped waveguide

Type/size of waveguide	Shape of the tip	Electrical field enhancement	Focal point from the tip (µm)	FWHM (µm)
SMF-28, 10 µm	Circular	4.4	5.9	0.625
	Elliptical	6.5	2.3	0.625
MMF, 50 µm	Circular	6.2	42.5	1.25
	Elliptical	8.1	20.5	1.25
MMF, 100 µm	Circular	5	89	1.8
MMF, TEQS coated, 200 µm	Circular	11.2	194	2.4
	Elliptical	22.5	94	1.2

Figure 4.59 shows the microscopic view of the spheroid tipped TEQS^{TM} coated multi-mode 200 µm fiber and the spheroid 100 µm silica fiber. The tips have been custom-made by Lovalite for our experiments. The 100 µm is not really spheroidal. There are many methods to realize a micro tips at the end of optical fiber: chemical etching, photo-lithography, tapering (heating and pulling), etc. The method is usually chosen depending on the desired tip shape. These methods are described in [21-26]. They have generally been developed to achieve optical fiber probes for the SNOM microscopy. The self-photolithography method is illustrated in Figure 4.60a, whereas the tapering method is in Figure 4.60b. Our tips have been achieved using this last method.

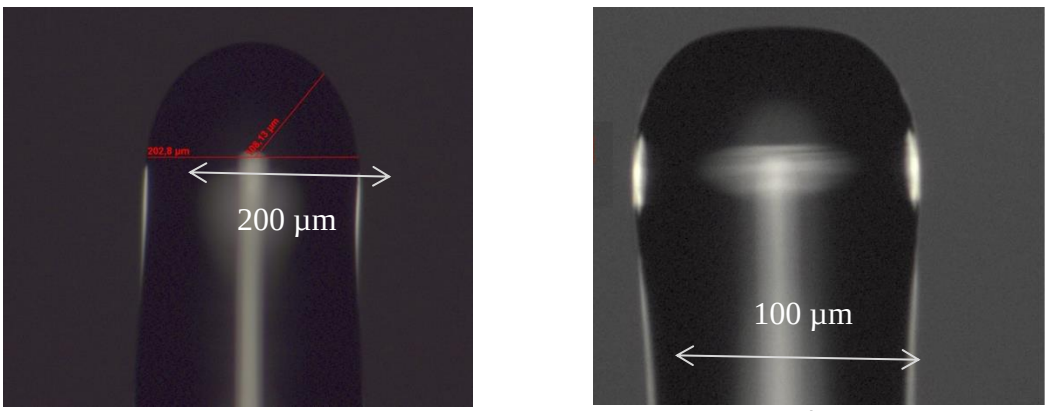

a. b.

Figure 4.59. The spheroid tipped of (a) our TEQS^{TM} coated multi-mode 200 µm fiber and (b) 100 µm silica fiber fabricated by Lovalite for our experiments

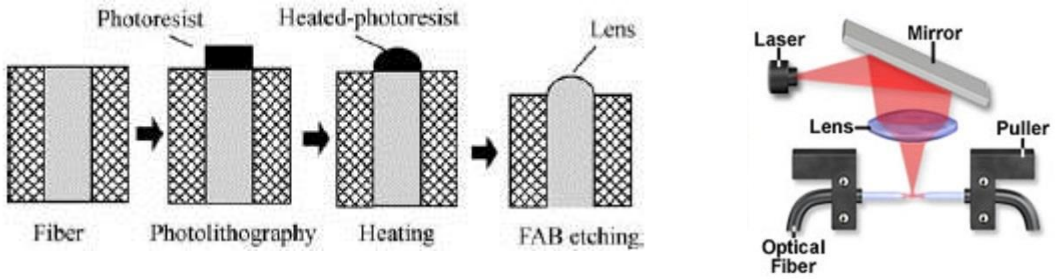

Figure 4.60. Illustrations of two tip fabrications technique: (a) self-photolithography [21] and (b) tapering by laser-based micropipette puller [26]

3. Experiment setup

The main objective of these experiments was to verify if it was really possible to obtain a PJ out of an optical fiber, with enough power to etch silicon without breaking-up the tip or blurring/polluting the tip's surface. For these experiments the scheme is illustrated in Figure 4.61.

As source, only the 160 ns YLIA laser has been used because its power delivered via a flexible output fiber and collimating optics was easier to inject in the optical fiber.

List of used instruments:

- Laser source: YLIA M20 Quantel fiber laser
  - λ = 1060 nm, P_{max} = 20 W, σ = 160 ns, f_{rate} = 20 – 100 kHz;
  - D_{beam} = 9.0 mm, M^2 = 2.6
- Injection : three optical components have been tested
  - Lens (∅=½ inch, f = 50 mm, spot-point size 20 µm)
  - Thorlabs AC127-019-C achromatic lens (∅ = 12.7 mm, f = 19 mm)
  - Thorlabs LMH-10X-1064 focusing lens (∅=15 mm, EFL=20 mm, NA= 0.25)
- Fiber optics:
  - SMF28 ∅ = 10 µm, NA = 0.14
  - MMF ∅ = 50 µm, NA = 0.2
  - MMF ∅ = 100 µm, NA = 0.22 with spheroid tip (Figure 4.59b)
  - MMF TEQS^{TM} coated - high power optical fibers (NA=0.22, $\varnothing_{core}$ = 200 $\pm$ 8 µm); with and without spheroid tip (Figure 4.59a)
- Calorimeter: OPHIR VEGA laser power meter with thermal sensor
  - OPHIR 30A-N-18 (maximum average power density 5 kW/cm²)
  - OPHIR 12A-P (maximum average power density 0.05 kW/cm²)
- A three-axis micrometer translation stage (error $\pm$ 5 µm, maximum translation: 2.55 cm) to move the fiber tip
- Studied sample materials:
  - Main: silicon-wafer.
  - Auxiliaries: photo-paper sheets and glass plates.

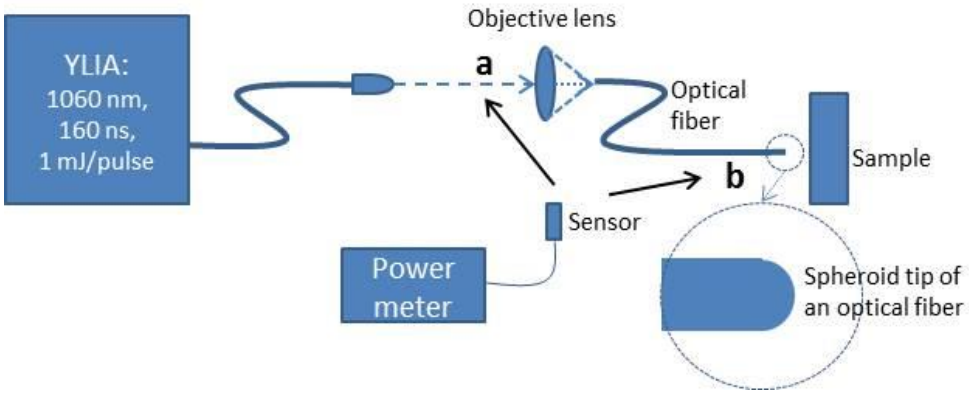

Figure 4.61. Experiment scheme for PJ etching using spheroid tip fiber optics

All properties of instruments and components can be found in the Appendix 5.

The experiments were done in four steps: (1) the laser beam characterization, (2) the laser injection tests and optimization, (3) the general static PJ-material interaction characterization and (4) the optimized PJ etching validation using spheroid optical fiber in motion.

A. Laser beam characterization

The laser interface software uses digital steps (called bit) to control the laser power. Therefore the power calibration is essential. Here the calorimeter with thermal sensor 30A-N-18 was used to measure the direct collimated laser power. The sensor is laid perpendicularly in front of laser head. The laser oscillator and booster are switched on and power characterization has been done starting from 0.6 W because the laser power is not stable below 0.6 W, until 19 W (maximum power). These characterizations were conducted deliberately at these two frequencies since YLIA M20 Quantel's working frequency rate is in a range of 20 kHz to 100 kHz. In addition, for the reason of reliability, we always measure these powers before every experiment.

The beam profile has also been characterized. As presented in Chapter 3, YLIA M20 Quantel has an ellipsoid beam profile at the focus point with the four-sigma width respectively 85.6 µm and 97.8 µm in two orthogonal axes; the mean four-sigma width $D_{4\sigma}$ is 91.7 µm. Divided by 2, it gives the beam waist at the focus point w_0 = 45.8 µm.

B. Laser injection

Optimizing laser injection is a process in order to adjust the position of a focusing optical system (lens or microscope objective) and an optical fiber in order to obtain as many as possible power injected into the optical fiber. Before to inject the laser beam into the optical fiber, the laser head, the objective and the optical fiber must be well aligned and they all must be perpendicular to the laser beam propagation axis. The YLIA M20 Quantel is equipped with a red light pointer that is very useful to have the good alignment. Then, the calorimeter was laid at the fiber output at the safe distance i.e. that the beam size is the same than the size of the detector sensitive part. The laser injection process

depends on several parametrs: the focusing lens choice, the beam diameter, the core diameter and the numerical aperture of the optical fiber. So to obtain a maximal injection, the focus size and numerical aperture of the lens must be smaller respectively than the core diameter and the numerical aperture of the fiber.

Six combinations of lens and optical fiber have been investigated:

(1) a lens (f = 50 mm, ∅ = 25,4mm) and a SMF28 ∅ = 10 µm;

(2) a lens (f = 50 mm, ∅ = 25,4mm) and a MMF ∅ = 50 µm;

(3) a Thorlabs AC127-019-C achromatic lens (f = 19 mm, ∅ = 12.7 mm) and SMF28 ∅ = 10 µm;

(4) a Thorlabs LMH-10X-1064 lens (EFL=20 mm, ∅ =15 mm, NA= 0.25) and SMF28 ∅ = 10 µm;

(5) a Thorlabs LMH-10X-1064 lens (EFL=20 mm, ∅ =15 mm, NA= 0.25) and a MMF ∅ = 50 µm;

(6) a Thorlabs LMH-10X-1064 lens (EFL=20 mm, ∅ =15 mm, NA= 0.25) and a MMF TEQS^{TM}-coated high power optical fibers (NA=0.22, $\varnothing_{core}$ = 200±8 µm).

These combinations of lens and optical fiber were considered to obtain a maximal injection without risking the destruction of the optical fiber due to the laser power.

The injection ratios in the SMF-28 (10 µm) and the MMF-50 µm fibers with the lens (f = 50 mm, ∅ = 25,4mm), combination (1) and (2), that is the ratio between the incident laser power injected into the fiber to the emitted laser power have been measured. The 24% (max 3.5 W) injection ratios obtained into the SMF-28 is not suitable. The injection ratio reaches 75% (max 11 W) for the MMF-50 µm. For our PJ etching application the injection ratio must be as high as possible in order to have enough power etching hard material and, as we will see later, to minimize the light injected into the cladding. The spot diameter at the focus of this lens (f = 50 mm) is D_f, given by formula (4.9). Here D_f = 19 µm is larger than the SMF28 core diameter. It is the reason why the laser is badly injected in this fiber. Inversely a high injection ratio is logically obtained in the 50 µm MMF, because D_f is smaller than the core diameter of the fiber. Even though the laser spot is larger than the core of the SMF28 the injection was conducted because sometime we do not need too high injected power laser.

$$D_f \approx 1.22 \frac{\lambda f}{D_{beam}} M^2, \tag{4.9}$$

We also see formula (4.9), that the focus diameter would be smaller and therefore the injection better, if the M2 of laser was closer to 1. It is also true because the modal adaptation would be better between the laser source and the guided modes.

In combination (3) (4) and (5), by using a lens of smaller focal (f = 20 mm), the spot diameter at the focus decreases to 7.6 µm. The injected ratio in the 50

µm MMF (combination (5)) reaches 92% (13 W). For the SMF28, the NA of the objective or of the achromatic lens (NA = 0.25) is almost two times larger than the one of the fiber (NA = 0.14), therefore the light could not be well injected. The fiber burnt, it is why the results are not presented.

In the previous cases the characterizations have not been achieved until the maximum laser power, because before this power, we have burned the fibers. These burnings were not at the entrance where the jacket is removed but at the other sections where the jacket is still attached. This shows the important role of the fiber jacket material. When the beam spot size is larger than the core or badly injected, some light is injected into the cladding and finally absorbed by the jacket that burnt the optical fiber. Figure 4.62 shows one of the burnt fibers (SMF28) for the combination (3). The SMF28 ∅ = 10 µm in combination (3) and (4) both burnt at the same injected laser power, around 5.2 watts. The 50 µm MMF in combination (5) burnt at an injected laser power around 13.8 watts.

a. b.

Figure 4.62. Thermal effects of laser injection burnt/melt SMF28 cladding, (a) at the jacket beginning and (b) near the jacket beginning

Even though the injection ratio using MMF ∅ = 50 µm in combination (1) to (5) can reach above 90%, it cannot stand to the highest laser powers. It means that this optical fiber and the SMF28 are not the best ones to use for PJ etching and that high-power optical fibers must probably be preferred.

We then have tested if an optical fiber with double cladding were more adapted for high-power laser. However the smallest core diameter of available optical fiber with double-cladding in the market was 200 µm. And so we used a 200 µm core MM fiber TEQS^{TM} coated. It is a “high-power” optical fiber from Thorlabs. The double optical cladding of this fiber allows guiding the badly injected light and thus absorbing it slowly by the jacket along the fiber without high local heating.

And so the characterization work of this fiber, combination (6), was conducted at repetition rates of 20 kHz and 100 kHz, the extreme frequencies available for YLIA M2 Quantel. No burnt mark on the fiber has been observed which means the 200 µm MM fiber TEQS^{TM} coated can stand to the highest power of YLIA laser injected. The injection ratio reaches 66%, that is 13 W injected.

After having validated that the MM fibers TEQS^{TM} coated can stand to the

highest power YLIA laser injected, we also characterized the transmitted power of the same fiber with the spheroid tipped end (Figure 4.59). The power of the beam coming out of the optical fiber decreases from 66% to almost 40%. The injection processes were the same at the fiber entrance, but the shape of the tip is changed. This difference comes from the reflection ratio inside the fiber at the tip. The reflection for flat tip of optical fiber end is around 4% and can generally be neglected. With the spheroid tip, the reflection increases as can be observed in Figure 4.56. Some parts of the incident light inside the fiber can undergo a total internal reflection because of locally high angles between the incident wave vector and the normal of the tip interface. Similar injection ratios have been obtained with the 100 µm core silica optical fiber.

C. PJ etching characterization

Our first objective was to validate the PJ' position that is the location of the highest beam concentration; the position where the light intensity out of the spheroid tipped optical fiber is the highest. It was not possible to capture direct measurement of this position. So, we practiced indirect measurement by trying to realize an etching using different pulse numbers at the minimum incident power and for different distance between the tip and a laser sensitive sample. The PJ position then corresponds to the tip to sample distance for which the etching size is the smallest.

Three high-precision micrometer translation stages are then used to control the position between the spheroid tipped optical fiber and the sample (Figure 4.63). In this experiment, the spheroid tipped fiber is grasped by two sponges patched to a three axis positioning micro stage so the tip will not be broken during translation or contact with the material surface (Figure 4.63a). This contact is observed using a magnifying lens and noted as the null distance. The tip-sample distance can then be controlled using the micro-translation stage (Figure 4.63b).

The laser injection is always checked at the beginning of each experiment. It is to be sure the injection is always optimized and agrees with the expected power.

The first considered sample was a photo-paper sheet. In industrial laser-applications (including in Irépa Laser, where we conducted our experiments), this sheet is often used as a cheap and practical indicator of laser position because it is very sensitive to low-power laser. The tests were done by applying between 10 and 40 laser pulses, at a repetition rate of 20 kHz, with a laser power (20 bit) ≈ 570 mW. The injected power was around 200 mW. The tip-sample distance was modified from 70 to 200 µm. This setup succeeded producing PJ marks and their sizes are presented in Table 4.19. The smallest diameter was obtained using 20 laser pulses at a distance of 150 µm which is no far to the distance of 194 µm simulated (Table 4.18). The translation stage must be probably recalibrated.

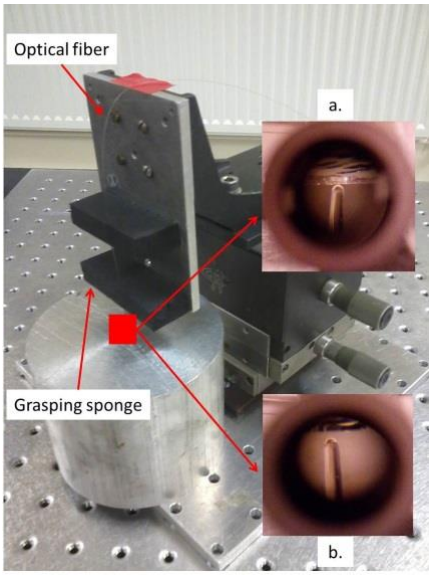

Figure 4.63. Optical fiber with spheroid tip is grasped by sponges patched to a three-axis positioning micro stage and moved (a) toward or (b) backward the sample to etch

Table 4.19. PJ mark diameter on photo paper using a repetition rate of 20 kHz and a laser power of 570 mW that generates PJ power of ≈ 200 mW

Tip distance (μm)	**Diameter of PJ mark (μm)**			
	40 pulses	**30 pulses**	**20 pulses**	**10 pulses**
35	115	92	64	-
45	115	90	65	-
55	112	95	64	-
65	105	96	63	-
75	105	89	57	-
80	106	92		
85	105	89		
90	108	90		
95	115	93		
100	107	90		

The next experiments, considering a sample of silicon wafer were conducted at a distance of 150 μm. The experiments on silicon wafer have been achieved using higher laser power and more pulses than on photo-paper. The power of PJ has been tested in a range from 0.22 to 7.19 watts, and the pulse number from 20 to 1,000,000. There was no PJ mark on silicon wafer at the lowest power and smallest number of pulses. The first laser power and pulse number combination scheme producing PJ marks on silicon wafer are in Figure 4.64. The figure shows that the etching process occurs confirming the PJ generation. It seems that the number of pulses could be more reduced at the highest laser powers. So, a second scheme was prepared for fewer pulse numbers (Figure

4.65).

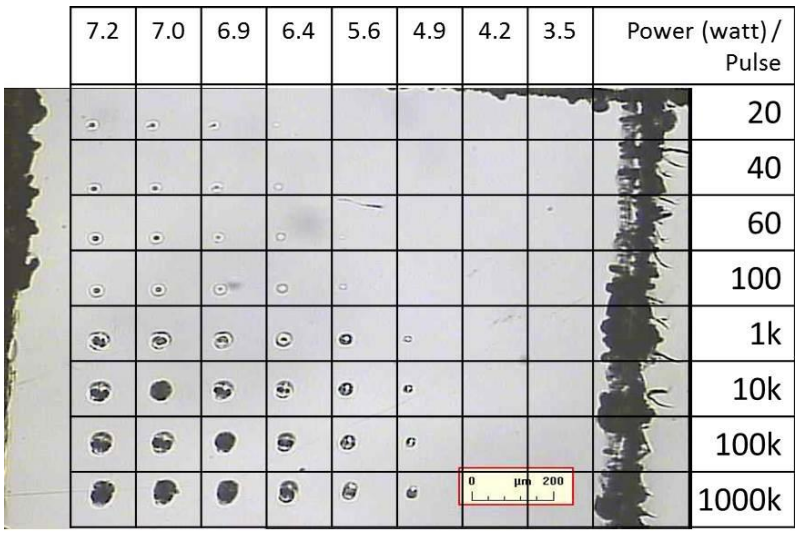

Figure 4.64. First etchings on silicon wafer using PJ out of a spheroid tipped optical fiber as function to PJ's power and laser pulses number.

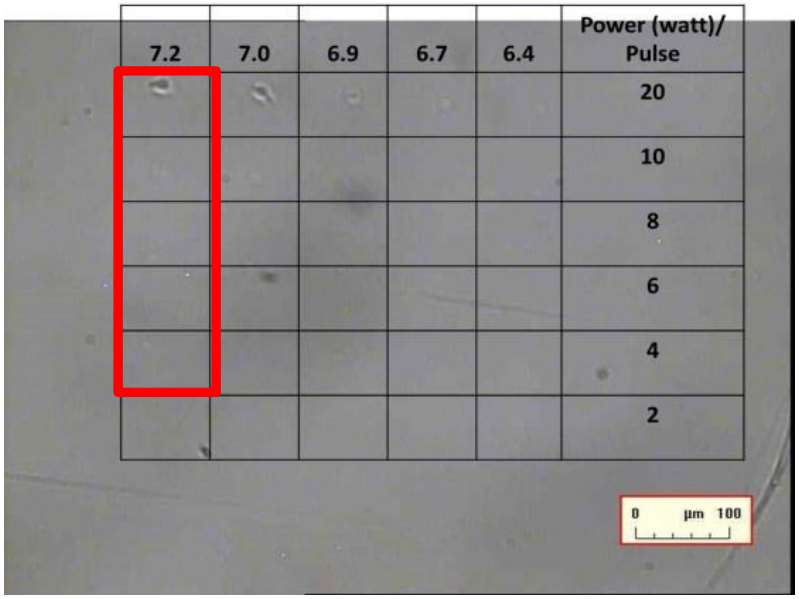

Figure 4.65. Second etching on silicon wafer using PJ out of spheroid tipped optical fiber as function to PJ's power and laser pulses. Five cells in red square are presented in Figure 4.66.

As for microspheres etching in Chapter 3, a Zygo™ profilometer has been used to characterize the PJ marks. Some etching profiles obtained with PJ's power of 7.2 watts are displayed in Figure 4.66. Lines crossing each PJ mark have been used to measure the mark diameter, which are summarized in Table 4.20. It appears that at the highest power (7.2 watts), at least 4 pulses are needed to etch silicon wafer.

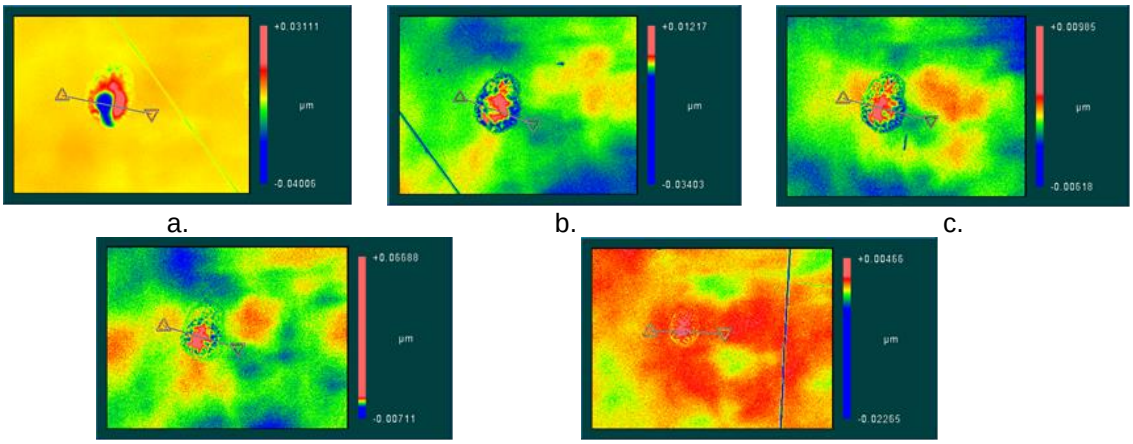

a. b. c.

d. e.

Figure 4.66. 2D profile of PJ marks on silicon wafer (five cells in the red square in Figure 4.65) for a power of 7.2 watts and for (a) 20, (b) 10, (c) 8, (d) 6 and (e) 4 pulses

Table 4.20. Diameters of PJ marks on silicon at a distance of 75 µm

Injected power laser (watt)	**Measured PJ power (watt)**	**PJ mark diameter (µm)**					
		20 pulses	**10 pulses**	**8 pulses**	**6 pulses**	**4 pulses**	**2 pulses**
19	7.2	27.4	27.7	27.8	27.4	17.5	-
18.6	7.1	26.4	25.5	26.8	22.8	-	-
17.9	6.9	28.1	-	-	-	-	-
17.2	6.7	25.9	-	-	-	-	-
16.4	6.4	20.2	-	-	-	-	-

The smallest etching diameter in Table 4.20 is around 17.5 µm, larger than the ones obtained using glass microspheres and larger than the ones predicted by simulations. The main reason of this discrepancy is that we used a source having a different intensity profile. The source was a plane wave for microspheres and a Gaussian wave (fundamental mode) for the waveguides. The real source into the waveguide is unfortunately more complex. Additional simulations have been performed to study the influence of the excited mode on the PJ properties. Figure 4.67 shows simulations of an optical fiber (with a diameter D_s = 80 µm, a tip length b = 20 µm and w = 0.405) for different modes excitations. These simulations were not conducted with the 200 µm fiber because of memory limitations. We see that the higher modes are focused at an off-axis position. Higher is the mode order, further is the off-axis position. So if several modes are excited, the PJ will be larger. If these off-axis spots have the fluence higher than the LIDT of the sample, the etching size increases.

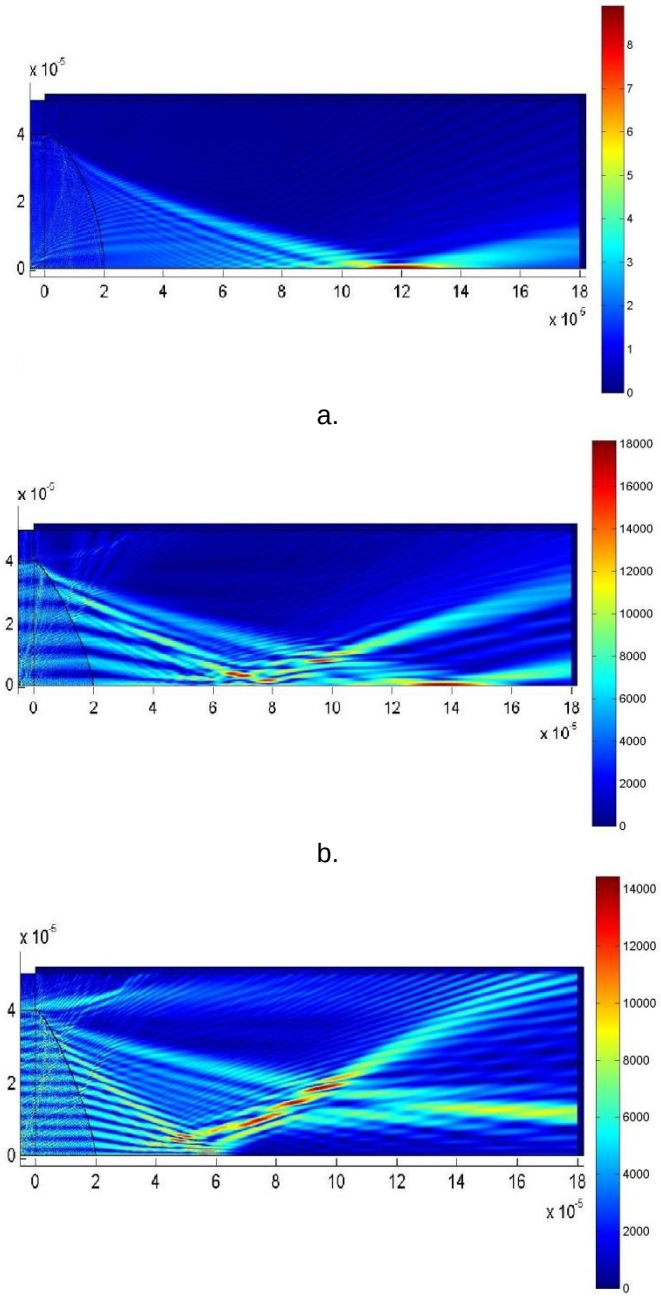

Figure 4.67. Total electric field of a half planar waveguide (D_s = 80 µm) with a sharp-curvature end (Bezier weight = 0.405, tip-length = 20 µm) for different excited mode: (a) fundamental mode, (b) mode 5 and (c) mode 13.

This off-axis focusing of higher order modes can be qualitatively understood. A guided mode in a planar waveguide can be expanded in the core as the sum of two plane waves tilted of θ from the x-axis:

$$E_0 \cos(uy) e^{i(\omega t - \beta x)} = \frac{E_0}{2}\left(e^{i(\omega t - \beta x + uy)} + e^{i(\omega t - \beta x - uy)}\right), \qquad (4.9)$$

having a wave vector modulus $|k|=2\pi n_{core}/\lambda_0=u^2+\beta^2$. As illustrated in Figure 4.68, β is the projection of the wave vector k on the x-axis and u the projection on the y-axis. θ is the angle between k and x, higher the mode order is, larger θ

is.

If now the tip is assumed be equivalent to a lens, we know that a plane wave tilted of θ from the optical axis will be off-axis focused. Obviously the tip cannot be rigorously assimilated to lens, but this analogy allows us to understand the phenomenon. The θ angle can be decreased by using an optical fiber with a lower number of modes or with a lower numerical aperture. The shape of the tip probably also plays a role in the increasing of PJ size.

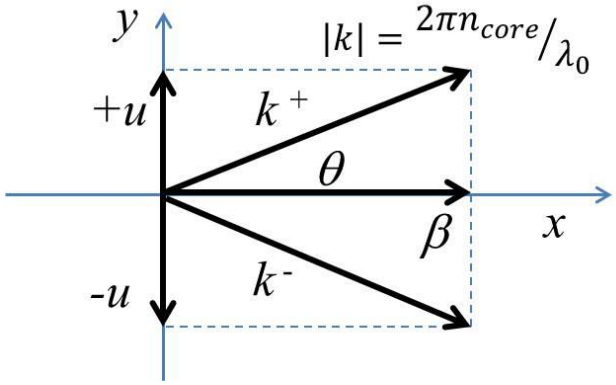

Figure 4.68. Mode propagation constant β, and, wave vectors k of the two plane waves used to expand the considered mode

As preliminary conclusion, we see that silicon can be etched using an optical fiber with spheroid tip and a 10W ns-NIR laser. A working distance of ~75 µm is enough in order not to disturb the optical fiber tip. However we see that the use of a multimode fiber increases the PJ size.

4. Potential improvements

In order to achieve a good PJ etching on silicon sample, some parameters and variables can be optimized one to each other:

- The parameters of the laser source;
- The parameters of the optical fiber;
- The parameters of the spheroid tip;
- The distance between the tip and sample;
- PJ's scanning speed.

Some parameters of a given laser cannot always be changed like the wavelength and the pulse duration. We have chosen nanosecond near infrared lasers for their industrial interest. We have seen that a low M2 factor of the laser beam will be an important parameter to improve the injection into the optical fiber. For the pulses number and the power, they depend on the material to etch.

For the optical fiber, the high power flux is the main issue. The laser is easier to inject in an optical fiber with a large core. We have seen that the fiber jacket plays an important role absorbing the badly injected light. This can destroy the fiber. A double optical cladding appears to be a sustainable solution; however the limitation is that available "high power" optical fibers proposed by companies are high multimode fibers with generally high numerical aperture. In

consequent, it leads to an increase of the PJ diameter. Smaller optical fiber diameter and fiber with smaller numerical aperture would be better to make decrease the PJ width.

Concerning the spheroid tipped, its geometry has still to be optimized. In order to avoid any material debris polluting the tip, a minimum distance must be put between the tip and the sample, so the PJ must not be too close from the tip. However putting the PJ further makes increase its width, what can be compensated by increasing the fiber core diameter. Therefore the working distance is not without relation with the optical fiber diameter. In our case, with a 200 µm core fiber a tip-sample distance of 75 µm has been chosen.

In the last experiments, discussed now, we have seen that the scanning speed can have a potential interest. The tip has been translated above the sample to etch a line. The system described in Figure 4.61, with a three-axis positioning micro stage (Figure 4.63) has been used to move the tip laterally. Because the translation is manual, the speed is not controlled. The tip-sample distance was ~150 µm and the laser was set at the highest power for one minute with a repetition rate of 20 kHz. The PJ marking obtained is presented in Figure 4.69. At the beginning, in the top of the picture, the etching width is large, but with the translation to the left (in five step), the etching size decrease until ~3 µm (Figure 4.69). It seems that when the etching has begun its size can decrease with the motion. These etchings may have smaller size than the static ones because when the etching line is begun the ablation threshold probably decrease in the center making possible higher PJ intensities focused on the optical axis to etch the material; whereas off-axis focused beam that have lower or dispersed intensities do not have enough fluence to etch the material. This result would have to be confirmed in the future.

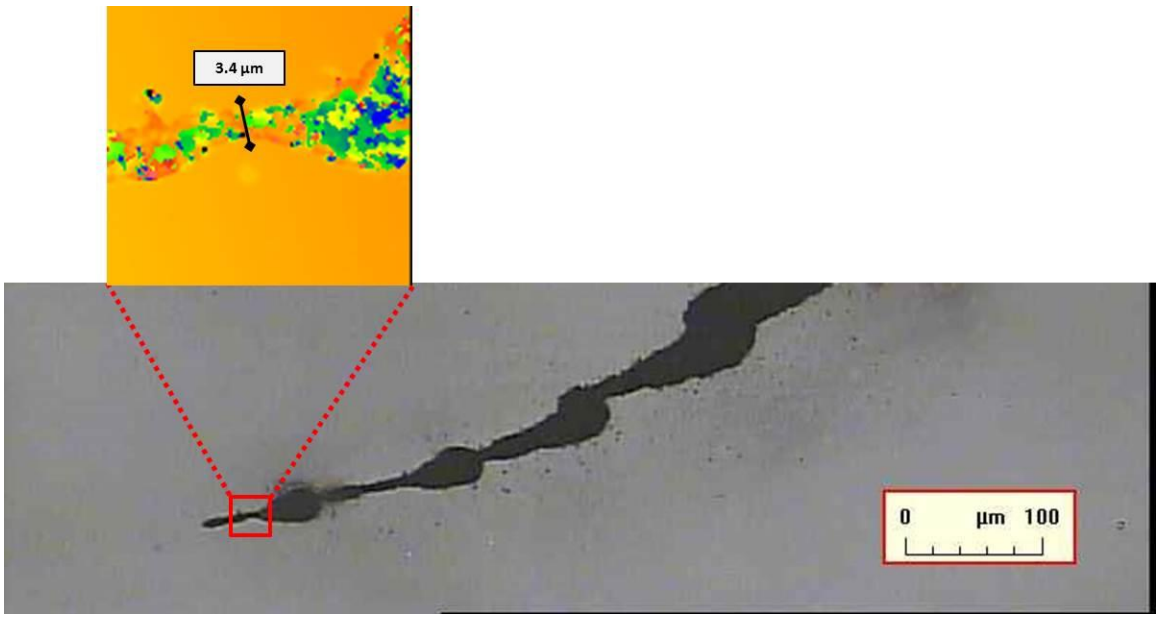

Figure 4.69. PJ etched line in motion on silicon and zoom-in on the smallest part

These experiments give an idea to achieve a ~3 µm etching by a PJ coming out of an optical fiber. However, this cannot be considered as a result yet because the motion was manually controlled.

Our best result has been obtained in the last month using the 100 µm core silica optical fiber (microscope view in Figure 4.59b). As shown in Figure 4.70 the etching marks have a diameter around 1 µm. 35 pulses were required. This result has been obtained with the contribution of Julien Zelgowski. The focus distance is around 100 µm.

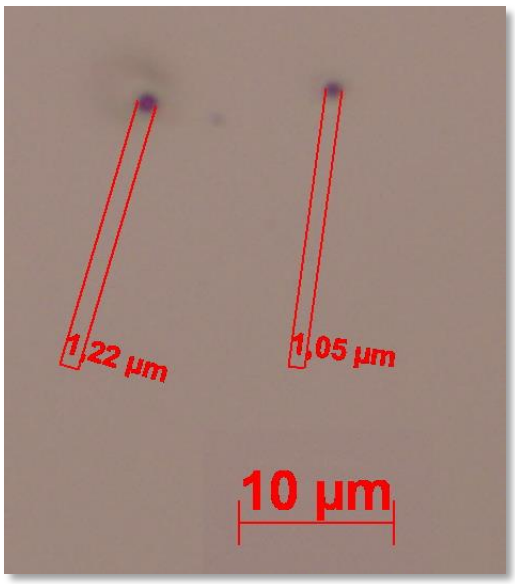

Figure 4.70. Smallest etching obtained with the 100 µm core silica optical fiber with a spheroid tip (NA = 0.22) at f = 100 µm and with 35 pulses.

5. Synthesis

In this chapter, we have studied how waveguides can generate PJ for micro-etching applications. First the possibilities were assessed by simulations of light coming out a spheroid tipped optical fiber in free-space. Three optical fibers with different sizes and two tip shapes were considered.

Then the laser injection has been tested: The tests show that multi-mode fibers are more adequate for PJ etching and that cladding adapted for high power laser can be useful. Our experiments have shown that a 100 µm core silica optical fiber and a 200 µm TEQSTM coated multimode fiber with double optical cladding were adapted to our 160 ns near infrared pulsed laser.

The first PJ etchings using a tipped 200 µm core fiber have shown the ability to achieve 17 µm marks at a 75 µm tip-material distance on a silicon wafer. This position agrees with the PJ simulation. The tip is not disturbed after etchings, stays clean and can be reused. The quite large size of the marks compared to the ones obtained with microspheres is due to the excitation of the higher modes of the fiber. On the basis of the simulations, a 2 µm diameter could have been expected if only the fundamental mode would have been excited. The best result has been obtained using a 100 µm core silica fiber (NA = 0.22) with a spheroid tip. Etching with a diameter of 1 µm has been achieved (with the contribution of Julien Zelgowski).

Several methods may be tested in the future to reduce the PJ marks sizes.

Optical fibers with a lower number of modes, that is, with smaller core diameters can be used. Optical fibers with smaller numerical aperture may also be considered. A specific work can also be done on the injection to facilitate the fundamental mode excitation. A first test let us imagine that the width of a line etched by a PJ in translating could be smaller and could reach ~3 µm (Figure 4.71).

References

[1] Z. Chen, A. Taflove, and V. Backman, "Highly efficient optical coupling and transport phenomena in chains of dielectric microspheres," *Optics Letters*, vol. 31, pp. 389-391, 2006.

[2] A. M. Kapitonov and V. N. Astratov, "Observation of nanojet-induced modes with small propagation losses in chains of coupled spherical cavities," *Optics Letters*, vol. 32, pp. 409-411, 2007.

[3] S. Yang and V. N. Astratov, "Photonic nanojet-induced modes in chains of size-disordered microspheres with an attenuation of only 0.08 dB per sphere," *Applied Physics Letters*, vol. 92, 2008.

[4] V. N. Astratov, A. Darafsheh, M. D. Kerr, K. W. Allen, and N. M. Fried, "Focusing microprobes based on integrated chains of microspheres," *PIERS Online*, vol. 6, pp. 793-797, 2010.

[5] V. N. Astratov, A. Darafsheh, M. D. Kerr, K. W. Allen, N. M. Fried, A. N. Antoszyk, *et al.* (2010) Photonic nanojets for laser surgery. *SPIE-Newsroom*.

[6] A. Darafsheh, A. Fardad, N. M. Fried, A. N. Antoszyk, H. S. Ying, and V. N. Astratov, "Contact focusing multimodal microprobes for ultraprecise laser tissue surgery," *Optics Express*, vol. 19, pp. 3440-3448, 2011.

[7] K. W. Allen, A. F. Kosolapov, A. N. Kolyadin, A. D. Pryamikov, N. Mojaverian, N. I. Limberopoulos, *et al.*, "Photonic jets produced by microspheres integrated with hollow-core fibers for ultraprecise laser surgery," in *Transparent Optical Networks (ICTON), 2013 15th International Conference on*, 2013, pp. 1-4.

[8] P. Ghenuche, H. Rigneault, and J. Wenger, "Hollow-core photonic crystal fiber probe for remote fluorescence sensing with single molecule sensitivity," *Optics Express*, vol. 20, pp. 28379-28387, 2012.

[9] L. Han, Y. P. Han, J. J. Wang, G. Gouesbet, and G. Grehan, "Controllable and enhanced photonic jet generated by fiber combined with spheroid," *Optics Letters*, vol. 39, pp. 1585-1588, Mar 2014.

[10] C. H. Li, G. W. Kattawar, P. W. Zhai, and P. Yang, "Electric and magnetic energy density distributions inside and outside dielectric particles illuminated by a plane electromagnetic wave," *Optics Express*, vol. 13, pp. 4554-4559, Jun 13 2005.

[11] H. Halaq, S. Lecler, Y. Takakura, S. Robert, and B. Sauviac, "Waveguide driven photonic jet: FEM, issues and perspectives," presented at the Workshop EM IEEE 2010, Saint-Malo, France, 2010.

[12] Y. Takakura, H. Halaq, S. Lecler, S. Robert, and B. Sauviac, "Single and Dual Photonic Jets With Tipped Waveguides: An Integral Approach," *IEEE Photonics Technology Letters*, vol. 24, pp. 1516-1518, Sep 2012.

[13] Y. Takakura, S. Lecler, B. Ounnas, S. Robert, and B. Sauviac, "Boundary Impedance Operator to Study Tipped Parallel Plate Waveguides," *Antennas and Propagation, IEEE Transactions on*, vol. 62, pp. 5599-5609, 2014.

[14] J. Dou, J. Li, P. R. Herman, J. S. Aitchison, T. Fricke-Begemann, J. Ihlemann, *et al.*, "Laser machining of micro-lenses on the end face of single-mode optical fibers," *Applied Physics A*, vol. 91, pp. 591-594, 2008.

[15] Y. Murakami, J.-I. Yamada, J.-i. Sakai, and T. Kimura, "Microlens tipped on a single-mode fibre end for InGaAsP laser coupling improvement," *Electronics Letters*, vol. 16, pp. 321-322, 1980.

[16] V. M. Sundaram and S.-B. Wen, "Fabrication of micro-optical devices at the end of a multimode optical fiber with negative tone lift-off EBL," *Journal of micromechanics and microengineering*, vol. 22, 2012.

[17] G. P. Agrawal, *Nonlinear Fiber Optics*, 3rd ed. San Diego: Academic Press, 2001.

[18] V. Alwayn, *Optical Network Design and Implementation*: Cisco Press, 2004.

[19] D. Marcuse, "Gaussian approximation of the fundamental modes of graded-index fibers," *Journal of the Optical Society of America*, vol. 68, pp. 103-109, 1978.

[20] G. Farin, *Curves and Surfaces for CAGD: A Practical Guide*, 5th ed. San Fransisco: Morgan Kaufmann, 2002.

[21] P. N. Minh, O. Takahito, and E. Masayoshi, *Fabrication of Silicon Microprobes for Optical Near-Field Applications*: CRC Press, 2002.

[22] H. Ji, H. Y. Hsu, J. Chua, L. X. Kong, A. B. Wedding, M. She, *et al.*, "Fabrication of integrated optic fibre tip for micron CMMs touch trigger probe application," in *Microelectronics: Design, Technology and Packaging II*, Bellingham, WA, USA, 2006, p. 603505.

[23] H. Ji, J. Chua, H. Y. Hsu, and A. B. Wedding, "Development of a Fabrication Process for the Manufacturing of a Microspherical Probe for Coordinate Measuring Machine Applications," *Journal of Mechanical Design*, vol. 133, p. 111003, 2011.

[24] K.-C. Fan, H.-Y. Hsu, P.-Y. Hung, and W. Wang, "Experimental study of fabricating a microball tip on an optical fibre," *Journal of Optics A: Pure and Applied Optics*, vol. 8, p. 782, 2006.

[25] M. Tao, Y. Jin, N. Gu, and L. Huang, "A method to control the fabrication of etched optical fiber probes with nanometric tips," *Journal of Optics*, vol. 12, p. 015503, 2010.

[26] J. R. Cummings, T. J. Fellers, and M. W. Davidson. (2012, 25-05-2015). *Near-field Scanning Optical Microscope Probe*.

CONCLUSIONS AND PERSPECTIVES

We have presented in this thesis a study of the potential use of the “photonic jet” created by dielectric microspheres or fiber optic with a spheroid tip, for material etching. To make the solution compatible with an industrial process, we have considered near infrared nanosecond pulsed lasers, sources commonly used for this application. The goals were twofold:

- make an experimental and theoretical study of the PJ-matter interaction,
- improve the resolution of laser etching.

In Chapter 1, we have presented the state of the art of laser etching. We have shown that this cheap and flexible technique has found its place next to massive production of microsystems using photolithography, extremely high accurate FIB or e-beam. We have also highlighted the specific issue of the development of new industrial etching techniques in the micrometer range.

Namely, these high focused beams in the near field of dielectric micro-particles, called photonic jet, have two advantages: high power density and spatial localization, beyond the diffraction limit. Their properties have been described in Chapter 2 with their potential applications.

Our first results, described in chapter 3, were about direct laser etching with dielectric micro-spheres. We have demonstrated the ability to reduce the etching size using photonic jet. Beyond this result, the main goal was to understand the PJ-matter interaction. We have considered samples of silicon wafers; they have many applications and can be easily etched with nanosecond pulsed lasers. The second material was a glass plate, not easily etched with nanosecond laser because of low absorption in the infrared. Finally, the advantages and drawbacks of laser etching using PJ generated by dielectric microspheres have been listed.

In Chapter 4, we have considered waveguide driven PJ, as a way to alleviate two drawbacks of microspheres: an optical fiber is easier to manipulate in an

etching process and the distance between the fiber and the sample can be controlled. We have demonstrated the first PJ etching using an optical fiber with spheroid tip. It has been achieved on a silicon wafer.

We summarize below the main conclusions of our first studies with microspheres:

(1) PJ allows increasing the lateral resolution of laser etching. By using glass microspheres and ns-pulsed NIR laser to create a PJ, it is possible to realize marks on silicon wafer about 40 times smaller than without PJ.

(2) The use of larger glass spheres to reach higher power density makes possible glass etching with ns-pulsed NIR laser, a result which can normally be obtained with the use of picosecond, femtosecond laser or UV laser.

(3) Larger spheres, or spheres with lower refractive index, generate photonic jet further from their surface. On the surface the intensity distribution is more complex: etchings with rings are achieved on the material.

(4) Smaller spheres, or spheres with higher refractive index (as barium-titanate sphere) generate photonic jet closer to or inside the sphere. We have observed that the spheres easily break in this situation.

(5) After the first etching, the sphere in contact with the sample is altered by the ejected matter. No more etching can be achieved.

Concerning the second setup using tipped waveguide, the following observations have been done:

(1) Photonic jet can be generated out of 2D waveguide or optical fiber with elliptical tip.

(2) The PJ position depends on the tip shapes. Sharp and elongated tips generate photonic jets closer from the microsphere than short and flat tips.

(3) The fundamental waveguide mode is well focused on the optical axis, whereas the higher order modes are off-axis focused, increasing the spot size.

(4) Single-mode fibers allow generating the PJ with smallest width.

(5) For multimode fiber, smaller numerical aperture makes possible to obtain smaller PJ size.

(6) For the fiber diameter and the numerical aperture choice a compromise must be found. Decreasing the focus spot size makes the laser injection more complicated.

(7) The bad injected light can burn the mechanical cladding of the fiber. Thus the optical fiber jacket choice is also a key feature.

(8) A 200 µm double cladding silica fiber with a spheroidal tip allows supporting enough injected power to etch silicon with a resolution of 17 µm at 150 µm of the tip, without disturbing the tip.

(9) A 100 µm core silica fiber with spheroid tip has achieved 1 µm diameter etching marks.

We consider that the demonstration of the potential use of PJ for improved material etching with an ns-NIR laser has been made, and practical solution proposed. For further decrease of the PJ etching size obtained with tipped optical fiber we formulate the following recommendations that can be considered as perspectives for our study:

(1) Optical fiber must be chosen and the injection optimized in order to excite only the fundamental or lower modes. Single-mode fibers or single-mode fiber welded with multimode fiber can be tested.

(2) Optical fibers with smaller diameters and smaller numerical apertures must be considered.

(3) The optical fiber tip can be placed on a translation stage to be easily moved above the sample surface. The etching in a dynamic configuration could be smaller than the static one. This must be confirmed.

Post-scriptum :

A patent has been submitted. The content deals with the fiber tip for direct laser etching; a demonstrator that could be presented to an industrial partner is being completed with the help of Irépa laser and the financial support of SATT Connectus.

APPENDIX

APPENDIX

1. Electric field around a microsphere using Mie theory

The Mie theory has been used to calculate the electromagnetic field around the studied microspheres. The theory is described here.

The Maxwell equations may be written as:

$$\nabla \cdot \epsilon(r,\omega)\boldsymbol{E}(r,\omega) = 0 \quad \text{(A.1)}$$

$$\nabla \cdot \boldsymbol{B}(r,\omega) = 0 \quad \text{(A.2)}$$

$$\nabla \times \boldsymbol{E}(r,\omega) = \mathrm{i}\omega\mu_0\boldsymbol{H}(r,\omega) \quad \text{(A.3)}$$

$$\nabla \times \boldsymbol{H}(r,\omega) = -\mathrm{i}\omega\mu_0\epsilon(r,\omega)\boldsymbol{E}(r,\omega) \quad \text{(A.4)}$$

for $\epsilon(r,\omega)$is the dielectric function of the response of material to exciting electromagnetic fields. It is physically useful for problems where the particle size is large enough to justify the use of such a global property.

For convenience, the medium discussed here is considered to be linear, homogeneous, isotropic and non-magnetic with harmonic time dependence fields. So that all satisfy the wave equation:

$$\nabla^2\boldsymbol{E} + k^2\boldsymbol{E} = 0, \quad \nabla^2\boldsymbol{H} + k^2\boldsymbol{H} = 0, \quad \text{(A.5)}$$

where the wave vector is:

$$k^2 = \frac{\omega^2}{c^2}\epsilon(\omega).$$

Also, since each material is also considered as a homogeneous one and does not carry density, the electromagnetic field must be divergence-free:

$$\nabla \cdot \mathrm{E} = 0, \quad \nabla \cdot \mathrm{H} = 0. \quad \text{(A.6)}$$

Thus from the Maxwell equations (A.3) and (A.4), the fields are then derived as:

$$\mathrm{E} = -\frac{1}{\mathrm{i}\omega\mu_0}\nabla \times \mathrm{H}, \qquad \mathrm{H} = \frac{1}{\mathrm{i}\omega\mu_0}\nabla \times \mathrm{E}. \tag{A.7}$$

Finding the divergence-free solution of equation (A.7) is not too difficult. Finding the ones that satisfy the appropriate boundary conditions at interfaces is more delicate. The most common approach to resolve this is by expressing the solutions in a coordinate system where all surface-interfaces are at a constant coordinates. Since Mie theory is concerned with spherical objects, therefore the solutions consists is expressed in the field of spherical coordinates and finding the appropriate stitching conditions [1].

Now, suppose a given vector function M is

$$\mathrm{M} = \nabla \times (\mathrm{b}\psi)$$

for ψ is a scalar function and b is an arbitrary constant vector. The divergence of the curl of any vector function is vanished:

$$\nabla \cdot \mathrm{M} = 0.$$

Applying the vector identities to M will obtain:

$$\nabla^2\mathrm{M} + \mathrm{k}^2\mathrm{M} = \nabla \times [\mathrm{b}(\nabla^2\psi + \mathrm{k}^2\psi)].$$

Therefore, M will satisfy the vector wave equation if ψ is a solution to the scalar wave equation. Thus:

$$\nabla^2\psi + \mathrm{k}^2\psi = 0$$

and M may be written as $\mathrm{M} = -\mathrm{b} \times \nabla\psi$ to show that M is perpendicular to b. Another vector function is then constructed from M with divergence-free:

$$\mathrm{N} = \frac{\nabla \times \mathrm{M}}{\mathrm{k}},$$

which is also satisfies the vector wave equation

$$\nabla^2\mathrm{N} + \mathrm{k}^2\mathrm{N} = 0,$$

and

$$\nabla \times \mathrm{N} = \mathrm{kM}.$$

It means that M and N have all the required properties of an electromagnetic field, i.e.:

- satisfying the vector wave equation,
- divergence-free,
- the curl of M is proportional to N, and
- the curl of N is proportional to M.

Thereby the problem now reduces to the comparatively more uncomplicated problem of finding the solutions of the scalar wave equation. So that the scalar function ψ may be called a generating function for the vector harmonics M and N; the vector b is sometimes called the guiding or pilot vector.

Since the particle is a spherical one, it is more satisfied to choose the wave

equation in the spherical polar coordinates (Figure A.71) so that is $b = b(r, \theta, \phi)$. Thus the arbitrary vector b that must be perpendicular to M is r:

$$M = -b \times \nabla\psi$$

becomes

$$M = \nabla \times (r\psi),$$

where r is the radius vector. Thus in spherical polar coordinates M becomes a solution for the vector wave equation which is everywhere tangential to any sphere $|r|$ = constant, or $r \cdot M = 0$. Hence, in spherical polar coordinates the scalar wave equation can be written as

$$\frac{1}{r^2}\frac{\partial}{\partial r}\left(r^2\frac{\partial\psi}{\partial r}\right) + \frac{1}{r^2\sin\theta}\frac{\partial}{\partial\theta}\left(\sin\theta\frac{\partial\psi}{\partial\theta}\right) + \frac{1}{r^2\sin\theta}\frac{\partial}{\partial\theta}\left(\frac{\partial^2\psi}{\partial\phi^2}\right) + k^2\psi = 0, \quad \text{(A.8)}$$

with the solution in the form of:

$$\psi(r, \theta, \phi) = R(r)\Theta(\theta)\Phi(\phi)$$

and when substituted into wave equation in spherical polar coordinates (equation A.8) yields three equations :

$$\frac{d^2\Phi}{d\phi^2} + m^2\Phi = 0, \quad \text{(A.9)}$$

$$\frac{1}{\sin\theta}\frac{d}{d\theta}\left(\sin\theta\frac{d\Theta}{d\theta}\right) + \left[n(n+1) - \frac{m^2}{\sin^2\theta}\right]\Theta = 0, \quad \text{(A.10)}$$

$$\frac{d}{dr}\left(r^2\frac{dR}{dr}\right) + [k^2r^2 - n(n+1)]R = 0, \quad \text{(A.11)}$$

where n and m are the separation constants that determined by subsidiary conditions that ψ must satisfy.

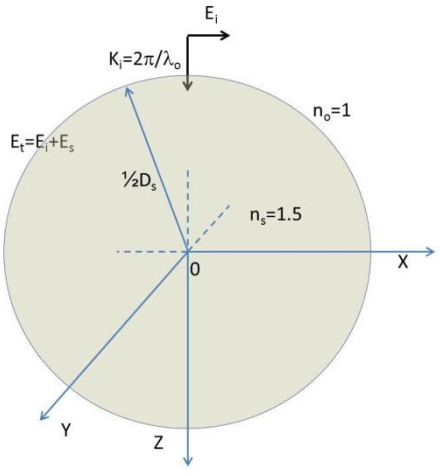

Figure A.71. Spherical polar coordinate center inside a sphere of diameter D_s

It is seen that for a given m, Φ_m is a solution to (A.9), then Φ_{-m} is not a linearly independent solution. The linearly independent solutions are:

$$\Phi_{even} = \cos m\phi, \quad \Phi_{odd} = \sin m\phi.$$

So that ψ is required to be a single-valued function in the angle ϕ:

$$\lim_{v \to 2\pi} \psi(\phi + v) = \psi(\phi), \tag{A.12}$$

for all ϕ. Condition (A.12) requires m to be an integer or zero; positive values of m are sufficient to generate all the linearly independent solutions to (A.9).

The solutions for (A.10), that are finite at $\theta = 0$ and $\theta = \pi$, are the associated Legendre functions of the first kind $P_n^m(\cos\theta)$ of degree n and order m, where $n = (0, 1, \ldots, m)$. These functions are orthogonal:

$$\int_{-1}^{1} P_n^m(\mu) P_{n'}^m(\mu) d\mu = \delta_{n'n} \frac{2}{2n+1} \frac{(n+m)!}{(n-m)!} \quad , \tag{A.13}$$

where $\mu = \cos\theta$ and the Kronecker delta, $\delta_{n'n}$, is unity if $n = n'$ and zero otherwise. When $m = 0$ the associated Legendre function are the Legendre polynomials, which are denoted by P_n.

If the dimensionless variable $\rho = kr$ is introduced and defined the function $Z = R\sqrt{\rho}$, equation (A.11) becomes:

$$\rho \frac{d}{d\rho}\left(\rho \frac{dZ}{d\rho}\right) + \left[\rho^2 - \left(n + \frac{1}{2}\right)^2\right] Z = 0. \tag{A.14}$$

The linearly independent solutions to (A.14) are the Bessel functions of first and second kind J_v and Y_v, where the order $v = n + ½$ is half-integer. Therefore, the linearly independent solutions to (A.11) are the spherical Bessel functions:

$$j_n(\rho) = \sqrt{\frac{\pi}{2\rho}} J_{n+1/2}(\rho), \tag{A.15}$$

$$y_n(\rho) = \sqrt{\frac{\pi}{2\rho}} Y_{n+1/2}(\rho), \tag{A.16}$$

with the constant factor $\sqrt{\pi/2}$ introduced for convenience. The spherical Bessel functions satisfy the recurrence relation:

$$z_{n-1}(\rho) + z_{n+1}(\rho) = \frac{2n+1}{\rho} z_n(\rho)$$

$$(2n+1) \frac{d}{d\rho} z_n(\rho) = n z_{n-1}(\rho) - (n+1) z_{n+1}(\rho)$$

where z_n is either j_n or y_n. Note that for all orders n, $y_n(kr)$ becomes infinite as r approaches the origin. Any linear combination of j_n and y_n is also a solution to (A.11). Or just take any two linearly independent combinations as fundamental solutions to (A.11), such as the spherical Bessel functions of the third kind (Hankel function) [2]:

$$h_n^{(1)}(\rho) = j_n(\rho) + i y_n(\rho), \tag{A.17}$$

$$h_n^{(2)}(\rho) = j_n(\rho) - iy_n(\rho). \tag{A.18}$$

Finally the generating functions that satisfy the scalar wave equation in spherical polar coordinates are:

$$\psi_{e,mn} = \cos m\phi P_n^m(\cos\theta)\, z_n(kr), \tag{A.19}$$

$$\psi_{o,mn} = \sin m\phi P_n^m(\cos\theta)\, z_n(kr), \tag{A.20}$$

where z_n is any of the four spherical Bessel functions (A.15 – A.18), and the subscripts "e" and "o" indicate "even" and "odd". Moreover, any function that satisfies the scalar wave equation in spherical polar coordinates may be expanded as an infinite series in the functions (2.20) and (2.21). The vector spherical harmonics generated by $\psi_{e,mn}$ and $\psi_{o,mn}$ are:

$$M_{e,mn} = \nabla \times (r\psi_{e,mn}), \qquad M_{o,mn} = \nabla \times (r\psi_{o,mn}),$$

$$N_{e,mn} = \frac{\nabla \times M_{e,mn}}{k}, \qquad N_{o,mn} = \frac{\nabla \times M_{e,mn}}{k},$$

which, may be written in component form:

$$M_{e,mn} = \frac{-m}{\sin\theta}\sin m\phi\ P_n^m(\cos\theta) z_n(\rho)\hat{e}_\theta - \cos m\phi\ \frac{dP_n^m(\cos\theta)}{d\theta}\ z_n(\rho)\hat{e}_\theta, \tag{A.21}$$

$$M_{o,mn} = \frac{m}{\sin\theta}\cos m\phi\ P_n^m(\cos\theta) z_n(\rho)\hat{e}_\theta - \sin m\phi\ \frac{dP_n^m(\cos\theta)}{d\theta}\ z_n(\rho)\hat{e}_\theta, \tag{A.22}$$

$$N_{e,mn} = \frac{z_n(\rho)}{\rho}\cos m\phi\, n(n+1)P_n^m(\cos\theta)\hat{e}_r + \cos m\phi\ \frac{dP_n^m(\cos\theta)}{d\theta}\ \frac{1}{\rho}\ \frac{d}{d\rho}[\rho z_n(\rho)]\hat{e}_\theta - m\sin m\phi\ \frac{dP_n^m(\cos\theta)}{\sin\theta}\ \frac{1}{\rho}\ \frac{d}{d\rho}[\rho z_n(\rho)]\hat{e}_\phi, \tag{A.23}$$

$$N_{o,mn} = \frac{z_n(\rho)}{\rho}\sin m\phi\, n(n+1)P_n^m(\cos\theta)\hat{e}_r + \sin m\phi\ \frac{dP_n^m(\cos\theta)}{d\theta}\ \frac{1}{\rho}\ \frac{d}{d\rho}[\rho z_n(\rho)]\hat{e}_\theta - m\cos m\phi\ \frac{dP_n^m(\cos\theta)}{\sin\theta}\ \frac{1}{\rho}\ \frac{d}{d\rho}[\rho z_n(\rho)]\hat{\mathbf{e}}_\phi, \tag{A.24}$$

where the r-component of N_{mn} has been simplified by using the fact that P_n^m satisfies (A.10). Any solution to the field equations can now be expanded in an infinite series of the functions (A.21) - (A.24). Thus, using these vector harmonics any problem of scattering by an arbitrary sphere may be solved. For this purposes a plane x-polarized wave must be written in spherical polar coordinates. The plane x-polarized wave is

$$E_i = E_0 e^{ikr\cos\theta}\hat{e}_x, \tag{A.25}$$

where

$$\hat{e}_x = \sin\theta\cos\phi\,\hat{e}_r + \cos\theta\cos\phi\,\hat{e}_\theta - \sin\phi\,\hat{e}_\phi.$$

Now re-writing (A.25) in vector spherical harmonics:

$$E_i = \sum_{m=0}^{\infty}\sum_{n=m}^{\infty}\left(B_{e,mn}M_{e,mn} + B_{o,mn}M_{o,mn} + A_{e,mn}N_{e,mn} + A_{o,mn}N_{o,mn}\right). \quad \text{(A.26)}$$

Since $\sin m\phi$ is orthogonal to $\cos m'\phi$ for all m and m', that means $M_{e,mn}$ and $M_{o,mn}$ are orthogonal:

$$\int_0^{2\pi}\int_0^{\pi} M_{e,m'n'}\cdot M_{o,mn}\sin\theta\ d\theta\,d\phi = 0 \qquad (\text{all } m, m', n, n').$$

Therefore, $(M_{o,mn}, N_{o,mn})$ and $(M_{e,mn}, N_{e,mn})$ are mutually orthogonal sets of functions. The orthogonality properties of all the vector spherical harmonics imply that the coefficients in the expansion (A.26) are of the form

$$B_{e,mn} = \frac{\int_0^{2\pi}\int_0^{\pi} E_i\cdot M_{e,mn}\sin\theta\ d\theta\,d\phi}{\int_0^{2\pi}\int_0^{\pi}\left|M_{e,mn}\right|^2\sin\theta\ d\theta\,d\phi},$$

with similar expressions for $B_{o,mn}$, $A_{e,mn}$ and $A_{o,mn}$. It follows that for the plane incidence wave in equation (A.25) $B_{e,mn} = A_{o,mn} = 0$ for all m and n. Moreover, the remaining coefficients vanish unless $m = 1$ for the same reason. Thus, the expansion for E_i in equation (A.26) has the form

$$E_i = \sum_{n=1}^{\infty}\left(B_{o,1n}M_{o,1n}^{(1)} + A_{e,1n}N_{e,1n}^{(1)}\right). \quad \text{(A.27)}$$

The additional superscript (1) to vector spherical harmonics indicates that the radial dependence of the generating functions is specified by $j_n(kr)$ that represent the finiteness of incident field at the origin. It requires that $j_n(kr)$ is the appropriate spherical Bessel function in the generating functions $\psi_{o,1n}$ and $\psi_{e,1n}$.

Based on the orthogonality properties of orthogonal sets of functions yields the expansion coefficients:

$$B_{o,1n} = i^n E_0\frac{2n+1}{n(n+1)} \quad \text{(A.28)}$$

and

$$A_{e,1n} = -iE_0 i^n\frac{2n+1}{n(n+1)}. \quad \text{(A.29)}$$

These two coefficients are substitute into equation (A.29), thus the expansion of a plane wave in spherical harmonics is:

$$E_i = E_0\sum_{n=1}^{\infty} i^n\frac{2n+1}{n(n+1)}\left(M_{o,1n}^{(1)} - iN_{e,1n}^{(1)}\right). \quad \text{(A.30)}$$

The corresponding incident magnetic field is obtained using (A.7) that is the curl of (A.27):

$$H_i = \frac{k}{i\omega\mu_0} E_0 \sum_{n=1}^{\infty} i^n \frac{2n+1}{n(n+1)} \left(M_{e,1n}^{(1)} + iN_{o,1n}^{(1)} \right). \quad \text{(A.31)}$$

If we define the scattered electromagnetic field (E_{sc}, H_{sc}) only outside the sphere, it makes the total field outside the sphere is the sum of the incidence and scattered field. The same kind of expansions of the incidence electromagnetic field in (A.30) and (A.31) also can be used to the scattered electromagnetic field (E_{sc}, H_{sc}) and the total field inside the sphere (E_s, H_s).

At the boundary between the sphere and the surrounding medium, the tangential components of the fields outside the sphere are equal to the tangential components of the fields inside the sphere:

$$E_{out} \times \hat{e}_r = E_{inside} \times \hat{e}_r$$
$$E_{out} = E_i + E_{sc}$$
$$E_{inside} = E_s.$$

Therefore,

$$(E_i + E_{sc} - E_s) \times \hat{e}_r = 0 \quad \text{(A.32)}$$

and

$$(H_i + H_{sc} - H_s) \times \hat{e}_r = 0. \quad \text{(A.33)}$$

The boundary conditions (A.32) and (A.33), the orthogonality of the vector harmonics and the form of the expansion of the incidence field wave in (A.5) specify the form of the expansions for the scattered field and the field inside the sphere: the coefficients in these expansions vanish for all $m \neq 1$. Thus, the field inside the sphere (E_s, H_s) is:

$$E_s = \sum_{n=1}^{\infty} E_n \left(c_n M_{o,1n}^{(1)} - id\, N_{e,1n}^{(1)} \right), \quad \text{(A.34a)}$$

$$H_s = \frac{k}{i\omega\mu_s} \sum_{n=1}^{\infty} E_n \left(d_n M_{e,1n}^{(1)} + ic_n\, N_{o,1n}^{(1)} \right), \quad \text{(A.34b)}$$

where $E_n = i^n E_0 \frac{2n+1}{n(n+1)}$ and μ_s is the permeability of sphere.

And, the scattered field is:

$$E_{sc} = \sum_{n=1}^{\infty} E_n \left(ia_n N_{e,1n}^{(3)} - b_n\, M_{o,1n}^{(3)} \right), \quad \text{(A.35a)}$$

$$H_{sc} = \frac{k}{i\omega\mu_0} \sum_{n=1}^{\infty} E_n \left(ib_n N_{o,1n}^{(3)} - a_n\, M_{e,1n}^{(3)} \right), \quad \text{(A.35b)}$$

where the additional superscript (3) to vector spherical harmonics indicates that the radial dependence of the generating function is specified by the spherical Hankel function. Namely the scattered field is no defined at the origin,

therefore no divergence can occur. In the far field, the Hankel function tends to be

$$h_n^{(1)}(kr) \sim \frac{(-i)^n e^{ikr}}{ikr} \quad , \qquad kr \gg n^2.$$

Even though it has been demonstrated that magnetic and electric field simulation result similarly, in the case of interaction of the radiation with material, it is important to consider only electric field [3].

2. Laser beam calibration

The maximum laser energies per pulse given in the data sheet of the lasers cannot directly used in the experiments because these lasers are not operated at their optimum frequency rate. Hence a new calculation to retrieve the maximum laser energy at the frequency rates operated in the experiments is compulsory. The laser energy per pulse at any frequency rate f_{rate} is for an average power P_{av} *is*:

$$E = \frac{P_{av}}{f_{rate}} \, , \tag{A.36}$$

so the laser fluence on the illuminated surface A_z at any defocused position z is:

$$F_z = \frac{E}{A_z} \, . \tag{A.37}$$

Then, since the lasers use different unit to control their powers, a calibration is needed to convert their unit into standard power unit (watts). For this purpose, the output average power P_{av} of the lasers has been measured without objective and galvanometer scanning system.

The peak powers P_{max}, the mean power density P_{dens} at position z and the laser fluence F_z are then calculated using equations (3.7) (3.8) and (3.10). The calibration of the YLIA laser and deduced physical parameters at frequency rate 20 kHz are in Table A.1.

Table A.1. YLIA laser calibration at f_{rate} = 20 kHz: the mean laser power density and the laser fluence are given at position z = 108 mm

Bit	20	40	60	80	100	120	140	160	180	200	220	240	250	255
P_{av} (W)	0.57	1.81	3.27	4.78	6.36	7.80	9.40	10.94	12.78	14.48	16.44	17.92	18.6	18.94
P_{max} (kW)	0.20	0.64	1.15	1.68	2.24	2.75	3.31	3.86	4.51	5.11	5.80	6.32	6.56	6.68
P_{dens} (kW/cm^2)	10.1	31.9	57.6	84.3	112	138	166	193	225	255	290	316	328	334
F_z (mJ/cm^2)	1.43	4.53	8.17	12.0	15.9	19.5	23.5	27.4	32.0	36.2	41.1	44.8	46.5	47.4

The calibration of the Nd:YAG laser and deduced physical parameters at frequency rate f_{rate} = 20 kHz are in Table 3.3. The maximum available peak power is P_{max} = 11.1 kW. Then, substituting the laser affected area from

equation (3.4) into equation (3.6) will yield the laser power density P_{dens}. All these power calibration, power density and laser fluence for Nd:YAG are in Table A.2.

Some experiments using the Nd:YAG laser have also be done at f_{rate} = 10 kHz at two different defocused distances, z = 14 mm and 22 mm. Hence, the calibration and deduced physical parameters in these cases are presented in Table A.3, and in Table A.4 for z = 57.5 mm.

Table A.2. Nd:YAG laser calibration at f_{rate} = 20 kHz: the mean laser power density and the laser fluence are given at position z = 22 mm

Percentage (%)	10	20	30	40	50	60	70	80	90	100
P_{av} (W)	0.55	1.1	1.65	2.2	2.75	3.3	3.85	4.4	4.95	5.5
P_{max} (kW)	1.11	2.22	3.32	4.43	5.54	6.65	7.76	8.87	9.97	11.1
P_{dens} (MW/cm²)	0.67	1.34	2.01	2.68	3.35	4.03	4.70	5.37	6.04	6.71
F_z (mJ/cm²)	16.6	33.3	49.9	66.6	83.2	99.9	117	133	150	166

Table A.3. Nd:YAG laser calibration at f_{rate} = 10 kHz and the mean power density at the position z = 14 mm and 22 mm

Percentage (%)		10	20	30	40	50	60	70	80	90	100
P_{av} (W)		0,55	1,1	1,65	2,2	2,75	3,3	3,85	4,4	4,95	5.5
P_{max} (kW)		2.22	4.43	6.65	8.87	11.1	13.3	15.5	17.7	19.9	22.2
P_{dens} (MW/cm2)	z=14 mm	3.03	6.05	9.08	12.1	15.1	18.2	21.2	24.2	27.2	30.3
	z=22 mm	1.34	2.68	4.03	5.37	6.71	8.05	9.39	10.7	12.1	13.4
F_z (mJ/cm2)	z=14 mm	75.1	150	225	300	375	451	526	601	676	751
	z=22 mm	33.3	66.6	99.9	133	166	200	233	266	300	330

Table A.4. YLIA laser power calibration with f_{rate} = 20 kHz: the laser power density and laser fluence at z = 57.5 mm

Bit	20	40	60	80	100	120	140	160	180	200	220	240	250	255
P_{av} (W)	0.57	1.81	3.27	4.78	6.36	7.80	9.40	10.94	12.78	14.48	16.44	17.92	18.60	18.94
P_{max} (kW)	0.20	0.64	1.15	1.68	2.24	2.75	3.31	3.86	4.51	5.11	5.80	6.32	6.56	6.68
P_{dens} (kW/cm²)	35.3	112	202	296	394	483	582	678	792	897	1018	1110	1152	1173
F_z (mJ/cm²)	5.01	15.9	28.7	42.0	55.9	68.5	82.6	96.1	112	127	144	157	163	166

3. Soda lime glass transmission as a function of wavelength

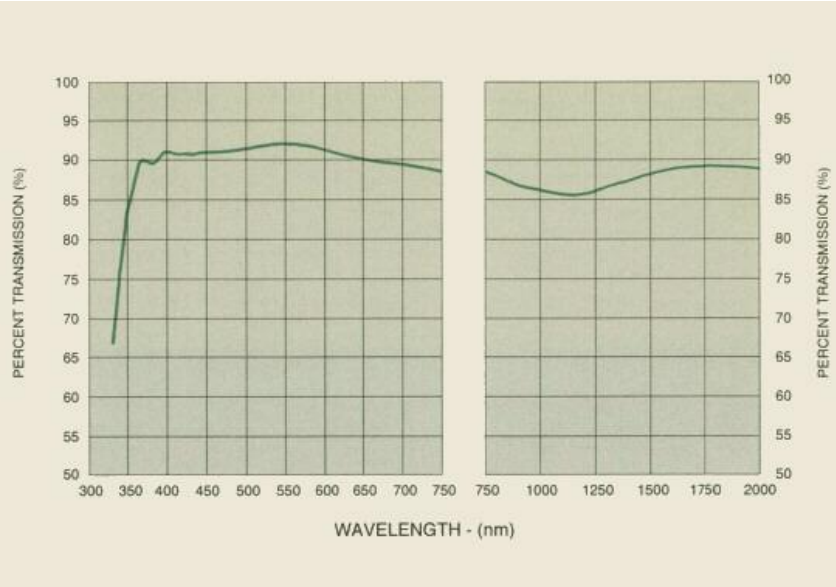

Figure A.72. Soda lime glass transmission as a function of wavelength is taken from S. M. Company. (2013, 14 June 2013). Optical transmission curve is available at http://www.sinclairmfg.com/datasheets/optical3.html

4. Photonic jet etching features

These are the photonic jet etching features on glass-slide and silicon wafer using microspheres and the Nd:YAG laser at defocused range z = 14.2mm and frequency rate f_{rate} = 10kHz with 5, 10 and 15 pulses and 50%, 75% and 100% of power

Power 50%

Material	Sphere size (μm)	5 pulses		10 pulses		15 pulse	
		Width (μm)	Depth (μm)	Width (μm)	Depth (μm)	Width (μm)	Depth (μm)
Glass	35	NA	NA	NA	NA	4.97	0.01
	24	5.04	0.01	4.87	0.01	3.74	0.02
Silicon wafer	35	4.91	1.52	3.01	0.55	7.27	1.38
	24	5.34	1.17	3.68	0.96	3.12	0.96
	4	0.70	0.00	1.46	0.01	1.36	0.02

Power 75%

Material	Sphere size (μm)	5 pulses		10 pulses		15 pulse	
		Width (μm)	Depth (μm)	Width (μm)	Depth (μm)	Width (μm)	Depth (μm)
Glass	35	7.64	0.03	6.63	0.02	8.96	0.10
	24	4.42	0.04	NA	NA	4.89	0.01
Silicon wafer	35	7.44	1.63	8.16	2.25	10.28	1.74
	24	3.23	1.47	NA	NA	NA	NA
	4	1.00	0.01	0.90	0.00	0.66	0.01

Power 100%

Material	Sphere size (µm)	5 pulses		10 pulses		15 pulse	
		Width (µm)	Depth (µm)	Width (µm)	Depth (µm)	Width (µm)	Depth (µm)
Glass	35	6.88	0.02	6.53	0.02	NA	NA
	24	5.26	0.02	4.85	0.02	4.97	0.03
Silicon wafer	35	11.32	2.55	11.86	2.43	7.01	1.87
	24	NA	NA	10.96	1.78	6.68	0.93
	4	0.90	0.01	0.84	0.01	0.92	0.01

Remarks:

- NA = Not Available: there is no etching mark correlated to the microsphere position before laser illuminations.
- The microsphere used in these tables is glass-microspheres.
- There is no etching mark correlated to glass-microsphere size 6 µm.
- The photonic jet etchings observed on glass-slide do not have a ring-shape, different to the experiment results conducted at defocused range z = 21.6 mm.

5. Specifications of instruments and components used in the experiments

A. Nd:YAG laser source VectorMark® Compact

VectorMark® Compact Laser Marking System

The VectorMark compact is TRUMPF's brand name for its diode pumped laser marking systems within the VectorMark product family. The VectorMark compact offers many advantages over older flash lamp pumped technologies including:

- Significantly improved life of the laser and longer system up times by replacing flash lamps with long life diodes.
- Over 100 built in sensors monitoring more than 250 key system operating parameters for easy diagnostics and troubleshooting either locally or via modem through TRUMPF's global technical support network.
- The ability to easily acquire data via the VectorMark's open system architecture, mark your product with a unique code, and to upload a complete history of each part you make to your data base for the ultimate in product traceability.

Other unique features include:

- Compact size (typically 1/5th of the total volume and floor space required by older technologies)
- Single phase 115 VAC 20 A connection.
- Integrated coding system
- Low cost of operation
- Excellent documentation, software, and operator training.
- Up to 2 1/2 times better mark resolution to convey your company's image of quality.
- The tightest specs in the industry for precision, accuracy, and mark repeatability.
- TRUMPF quality and durability

Included in Standard System:
Laser resonator, mounting brackets, galvonometers, RF power supply, PC, Monitor, keyboard, mouse, standard operating software, integrated cooling system, coaxial pilot laser, tele diagnostics, full I/O capability

Technical Specifications

Laser device		VMc1	VMc2	VMc3
Wave length	[nm]	1064	532	1064
Pulse repetition frequency	[kHz]	cw, 1-60	1-20	cw, 1-60
Marking field size	[mm]	60x 60	60x 60	60x 60
(standard optical system)	[mm]	120x120	120x120	120x120
	[mm]	180x180	180x180	180x180
Standard spot size	[µm]	45	35	45

Connection, consumption and installation		VM compact
Electrical connection		115 VAC, 60 Hz, single phase, <2kW
PC operating system		Windows NT
Network connection		PC - Ethernet network interface card, 10/100 Mbit data transfer rate, RJ-45 connector
Protection: Beam source and supply unit		IP 54
Beam source: Dimensions L x W x H	[mm]	610 x 200 x 260 (VMc 3 300H)
Beam source: Weight	[kg / lbs]	25 kg / 55 lbs
Supply unit: Dimensions W x H x D	[mm]	440 x 640 x 710
Supply unit: Weight	[lbs]	220
Approximate shipping weight w/o workstation	[lbs]	550
Approximate shipping weight w/ workstation	[lbs]	1100
Maximum ambient operating temperature	[°F]	95

As a result of continuous efforts for improvement technical specifications are subject to change.

TRUMPF
North American Headquarters
TRUMPF Inc.
3 Johnson Avenue
Farmington, CT 06032
Tel.: 877 232 9334
Fax: 860 409 0855
www.VectorMark.com

TRUMPF Inc.
Laser Technology Center
47800 Galleon Drive
Plymouth Township, MI 48170
Tel: 734.354.9770
Fax: 734.354.9769

TRUMPF Inc.
West Coast Technology Center
47273 Fremont Blvd.
Fremont, CA 94538-9689
Tel: 510.657.2657
Fax: 510.657.2866

TRUMPF Canada
118-2222 S. Sheridan Way
Mississauga, ON L5J 2M4
Tel: 800.306.1077
Fax: 905.823.2212

TUS-VMC-ORM-0101

B. Ytterbium-fiber laser source YLIA-M20 QUANTEL

Ylia M10 and M20 by Quantel

A rugged and compact pulsed fiber lasers intended for integration into industrial equipment. These lasers offer **10 W or 20 W** average power delivered via a flexible output fiber and collimating optics.

The Fast+ feature significantly reduces switch-off delay to 9 µs resulting in a significant time per job reduction and higher marking quality compared to other fiber lasers.
Due to excellent pump-to-signal efficiency in the optical fiber, these powerful air-cooled laser systems are **maintenance free** with **low operational costs.**

Pulse repetition rate and output power can be controlled either by 8-bits TTL signal or USB, providing the user both fast communication and **user-friendly** interfaces at the same time.

Typical specifications

MODEL	M10*	M20*
OPTICAL SPECIFICATIONS		
Wavelength [nm]	1064	1064
Average power [W]	10	20
Pulse Energy [mJ]	0.5	1.0
Pulse duration [ns]	100	100
Peak power [kW]	6.5 at 20 kHz	9 at 20 kHz
Repetition rate [kHz]	20 to 250	20 to 250
Switch on / off [µs]	150 / 9	150 / 9
BEAM CHARACTERISTICS		
Beam quality (4 sigma)	2.2	2.3
Beam diameter (99%) [mm]	8	8
Beam divergence (beam expander) [mrad]	< 1	< 1
FACILITY REQUIREMENTS		
Supply voltage [VDC]	24	24
Power consumption [W]	100	125
Cooling	Air cooled (heatsink and fans included)	Air cooled (heatsink and fans included)
Operating temperature [°C]	5 - 40	5 - 40
MECHANICAL DIMENSIONS		
Optical head dimensions [mm^3]	230 x 50 x 43	230 x 50 x 43
Laser box dimensions [mm^3]	286 x 215 x 95	286 x 215 x 95
Fiber delivery length [m]	5	3

* Beam expander 9mm

OPTIONS	
	BEAM EXPANDER 12 mm RED AIMING BEAM 100 mm FOCUSING LENGTH

Quantel - France
2 bis, avenue du Pacifique
Z.A. de Courtaboeuf - BP 23
91941 Les Ulis Cedex - France
Tel. +33 (0)1 69 29 17 00

Quantel - USA
601 Haggerty Lane
Bozeman, MT 59715 - 2001 - USA
Tel. +1 406 586 0131 / 1 877 QUANTEL

Quantel - Germany
Am Wolfsmantel 46
91058 Erlangen - Germany
Tel. +49 (0) 9131 94088-15

E-mail : quantel@quantel.fr www.quantel-laser.com

Pulsed Laser Solutions

C. Profilometer ZYGO® NewView 7200

NewView™ 7200 Specifications

System

Measurement Technique	Non-contact, three-dimensional, scanning white light interferometry
Scanner	Closed-loop piezo-based, with highly linear capacitive sensors
Objectives	1X, 2.5X, 5X, 10X, 20X, 50X, 100X; objectives available in Standard/Long /Super-Long Working Distance versions; see page 2 for availability and specifications
Objective Mounting Options	• Single objective dovetail • Manual 6-position turret • Motorized 6-position turret
Field Zoom Lenses	High-quality discrete zoom lenses; 0.5X, 0.75X, 1.0X, 1.5X, 2.0X
Image Zoom	Single user-interchangeable zoom lens
Field of View	From 0.03 to 14 mm; larger area imaged with field stitching; objective and zoom dependent
Illuminator	Unique single white-light LED design with superior life, uniform imaging and high efficiency
Controls	Filter Tray and Field Stop (Focus-aid)
Measurement Array	Selectable, includes standard- 640x480, 320x240, 160x120; optional- 992 x 992 (1K)
Part Viewing	Secondary LCD monitor
Focus	Motorized manual and auto focus
Z-Drive (Focus) Stage	DC brushless microstepper motor with ballscrew drive, 4 in. range, and 0.1 µm resolution.
Part Stage Options	• Manual Tip/Tilt/X/Y with ±6° tip/tilt, ±2 in. x/y • Motorized Tip/Tilt/X/Y with ±4° tip/tilt, ±3 in. x/y • Motorized Tip/Tilt/X-Theta (or Y-Theta) with ±4° tip/tilt, ±3 in. linear travel
Computer	High-performance Dell PC with LCD monitor
Software	ZYGO MetroPro software running under Microsoft Windows XP

Physical

Dimensions (H x W x D)	Overall System: 62 x 52 x 35 in. (157 x 132 x 89 cm) NewView: 32 x 23 x 16 in. (81 x 58 x 41 cm) Vibration Isolation Table: 30 x 24 x 24 in. (76 x 61 x 61 cm) Workstation Table: 33.5 x 52 x 35 in. (85 x 132 x 89 cm)
Weight	System: ~ 950 lb (430 kg) NewView: ~ 200 lb (90 kg) Vibration Isolation Table: ~ 600 lb (272 kg)

Performance

Vertical Scan Range	150 µm (5906 µin); Extended scan range to 20 mm (0.79 in.)
Vertical Res.	< 0.1 nm (0.004 µin)
Lateral Res.	0.36 to 9.5 µm; objective dependent
Data Scan Rate	≤26 µm/sec, user-selectable; camera and scan mode dependent
Maximum Data Points	307,200; camera dependent
RMS Repeatability	< 0.01 nm (0.0004 µin) RMSσ
Step Height	Accuracy ≤ 0.75% Repeatability ≤ 0.1% @ 1σ

Test Part Characteristics

Material	Various surfaces: opaque, transparent, coated, uncoated, specular, and nonspecular
Maximum Size (H x W x D)	3.5 x 8 x 8 in. (89 x 203 x 203 mm); larger sample sizes possible
Reflectivity	1-100%

Environmental Requirements

Temperature	15 to 30°C (59 to 86°F)
Rate of Temp. Change	<1.0°C per 15 min
Humidity	5 to 95% relative, noncondensing
Vibration Isolation	Required for vibration frequencies in the range of 1 Hz to 120 Hz

Utility Requirements

Input Voltage	100 to 240 VAC, 50/60 Hz
Compressed Air	60 to 80 psi (4.1 to 5.5 bar); dry and filtered source; 1/4 in. input

zygo

NewView 7200 Specifications

Interferometric Objective Specifications

Power	Type	Design	NA	WD (mm)	LRes (µm)	Turret Mount	Parfocal Dist (mm)	ZYGO P/N
1X	LWD	Michelson	0.03	8.3	9.50	No	122.8	6300-0316-01
1X	LWD	Michelson	0.03	8.3	9.50	Yes	122.8	6300-0318-01
1X	SLWD	Michelson	0.03	40.0	9.50	No	181.5	6300-0307-01
2X	LWD	Michelson	0.055	20.5	5.18	No	101.0	6300-0245-01
2.5X	STD	Michelson	0.075	10.3	3.80	Yes	80.1	6300-0592-01
2.5X	SLWD	Michelson	0.075	40.0	3.80	No	139.0	6300-0320-01
5X	STD	Michelson	0.13	9.3	2.19	Yes	56.5	6300-0593-01
5X	LWD	Michelson	0.14	20.5	2.04	No	101.0	6300-0249-01
5X	SLWD	Michelson	0.12	40.0	2.38	No	111.7	6300-0325-01
10X	STD	Mirau	0.30	7.4	0.95	Yes	56.5	6300-0194-01
10X	LWD	Michelson	0.28	18.8	1.02	No	125.1	6300-0263-01
20X	STD	Mirau	0.40	4.7	0.71	Yes	56.5	6300-0195-01
50X	STD	Mirau	0.55	3.4	0.52	Yes	56.5	6300-0597-01
100X	STD	Mirau	0.80	0.55	0.36	Yes	56.5	6300-0248-04

Specifications with Field Zoom Lens with standard 640x480 camera

Obj	with 0.5X ZOOM		with 0.75X ZOOM		with 1X ZOOM		with 1.5X ZOOM		with 2X ZOOM	
	HVFOV (mm)	Samp (µm)	HVFOV (mm)	Samp (µm)	HVFOV (mm)	Samp (µm)	HVFOV (mm)	Samp (µm)	HVFOV (mm)	Samp (µm)
1X	14.14 x 10.60	22.09	9.38 x 7.03	14.65	7.02 x 5.26	10.96	4.69 x 3.52	7.33	3.53 x 2.65	5.52
2.5X	5.65 x 4.24	8.84	3.75 x 2.81	5.86	2.81 x 2.10	4.39	1.88 x 1.41	2.93	1.41 x 1.06	2.21
5X	2.83 x 2.12	4.42	1.88 x 1.41	2.93	1.40 x 1.05	2.19	0.94 x 0.70	1.47	0.71 x 0.53	1.10
10X	1.41 x 1.06	2.21	0.94 x 0.70	1.47	0.70 x 0.53	1.10	0.47 x 0.35	0.73	0.35 x 0.27	0.55
20X	0.71 x 0.53	1.10	0.47 x 0.35	0.73	0.35 x 0.26	0.55	0.23 x 0.18	0.37	0.18 x 0.13	0.28
50X	0.28 x 0.21	0.44	0.19 x 0.14	0.29	0.14 x 0.11	0.22	0.09 x 0.07	0.15	0.07 x 0.05	0.11
100X	0.14 x 0.11	0.22	0.09 x 0.07	0.15	0.07 x 0.05	0.11	0.05 x 0.04	0.07	0.04 x 0.03	0.06

Specifications with Field Zoom Lens with optional 992x992 (1K) camera

Obj	with 0.5X ZOOM		with 0.75X ZOOM		with 1X ZOOM		with 1.5X ZOOM		with 2X ZOOM	
	HVFOV (mm)	Samp (µm)	HVFOV (mm)	Samp (µm)	HVFOV (mm)	Samp (µm)	HVFOV (mm)	Samp (µm)	HVFOV (mm)	Samp (µm)
1X	Ø21.91	22.09	14.54 x 14.54	14.65	10.88 x 10.88	10.96	7.27 x 7.27	7.33	5.48 x 5.48	5.52
2.5X	Ø8.77	8.84	5.81 x 5.81	5.86	4.35 x 4.35	4.39	2.91 x 2.91	2.93	2.19 x 2.19	2.21
5X	Ø4.38	4.42	2.91 x 2.91	2.93	2.18 x 2.18	2.19	1.45 x 1.45	1.47	1.10 x 1.10	1.10
10X	Ø2.19	2.21	1.45 x 1.45	1.47	1.09 x 1.09	1.10	0.73 x 0.73	0.73	0.55 x 0.55	0.55
20X	Ø1.10	1.10	0.73 x 0.73	0.73	0.54 x 0.54	0.55	0.36 x 0.36	0.37	0.27 x 0.27	0.28
50X	Ø0.44	0.44	0.29 x 0.29	0.29	0.22 x 0.22	0.22	0.15 x 0.15	0.15	0.11 x 0.11	0.11
100X	Ø0.22	0.22	0.15 x 0.15	0.15	0.11 x 0.11	0.11	0.07 x 0.07	0.07	0.05 x 0.05	0.06

Objective Terminology

Power Magnifying power of the objective.

Type STD=Standard Working Distance, LWD=Long Working Distance, SLWD=Super Long Working Distance; 50X objective is thermally compensated.

Design Interferometer type.

NA Numerical aperture, the sine of the half-angle of the objective acceptance cone.

WD Working distance, distance from the end of the objective to the test surface when focused.

LRes Lateral resolution, optical resolution of the imaging system. Sparrow Criteria = 0.5λ/NA, λ = 570 nm.

Turret Mount Indicates if objective can be turret mounted. No means single objective mount only.

Parfocal Dist Distance from the objective shoulder to the objective focal plane. Objectives with the same parfocal distance can be interchanged with little or no refocusing.

HVFOV Horizontal x Vertical Field of View. The size of imaged area of the test part, based on the camera size.

Samp Spatial sampling. Pixel size on the sample, based on the pixel size divided by the system magnification.

Specifications subject to change without prior notice.

zygo

ZYGO CORPORATION
LAUREL BROOK ROAD • MIDDLEFIELD, CT 06455
VOICE: 860 347-8506 • FAX: 860 346-4188
WWW.ZYGO.COM • EMAIL: Inquire@zygo.com

D. Laser power meters

a) OPHIR Nova II

Specifications	
Power Meter	High legibility 320 x 240 pixel graphics LCD with switchable electroluminescent backlight. Large 18mm digits. High resolution analog needle also can be chosen.
Features	Many screen features including power with bar graph, energy, average, exposure, frequency, graphs, scaling, special units, and more. Complete on line context sensitive help screens.
Outputs	USB, RS232 and 1, 2, 5 and 10 volt full scale analog output.
Screen Refresh	15 times/sec
Case	Molded high impact plastic with two level kickstand.
Size	Folds to a compact 208mm Lx 117mm Wx 40mm H
Battery	Rechargeable NiMH batteries with typically 18 hours between charges. The charger can be ordered from your local distributor. The charger also functions as an AC adapter.
Data Handling	Data can be viewed on board or transmitted to PC: On Board: Non volatile storage of up to 54000 data points in up to 10 files. Max data logging rate 4000 [a] points/s. Transmitted to PC: Data transmission rate of ~500 points/s. RS232 baud rate of 38400.
Sensor Features	Works with Thermopile, BeamTrack, Pyroelectric and Photodiode sensors. Automatic continuous background cancellation with PD300 sensors. Submicrojoule and multikilohertz capability with pulsed energy sensors.
Program Features	Preferred startup configuration can be set by user. User can recalibrate power, energy, response time and zero offset.
Notes: (a)	The above refers to the rate of logging every single point in turbo mode. Above that rate, the instrument will sample points but not log every single point.

b) OPHIR Vega

Specifications	
Power Meter	Brilliant color TFT 320 x 240 pixel graphics LCD. Large 16mm digits. High resolution analog needle also can be chosen.
Features	Many screen features including power with multicolor bar graph, energy, average, exposure, frequency, graphs, scaling, special units, and more. Complete on line context sensitive help screens.
Outputs	USB, RS232 and user selectable 1, 2, 5 and 10 Volt full scale analog output.
Screen Refresh	15 times/sec
Case	Molded high impact plastic with optimized angle two level kickstand. Rubberized sides for easy grip and protection against damage.
Size	Folds to a compact 208mm L x 117mm W x 40mm H
Battery	Rechargeable NiMH batteries with typically 18 hours between charges. The charger can be ordered from your local distributor. The charger also functions as an AC adapter.
Data Handling	Data can be viewed on board or transmitted to pc: On Board: Non volatile storage of up to 250,000 data points in up to 10 files. Max data logging rate 4000[a] points/s. Transmitted to PC: Data transmission rate of ~500 points/s. RS232 baud rate of 38400.
Sensor Features	Works with Thermopile, BeamTrack, Pyroelectric and Photodiode sensors. Automatic continuous background cancellation with PD300 sensors Submicrojoule and multikilohertz capability with pulsed energy sensors.
Program Features	Preferred start up configuration can be set by user. User can recalibrate power, energy, response time and zero offset.
Notes: (a)	The above refers to the rate of logging every single point in turbo mode. Above that rate, the instrument will sample points but not log every single point.

E. Thermal sensors

a) OPHIR 30A

Model	10A-P	30A-P-17	15(50)A-PF-DIF-18/ 50A-PF-DIF-18	30A-N-18
Use	**Short pulse to 10W**	**Short pulse to 30W**	**High energy density pulsed beams**	**High power density pulsed YAG**
Absorber Type	P type	P type	PF type + diffuser	N type
Spectral Range µm	0.15 - 8	0.15 - 8	0.24 - 2.2	0.532, 1.064
Aperture mm	φ 16mm	φ 17mm	φ 17.5mm	φ 17.5mm
Power Mode				
Power Range	40mW - 10W	60mW - 30W	140mW - 50W	60mW - 30W
Maximum Intermittent Power W	NA	NA	(for 15(50)A-PF-DIF-18 only) 50W for 5min, 15W continuous	NA
Power Scales	10W / 2W / 200mW and dBm	30W / 3W	50W / 5W	30W / 3W
Power Noise Level	2mW	3mW	7mW	3mW
Maximum Average Power Density kW/cm²	0.05	0.05	0.5	5
Response Time with Meter (0-95%) typ. s	3.5	2.5	2	2
Power Accuracy +/-%	3	3	5	3
Linearity with Power +/-%	1.5	1.5	1.5	1
Energy Mode				
Energy Range	10mJ - 10J	40mJ - 30J	60mJ - 200J	30mJ - 200J
Energy Scales	10J / 2J / 200mJ	30J / 3J	200J / 30J / 3J	200J / 30J / 3J
Minimum Energy mJ	10	40	60	30
Maximum Energy Density J/cm² (a)				
Pulse rate:	Single 10 - 30Hz	Single 10 - 30Hz	10 - 50Hz	10 - 50Hz
<1µs	10 1	10 1	4	1
0.5ms	10 1	10 1	15	20
5ms	10 1	10 1	50	>100
Cooling	convection	convection	convection	convection
Fiber Adapters Available (see page 63)	ST, FC, SMA, SC	ST, FC, SMA, SC	NA	ST, FC, SMA, SC
Weight kg	0.2	0.3	0.35	0.3
Version	V3			
Part number	**7Z02649**	**7Z02693**	**7Z02740/ 7Z02738**	**7Z02695**

Note: (a) For shorter wavelengths derate maximum energy density as follows:

Wavelength	Derate to value	Wavelength	Derate to value
1064nm	Not derated	1064nm	Not derated
532nm	Not derated	532nm	80% of stated value
355nm	40% of stated value	355nm	60% of stated value
266nm	10% of stated value	266nm	40% of stated value
193nm	10% of stated value	193nm	NA

b) OPHIR 12A-P

Model	12A	12A-P	
Use	**General purpose**	**Short pulses**	
Absorber Type	Broadband	P type	
Spectral Range µm	0.19 - 20	0.15 - 8	
Aperture mm	φ 16mm	φ 16mm	
Power Mode			
Power Range	2mW - 12W	2mW - 12W	
Power Scales	12W to 20mW	12W to 20mW	
Power Noise Level	50µW	50µW	
Thermal Drift (30min) (a)	40 - 150µW	40 - 150µW	
Maximum Average Power Density kW/cm²	25	0.05	
Response Time with Meter (0-95%) typ. s	2.5	3.5	
Power Accuracy +/-%	3	3	
Linearity with Power +/-%	1.5	1.5	
Energy Mode			
Energy Range	1mJ - 30J	1mJ - 30J	
Energy Scales (b)	30J to 30mJ	30J to 30mJ	
Minimum Energy mJ	1	1	
Maximum Energy Density J/cm² (c)			
Pulse rate:		Single	10 - 30Hz
<100ns	0.3	10	1
0.5ms	5	10	1
2ms	10	10	1
10ms	30	10	1
Cooling	convection	convection	
Fiber Adapters Available (see page 63)	ST, FC, SMA, SC	ST, FC, SMA, SC	
Weight kg	0.35	0.35	
Version	V1		
Part number	**7Z02638**	**7Z02624**	

Notes: (a) Depending on room airflow and temperature variations

Notes: (b) For the 30mJ energy scale measurements it is recommended to use the screw on barrel supplied with the sensor to protect from direct air flow

Note: (c) For P type and shorter wavelengths derate maximum energy density as follows:

Wavelength	Derate to value
1064nm	Not derated
532nm	Not derated
355nm	40% of stated value
266nm	10% of stated value
193nm	10% of stated value

F. NanoScan beam-profiler

The scanning slit beam profiler moves a narrow slit in front of a photo-detector through the beam under analysis. Light passing through the slit onto the detector creates a photo-induced current in the detector. The slit acts as a physical attenuator in the scanning slit beam profiler, and the amplification gain on the detector can be set to avoid detector saturation for most beam profiling. A digital encoder precisely measures slit position. The photo-induced current is then plotted as a function of slit position to determine a linear profile of the beam. From this linear profile, important spatial information such as beam width, beam position, beam quality, and other characteristics are determined. This technique can accommodate a wide variety of test conditions.

Because slit scanners measure beams at high powers with little or no attenuation, they are ideal to profile beams used in material processing. Carbon dioxide (CO_2) lasers are widely used in materials processing, and have a 10.6 micron wavelength that cannot be profiled with most cameras. Slit scanners, therefore, provide an convenient means of measuring high-resolution CO_2 lasers with powers up to and exceeding 1000 watts.

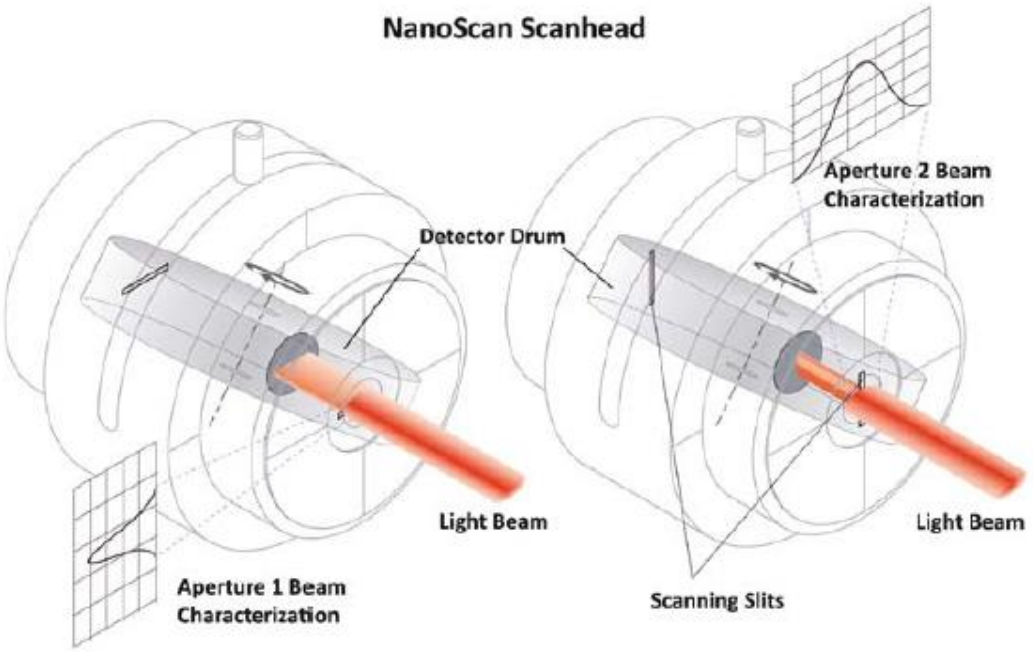

3.3.1 NanoScan

The most versatile and flexible beam profiling system available

Photon's NanoScan scanning slit profilers provide major performance enhancements while maintaining the ease-of-use and flexibility that customers have come to expect with its predecessor, the world-renowned BeamScan. NanoScan scanheads are available to measure CW and pulsed beams across the entire spectral range from UV to far infrared.

Capabilities

The NanoScan digital controller, available with USB2 interface, operates with the latest Microsoft operating systems, including 64-bit Windows 7, and provides deep, 12-bit digitization of the signal for enhanced dynamic range up to 35dB power optical. The digital controller improves the accuracy and stability of the beam profile measurement by orders of magnitude. It is now possible to measure beam size and beam pointing with a 3-sigma precision of several hundred nanometers. The software controllable scan speed and a "peak-connect" algorithm allow the measurement of pulsed and pulse width modulated lasers with frequencies of a few kHz and higher with any detector.* The ability to alter the drum speed also helps to increase the dynamic range allowing a much larger operating space for any given scanhead (see operating space charts for a graphic explanation).

- All NanoScan systems are calibrated to a NIST traceable source to ensure the ultimate in accuracy
- The software finds a beam in less than 0.3 seconds and displays real-time updates up to 20Hz. The efficient code uses minimal computer resources allowing for smooth integration into automated test equipment via the ActiveX server.
- The Z-axis datum plane of the NanoScan is known to ±25µm making the locating of beam waist position simple and accurate.
- Along with the ability to measure pulsed beams' diameters, the NanoScan accurately measures and reports the pulse frequency of the laser, ensuring that the pulsed beam measurements are stable and accurate.
- The sampling interval for beam measurements is adjustable to as little as 5.7nm, providing the extreme accuracy required to measure very small beams.
- Profile averaging and rolling averages are available to clean up noisy profiles.
- NanoScan software has built in capability to control a mechanical linear stage for automated measurement of beam caustic.
- Software has a built-in M^2 Wizard to assist in making manual propagation ratio measurements
- Time statistics allow any ISO beam parameter to be charted over time.
- ActiveX Automation commands included as standard in the software with samples of automation programs for Excel VBA, LabView and Visual Basic.net
- Data logging to files or COM ports available

*** The minimum frequency is a function of the beam size and the scan speed. This is a simple arithmetic relationship; there must be a sufficient number of pulses during the time that the slits sweep through the beam to generate a meaningful profile. Please refer to Photon's Application Note, Measuring Pulsed Beams with a Slit-Based Profiler.**

Multiple Beam Analysis Software

In addition to the hardware, the NanoScan has an integrated software package for Microsoft Windows operating systems, which can measure from one to 16 beams in the NanoScan aperture, all with sub-micron precision. The software includes ActiveX automation for users who want to integrate the NanoScan into OEM systems or write their own user interface screens.

Optional Power Meter

The silicon and germanium NanoScan systems offer the 200mW or the more accurate 75mW power meter as options. The power meter can be calibrated against the user's ISO- or NIST- traceable power meter. The 200mW power meter has a quartz attenuator window that provides a uniform response across a broad wavelength range with a 1.5% accuracy when used in the same geometry as calibrated. The P75 uses a more uniform Kodak Wratten filter that provides better than 1% accuracy, but it has an upper power limit of 75mW and must be supplied for a specific wavelength of use.
The power meter screen in the software shows both the total power and the individual power in each of the beams being measured. The power meter option is not available with pyroelectric detectors due to the broad range of power levels and wavelengths encountered with these scanheads.

M^2 Wizard

M-squared (M^2) software Wizard is included in NanoScan Analysis and Acquisition Software 1.2 and above, and is discussed in the M^2 section of the catalog.

Available Detectors

The NanoScan is available with silicon, germanium and pyroelectric detectors to cover the light spectrum from UV to far infrared beyond 100µm. The scanheads are available in several sizes, apertures and slit dimensions.

Features

- Sub-micron precision for position and beam size
- Easy-to-use integrated software package
- Single and multiple beam analysis standard in one software package
- Software controllable scan speed (update rate)
- Peak-connect algorithm for pulsed beam measurement
- USB2 interface and digital head control
- 12-bit digitization of signal
- ActiveX automation for communication with other software packages
- Optional power meter with silicon and germanium scanheads
- Silicon, germanium, and pyroelectric detectors available

Benefits

- Laser beam XY position measurement uncertainty better than 300nm
- Beam size measurement precision to better than 0.5%
- High dynamic range (~35dB$_{power}$)
- Low instrument noise/jitter
- Precise knowledge of components' beam configuration possible to allow precise component assembly
- OEM automation integration capability
- Simple, intuitive software GUI for minimal learning curve
- Flexibility to control more head parameters increases range of operation
- Low-power pulsed beams can be measured
- Many high-power beams can be measured at focus without attenuation

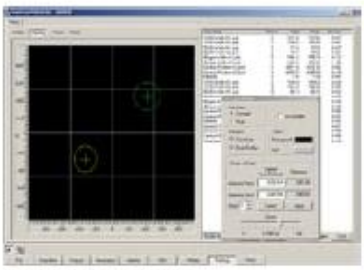

NanoScan Pointing Screen

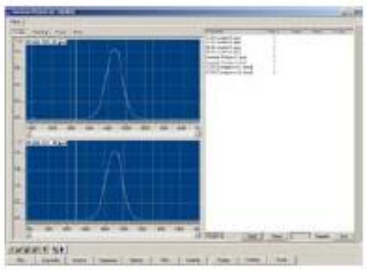

NanoScan Dual Profile and Statistics

Power Window

NanoScan Configurations

Detector Type	Power Range	Wavelength	Aperture	Slits	Scanhead Size
Silicon	~100nW–~100mW	190nm-1000nm	3.5mm	1.8µm	63mm
				1.0µm	
			9mm	5µm	63mm
				25µm	
			25mm	25µm	100mm
Germanium	~1µW–~100mW	700nm-1800nm	3.5mm	1.8µm	63mm
				1.0µm	
			9mm	5µm	63mm
				25µm	
			25mm	25µm	100mm
Pyroelectric	100mW-100W	190nm- >100µm	9mm	5µm	63mm

Minimum Beam Size per Pulse Frequency

NanoScan	Normal Drum					Large Drum (HP)			
Rotation Rate (Hz)	1.25	2.50	5.00	10.00	20	1.25	2.50	5.00	10.00
Slit Speed (µm/msec)	116.63	233.25	466.50	933.01	1866.01	233.25	466.50	933.01	1866.01
Data Points per Profile	15	15	15	15	15	15	15	15	15
Pulse Frequency (kHz)	**Minimum Beam Diameter in µm**					**Minimum Beam Diameter in µm**			
0.5	3499	6998	N/A	N/A	N/A	6998	13995	N/A	N/A
1	1749	3499	6998	N/A	N/A	3499	6998	13995	N/A
2	875	1749	3499	6998	N/A	1749	3499	6998	13995
3	583	1166	2333	4665	N/A	1166	2333	4665	9330
4	437	875	1749	3499	6998	875	1749	3499	6998
5	350	700	1400	2799	5598	700	1400	2799	5598
6	292	583	1166	2333	4665	583	1166	2333	4665
7	250	500	1000	1999	3999	500	1000	1999	3999
8	219	437	875	1749	3499	437	875	1749	3499
9	194	389	778	1555	3110	389	778	1555	3110
10	175	350	700	1400	2799	350	700	1400	2799
11	159	318	636	1272	2545	318	636	1272	2545
12	146	292	583	1166	2333	292	583	1166	2333
13	135	269	538	1077	2153	269	538	1077	2153
14	125	250	500	1000	1999	250	500	1000	1999
15	117	233	467	933	1866	233	467	933	1866
16	109	219	437	875	1749	219	437	875	1749
17	103	206	412	823	1646	206	412	823	1646
18	97	194	389	778	1555	194	389	778	1555
19	92	184	368	737	1473	184	368	737	1473
20	87	175	350	700	1400	175	350	700	1400
21	83	167	333	666	1333	167	333	666	1333
22	80	159	318	636	1272	159	318	636	1272
23	76	152	304	608	1217	152	304	608	1217
24	73	146	292	583	1166	146	292	583	1166
25	70	140	280	560	1120	140	280	560	1120
50	35	70	140	280	560	70	140	280	560
100	17	35	70	140	280	35	70	140	280
150	12	23	47	93	187	23	47	93	187

G. Multimode fiber TEQS™ coated

Fiber Optics

0.22 NA TEQS™ Coated Silica/Silica Multimode Fiber

FG Silica/Silica Multimode Fibers

Features of Silica/Silica Fiber Construction

- Stability of Silica Cladding Allows for High-Power Handling Capability
- Low-Index Fluorine-Doped Silica Cladding Design Provides Superior UV and Near-IR Transmission
- Secondary Hard Cladding (TEQS) Provides a Dual-Waveguide Design, Resulting in Improved Bend Performance
- Strong Bonding of Silica to (TEQS) Cladding Prevents Pistoning and Provides More Stable Terminations

No Minimums

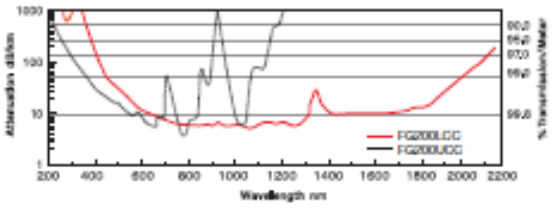

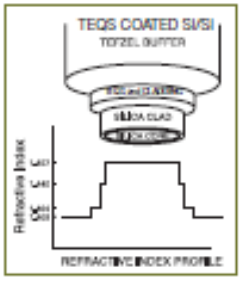

Visible to Near-IR Transmission (Low OH)

ITEM#	CORE DIAMETER	CLADDING DIAMETER	BUFFER DIAMETER	COATING DIAMETER	NUMERICAL APERATURE	MAXIMUM POWER CAPABILITY PULSED[1]	MAXIMUM POWER CAPABILITY CW[2]	MAXIMUM CORE OFFSET	BEND RADIUS SHORT TERM / LONG TERM	STRIPPING TOOL SEE PAGE 1050
FG200LCC	200±8µm	240±5µm	260±6µm	400±30µm	0.22±0.02	1.0MW	0.2kW	5µm	9mm/18mm	T12S18
FG273LEC	273±10µm	300±6µm	325±10µm	430±30µm	0.22±0.02	2.0MW	0.4kW	6µm	12mm/24mm	T12S18
FG365LEC	365±14µm	400±8µm	425±10µm	730±30µm	0.22±0.02	3.4MW	0.7kW	7µm	16mm/32mm	T21S31
FG550LEC	550±19µm	600±15µm	630±30µm	1040±30µm	0.22±0.02	7.6MW	1.5kW	9µm	25mm/50mm	T28S46

1) Based on 5GW/cm² for 1064nm Nd:YAG laser with 10nsec pulse length and input spot size equal to 80% of the core diameter
2) Based on 1MW/cm² for 1064nm Nd:YAG laser and input spot size equal to 80% of the core diameter

Price Schedule

ITEM#	$ 1-9m	$ 10-49m	$ 50-249m	£ 1-9m	£ 10-49m	£ 50-249m	€ 1-9m	€ 10-49m	€ 50-249m	RMB 1-9m	RMB 10-49m	RMB 50-249m
FG200LCC	$ 8.50	$ 6.90	$ 5.40	£ 5.35	£ 4.35	£ 3.40	€ 7,90	€ 6,40	€ 5,00	¥ 81.20	¥ 65.90	¥ 51.55
FG273LEC	$ 11.80	$ 9.70	$ 7.55	£ 7.45	£ 6.10	£ 4.75	€ 10,95	€ 9,00	€ 7,00	¥ 112.70	¥ 92.65	¥ 72.10
FG365LEC	$ 22.60	$ 18.50	$ 14.35	£ 14.25	£ 11.65	£ 9.05	€ 21,00	€ 17,20	€ 13,35	¥ 215.35	¥ 176.70	¥ 137.05
FG550LEC	$ 38.90	$ 31.75	$ 24.80	£ 24.50	£ 20.00	£ 15.60	€ 36,20	€ 29,55	€ 23,05	¥ 371.50	¥ 303.20	¥ 236.85

Call For Quantities Over 250m

UV to Visible Transmission (High OH)

ITEM#	CORE DIAMETER	CLADDING DIAMETER	BUFFER DIAMETER	COATING DIAMETER	NUMERICAL APERATURE	MAXIMUM POWER CAPABILITY PULSED	MAXIMUM POWER CAPABILITY CW	MAXIMUM CORE OFFSET	BEND RADIUS SHORT TERM / LONG TERM	STRIPPING TOOL SEE PAGE 1050
FG200UCC	200±8µm	240±5µm	260±6µm	400±30µm	0.22±0.02	1.0MW	0.2kW	5µm	9mm/18mm	T12S18
FG365UEC	365±14µm	400±8µm	425±10µm	730±30µm	0.22±0.02	3.4MW	0.7kW	7µm	12mm/24mm	T21S31
FG550UEC	550±19µm	600±15µm	630±30µm	1040±30µm	0.22±0.02	7.6MW	1.5kW	9µm	25mm/50mm	T28S46

Price Schedule

ITEM#	$ 1-9m	$ 10-49m	$ 50-249m	£ 1-9m	£ 10-49m	£ 50-249m	€ 1-9m	€ 10-49m	€ 50-249m	RMB 1-9m	RMB 10-49m	RMB 50-249m
FG200UCC	$ 9.40	$ 7.65	$ 5.90	£ 5.90	£ 4.80	£ 3.70	€ 8,75	€ 7,10	€ 5,50	¥ 89.75	¥ 73.05	¥ 56.35
FG365UEC	$ 22.60	$ 18.50	$ 14.35	£ 14.25	£ 11.65	£ 9.05	€ 21,00	€ 17,20	€ 13,35	¥ 215.85	¥ 176.70	¥ 137.05
FG550UEC	$ 33.20	$ 29.80	$ 23.20	£ 20.90	£ 18.75	£ 14.60	€ 30,90	€ 27,70	€ 21,60	¥ 317.05	¥ 284.60	¥ 221.55

Call For Quantities Over 250m

References

[1] E. C. Le Ru and P. G. Etchegoin, "Appendix H - Mie theory and its implementation," in *Principles of Surface Enhanced Raman Spectroscopy and related plasmonic effects*, ed Amsterdam: Elsevier, 2009, pp. 589-628.

[2] C. F. Bohren and D. R. Huffman, *Absorption and Scattering of Light by Small Particles*. New York: John Wiley & Sons, 1983.

[3] C. H. Li, G. W. Kattawar, P. W. Zhai, and P. Yang, "Electric and magnetic energy density distributions inside and outside dielectric particles illuminated by a plane electromagnetic wave," *Optics Express,* vol. 13, pp. 4554-4559, Jun 13 2005.

[4] S. Humphries, *Finite-element Methods for Electromagnetics*. Alburquerque: Field Precision LLC, 2010.

RÉSUMÉ

1. Introduction

La gravure de matériaux à l'échelle du micromètre peut aujourd'hui être réalisée par de nombreuses techniques. La photolithographie est une technique à base de masquage, nécessitant une étape chimique de gravure. Elle est adaptée à la réalisation de gravures, toujours similaires, sur un grand nombre de pièces. Les techniques à base de lasers de puissance pulsés ultra-brefs, comme les lasers pico ou femto-secondes permettent, elles, la gravure directe de motifs micrométriques uniques sur un faible nombre de pièces. Elles nécessitent cependant des sources onéreuses non encore compatibles avec les exigences de coût de la plupart des applications industrielles. Les sources laser plus classiques sont, elles, limitées par la diffraction de leur optique de focalisation à des gravures de plusieurs dizaines de microns de diamètre. Dans ce contexte, l'objectif de la thèse était d'étudier la capacité de concentrer des faisceaux au-delà de la limite de diffraction en champ proche de microbilles diélectriques pour de telles applications, faisceaux concentrés qualifiés de jet photonique (JP dans la suite). Les sources que nous avons considérées dans ce travail sont des lasers proches infrarouges pulsés nanosecondes car ces sources, moins chères, existent sous forme packagées et sont déjà très utilisées dans l'industrie (marquage, soudure, etc.). Ces lasers sont capables de graver à une résolution voisine de 50 microns des matériaux tels que le silicium. Dans un premier temps, à l'aide de JP généré par des microbilles de verre, nous avons montré la possibilité de réduire considérablement leur résolution de gravure sur du silicium. Ensuite, sur la base des hautes densités de puissance obtenues, nous avons montré que ces lasers qui usuellement ne peuvent pas graver le verre en raison de sa trop faible absorption en proche infrarouge, étaient capables de le faire grâce aux JP. Enfin, nous avons montré que de telles gravures pouvaient être réalisées par des JP obtenus en sortie de fibre optique. Le fait d'obtenir un JP en sortie d'une fibre optique avec un embout façonné est une première, mais c'est surtout une technique beaucoup

plus adaptée à la mise en œuvre d'un procédé de gravure laser réaliste que celle utilisant une microbille.

2. Jet photonique

Concentration de faisceau et limite de diffraction

Un des premiers articles ayant proposé une technique de lithographie en utilisant des sphères pour concentrer le faisceau laser a été publié en 2000 [1]. Le concept de jet photonique n'était pas apparu. Une gravure sub-longueur d'onde avait été réalisée sur du silicium cristallin avec un laser UV nanoseconde concentré par des sphères de silice de 500 nm. Le concept de jet photonique, également nommé nanojet photonique, fut défini en 2004 par l'équipe de Allen Taflove [2]. Il s'agit d'un faisceau propagatif concentré sur une largeur inférieure à une demi-longueur d'onde et obtenu juste à l'arrière d'un cylindre ou sphère diélectrique de quelques microns (fig. 1) [3]. Le point de plus forte densité de puissance est idéalement en surface de la particule diélectrique. Sa résolution outrepasse la limite de diffraction mais n'est pas basée sur la physique des ondes évanescentes. Il ne s'agit pas non plus d'un phénomène résonant. Le faisceau peut rester avec une largeur plus petite que la longueur d'onde sur une distance allant de quelques longueurs d'onde jusqu'à plusieurs dizaines. La densité de puissance peut être augmentée d'un facteur supérieur à 200. C'est cette forte concentration de la puissance incidente sur une zone de largeur inférieure à la longueur d'onde qui nous a amené à considérer l'intérêt des JP pour la micro-gravure laser directe.

Observation des jets photoniques et possibles applications

Après leur mise en évidence théorique, les JP ont pu être observés directement d'abord dans le domaine hyperfréquence à l'aide d'une antenne localisée dans la paroi d'un guide d'onde planaire [3], puis dans le domaine visible à l'aide d'un microscope confocal [4]. Leur mise en évidence a également été faite de façon indirecte en mesurant la taille de gravures induites ou l'amplification de la rétrodiffusion occasionnée par le passage d'une particule métallique nanométrique dans le JP [4,6]. Les JP ont été considérés pour de nombreuses applications : microscopie à forte résolution [2,7], amplification de fluorescence (Raman [8], absorption à deux-photons [9], étude de la fluorescence de molécule unique [9]), détection de nanoparticules [4,6], mémoires optiques à haute densité [11], chirurgie laser [12], etc. L'application que nous avons considérée est celle de gravure par laser. Des travaux ont déjà été menés considérant des sources pulsées ultra-brèves [13] ou des sources UV [14]. Nous avons considéré des sources infrarouges nanosecondes pour leur intérêt décrit plus haut.

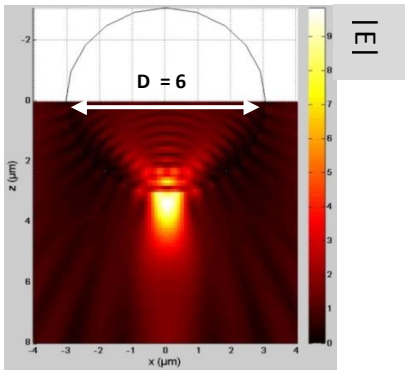

Figure 1 : jet photonique simulé derrière une sphère de verre 6 µm. Concentration x10 en champ, x100 en intensité. λ = 1 µm.

3. Gravure par jet photonique à l'aide de microsphères

La première méthode considérée pour générer des jets photoniques est celle bien connue utilisant des microsphères. Notre objectif a été d'abord de comprendre l'interaction JP-matière. Pour un faisceau donné et une sphère diélectrique donnée, la cartographie de champ obtenue peut être calculée rigoureusement par la théorie de Mie. L'observation des marques laissées dans la matière sur laquelle reposent les billes nous donne donc une information sur cette interaction JP-matière. Le second objectif a été de déterminer les paramètres d'un jet photonique qui permettent de graver au mieux (en particulier, le plus petit possible) le matériau considéré.

Montage expérimental

Le montage réalisé est assez proche de ce que l'on rencontre dans la littérature [1]. Ces deux différences distinctives sont :

- l'utilisation de sources laser nanoseconde proche infrarouge là où la littérature considère généralement des lasers UV ou des lasers à impulsions ultra brèves. Le premier laser considéré est un laser à Nd :YAG (λ = 1064 nm) produisant des impulsions de 28 ns à 20 kHz à une puissance moyenne max de 5 W.
- l'illumination des microsphères sur l'échantillon à graver par un faisceau laser défocalisé ; le but recherché est de couvrir un carré de plusieurs centaines de microns de côté pour illuminer de nombreuses billes et ainsi avoir une notion statistique sur la taille des gravures et observer l'influence du profil d'intensité gaussien.

Fig. 2a schématise le montage avec un faisceau laser défocalisé illuminant des microbilles posées sur le matériau à graver.

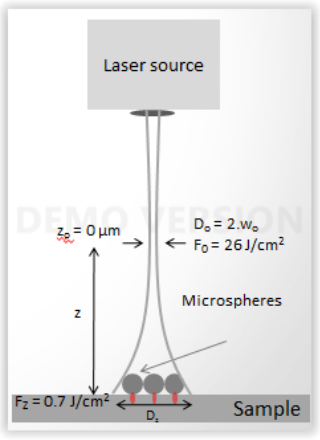

a.

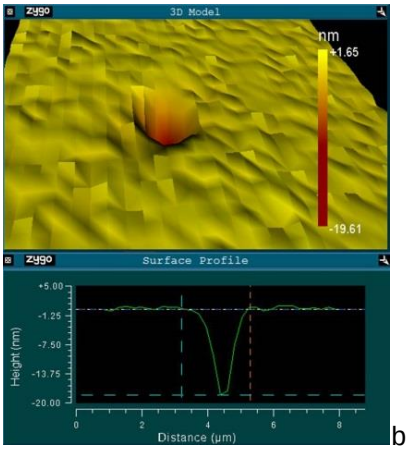

b.

Figure 2. (a) Montage expérimental pour la gravure par JP à l'aide de microsphères (b) Profil d'une gravure typique réalisée dans un wafer de silicum wafer à l'aide de microsphères de verre de 6 µm. Fluence sur les billes : 0,7 J/cm². Fluence calculée au niveau du jet photonique : 71/cm².

Pour étudier l'influence de la taille et de l'indice des billes, nous avons utilisé des billes de verre (indice n_s = 1.5, diamètre moyen D_s = 4, 6, 24 et 35 µm), et des billes de titanate de baryum (indice n_s=1.9, diamètre moyen D_s= 42, 69 et

87 µm). Des marques ont été faites préalablement sur les matériaux à graver pour faciliter la localisation des sphères. Sur silicium, ces marques ont été gravées avec le faisceau laser focalisé. Sur verre, les zones ont été marquées par retrait au laser d'une couche d'encre préalablement déposée. Les paramètres du laser que nous avons fait varier sont la puissance moyenne, la fréquence de répétition, le nombre d'impulsions et la distance de défocalisation (*z* sur la figure). Les gravures réalisées par JP ont été observées et mesurées à l'aide d'un microscope Olympus® Vanox-T et d'un profilomètre optique Zygo NewView®.

Gravures par JP d'un wafer de silicium

Les premiers tests de gravure par JP sur silicium ont été réalisés avec des billes de verre. Des gravures ont été observées à partir de la 2^{ième} impulsion laser (fig. 2b). Les plus petites gravures observées ont une taille de 1.1 ± 0.2 µm de moyenne et ont été obtenues avec des sphères de verre de 4 µm avec 2 impulsions de 1 mJ chacune, d'un laser Nd :YAG, (impulsions de 28 ns), défocalisé de manière à éclairer les sphères avec une fluence de 0,7 J/cm². Cette gravure à l'échelle du micron est 44 fois plus petite que celle obtenue par une gravure directe, sans sphère au point focal du laser.

L'utilisation de sphères plus larges augmente la taille des gravures, ce qui peut s'expliquer par un éloignement du JP de la surface de la sphère et donc de celle du matériau à graver, ainsi que par l'augmentation de la densité de puissance obtenue. Pour compenser cet éloignement, nous avons testé des sphères de Titanate de Baryum d'indice plus élevé. Mais dans ce cas, l'indice trop élevé a conduit à une focalisation à l'intérieur des billes et à leur destruction.

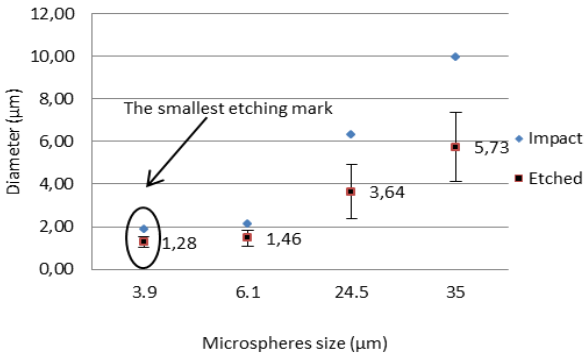

Figure 3 : Diamètre des gravures obtenues sur silicum en fonction du diamètre des billes de verres utilisées. Fluence incidente 0,7 J/cm². « Etched » : diamètre de la gravue centrale. « Impact » : taille globale de l'impact.

Gravure par JP d'une lame de verre de microscope

Malgré la très faible absorption du verre en proche infrarouge des gravures ont été réalisées mais avec des billes de verre de diamètre plus grand (24 et 35 µm). L'utilisation de billes plus larges permet d'atteindre des densités de puissance plus élevées (123 J/cm² en surface du verre sous une bille de 24 µm de diamètre) nécessaires pour atteindre le seuil d'ablation du verre. Les gravures ont des formes différentes de celles sur silicium. Elles sont faites d'un cratère central entouré d'anneaux (fig. 4a). Les plus petits cratères centraux font 1,5 ± 0,4 µm avec une zone impactée de 4,4 ± 0,5 µm et sont obtenus avec les billes de verre de 24 µm.

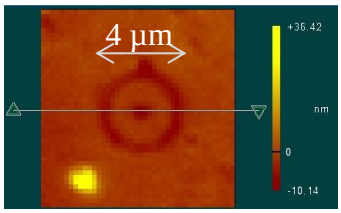

(a)

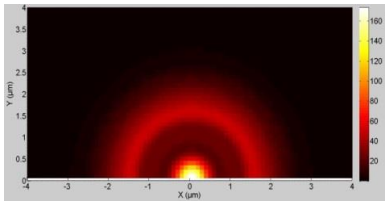

(b)

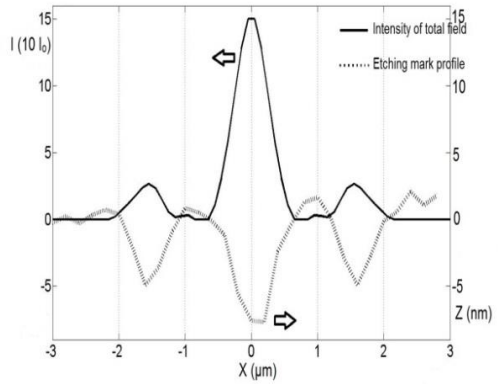

(c)

Figure 4. (a) Profil d'une gravure par JP sur du verre mesuré avec le microscope interférométrique Zygo®. (b) Distribution d'intensité $|E|^2$ calculée sur la surface de la lame de verre (ua). (c) Correspondance entre profil de la gravure et distribution de champ calculée |E|.

La forme des gravures n'est pas la même sur le silicium que sur le verre ; cela vient du fait que des billes plus larges ont dû être utilisées pour graver le verre. Dans ce cas le JP n'est plus en surface du matériau à graver mais plus en profondeur. Or l'ablation s'effectue en surface dans une zone où la densité de puissance a une cartographie plus complexe. Nous l'avons simulée, le résultat est montré sur la figure 4b. La figure 4c montre la bonne correspondance entre la cartographie du champ calculé et le profil d'intensité mesuré.

Discussion

Plusieurs autres résultats sont à souligner :

- Deux impulsions sont nécessaires pour faire la première gravure. La raison est que l'interaction se fait généralement légèrement sous le seuil d'ablation. La première impulsion crée des défauts qui contribuent à baisser ce seuil et permettent à la deuxième impulsion de graver.

- Nous constatons que la profondeur de gravure moyenne n'augmente pas avec le nombre d'impulsions. Ceci semble dû au fait qu'après la première gravure, la matière arrachée se dépose sur la bille empêchant, pour les impulsions suivantes, la création de jet photonique. C'est une limitation forte.

- Avec l'augmentation de la taille des billes, l'augmentation associée de la densité de puissance et donc de l'ablation de la matière peut causer un déplacement des billes. Ce phénomène n'intervient que pour les billes de diamètre supérieur à 40 µm. Toutes les dimensions données dans la thèse le sont toujours pour des gravures dont la position est corrélée à celle d'une bille avant, mais aussi après la gravure.

4. Gravure par JP à l'aide de fibre optique à embout sphérique

Des travaux préliminaires de notre équipe, en collaboration avec le LT2C à Saint-Etienne avaient permis de montrer que des JPs pouvaient également être obtenus en sortie de guide d'onde planaire à bords parfaitement conducteurs. La démonstration expérimentale avait été faite en radiofréquence. Sur cette base, nous avons considéré dans cette thèse la possibilité d'obtenir un jet photonique en sortie d'une fibre optique. Ceci a été motivé par la volonté de répondre aux principales limitations que nos travaux sur les microbilles ont mises en lumière :

- Une fibre optique peut être déplacée à souhait pour graver des motifs complexes et non pas juste faire une gravure ponctuelle comme une sphère posée sur l'échantillon.
- Avec une fibre optique, il est possible de contrôler la distance entre l'embout de la fibre et l'échantillon à graver. Le JP n'est donc plus limité à l'embout de la fibre. En outre, cette distance entre la fibre et le matériau permet d'envisager qu'après une gravure, l'embout ne soit pas pollué par la matière ablatée et puisse être réutilisé pour d'autres gravures.

A notre connaissance, l'obtention de JP en embout de fibre optique pleine à embout façonné, ainsi que leur utilisation pour de la gravure est une première.

Jet photonique en sortie de guide d'onde

Pour permettre l'injection d'un laser de puissance dans la fibre, des fibres multimodes de diamètre de cœur de 100 µm et 200 µm ont été considérées. Plusieurs formes d'embouts ont également été étudiées. Nous présentons ici le résultat d'une fibre optique en silice de 100 µm de cœur, une ouverture numérique 0,22 et avec un embout sphérique, résultats finaux obtenus avec la contribution de Julien Zelgowski. La cartographie de champ en sortie d'un guide 2D planaire est représentée Fig. 5a pour une onde incidente de maximum unité. La simulation est faite sur un modèle 2D afin de permettre la simulation par une méthode élément fini. On constate l'apparition d'un jet photonique à une distance de 100 µm de l'embout. Un embout plus pointu permettrait d'avoir un jet photonique plus concentré et proche de l'embout mais rendrait l'embout plus vulnérable. La figure 5b montre l'embout réel réalisé par la société Lovalite.

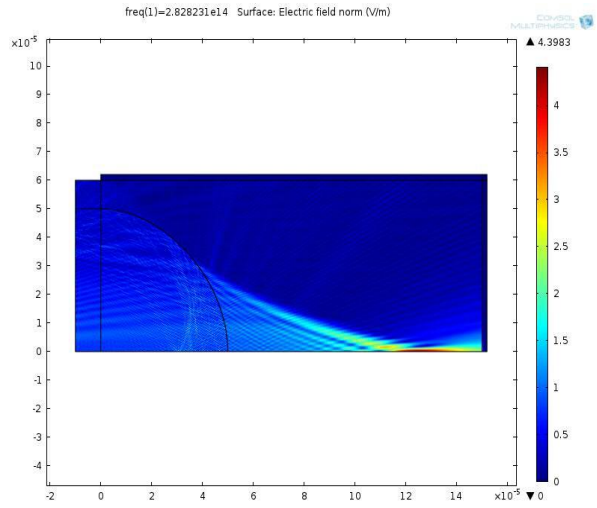

A

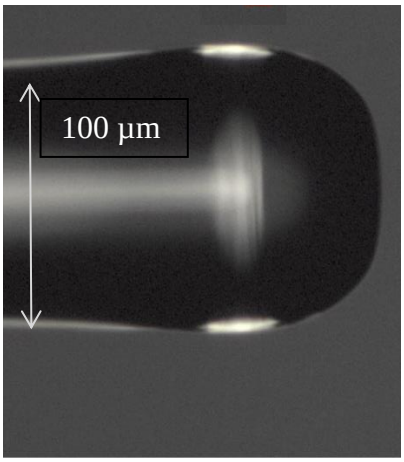

B

Figure 5. (a) Champ électrique en sortie d'un guide d'onde diélectrique planaire de 100 µm de cœur avec son embout sphérique. L'axe des *x* est un axe de symétrie. (b) Vue au microscope de la fibre correspondante réalisée pour effectuer les gravures.

Résultats expérimentaux

Des tests de gravure ont été effectués sur un wafer de silicium. Trois platines de translation micrométriques ont été utilisées pour ajuster la position de la fibre par rapport à l'échantillon. La figure 6a montre des exemples de gravures fonction de la puissance injectée dans la fibre (200 µm ici) et du nombre d'impulsions. Le nombre d'impulsions permet désormais de modifier la nature de la gravure, prouvant ainsi que l'embout n'est pas détérioré après avoir gravé. La figure 6b montre les plus petites gravures réalisées. Elles ont un diamètre de l'ordre du micron et ont été gravées en sortie de la fibre de 100 µm. La distance de focalisation trouvée, de l'ordre de 100 µm, est en accord avec les simulations.

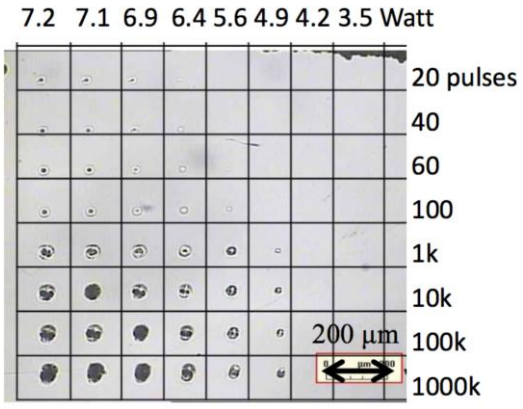

a

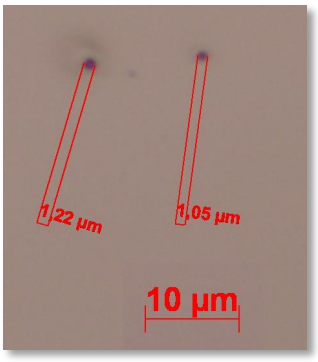

b

Figure 6. (a) Vue au microscope de gravures obtenues en sortie de la fibre optique en silice de 200 µm de cœur fonction de la puissance injectée et du nombre d'impulsions. (b) Vue des plus petites gravures réalisées avec la fibre en silice de 100 µm de cœur (35 impulsions, 7,2 W).

Discussion

Nos premières gravures avec la fibre de 200 µm avaient des diamètres plus grands de l'ordre de la dizaine de micron. Cela était dû à deux raisons. La première, simple à comprendre, était que la puissance injectée était trop grande. La gravure est la plus petite lorsque la densité de puissance maximale est juste au-dessus du seuil d'ablation. La deuxième raison est que, dans nos premières simulations, comme celle montrée sur la figure 5a avec la fibre de 100 µm, nous n'avions considéré qu'une excitation du premier mode. Or nos fibres sont multimodes et le contrôle de l'excitation des modes à l'injection est difficile. Nous avons donc simulé la contribution des modes d'ordres supérieurs et avons constaté qu'ils étaient focalisés hors axes (en anneaux) et ce d'autant plus que l'ouverture numérique de la fibre est grande. Par chance, plus un mode est d'ordre élevé, moins la puissance injectée le concernant est grande et plus la surface irradiée est grande. Les densités de puissances ainsi obtenues hors axes sont donc faibles et possiblement en-dessous du seuil d'ablation, permettant de graver à l'échelle du micron, comme sur la figure 6b.

Pour réduire encore la taille de gravure ou améliorer leur qualité, des fibres avec une plus faible ouverture numérique seraient souhaitables afin de réduire la focalisation hors axe des modes d'ordres supérieurs. Des fibres monomodes à large cœur pourraient être également considérées. Mais avec un cœur plus petit, il sera, d'une part, plus difficile de façonner l'embout et, d'autre part, le JP obtenu risque d'être plus près de la fibre et de l'endommager lors de gravures.

5. Conclusions et perspectives

Ce travail de thèse a permis de montrer que la résolution latérale de gravure de lasers proches infrarouges nanosecondes pouvait être réduite en faisant passer le faisceau à travers des microbilles de verre ou des fibres de silice à embouts façonnés de telle manière à générer des jets photoniques. Sur du silicium la taille de gravure peut être réduite d'un facteur 44 comparée à celle d'une gravure directe sans jet photonique. Les densités de puissances atteintes permettent même d'envisager de graver le verre avec ce type de laser malgré sa très faible absorption à ces longueurs d'onde.

Pour la première fois nous avons montré la possibilité d'obtenir des jets photoniques en sortie de fibre optique à embout façonné. Nous avons montré leur capacité à graver le silicium à l'échelle du micron et ce avec un laser proche infrarouge nanoseconde. La possible utilisation de fibres optiques est une condition clairement décisive à la réalisation d'un réel procédé laser capable de graver des motifs complexes et de façon répétée.

Publications

1. "Photonic jet out of optical fiber: potential for laser with matter interaction", S. Lecler, **A. Abdurrochman**, J. Zelgowski, F. Mermet, B. Tumbelaka and J. Fontaine, Applied Surface Science (Submitted).
2. "Photonic jet breakthrough for direct laser micro-processing using near-IR nanosecond laser", **A. Abdurrochman**, S. Lecler, F. Mermet,

B.Tumbelaka, B. Serio and J. Fontaine, **Applied Optics**, vol. 53, pp. 7202-7207, October 2014.

Communications

1. “Photonic jet etching: justifying the shape of optical fiber tip”, **A. Abdurrochman**, J. Zelgowski, S. Lecler, F. Mermet, B. Tumbelaka and J. Fontaine, **The PIPS 2015** (Padjadjaran International Physics Symposium), Bandung – Indonesia, 2-3 September 2015.
2. “Photonic jet out of optical fiber: potential for laser with matter interaction”, S. Lecler, **A. Abdurrochman**, J. Zelgowski, F. Mermet, B. Tumbelaka and J. Fontaine, **The 2015 E-MRS Spring Meeting**, Lille – France, 11-15 May, 2015.
3. “Photonic jets for micro-etching”, **A. Abdurrochman**, S. Lecler, F. Mermet, J. Fontaine, and B. Tumbelaka, **International Conference on Physics**, Yogyakarta – Indonesia , 25-26 August, 2014.
4. “Photonic jet to improve the lateral resolution of laser etching”, **A. Abdurrochman**, S. Lecler, J. Fontaine, F. Mermet, P. Meyrueis, B. Tumbelaka and P. Montgomery, **SPIE-Photonics Europe 2014**, Brussel – Belgium, 14-17 April, 2014.
5. “Increasing the lateral resolution of direct laser surface micro-processing using photonic jet”, **A. Abdurrochman**, S. Lecler, F. Mermet, B.Y. Tumbelaka, P. Meyrueis and J. Fontaine, **JNTE 2013** (Journée Nationale des Technologies Emergentes en micro et nano fabrication), Evian-les-Bains – France, 21-23 May 2013.

Bibliographie

[1] Y. F. Lu, L. Zhang, W. D. Song, Y. W. Zheng, and B. S. Luk’yanchuk, "Laser writing of a subwavelength structure on silicon (100) surfaces with particle-enhanced optical irradiation," Journal of Experimental and Theoretical Physics Letters, vol. 72, pp. 457-459, 2000.

[2] Z. G. Chen, A. Taflove, and V. Backman, "Photonic nanojet enhancement of backscattering of light by nanoparticles: a potential novel visible-light ultramicroscopy technique," Optics Express, vol. 12, pp. 1214-1220, 2004.

[3] S. Lecler, Y. Takakura, and P. Meyrueis, "Properties of a three-dimensional photonic jet," Optics Letters, vol. 30, pp. 2641-2643, 2005.

[4] L. Zhao and C. K. Ong, "Direct observation of photonic jets and corresponding backscattering enhancement at microwave frequencies," Journal of Applied Physics, vol. 105, 2009.

[5] P. Ferrand, J. Wenger, A. Devilez, M. Pianta, B. Stout, N. Bonod, et al., "Direct imaging of photonic nanojets," Optics Express, vol. 16, pp. 6930-6940, 2008.

[6] Z. Chen, X. Li, A. Taflove, and V. Backman, "Backscattering enhancement of

light by nanoparticles positioned in localized optical intensity peaks," Applied Optics, vol. 45, pp. 633-638, 2006.

[7] Z. Wang, W. Guo, L. Li, B. Luk'yanchuk, A. Khan, Z. Liu, et al., "Optical virtual imaging at 50 nm lateral resolution with a white-light nanoscope," Nature Communications, vol. 2, pp. 1211-1218, 2011.

[8] P. K. Upputuri, Z. Wu, L. Gong, C. K. Ong, and H. Wang, "Super-resolution coherent anti-Stokes Raman scattering microscopy with photonic nanojets," Optics Express, vol. 22, pp. 12890-12899, 2014.

[9] S. Lecler, S. Haacke, N. Lecong, O. Cregut, J. L. Rehspringer, and C. Hirlimann, "Photonic jet driven non-linear optics: example of two-photon fluorescence enhancement by dielectric microspheres," Optics Express, vol. 15, pp. 4935-4942, 2007.

[10] D. Gérard, J. Wenger, A. Devilez, D. Gachet, B. Stout, N. Bonod, et al., "Strong electromagnetic confinement near dielectric microspheres to enhance single-molecule fluorescence," Optics Express, vol. 16, pp. 15297-15303, 2008.

[11] S. C. Kong, A. V. Sahakian, A. Heifetz, A. Taflove, and V. Backman, "Robust detection of deeply subwavelength pits in simulated optical data-storage disks using photonic jets," Applied Physics Letters, vol. 92, 2008.

[12] A. Darafsheh, A. Fardad, N. M. Fried, A. N. Antoszyk, H. S. Ying, and V. N. Astratov, "Contact focusing multimodal microprobes for ultraprecise laser tissue surgery," Optics Express, vol. 19, pp. 3440-3448, 2011.

[13] D. J. Hwang, C. P. Grigoropoulos, and T. Y. Choi, "Efficiency of silicon micromachining by femtosecond laser pulses in ambient air," Journal of Applied Physics, vol. 99, 2006.

[14] E. McLeod and C. B. Arnold, "Subwavelength direct-write nanopatterning using optically trapped microspheres," Nature Nanotechnology, vol. 3, pp. 413-417, 2008.

SUMMARY

1. Introduction

In material processing, a micrometer size etching is commonly subjected to photo-lithography or ultra-short pulsed laser that need complex processes or expensive production costs. The photonic jet (PJ) has interest to propose cheaper costs. So, we consider to choose nanosecond pulsed near-infrared (ns NIR) lasers: a Nd:YAG laser and a YLIA fiber laser, to advocate the proposal, because these lasers are commonly used in industrial processes for their quite cheap price and their availability of well-packaged sources. These lasers can realize direct laser etching on silicon wafer at typically around 50 µm. Yet, by applying PJ we demonstrated the potential of decreasing this size and also allowing ns NIR laser to etch a glass slide. Hence, the main objective of this thesis is to propose PJ as a new way to decrease direct laser etching of ns NIR laser in industrial applications. The PJ's feasibility is then assessed logically by both simulations and experiments. And, since we use glass microspheres and optical fiber to generate PJs, the thesis might be divided into two parts accordingly. But it will be commenced with a briefly preview on the PJ.

A. The photonic jet: field enhancement and diffraction limit

The first article proposing a novel lithography technique by applying sphere-enhanced laser was published in 2000. It reported subwavelength structures on Si (100) using 0.5 µm silica spheres and 200 pulses of 23 ns ultraviolet laser, whereas without spheres this laser setting cannot damage the surface. Some articles have also reported the similar structures which is capable to go beyond the diffraction limit of optical system. In 2004 this phenomenon was called photonic nanojet or we simply call it photonic jet (PJ). It is defined as a high localized non-evanescent propagating beam generated at the shadow-side of a micrometric dielectric sphere or cylinder. This naming is necessary to distinguish it from already well-known near-field optics; namely: (1) it is a non-evanescent propagating beam that has sub-wavelength width along a pathway

which can extend to more than ~2λ; (2) it's minimum full-width at half maximum (FWHM) can be smaller than the classical diffraction limit; (3) it is non-resonant phenomenon; (4) it has a high intensity – the enhancemen of the incident wave intensity can be more than 200 times. Hence, the parameters concerned in micro-etching are: (1) intensity concentration factor; (2) FWHM; (3) the position of the highest intensity from the sphere; and (4) the length of PJ.

B. Photonic jet validations and material's interaction

PJ's exhibition can be conducted by direct or indirect observation. Capturing the PJ using such apparatus like a confocal microscope for visible range or an antenna for radio/microwave frequency is direct observation. Indirect observation is acquired from the effect of PJ, such as a marking on a material. Some articles have reported this marking, one of them is mentioned above. The authors called the phenomenon resulting the marking as particle/micro-sphere enhanced optical irradiation or optical/local field enhancement. And, we used the similar method to study PJ–material interaction as the basis of our thesis.

C. Potential applications of photonic jet

There are many PJ's potential applications have been proposed and they will be reviewed briefly in chapter two of the theses, i.e.: microscopy, low-losses waveguide, laser surgery, fluorescence enhancement, nanoparticle detection, optical trapping, optical data storage and nano-sphere lithography/ patterning.

2. Photonic jet etching using glass-microsphere

It is the first part of our experiments. It will be detailed in chapter 3 of the thesis with the main objective: studying the PJ–material interaction. It is also accompanied by electric field simulations in the shadow side of glass microsphere (n_s=1.5) in free-space (n_s=1) for unitary incident plane-wave (E_o = 1 V/m and λ = 1 μm). The glass microsphere diameters we used are D_s = 4, 6, 24 and 35 μm. The PJ parameters obtained from simulations will then be compared with the etching features.

A. Experiment setup

Our experimental scheme was adapted from previous publications. Even so there are two main distinctive points:

1. First, the laser source we use is ns NIR lasers whilst previous reports used ultra-short pulsed or ultraviolet lasers. It is simply because our objective is to increase the lateral resolution of industrial ns NIR laser marking.
2. Second, the microspheres on substrate in our experiments are illuminated at defocused range of the laser beam so it can cover larger area and as many microspheres as possible can be illuminated at the same time.

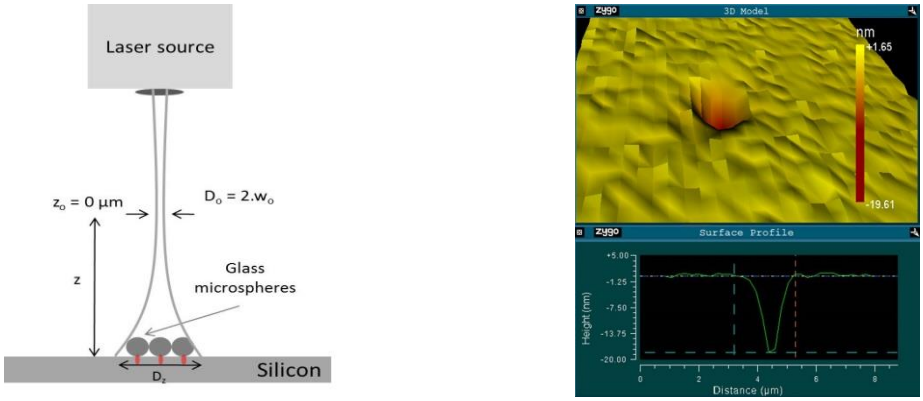

a. b.

Figure S.73. (a) The experimental schematic of PJ etching using glass (also barium-titanate) microspheres on silicon wafer and glass-slide as the sample material. (b) A typical etching shape of PJ etching on silicon wafer using 6 µm glass microspheres

Figure S.78a shows our experiments setup using microspheres and silicon wafer or glass-slide at defocused range of the laser beam (z). The microspheres are glass microsphere (n_s = 1.5) with mean diameter D_s = 4, 6, 24 and 35 µm, and barium-titanate microsphere (n_s=1.9) with mean diameter D_s= 42, 69, and 87 µm. We also prepared some cells to localize microspheres on the materials so it is easier to locate any etching mark. These cells also allowed us to apply laser illumination schemes for each corresponding cell. The laser illumination scheme variables we applied are frequency rates, number of pulses, defocussed positions and laser beam power. As for observing and measuring the PJ etching we used Olympus® Vanox-T microscope and Zygo® profilometer.

B. Photonic jet etching obtained on silicon wafer

- Using glass microsphere:

  Due to the laser illuminations some glass microspheres can be moved from their initial position. This event is more obvious observed for two large microspheres. PJ etching was obtained only for more than one laser pulse, just like on laser beam' focus range without sphere. The smallest PJ etching is $\overline{D}_{etch}$ = 1.1 $\pm$ 0.2 µm obtained using 4 µm a glass microsphere and the laser setting scheme was: two pulses of 28 ns and 1 mJ Nd:YAG laser at z = 21.6 mm. This is 44 times smaller than obtained without PJ. It is just we found no-correlation between etching size and number of laser pulses applied. But, for the two smaller glass microspheres: D_s = 4 and 6 µm, the lateral size (diameter) of PJ etching is in a good agreement with the FWHM obtained in the simulations.

- Using barium titanate microsphere

  Due to the laser illuminations, several barium titanate microspheres are also moved from their initial position; event for a single pulse illumination. Also some broken microspheres are observed. And, the shapes of PJ marking obtained are more complex and larger than ones yielded using glass microspheres. So, using barium titanate microsphere and ns NIR laser for PJ etching is out of the option.

C. Photonic jet etching on glass

- Despite of the low absorption properties of glass in infrared range, some PJ etching marks are obtained on glass slide using Nd:YAG laser and larger glass sphere: Ds = 24 and 35 µm or barium titanate microsphere.
- The typical shape of PJ etching is a crater like in the center (Figure S.78b), which was different to the ones on glass slide (Figure S.79a).

D. Conforming experiment results

One reason can explain this etching shape difference. For two large spheres, the PJ is not located on the sphere surface but a few micrometers further. Because of direct contact between microspheres and substrate sample, the interactions do not take place on the PJ beam but on the substrate's surface. So the simulations were re-run to acquire the intensity map on the surface of material. Then, a cross-section of intensity map is compared to the PJ profile by putting them in the same reference axis (Figure S.79).

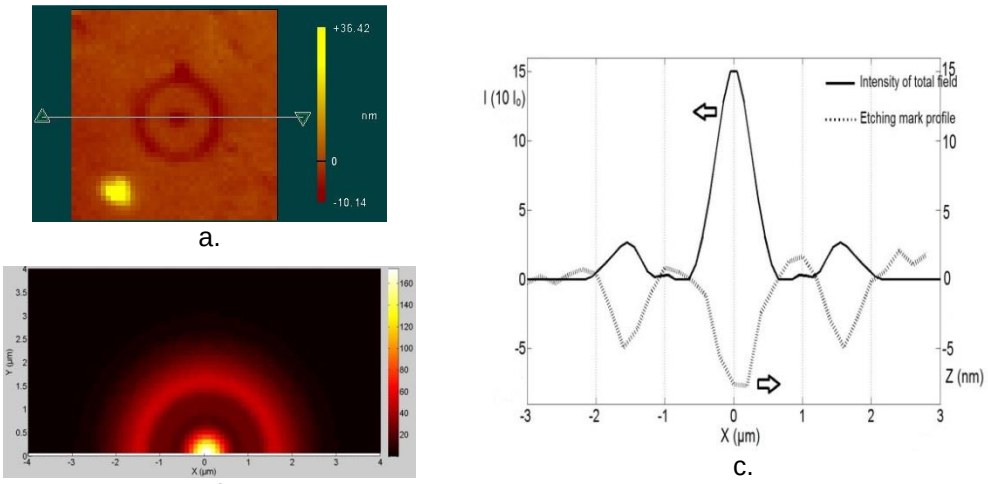

Figure S.74. (a) A PJ etching on glass slide taken by Zygo®. (b) The computed intensity distribution map on the surface. (c) The correspondence between PJ etching profile and intensity profile.

We also discuss the effect of damage threshold and the pulse duration by comparing PJ etching achieved using 160 ns YLIA laser and 28 ns Nd:YAG laser. The discussion was conducted by taking into account the laser-induced damage threshold (LIDT) of sample materials. Then, by considering the PJ etching diameter and applying a threshold on the intensity map so they both will have the same lateral size. On silicon wafer the threshold appears to be linked to the fluence, whereas on glass slide the maximum power density appears to be more relevant parameter.

3. Photonic jet etching using optical fiber with spheroid tip

There are three main issues can be delivered if we use optical fiber for PJ etching instead of a microsphere:

1) Mobile action; by moving the optical fiber to produce etching-line/curve and can adapt to large scale coverage area.
2) Precision; by controlling the optical fiber/sample distance to apply the PJ

precisely on the surface of material which also can control the etching depth and diameter.

3) Extra utility, e.g.: an optical fiber is reusable for many times and number of pulse applied can be as many as it necessary for any use.

We can say that we are the pioneer in realizing PJ etching using an fill-core optical fiber with spheroid-tipped, since no one has published any article related to this demonstration before. The tip shape chosen was tended to be more spheroid than ellipsoid. It was intended to keep the highest intensity of PJ not too close to the fiber tip. And finally we succeed realizing PJ using a multimode high-power optical fiber.

A. Wave-guide driven photonic jet

The possibility of PJ etching using optical fiber arise since our team found the possibility to have PJ at the outlet of waveguide. Figure S.80 shows one of our simulations for the case of 100 µm planar waveguide. For this thesis, we have considered multimode TEQS^{TM} coated fiber with double optical cladding, 200 µm core diameter and spheroid tip. Using this fiber the highest PJ's power is 7.2 watts.

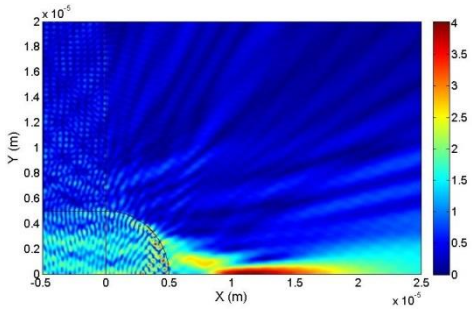

Figure S.75. Total electric field of a half planar-waveguide (diameter of 100 µm) with spherical tip

B. Realizing photonic jet etching on silicon using optical fiber with spheroid tip

When attempting PJ etching, we also conducted PJ – material interaction which is intended to acquire PJ parameters base on the etching mark on the material. The material in our concern is silicon wafer.

In this experiment, the end of optical fiber with spheroid tip was pasted to a XYZ positioning micro stage, so we can move the tip toward or backward the material (Figure S.81). And, some noticeable points were observed, e.g.:

- The highest intensity is around 75 $\pm$ 5 µm from the tip.
- The least number of pulses needed is 4 pulses.
- The smallest etching size on silicon is 17.5 µm.

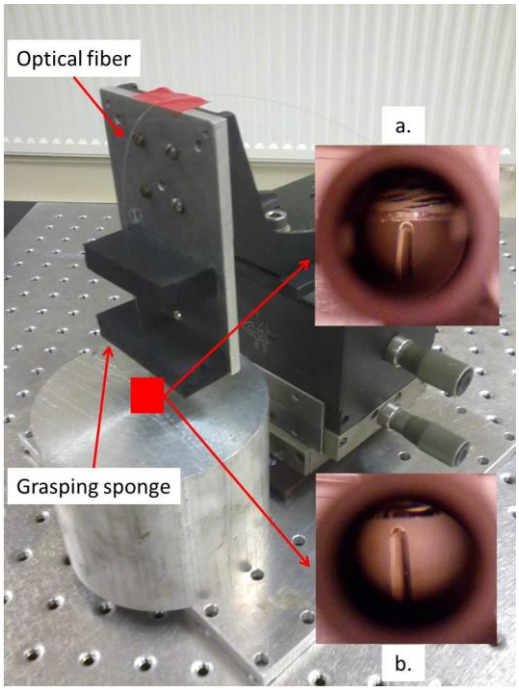

Figure S.76. Optical fiber with spheroid tip is grasp by sponges patched to a XYZ positioning micro stage and moved (a) toward or (b) backward the material

A. Confirming experimental results

Prior to the experiments, we had simulation results of planar waveguide-driven PJ with circular tip which is the two-dimension version of optical fiber with spheroid tip. For these simulations we used some variables/parameters:

- A fundamental mode of Gaussian beam propagates inside the waveguide (λ=1 µm; E_{max} = 1 V/m).
- The planar waveguide is located in free space (n_o = 1) with a core diameter of 200λ, n_{core} = 1.457 and first optical cladding n_{cladd} = 1.44.
- The ratio between major and minor axis for circular tip is 1 with the Bézier's curvature weight w = 0.707 (close to circular shape).

Based upon simulations, there are two important remarks:

1) The highest intensity is located at 156 µm from the tip, which is in a good agreement with the experiment.
2) The FWHM is 1.2 µm, which mean the smallest PJ etching is almost 15 times larger than FWHM.

The second remark draw us more attention. We assumed it relates to the mode propagates inside the waveguide, because in simulations we only considered the fundamental mode (with Gaussian profile) whereas in experiments a multimode optical fiber was used. To check this assumption we ran other simulations applying different modes. The simulations show other propagation mode have off-axis highest intensity. These can yield larger etching mark. The PJ's FWHM for a multimode optical fiber depends on its numerical aperture (NA). Therefore, in order to obtain smaller PJ etching we can use (1) single-mode optical fiber, (2) multimode fiber with low NA or (2) to excite only the weak order modes of a multimode optical fiber.

4. Conclusions and perspectives

Based upon our researches, we draw up three conclusions, e.g.:

1) PJ allows high beam concentration; in case of using ns NIR laser and glass microspheres: it can etch silicon wafer 44 times smaller than without PJ and it allows a ns NIR laser to etch glass
2) The lateral shape and size of PJ etching can be estimated using electromagnetic simulation in free space by taking into account fluence threshold for silicon and maximum power density for glass slide.
3) We have demonstrated the first PJ etching using an optical fiber with spheroid tip on silicon. Even though the obtained etching size is not as small as estimated, some facts have been disclosed.

Further, after succeeding PJ etching we have suggestions e.g.:

1) In order to obtain smaller lateral size of PJ etching using optical fiber with spheroid tip, some parameters must be considered, e.g.:
   a. The laser source injected into the optical fiber ought to excite only the weak order mode for the optical fiber.
   b. Multimode optical fibers with low NA have to be considered.
   c. Single-mode fibers also have to be considered.
2) Finally, we can put the optical fiber with spheroid tip on an actuator to realize a dynamic PJ etching that can write on any substrate material.

5. Publications

1. "Photonic jet out of optical fiber: potential for laser with matter interaction", S. Lecler, **A. Abdurrochman**, J. Zelgowski, F. Mermet, B. Tumbelaka and J. Fontaine, Applied Surface Science (Submitted).
2. "Photonic jet breakthrough for direct laser micro-processing using near-IR nanosecond laser", **A. Abdurrochman**, S. Lecler, F. Mermet, B.Tumbelaka, B. Serio and J. Fontaine, **Applied Optics**, vol. 53, pp. 7202-7207, October 2014.

6. Communications

1. "Photonic jet etching: justifying the shape of optical fiber tip", **A. Abdurrochman**, J. Zelgowski, S. Lecler, F. Mermet, B. Tumbelaka and J. Fontaine, **The PIPS 2015** (Padjadjaran International Physics Symposium), Bandung – Indonesia, 2-3 September 2015.
2. "Photonic jet out of optical fiber: potential for laser with matter interaction", S. Lecler, **A. Abdurrochman**, J. Zelgowski, F. Mermet, B. Tumbelaka and J. Fontaine, **The 2015 E-MRS Spring Meeting**, Lille – France, 11-15 May, 2015.
3. "Photonic jets for micro-etching", **A. Abdurrochman**, S. Lecler, F. Mermet, J. Fontaine, and B. Tumbelaka, **International Conference on Physics**, Yogyakarta – Indonesia , 25-26 August, 2014.
4. "Photonic jet to improve the lateral resolution of laser etching", **A. Abdurrochman**, S. Lecler, J. Fontaine, F. Mermet, P. Meyrueis, B. Tumbelaka and P. Montgomery, **SPIE-Photonics Europe 2014**, Brussel – Belgium, 14-17 April, 2014.
5. "Increasing the lateral resolution of direct laser surface micro-processing using photonic jet", **A. Abdurrochman**, S. Lecler, F. Mermet, B.Y. Tumbelaka, P. Meyrueis and J. Fontaine, **JNTE 2013** (Journée Nationale des Technologies Emergentes en micro et nano fabrication), Evian-les-Bains – France, 21-23 May 2013.